

Computational Fluid Dynamics Modelling
Of
Wind Turbine Wake Losses
In
Large Offshore Wind Farms,
Incorporating Atmospheric Stability

By
Peter Argyle

A Doctoral Thesis

Submitted in partial fulfilment of the requirements for the award of
Doctor of Philosophy of Loughborough University

December 2014

© by Peter Argyle 2014

Abstract

Offshore wind power generation is projected to be the United Kingdom's largest contributor to the European Union's 2020 renewable energy target, with large numbers of wind turbines clustered into wind farms with capacities comparable to fossil fuelled power stations. The degree of power loss caused by the wake affected region behind each turbine is known to vary under different atmospheric stability conditions. Accurately predicting these losses for a variety of likely scenarios before new farms are built can significantly reduce the financial risk of private investment.

The aim of this work was to investigate the structure of the offshore atmosphere and incorporate the findings relating to atmospheric stability into Computational Fluid Dynamics (CFD) simulations of large offshore wind farms to reduce financial investment risk in non-neutral stability conditions. This work incorporates three meteorologically established methods of calculating stability conditions into CFD simulations of large offshore wind farms using the Monin-Obukhov Similarity Theory (MOST). As MOST ideally requires meteorological parameters measured on-site using a mast for extended periods of time to obtain even a small collection of validation data, alternative methods of describing atmospheric conditions and corresponding wake behaviour are investigated which only require data obtainable by LiDAR. This has the potential to reduce the length of data collection campaigns, whilst also using more flexible instruments and thus increasing cost efficiency.

The software front-end tool Windmodeller, which drives the ANSYS CFX software, is used to benchmark four separate two-equation turbulence models, each assuming neutral atmospheric stability conditions. Production data from four European offshore wind farms are used for validation purposes. Of these models, the Shear Stress Transport (SST) model consistently performed the worst, whilst modifying the RANS turbulence constant, C_μ , only alters the location within a line of turbines where the standard $k-\varepsilon$ model was most accurate. The unsteady RANS model variation, which incorporates both the Coriolis effect and a stably stratified capping layer, was found

to have the smallest root-mean-squared error values for the largest wind farm and so was chosen to form the basis of the simulations incorporating atmospheric stability.

The Obukhov Length required for MOST is incorporated into the CFD simulations using surface fluxes, water temperatures and atmospheric thermal gradients. There are only small variations in simulation accuracy between methods when simulating Neutral conditions, with the thermal gradient method performing best. Under stable conditions the sea surface temperature approach is most accurate, although it is also the least accurate under unstable conditions and was unable to generate the more extreme Unstable conditions. Although the flux method was less accurate than the gradient method in absolute terms, the variance of its errors at individual turbine locations was consistently smaller. The validation process for using MOST techniques was complicated by a lack of sufficient field data after the rigorous filtering required by the theory's assumptions.

The preliminary work using alternative methods of describing atmospheric conditions within CFD simulations did not suffer from a lack of validation data, but was unsuccessful at maintaining the required wind shear profiles across the whole domain. Recommendations are made to improve control over these parameters with models such as unsteady RANS, and to find a suitable successor to the actuator disc theory now wind shear values across a turbine are becoming significant.

Declaration of Originality

This is to certify that I am responsible for the work submitted in this thesis, that the original work is my own except as specified in acknowledgements or in footnotes and that neither the thesis nor the original work contained therein has been submitted to this or any other institution for a degree.

..... (Signed)

..... (Date)

Acknowledgements

I would like to thank the BMU (Bundesministerium fuer Umwelt, Federal Ministry for the Environment, Nature Conservation and Nuclear Safety) and the PTJ (Projekttraeger Juelich, project executing organisation) for providing data from the FINO1 and FINO3 meteorological masts. I would also like to thank E.ON for sponsoring this research through an EPSRC CASE award and the EPSRC Supergen Wind Energy Technologies consortium (grant number: EP/H018662/1) for additional support.

Special thanks are also due to Prof. Simon Watson who supervised this project, co-authored many academic journal and conference papers and posters, and introduced me to the powers of SQL and CFD.

I am also very grateful to Prof. Malcolm Cook, Dr. Christiane Montavon, Dr. Cian Desmond, Mr. Luca Lavaroni, and the online community at stackoverflow.com for helping me overcome cryptic software error messages.

Thank you to the people and intellectual webcomics whose humour, wisdom, and companionship have helped support and inspire me through the challenges, specifically WXCD.com and phdcomics.com.

Thank you to the people of Loughborough, particularly members of The Well Church who provided a welcoming and friendly environment in which to study. Your kindness and competitive board gaming has helped me through countless times of stress.

Finally, but definitely the most important, I would like to thank my wife Elizabeth for constant support, strength, grace, patience and dedication across six time zones.

Table of Contents

Section	Title	Page
Chapter One	Thesis Map	1
Chapter Two	The Offshore Atmosphere: Background and Current Theory	3
2.1	The Offshore Advantage	3
2.2	Offshore Data	4
2.3	Structure of the Atmosphere	6
2.3.1	The Marine Atmosphere	10
2.3.2	The Coastal Atmosphere	12
2.4	Monin-Obukhov Similarity Theory	13
2.4.1	Calculating L using the Flux Method	16
2.4.2	Calculating L using the Bulk Method	17
2.4.3	Calculating L using the Gradient Method	18
2.5	Appropriate Measurements	18
2.6	The Significance of Atmospheric Stability for Wind Energy	23
Chapter Three	Analysis of North Sea Data	27
3.1	Calculating Stability from Wind Speed Alone	27
3.2	Data Sets	27
3.3	Stability Categorisation and Frequency	29
3.4	Wind Profile Gradient Analysis	33
3.5	Turbulence Intensity	35
3.6	Combining Shear with Turbulence	36
3.7	Study Conclusions	41
Chapter Four	Benchmarking CFD Models of Large Wind Farms in the Neutrally Stratified Offshore Atmosphere	43
4.1	Introduction	43
4.2	Wake Modelling Review	44
4.3	An Overview of CFD	50
4.3.1	Actuator Disc Theory	54
4.3.2	Introduction to Windmodeller	56
4.4	Benchmarking Windmodeller	59
4.4.1	SST RANS	69
4.4.2	$k-\varepsilon$ RANS	70
4.4.3	Modified $k-\varepsilon$ RANS	72
4.4.4	URANS	73
4.4.5	Comparison of Models	77
4.4.6	Comparison using Neutral Stability Filtered Data	79
Chapter Five	Modelling of Large Wind Farms in the Offshore Atmosphere with Various Stability Conditions	81
5.1	Introduction	81
5.2	Review	81
5.3	Modelling Using Variable Values of L	82
5.3.1	Validation Data	83
5.3.2	Production Variability due to Stability	88
5.3.3	Modelling Stability via Domain Surface Parameters	90

5.3.3.1	Surface Heat Flux	91
5.3.3.2	Sea Surface Temperature	93
5.3.4	Modelling via Gradient Richardson Numbers	96
5.3.5	Comparison of Richardson Number Methods	100
5.3.6	Comparison of Model Accuracy With and Without Stability	104
5.3.6.1	Possible Over Stipulation of Meteorological Conditions	105
5.3.6.2	Model Results Comparison	114
5.4	Modelling Atmospheric Stability Without Using L	118
5.4.1	Validation Data	119
5.4.2	Simulating Stability by Varying Only the Wind Shear	121
5.4.3	Simulating Stability by Varying Only the TI	124
5.4.4	Combining Shear and TI Changes	128
Chapter Six	Summary and Conclusion	131
6.1	Summary of Chapters 2 and 3	131
6.2	Summary of Chapter 4	132
6.3	Summary of Chapter 5	135
6.4	Conclusion	139
Appendix A	A Paper Published in the Journal of Wind Engineering and Industrial Aerodynamics	A1
Appendix B	Simulation Mesh Images	A26
Bibliography		

List of Figures

Figure	Caption	Page
Figure 2.1	Illustration of the lower atmosphere showing key layers (heights are meteorologically accepted approximations and not to scale). Layer boundary heights are variable in time and space.	6
Figure 2.2	Idealistic speed and thermal profiles through the ABL for onshore daytime conditions. Note the wind speed profile indicates the theoretical geostrophic case if friction was not accounted for. For a marine approximation, narrow the residual layer by reducing the height of the entrainment zone and Z_{ABL} . Layer boundary heights and profiles (of U and θ_v) are not to scale and vary in time and space.	9
Figure 2.3	Locations of offshore meteorological masts which supplied atmospheric data for this work, not associated to any fully-commissioned wind farm. A=FINO1, B=FINO2, C=FINO3, D=Humber Gateway, E=Shell Flats. Note there are two masts at the Shell Flats site, but on account of their close proximity to each other, they are shown here with only one marker.	19
Figure 2.4	Averaged wind profiles from the Humber Gateway offshore mast under various stability conditions, given a wind speed of 7.5ms ⁻¹ at 33m. Data has been filtered to only include marine directions and events which satisfy the steady state homogeneous atmospheric assumptions required by MOST, see reference [17]. For reference, an idealised MOST profile using equation 2.5 is also shown.	24
Figure 3.1	Frequency distribution of atmospheric stability split into 5 categories	30
Figure 3.2	Frequency distribution of atmospheric stability split into 7 categories	31
Figure 3.3	Wind shear for the five case studies filtered by five stability categories	33
Figure 3.4	Wind shear for the five case studies filtered by seven stability categories	33
Figure 3.5	Turbulence intensity filtered by stability category	36
Figure 3.6	Correlations between TI , α and L	37
Figure 3.7	Correlations between TI , α and L with new stability regions highlighted	39
Figure 3.8	Frequency distribution of atmospheric stability split by defining parameters in Table 3.5	40
Figure 3.9	Locations of suggested simulation values in Table 3.6 with measured events.	41
Figure 4.1	Mesh geometry showing both inner and outer mesh blocks.	57
Figure 4.2	Locations offshore wind farms which supplied production data for this work. A=Horns Rev, B=Nysted, C=Scroby Sands, D=Robin Rigg.	60
Figure 4.3	Layout of turbines (red dots) and meteorological masts/LiDAR (green dots) at each of the four offshore wind farms which supplied production data for this work. The 'key turbine' used as a reference for free-stream wind direction and speed is highlighted by a blue circle. All dots are the same size and do not represent the scale of object they symbolise. Objects are located at the centre of a dot and distances between objects are indicated by the scale (in km) on the diagram edges. In all four plots, North is to the top of the image.	61
Figure 4.4	Plots of wind turbine power curves (blue) and their corresponding thrust coefficients (green) according to wind speed. Since Windmodeller struggled to converge any simulation using the sharp variations in thrust coefficient for turbines at the Nysted wind farm, so an alternative, smoothed curve (red dots) was used as an acceptable substitute.	63
Figure 4.5	Layout of turbines at the Robin Rigg offshore wind farm. Highlighted (black) are the turbines B2 and C3 which had significantly fewer events suitable for validation purposes and so were excluded from the analysis along with the turbines downstream of them. Highlighted (blue) are the free-stream turbines for case studies with wind direction 249° (indicated by arrow) showing that whilst they are not directly in the wake of an upstream machine, at least three turbines are likely to be effected by venturi processes as air flows between two other turbines. There are also five turbines which may be partially affected in this way as they are located diagonally behind at least one other machine.	64
Figure 4.6	Plots showing measured power generated by each turbine normalised by the power generated by a turbine in the free-stream. Top left shows production data averaged across turbines in the six central rows at Horns Rev for case HR270 with the position number referring to each turbine's position in the 'down the line' row with position one being the free-stream turbine, Top right shows production	66

	data from Nysted case N180 in blue and N278 in red. Bottom left shown production data from Scroby Sands case SS77 in blue and SS90 in red. Bottom right shows production data from Robin Rigg case RR204 in red and RR249 in blue.	
Figure 4.7	Plots of averaged power ratios through the farm. Edge effects are assumed to be negligible, considering the 5° direction bin and it dramatically simplifies calculations for Robin Rigg with its non-parallel boundary and two erroneous turbines. Position number referring to each turbine's position in the 'down the line' row with position one being the free-stream turbine. Due to farm layout, free-stream turbines for RR249 may experience some venturi effects as suggested in Figure 4.5.	68
Figure 4.8	Results from SST simulations of the four farms marked as "+" symbols while dots denote the measured values for each farm. Top left shows Horns Rev for case HR270, top right shows Nysted case N180 in blue and N278 in red, bottom left shown Scroby Sands case SS77 in blue and SS90 in red and bottom right shows Robin Rigg case RR204 in red and RR249 in blue.	69
Figure 4.9	Results from initial $k-\epsilon$ simulations of the four farms marked as "+" symbols while dots denote the measured values for each farm. Top left shows Horns Rev for case HR270, top right shows Nysted case N180 in blue and N278 in red, bottom left shown Scroby Sands case SS77 in blue and SS90 in red and bottom right shows Robin Rigg case RR204 in red and RR249 in blue.	71
Figure 4.10	Results from the Modified $k-\epsilon$ simulations of the four farms marked as "+" symbols while dots denote the measured values for each farm. Top left shows Horns Rev for case HR270, top right shows Nysted case N180 in blue and N278 in red, bottom left shown Scroby Sands case SS77 in blue and SS90 in red and bottom right shows Robin Rigg case RR204 in red and RR249 in blue.	72
Figure 4.11	Results from the different options for URANS model simulations of case N278 ("+" symbols) using the colours described in Table 4.4. Measured values from the Nysted wind farm are shown as black dots. For comparison, the results from the standard $k-\epsilon$ RANS simulations from section 4.4.2 are also displayed (black "+" symbols).	75
Figure 4.12	Results from the URANS simulations of the four farms marked as "+" symbols while dots denote the measured values for each farm. Top left shows Horns Rev for case HR270, top right shows Nysted case N180 in blue and N278 in red, bottom left shown Scroby Sands case SS77 in blue and SS90 in red and bottom right shows Robin Rigg case RR204 in red and RR249 in blue.	76
Figure 4.13	Rout Mean Squared (RMS) error for each of the seven cases in Figure 4.8 to Figure 4.12.	78
Figure 4.14	Standard Deviation (σ) for each of the seven cases in Figure 4.8 to Figure 4.12.	78
Figure 4.15	Comparison of the four models against unfiltered data and data filtered for neutral stability. Unfiltered measurements are represented by black dots whilst measurements filtered to ensure neutral stability are shown as black 'X' symbols. Model results are represented by '+' symbols, SST in red, $k-\epsilon$ in green, Modified $k-\epsilon$ in blue and URANS in magenta.	80
Figure 5.1	Comparison of bulk stability calculated at masts 2 and 3 at the Nysted farm.	86
Figure 5.2	Comparison of gradient stability calculated at masts 1 and 2 at the Nysted farm.	87
Figure 5.3	Plots of averaged power ratios through the farms, similar to those in Chapter 2. Production from turbines on the farm edges have been ignored to remove edge effects. Turbine position number refers to the location of each turbine in the 'down the line' row with position one being the free-stream turbine. There is no plot of N278S as there were no events coinciding within the set limits of incident wind speed, direction and stability without occurrences of individual turbine downtime.	88
Figure 5.4	Comparison of measured production data against with simulations using a surface heat flux to generate three Obukhov lengths for the Stable (red, $L = 105m$), Neutral (green, $L = \pm 1000m$) and Unstable (blue, $L = -125m$) atmospheres as measured at the relevant mast locations.	92
Figure 5.5	Temperature profiles at the Nysted met mast 2 showing non-linearity between air temperature (measured at 10m and 65m) and sea temperature (measured at -2m). Left shows profiles with L calculated via the Bulk method whilst Right shows profiles with L calculated via the Gradient method. Event profiles have been filtered to include only wind directions $180 \pm 5^\circ$ and $278 \pm 5^\circ$ with hub height wind speeds $8 \pm 0.5 \text{ms}^{-1}$ and are displayed according to their values of L . Red=Stable ($L = 105m$), Green=Neutral ($L = \pm 1000m$) Blue=Unstable ($L = -125m$). Note, there were no Unstable events with required wind speed and directions using the Bulk method.	94

Figure 5.6	Results from simulations using a sea surface temperature to replicate Obukhov lengths for the Stable (red, $L = 105\text{m}$), Neutral (green, $L = \pm 1000\text{m}$) and Unstable (blue, $L = -125\text{m}$) atmospheres as measured at the relevant mast locations.	95
Figure 5.7	Cartoon of the thermal inlet profile for a default URANS simulation (left) and the modified profile for simulations using the gradient method of calculating L (centre) where a constant value of θ is defined in the θ_{upper} region above a separate constant value of θ defined in the θ_{lower} region. As the simulated flow progresses through the domain, the difference values of θ in the two sub-layers interact and merge into smooth gradients (right) before it reaches the mast where stability is classified. The vertical axis is not to scale.	98
Figure 5.8	Results from simulations using variations in air inlet temperatures to generate three Obukhov lengths for the Stable (red, $L = 105\text{m}$), Neutral (green, $L = \pm 1000\text{m}$) and Unstable (blue, $L = -125\text{m}$) atmospheres.	99
Figure 5.9	Combined results from the three Richardson Number simulation techniques showing the accuracy as a function of measured power generation at each farm using equation 3.3.5.1. Note there are no error statistics for case N278S as there were no measured events suitable for comparison.	100
Figure 5.10	Combined results from the three Richardson Number simulation techniques showing the total standard deviation between the simulated and measured power generated by each turbine. Note there are no statistics for case N278S as there were no measured events available for comparison.	103
Figure 5.11	Power ratios measured at the Nysted wind farm during each of the ten-minute stability case study events with a wind direction of $278 \pm 5^\circ$. The graph on the left shows measurements from row 5 (the centre of the farm) whilst the right graph shows power ratios averaged across all fully operational turbine rows (excluding the turbines on the farm's edges parallel to the wind direction) during the same two events.	106
Figure 5.12	Simulated power ratios (blue) for the Nysted wind farm for both of the ten-minute stability case study events. The graph on the left shows results from row 5 (the centre of the farm) whilst the right graph shows results averaged across the rows used to calculate the corresponding validation data (black).	107
Figure 5.13	Comparison of measured (black) and simulated (blue) wind speed (top) and temperature (bottom) profiles for both events. The standard deviations of measurements taken during the ten minute intervals are also shown for reference, although the variance in temperature is small. Note that the 55m wind speed measurement for event 2 was 0.3ms^{-1} with a variance of 0ms^{-1} , suggesting a fault with the instrument.	110
Figure 5.14	Comparison of measured power ratios (black filled squares) against five different simulation configurations: the 'URANS gradient' simulation (black open circles) are the same simulations used earlier in this section using the gradient method of calculating L , the other simulation results (various coloured plus symbols) show results from models used in Chapter 4 with assumed neutral stability. Simulation results have been filtered to only include the rows of ADs which represent the operational turbine rows in the farm during each ten-minute period.	111
Figure 5.15	Three graphs showing the power ratio results of the URANS model from Chapter 4 alongside the stability simulations from earlier in this chapter utilising the Gradient approach. The relevant validation data for each simulation are also plotted for reference. Anticlockwise from top: westerly flow at the Horns Rev offshore wind farm, westerly flow at the Nysted offshore wind farm, southerly flow at the Nysted offshore wind farm.	115
Figure 5.16	To increase clarity, these three graphs show the difference in power ratios between simulated events and their corresponding validation data where positive values indicate the simulation predicted greater than measured wake losses while negative values indicate where the simulation under predicted the wake losses. Anticlockwise from top: westerly flow at the Horns Rev offshore wind farm, westerly flow at the Nysted offshore wind farm, southerly flow at the Nysted offshore wind farm.	117
Figure 5.17	Normalised power production at the Robin Rigg and Nysted Wind farms, filtered by free-stream wind shear as indicated by atmospheric stability category: Stable (red, $\alpha = 0.2$), Neutral (green, $\alpha = 0.1$) and Unstable (blue, $\alpha = 0.05$).	122
Figure 5.18	Normalised power production at the Robin Rigg and Nysted Wind farms, averaged by free-stream turbulence intensity as indicated by atmospheric stability categories: Stable (red, $TI = 5\%$), Neutral (green, $TI = 6\%$) and Unstable (blue, $TI = 7\%$).	125
Figure 5.19	Normalised power production at the Robin Rigg and Nysted Wind farms,	127

	averaged by free-stream turbulence intensity as indicated by atmospheric stability categories: Stable (red, $TI = 5\%$), Neutral (green, $TI = 6\%$) and Unstable (blue, $TI = 7\%$). Results from $k - \varepsilon$ simulations are shown as plus (+) symbols whilst real-world measurements are shown as dots.	
Figure 5.20	Measurements of Power Ratio from the Nysted offshore wind farm where events are filtered by both α and TI to generate the three stability categories according to Table 5.6.	129
Figure 6.1	Comparison between stability classification techniques. The left graph shows measured Power Ratio for westerly flow at the Horns Rev wind farm with events filtered by L as described in section 3.3.2. The right graph shows measured Power Ratio for westerly flow at the Nysted wind farm with events filtered by both α and TI as described in section 3.4.2.	139
Figure A1	Distribution of stability for each case study dataset.	A7
Figure A2	Distribution of stability at FINO1 as calculated via the gradient method, compared alongside results from reference [11] using their flux and bulk methods. For consistency with [11], Cases A, B and C have been filtered by wind direction to only include the sector 240° - 360° .	A8
Figure A3	Virtual potential temperatures at FINO1 (top) and FINO3 (bottom) by direction sector.	A10
Figure A4	Absolute temperature profiles at FINO1 by direction sector.	A11
Figure A5	Wind speed profiles under different atmospheric conditions – top left = very unstable, top right = unstable, centre = neutral, bottom left = stable, bottom right = very stable. Solid lines show profiles from FINO1, while dotted lines represent FINO3 profiles.	A13
Figure A6	Scatter plots comparing the ratios of wind speeds at FINO1 (left) and FINO3 (right) at heights indicated on the left axis against corresponding predicted ratios (black lines) using equation 5. Binned average values are shown as crosses with error bars signifying ± 1 standard deviation about each bin.	A14
Figure A7	Scatter plots as shown in Figure A6 broken down by wind speeds as measured at the top of the two anemometers, with high wind speed ($u > 14\text{ms}^{-1}$) events on the left, low ($u < 8\text{ms}^{-1}$) wind speed events on the right and intermediate wind speed ($8 < u < 14\text{ms}^{-1}$) events in the centre.	A17
Figure A8	Wind Roses for FINO1 (left) and FINO3 (right). The rose for FINO1 clearly shows the effect of filtering to account for mast shadow over a large sector around 310° whilst the FINO3 rose appears less effected by shadow as the narrow filtering does not occupy a whole segment at 170° .	A18
Figure A9	Wind Roses for FINO1 (left) and FINO3 (right) for each of the six case studies split into the five stability categories such that: top left: VU, top right: U, centre: N, bottom left: S, bottom right: VS. Wind directions were measured at 90m and 100m at FINO1 and FINO3 respectively.	A20
Figure A10	Scatter plots as in Figure A6 split into directions with a longer offshore fetch ($> 200\text{km}$) and shorter offshore fetch ($< 200\text{km}$) as measured by the wind vanes at the top of each mast. The black lines show the MOST expected shear values.	A22
Figure B1	Horizontal mesh structure in the central 10km square region for each of the four wind farms, clockwise from top left: Horns Rev, Nysted, Robin Rigg and Scroby Sands. Due to image scale and resolution, the light gray cell areas are 50m by 50m whilst the dark regions are areas of much higher mesh resolution around each actuator disk as Windmodeller has refined the mesh around each AD. Each mesh is shown at the relevant farm's hub height.	A26
Figure B2	Vertical mesh structure in the central 10km square region. Due to turbine layout complications, cross-sections from only the farms Nysted (top, facing due east) and Horns Rev (bottom, facing due north) are shown. Each mesh is shown as a slice through the centre of a turbine line.	A27
Figure B3	Horizontal mesh structure around actuator disks from the simulations of the Horns Rev (top) and Robin Rigg (bottom) farms. Note that the mesh refinement process does not always result in symmetrical mesh structures around each disk owing to flow direction and complexity. For reference, the larger squares are 50m in length along each edge.	A27
Figure B4	Vertical mesh structure around actuator disks from the front (top) and side (bottom). Note that the mesh refinement process does not always result in symmetrical mesh structures around each disk owing to flow direction and complexity. For reference, the largest cells are 50m wide and the height of the cells outside of the mesh-adaption regions increase with height from 2m at the domain surface.	A28

List of Tables

Table	Caption	Page
Table 2.1	Typical Definition of stability categories	16
Table 2.2	Alternative Definition of stability categories	16
Table 2.3	Comparison of offshore met masts and their installed instrumentation. Additional instruments (such as rain gauges) are present at some masts, although these have been left out of this table as their measurements were not used as part of this work. Data availability is not always uninterrupted between dates and contains sections of erroneous recordings.	20
Table 3.1	Relevant measurement heights for each case study	28
Table 3.2	Atmospheric stability defined as five symmetric categories	29
Table 3.3	Atmospheric stability defined as seven asymmetric categories	29
Table 3.4	Frequency of each stability category depending on assessment method (%)	30
Table 3.5	Atmospheric stability defined by TI and α	39
Table 3.6	Suggested input parameters for simulations	40
Table 4.1	Comparison of met masts associated with wind farms and their installed instrumentation. Additional instruments (such as rain gauges) are present at some masts, although these have been left out of this table as their measurements were not used as part of this work.	62
Table 4.2	Comparison of wind turbines installed at each of the four offshore wind farms.	63
Table 4.3	List of seven validation case studies for benchmarking	65
Table 4.4	List of four URANS configuration options	74
Table 5.1	Range and representative Obukhov lengths of stability groups for simulation	84
Table 5.2	List of nine case studies for comparison	85
Table 5.3	Details of two ten-minute measured events, randomly selected from the Nysted validation data used in previous sections, displayed in Figure 5.11 below.	105
Table 5.4	Details of the two simulations compared below.	107
Table 5.5	Comparison of simulation accuracy defined as: the average of each turbine position's measured power ratio minus its simulated power ratio. Thus a positive value means the simulation over predicted the farm's output whilst a negative value shows an over prediction of wake losses.	116
Table 5.6	Values of meteorological parameters defining the three stability categories (without using L to define atmospheric conditions) and the range of values in measured field data they represent.	120
Table 5.7	List of nine case studies for comparison	121
Table A1	Heights of instruments used to measure the five variables necessary. An asterix implies the use of a sonic anemometer whilst numbers in brackets imply multiple instruments at specific heights.	A4
Table A2	Height in metres of temperature, humidity and wind speed measurements for each case study. †Temperature at 90m was estimated via linear interpolation between 70m and 100m.	A6
Table A3	Classification of atmospheric stability. The abbreviations are used to refer to specific stability conditions in figures throughout this work.	A6
Table A4	Variation in vertical wind speed ratio across different stability conditions, as calculated using equation 5, expressed as a percentage difference from values obtained using the standard $z_0 = 0.2\text{mm}$. Values of $10/L$ have been partitioned into bins based on one decimal place.	A14
Table A5	Average values of z_0 (in m) for each Case across the specified stability gates.	A16
Table A6	Standard deviation values of z_0 (in m) for each Case across the specified stability gates.	A16

Symbols

Symbol	Name	SI Base Units	Value
A	Empirical Constant		1.79
a	Area	m^2	
B	Empirical Constant		4.5
C_n	Empirical Constant		
C_p	Specific Heat Capacity of Air at Constant Pressure	$m^2s^{-2}K^{-1}$	1004.67
C_μ	Empirical Constant		0.09
$C_{1\varepsilon}$	Empirical Constant		1.44
$C_{2\varepsilon}$	Empirical Constant		1.92
c_1	Empirical Constant		
c_2	Empirical Constant		
D	Rotor Diameter	m	
E	Sum of Thermal (Internal) and Kinetic Energy	kgm^2s^{-2}	
f	Coriolis Parameter	s^{-1}	
G	Geostrophic Wind Speed	ms^{-1}	
g	Gravitational Acceleration	ms^{-2}	9.81
H_s	Surface Heat Flux	kgs^{-3}	
i	Specific Internal Energy	kgm^2s^{-2}	
k	Turbulent Kinetic Energy	m^2s^{-2}	
L	Obukhov Length	m	
P	Air Pressure	$kgm^{-1}s^{-2}$	
P_0	Reference Air Pressure	$kgm^{-1}s^{-2}$	100000
q	Turbulent Heat Flux	kgs^{-3}	
q_v	Specific Humidity	gkg^{-1}	
R	Gas Constant of Dry Air	$kgm^2s^{-2}K^{-1}mol^{-1}$	286.9
R_v	Water Vapour Gas Constant	$kgm^2s^{-2}K^{-1}mol^{-1}$	461.5
Ri	Richardson Number		
Ri_B	Bulk Richardson Number		
Ri_G	Gradient Richardson Number		
Ri_{Gcrit}	Critical Gradient Richardson Number		0.2
S_E	Source of Energy per Unit Volume per Unit Time	$kgm^{-1}s^{-3}$	
S_i	Source of Specific Internal Energy per Unit Time	$kgm^{-3}s^{-1}$	
S_{MX}	Source of Momentum in x co-ordinate direction	$kgms^{-1}$	
S_{MY}	Source of Momentum in y co-ordinate direction	$kgms^{-1}$	
S_{MZ}	Source of Momentum in z co-ordinate direction	$kgms^{-1}$	
T	Absolute Temperature	K	
T_0	Mean Temperature of Analysed Region	K	

T_{sea}	Bulk Sea Temperature	K	
T_v	Virtual Temperature	K	
TI	Turbulence Intensity		
TI_C	Critical Value of Turbulence Intensity		0.06
U	Horizontal Wind Speed	ms^{-1}	
u	Horizontal Wind Velocity in x co-ordinate direction	ms^{-1}	
u_a	Axial Flow Interference Factor		
u_z	Horizontal Wind Velocity in x co-ordinate direction at height z	ms^{-1}	
u_*	Friction Velocity	ms^{-1}	
v	Horizontal Wind Velocity in y co-ordinate direction	ms^{-1}	
w	Vertical Wind Velocity in z co-ordinate direction	ms^{-1}	
$\overline{w'T'}$	Turbulent Heat Flux	Kms^{-1}	
X	Distance From Coastline	m	
z	Height Above Sea Level	m	
z'	Reference Height for Richardson Number	m	
z_0	Surface Roughness	m	
z_{ABL}	Height of Atmospheric Boundary Layer	m	
z_{CABL}	Height of Developing Marine Atmospheric Boundary Layer	m	
z_{MABL}	Height of Marine Atmospheric Boundary Layer	m	
α	Wind Profile Shear Factor		
α_C	Critical Value of Wind Profile Shear Factor		0.1
α_c	Empirical Constant		0.0185
β	Empirical Constant		5
γ	A Fluctuating Property		
ϵ	Ratio of Gas Constants		0.622
ϵ	Eddy Dissipation Rate	m^2s^{-3}	
θ	Potential Temperature	K	
θ_v	Virtual Potential Temperature	K	
K	Von Karman Constant		0.4
μ	Dynamic Viscosity	$kgm^{-1}s^{-1}$	
ρ	Air Density	kgm^{-3}	
σ	Standard Deviation		
τ	Shear Stress	$kgm^{-1}s^{-2}$	
ϕ	Energy Dissipation Function	$kgm^{-3}s^{-1}$	
$\Psi_m(z/L)$	Universal Stability Function		
ω	Specific Turbulence Dissipation Rate	s^{-1}	

Acronyms

Abbreviation	Definition	Page first used
ABL	Atmospheric Boundary Layer	6
AD	Actuator Disc	47
AL	Actuator Line	48
asl	Above Sea Level	6
CFD	Computational Fluid Dynamics	43
DNS	Direct Numerical Simulation	46
LES	Large-Eddy Simulation	46
MABL	Marine Atmospheric Boundary Layer	10
MOST	Monin-Obukhov Similarity Theory	13
MSL	Marine Surface Layer	11
RANS	Reynolds-Averaged Navier-Stokes	46
RH	Relative Humidity	20
RL	Residual Layer	8
RMS	Root Mean Squared	77
SL	Surface Layer	7
SST	Shear Stress Transport	58
URANS	Unsteady Reynolds-Averaged Navier-Stokes	73

Chapter 1. Thesis Map

The aim of this work was to investigate the structure of the offshore atmosphere and incorporate the findings relating to atmospheric stability into Computational Fluid Dynamics (CFD) simulations of large offshore wind farms in order to reduce financial investment risk under non-neutral stability conditions. To this end, presented in the following chapters are analysed measurements from offshore meteorological masts, a comparison of four commercially available CFD options, and results from CFD simulations using various methods to incorporate atmospheric stability.

Chapter two describes the background motivation for research into computer models of offshore wind farms, a brief history of atmospheric stability research and the current scientific understanding of the offshore atmosphere. The Monin-Obukhov Similarity Theory is introduced along with three different ways to calculate the related Obukhov length and a discussion about suitable atmospheric measurements, particularly the resulting effects of significant variations in meteorological mast instrumentation. The chapter concludes with a literature review of how atmospheric stability interacts with wind farms, causing variations in levels of power generation by altering how turbine wakes interact and dissipate.

Chapter three analyses meteorological data collected at two tall offshore masts on separate sides of the North Sea. Atmospheric stability at each site is compared using the gradient Richardson number approach, a variety of measurement heights and two alternative classification methods. Wind shear and turbulence intensity are analysed for each group of binned Obukhov lengths, leading to a proposal to classify atmospheric stability for wind energy purposes according solely to the physical atmospheric conditions, rather than the more meteorologically traditional combination of physical and thermal properties required by the Obukhov length.

Chapter four contains a review of past and current techniques used to model atmospheric flow through wind farms and the resulting wake interactions. A brief overview of the governing equations and theory used by Reynolds-Averaged Navier-Stokes is given, followed by an introduction to the software package Windmodeller

Ansys CFX. Results from benchmark simulations are discussed, comparing four alternative turbulence models (assuming a neutrally stratified atmosphere) against production data from four offshore wind farms.

Chapter five develops the most promising turbulence model from the previous chapter and compares three different methods of incorporating atmospheric stability via a thermal gradient within the surface layer, as appropriate for Monin-Obukhov Similarity Theory. Results are then discussed from preliminary work, using concepts developed in chapter 3 to focus on the physical effects of atmospheric stability on air flow through wind farms rather than the thermally induced effects required by traditional approaches.

Finally, the main results of each chapter are reviewed in Chapter six with conclusions from the research undertaken and recommendations are made for areas to focus future research. The thesis concludes with two appendixes containing a published journal paper of significance to this research co-authored by the thesis author and primary supervisor, and some images of final simulation meshes for reference purposes.

**When the winds of change blow,
some people build walls and others build windmills.
- Chinese Proverb**

Chapter 2. The Offshore Atmosphere: Background and Current Theory

2.1 The Offshore Advantage

Humanity has an ever growing demand for electricity. The constant need for new sources, combined with the growing societal awareness of climate change and recent concern about the safety of nuclear technologies is encouraging governments to invest in renewable sources. The European Union for example, has a target of 20% of its energy production to be renewably sourced by 2020 [1] with some individual members adopting higher targets. Since this target is for “energy production”, rather than just “electricity generation”, the required level of renewable penetration within the European electrical markets will be considerably higher than 20%. However, significant generation using renewable technologies, such as wind farms and open field solar photovoltaic arrays, requires large amounts of space, often drawing opposition from local communities.

Whilst incurring extra initial expenditure in construction and maintenance costs, corresponding to new infrastructure challenges and the weather dependency on access, it has long been known that offshore locations offer higher wind speeds [2] and thus potentially higher wind farm power yields [3]. The lower values of surface roughness result in lower background turbulence [4] and lower levels of fatigue damage [5] thus improving long-term maintenance expenditure. In addition, height restrictions on new offshore structures are less strict than onshore, allowing for turbines with longer blades, able to harvest the wind across larger areas and access the faster winds found at greater heights. Since offshore turbines therefore have the potential for higher power capacities than onshore machines, fewer are needed to reach the equivalent levels of farm rated capacity, thus lowering the average cost per megawatt, assuming other costs remain equal. As an example of offshore wind capabilities, the twenty turbines at the Middelgrunden offshore wind farm deliver more than 3% of power consumed in the nearby city of Copenhagen [6].

2.2 Offshore Data

Windfarms are expensive to build and require feasibility studies to assess, amongst many other factors, the local wind resource and thus the level of investment risk. For onshore farms, measurement campaigns involving numerous meteorological masts are common. However, installing an offshore met mast involves significant financial risk in itself, costing upwards of £10M and does not guarantee the construction of a lucrative farm, as in the case of the two masts at Shell Flats in the Irish Sea. The high cost of installing offshore masts along with their purpose for assessing the financial risk of further investment, means each dataset has a high commercial value. Therefore, there are heavy restrictions on the availability of offshore wind speed datasets for either researchers or other developers. It is clear that any modelling technique that can either utilise currently available datasets or reduce the number of new masts required whilst also significantly reducing the financial risk of farm construction is worth developing. There have been many attempts to predict near-shore wind speeds using data from onshore locations for example [7] and [8] or via mesoscale forecasting models and satellite observations [9] but usually, at least one met mast will be erected, either to verify model predictions or measure parameters that cannot be modelled to a sufficient accuracy.

Since offshore wind resource assessment is expensive, commercially sensitive and often follows purpose-built specifications; there are barely any reliable measurement sources from outside the industry, and certainly none to the heights required by modern turbines. Therefore, with a push to offshore wind farms due to land constraints, new wind farms are forced into meteorologically uncharted waters, with all the associated costs and risk. Anticipating the financial costs involved in offshore measurements and subsequent gaps in knowledge, a German government policy adopted in 2001 led to the construction of three high quality research masts [10], two in the North Sea and one in the Baltic Sea and made the measurements available free of charge for scientific institutions within the European Union. Even though the furthest mast, FINO³, is roughly 80km from shore, all three masts are now surrounded by wind farms in various stages from planning to full operation and therefore the quality of their free-flow measurements will be steadily compromised by local developments.

Owing to the variable nature of weather from year to year, [11] recommends five to ten years of on-site measurements for confidence in energy yield predictions, although it is generally considered that the minimum data collection needed on site is one year, with investment risk decreasing with every additional year of measurements. Campaigns between one and two years may result in worse resource predictions than just a single year's worth of data on account of variation in weather patterns throughout the year. Whilst offshore resource predictions (far from the coast) do not suffer from complications with terrain or the annual changes of forestry canopy, they are susceptible to mesoscale and synoptic scale meteorological events [12] which vary in frequency with the seasons. For example, estimates based on a data set including measurements from two winters but only one summer in the North Sea are likely to over-predict the average annual wind speed, and thus a potential wind farm's yield. For offshore farms, particularly those planned to be far from the coast and other farms, the installation of a met mast is not only vital for reliable resource assessment, it needs to be installed as soon as possible in order to maximise the period of measurements made before turbine construction. Combining the cost of a met mast with the urgency of its installation, preliminary resource assessments of the region (before on-site measurements are made) needs to be both fast and reliable.

In locations far from shore, where no influence is felt from any land mass, the site physical boundary conditions are similar to any other truly offshore location at that latitude. At locations such as these, it may not be necessary to make meteorological measurements before turbines are installed. Site resource assessment could be conducted based on vertical atmospheric profile averages, frequency observations of synoptic scale systems from archived weather forecasts or by comparison to another far offshore location using the geostrophic drag law below:

$$G = \frac{u_*}{K} \sqrt{\left[\ln\left(\frac{u_*}{f z_0}\right) - A\left(\frac{z}{L}\right) \right]^2 + B^2 \left(\frac{z}{L}\right)} \quad 2.1$$

where G is the geostrophic wind speed, u_* is the friction velocity (described later in section 2.3), K is the von Karman constant, z_0 is the surface roughness, z is the height above sea level (asl), L is the Obukhov length (described later in section 2.4), f is the Coriolis parameter and A and B are empirical constants dependent on L , often assumed to be 1.79 and 4.5 respectively [8]. If reliable offshore resource assessment without on-site measurements is to be sufficient to justify the required financial investment, three questions need answering; firstly, what does the typical offshore atmospheric profile look like? Secondly, how do local wind speeds vary with changes in parameters u_* and L ? Thirdly, how far from shore can coastal effects still be observed? To answer these, detailed analysis of current mast data needs to be considered.

2.3 Structure of the Atmosphere

The earth's troposphere consists of many distinct layers and sub-layers, the most important being the Atmospheric Boundary Layer (ABL), shown in Figure 2.1, defined by [13] as the region of the troposphere directly influenced by the planet's surface and reacts within a timescale of about an hour or less to any surface forcing. Above this, the free atmosphere reacts slower to changes in surface forcings, if at all.

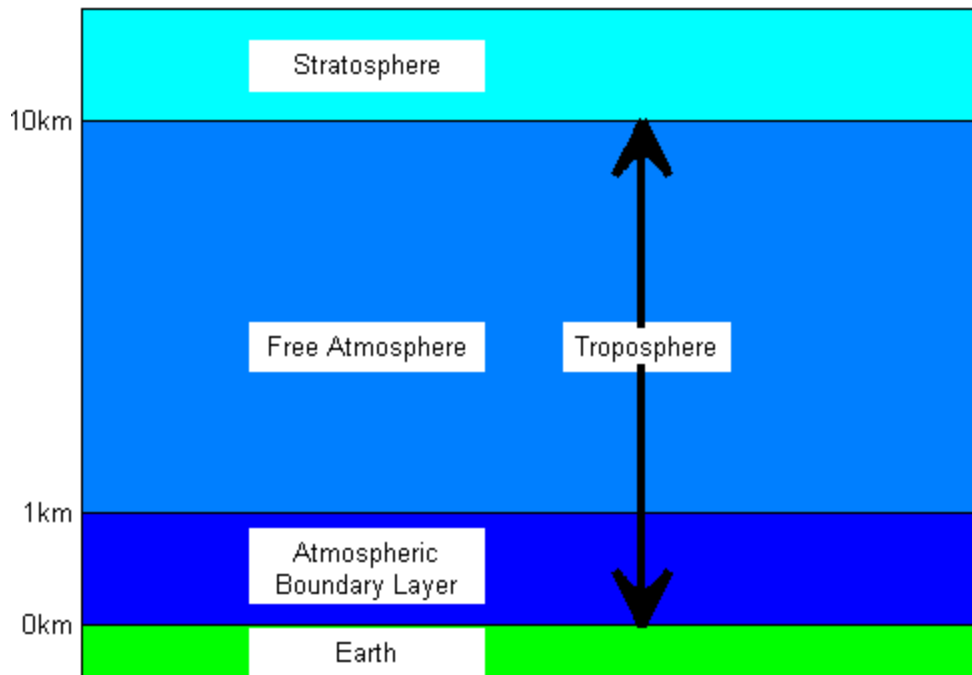


Figure 2.1 Illustration of the lower atmosphere showing key layers (heights are meteorologically accepted approximations and not to scale). Layer boundary heights are variable in time or space.

Since the depth of the ABL depends on the terrain roughness and strength of surface forcings, which can vary strongly over land through the diurnal cycle; depth variations between 100m and 3000m are possible within a single day. As a result, layer boundaries are not as sharply defined, leading to theories of varying complexity to predict the height of the ABL using time dependent variables [14]. Although as proposed by [15], they are often simplified to functions of mechanical parameters:

$$z_{ABL} = \left(\frac{500}{g}\right) \frac{\rho}{\Delta\rho} u_*^2 \quad 2.2$$

Where ρ is air density, $\Delta\rho$ is the difference in air density between the surface and geostrophic level, g is gravitational acceleration and u_* is the friction velocity:

$$u_* = \left(\overline{(u'w')^2} + \overline{(v'w')^2}\right)^{0.25} \quad 2.3$$

Where u and v are perpendicular wind speeds in the horizontal plane, w is the vertical wind speed. A prime symbol indicates the deviation from a temporal mean value. Alternative methods derive from unit analysis techniques, such as the established Rossby-Montgomery formula:

$$z_{ABL} = C_n \frac{u_*}{|f|} \quad 2.4$$

Where C_n is a dimensionless constant. A comprehensive discussion concerning the calculation of the ABL height is given in the review paper [16].

Within the ABL, a sub-layer called the Surface Layer (SL) is normally defined as the region where fluxes from the surface vary within 10% of their surface values [13] although for simplicity, some authors have defined it as the lowest 10% of the ABL [17], or the region where the Coriolis force can be ignored [18]. Results from studies such as [19] suggest the SL height may correlate to roughly 80m for onshore environments, although it is likely to be dependent on both surface roughness and wind speed. Understanding the SL is important to the wind industry as wind turbines generate electricity traditionally from within this region and as its height fluctuates

[20], variations occur in wind shear and turbulence amongst other characteristics; each of which affect both the quantity of electricity generated and the lifetime of the turbines. As the development of new turbine designs continually increases blade length and hub height, rotors in modern farms now sweep through heights around the top of the SL (dependent on atmospheric conditions), simultaneously exposing the blades to multiple flow regimes. With bigger blades, each turbine is more likely to interact with the SL boundary across a wider range of heights, so an understanding of interactions between the SL and sub-layers above, along with resulting variations in wind shear with height can only become more important with time. For this reason, the study and measurement around the top of the SL becomes vital for resource analysis and the risk assessment [5].

Figure 2.2 below shows idealised profiles of wind speed and temperature through the ABL and into the free atmosphere above. The deep Residual Layer, (RL) is symptomatic of high diurnal variability caused when the entrainment zone is elevated; fuelled by surface heated convection during the day, it slowly sinks again when the convection subsides (typically at night) before returning the next day. Whilst velocity appears to decrease logarithmically to zero in the SL, the mean velocity actually becomes zero at the aerodynamic roughness length z_0 (where the following formula is the adiabatic form of the so-called 'log law'):

$$u_z = \frac{u_*}{K} \left[\ln \left(\frac{z}{z_0} \right) \right] \quad 2.5$$

Whilst z_0 is not the actual length of roughness elements, it is strongly influenced by both their height and density over a surface. It is called 'aerodynamic' as although linked to the friction velocity, there is no way to calculate it accurately and it must be determined via extrapolation of measurements [13].

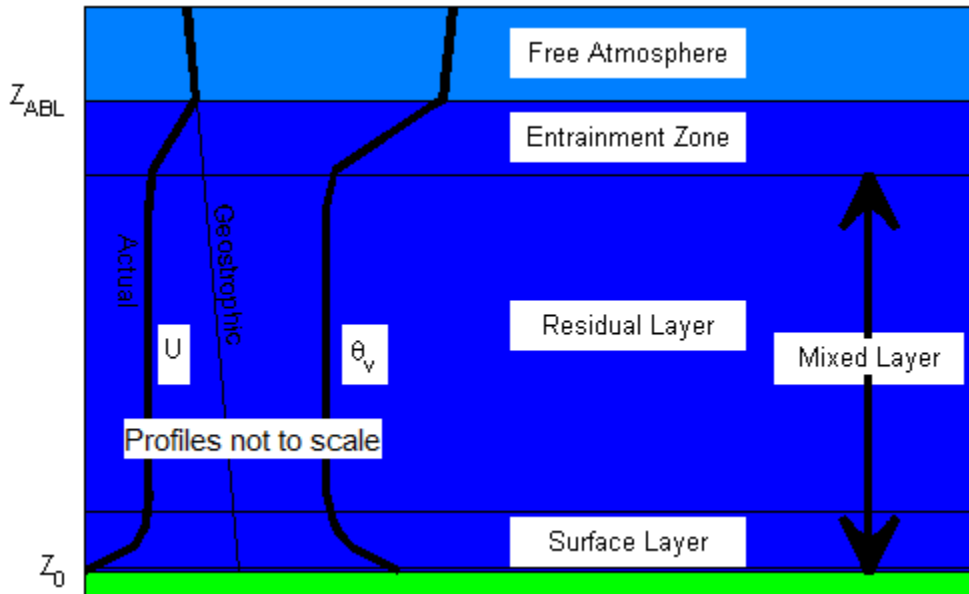


Figure 2.2 Idealistic speed and thermal profiles through the ABL for onshore daytime conditions. Note the wind speed profile indicates the theoretical geostrophic case if friction were not accounted for. For a marine ABL, the residual layer is reduced in height by a reduction in the height of the entrainment zone and Z_{ABL} . Layer boundary heights and profiles (of U and θ_v) are not to scale and vary in time and space.

The levels of wind shear and turbulence in the ABL are intrinsically linked, both are directly related to Z_{ABL} . Although locally varying with height, the average wind shear across the ABL is simply the geostrophic wind speed divided by Z_{ABL} . Whilst the size and strength of turbulent eddies generated by mechanical and thermal surface fluxes help determine the value of Z_{ABL} . The strength and height of both wind shear and turbulence are important to farm developers as they significantly affect the turbine wake structure and dissipation rate. For example, whilst two different flow regimes with a hub height velocity of 8ms^{-1} may cause a wind turbine in the free stream to generate very similar power levels, the regime with the greater wind shear across the turbine heights will result in significantly lower power output from any turbine located behind it than for the same pair of turbines located in the low wind shear regime. This is because higher shear events correspond to lower levels of turbulence, with smaller eddies mixing less kinetic energy into the wake region from the faster moving air above and thus the wakes propagate further downstream. As such, wind farms located in higher wind shear environments suffer greater wake losses and so generate less power than average and return a lower financial yield, emphasising the need for a suitable resource measurement campaign before farm construction.

2.3.1 The Marine Atmosphere

In the same way that the onshore ABL is a response to conditions of the ground, the Marine Atmospheric Boundary Layer (MABL) is directly linked to conditions of the sea. Therefore, the most significant difference between the ABL and MABL is a result of the largest difference between land and sea: land is a solid whilst the sea is a liquid with different physical and thermal properties. This obvious fact has large implications when calculating the MABL height, z_{MABL} . Since liquids at rest exhibit level surfaces, even with the complex effects of waves, the marine values of z_0 are over an order of magnitude smaller than on shore. The ocean water also exhibits boundary layer features, although as water has significantly higher viscosity compared to air, levels of turbulence and thus the boundary layer depths differ with associated thermal and velocity profiles each side of the air/water interface accordingly. As both surfaces are constantly moving and interacting in a non-linear manner, profiles across the interface are often discontinuous with the atmospheric profiles varying more significantly than their oceanic equivalents. Over the last 60 years there has been great debate about the size of z_0 for water bodies, namely because in marine environments it is not a constant, but dependent on ever changing wave patterns and their size, which themselves are functions of wind speed and thus a feed-back system develops. Attempts have been made to quantify this feedback system, such as [21] by using equation 2.3, although the more classical relation suggested by [22] has endured in what has become known as “Charnock’s equation”:

$$z_0 = \alpha_c \frac{u_*^2}{g} \quad 2.6$$

The quantity α_c is a parameter referring to the fetch and type of water body and has been noted between 0.012 and 0.035 [23], although often taken as 0.0185 after review [24]. Following the ideal log-wind profile equation 2.5, Charnock’s equation has been shown [13] to directly link mean marine wind speed with the friction velocity:

$$u_*^2 = 0.00044\bar{u}^{2.55} \quad 2.7$$

Taken together, equations 2.4 and 2.6 imply $z_{MABL} < z_{ABL}$ and therefore it follows that for offshore locations; the geostrophic wind speeds found in the free atmosphere, along with the strong wind speed and temperature gradients associated with the entrainment zone (Figure 2.2) are observable at lower heights than over land. As smaller surface roughness values result in shallower ABL depths, it follows that the SL at offshore locations will also be proportionately shallower at around 50m [25] [26], although the depth of the sub-layer is more complex and more dependent on the different variables in other surface forcings. Combined with the larger scale of offshore turbines, shallower atmospheric layers offshore ensure new farms, with larger turbines, will either need to endure conditions within multiple sub-layers or deliberately increase their tower heights further to ensure turbine rotors always remain above variable SL depths.

Alternative methods to calculate z_0 based on fetch or wave age have been suggested [27], although computer simulations prefer the use of constant values to reduce computational complexity with WAsP using $z_0 = 0.2mm$ [28]. Analysis by [29] showed the wave age dependent method of calculating z_0 produced the most accurate results, although later studies of the same site by the same authors [17] [30] showed insignificant variation between the three methods. Despite small variations in assumptions used to calculate u_* or z_0 having little effect on resulting wind speeds [31] [32]; the lower surface roughness of water is known to effect levels of Turbulence Intensity (TI), with typical offshore values of 6-8% compared to 10-12% over land [33]. Since the wake regions of low velocity behind each turbine are primarily eroded by vertical exchanges of momentum from regions of higher velocities, according to [34], the lower offshore values of TI significantly contribute to 10-20% power losses in large offshore farms by prolonging the wake recovery times. The second significant difference between the land and sea boundary-layers is a result of the much greater thermal capacity of water compared with land, which reduces the magnitude of the diurnal variation in surface temperature [35] leading to less induced convection in the Marine Surface Layer (MSL). Therefore, a MABL idealised profile would show an entrainment zone much closer to, and possibly touching, the MSL. This results in increased levels of wind shear in the entrainment

zone as it marries the friction influenced MSL winds with the geostrophic speeds in the free atmosphere above.

2.3.2 The Coastal Atmosphere

While the marine environment may be considered a simplified version of onshore conditions, [21] describes a region of thermal and mechanical interaction between the two and [11] advises caution and special procedures for regions of limited fetch. In fact, the coastal atmosphere can be horizontally split into two sub regions, an area above ground that is affected by the local water mass and an area of sea and MABL that is affected by the local land mass. The onshore coastal region is normally used for studies into the effects of changes in surface roughness [36] and [2], or as a proxy for the offshore environment to reduce experimental costs [37]. In the offshore coastal region, (more clearly defined by [38] as “the zone extending from the coastline where the wind speed and turbulence profiles are not in equilibrium with the underlying sea surface”) the shape of profiles, such as those in Figure 2.2, depend strongly on the variability of the wind direction. For example, if a location is near a shoreline in the east, but the wind direction is continually from the west, the site will likely exhibit offshore profiles, although [17] found greater deviation from expected values when considering directions with longer fetch. It has been found at near shore sites [39] that the significance of land to an offshore wind profile changes with height, clearly showing a lag between change in surface roughness and change in wind regime. Studies of mechanical processes by [38] and [40] have shown winds blowing from land to sea still retain aspects of their onshore profiles 20km, 70km and possibly 100km from the coastline whilst studies by [41] and [42] indicate the importance of thermal forcings in calculating the influence of surface change. These forcings combine to complicate coastal predictions with unique mesoscale features such as sea breezes [40] that have strong diurnal or seasonal [43] signatures. Attempts to parameterise the location of offshore conditions with respect to distance from shore (fetch) vary from very complex methods [13] incorporating parameters not measured on the average mast, to more simplistic [7], [32] and [44] in the format:

$$z_{CABL} = c_1 X^{c_2} \quad 2.8$$

Where c_1 and c_2 are empirical constants, X is the distance from the coast and z_{CABL} is the height below which the atmosphere has marine properties while above is as yet unaffected by crossing the coast. By this definition, it follows that the coastal atmosphere ends and the marine atmosphere begins in earnest where $z_{CABL} = z_{MABL}$ although a residual of the land ABL may continue to exist above this until the entrainment zone erodes it away. The differences between flow speed, direction and turbulence structure can be significant and may be a leading cause of features such as low-level jets or increased turbine fatigue.

Whilst focusing solely on using datasets which experience truly offshore conditions removes complexities resulting from z_{CABL} , in reality, all current offshore farms are located in coastal waters with [41] suggesting the whole of the Baltic Sea should be considered coastal. Furthermore, the scarcity of measurements far from shore means it is unclear just how far offshore the coastal zone extends.

2.4 Monin-Obukhov Similarity Theory

The theory of boundary layers, conceived in 1904 by Ludwig Prandtl, describes the dynamic behaviour of moving fluids beside a wall, where the speed of flow near the wall is retarded by friction. Using Prandtl's vision of sub-layers in a flow to describe the atmosphere results in a region directly affected by surface friction (the SL) below a region of well mixed flow formed by a combination of turbulence ejected from the SL and fluctuations in the SL height (the RL). The RL is constantly eroded by the high levels of shear in the entrainment zone by the dominant effects of the free atmosphere above, as the laws of physics strive for equilibrium between fluid atmosphere and rotating Earth. For over a hundred years, boundary-layer theory has been developed, refined, validated and evolved. As part of this, in 1946, the Russian scientist, Alexander Obukhov published a fundamental paper "‘Turbulentnost’ v temperaturnoj – neodnorodnoj atmosfere (Turbulence in an Atmosphere with a Non-uniform Temperature)" in which he presented a universal length scale for atmospheric exchange processes near the ground. Above heights equalling his Obukhov Length (L), buoyancy dominates the generation of turbulence whilst mechanical forces dictate processes below. Owing to world conflict at the time of its writing in 1943, and its eventual publication in a very limited first issue journal three years later, few copies are now available and its content is best known via a follow

up paper written with fellow Russian, Andrei Monin, in 1954 [45]. This Monin-Obukhov Similarity Theory (MOST), whilst developed over land, has been shown by [46] to be valid in the MSL above the wave boundary layer.

As described by equation 2.5, the wind speed within the SL follows a pseudo-logarithmic profile considered dependent solely on friction levels defined by surface roughness. However, this assumes neutral stability or in other words, the thermal properties within a column of air are constant. (The Charnock and Rossby-Montgomery relations are also based on this assumption.) Yet since solar radiation is absorbed by the planet's surface and then released into the air on a diurnal cycle, the SL is rarely in a neutral thermal state [47] and the assumption is made on the basis of statistical averages and theory simplification. Based on water's higher thermal capacity, sites far from shore should exhibit higher proportions of neutral events yet by this measure, [48] suggests measurements from current offshore locations are still coastal, despite filtering by length of fetch. The thermal gradient either generates or suppresses turbulence systematically perturbing the mean value from this idealistic model and can be accounted for by the inclusion of a stability function as in equation 2.9 below. For the wind industry this is significant; not only in terms of wake losses [34] but also as [49] show the MSL depth to be dependent on L , along with wind speeds below 100m when L is positive [19].

$$u_z = \frac{u_*}{K} \left[\ln \left(\frac{z}{z_0} \right) - \Psi_m \left(\frac{z}{L} \right) \right] \quad 2.9$$

Where $\Psi_m(z/L)$ is a function of both height and the Obukhov length, which itself is a function of ratios between velocity and temperatures as originally defined by [45]:

$$L = - \frac{u_*^3}{K \frac{g}{T_0} \frac{q}{c_p \rho}} \quad 2.10$$

Where T_0 is the mean temperature of the layer in consideration, q is the turbulent heat flux and c_p is the specific heat of air at constant pressure. Since changes in L are a function of fluctuations in q ; it is reasonable to assume that owing to water's

higher heat capacity than land, unless under conditions of large advection from coastal regions, marine values of L will exhibit a significantly dampened diurnal cycle [35] [41] [43]. This could lead to the assumption that while onshore stability is highly sensitive to diurnal forcings, and thus coastal regions through advection, truly marine locations not currently influenced by synoptic weather systems may be assumed neutrally thermally stratified. This increases the value of accurately defining where coastal regions end and truly marine environments begin.

Since its creation, there have been many attempts to refine the Monin-Obukhov Similarity Theory, (MOST) or incorporate additional parameters such as atmospheric humidity [50]. There have also been attempts to approximate equation 2.10, particularly for when datasets do not include all the necessary parameters or when measurements are not taken at significantly high frequencies to calculate the turbulent heat flux. Studies such as [17], [51] and [52] have attempted to determine the most suitable approach for best practice with comparisons of results, but usually, the choice of data analysis method is dependent on how measurements are collected at the particular locations. This should concern the industry and provoke standardization or “best practice” measurements as the studies also show each method produces differing analysis of the available data. Summaries of three basic categories of variations of equation 2.10 are given in the following subsections although within each category many authors have experimented with the inclusion of constants or variations of thermal measurements such as potential temperature [53] or virtual potential temperature [54].

For convenience in data analysis, values of L are grouped together into bins of five similar levels of stability; an example of this is Table 2.1 as used by [12], [48] and [55]. Whilst there is some general agreement in the literature as to the different category definitions, variations in the exact values of L do exist [56]. An older method of using only three basic stability categories [39] is now less common, while the use of seven categories, asymmetric around the neutral category such as in Table 2.2, are becoming more common [47] [35]. It should be noted the more complex categorisations often do not include values of L near zero.

Table 2.1 Typical Definition of stability categories

Obukhov Length [m]	Stability Category
$-200 \leq L < 0$	Very Unstable
$-1000 \leq L < -200$	Unstable
$1000 < L $	Neutral
$200 < L \leq 1000$	Stable
$0 < L \leq 200$	Very Stable

Table 2.2 Alternative Definition of stability categories

Obukhov Length [m]	Stability Category
$-100 \leq L < -50$	Very Unstable
$-200 \leq L < -100$	Unstable
$-500 \leq L < -200$	Near Unstable
$500 < L $	Neutral
$200 < L \leq 500$	Near Stable
$50 < L \leq 200$	Stable
$10 < L \leq 50$	Very Stable

Possibly because it was developed at the height of the Soviet Union’s power, throughout the following decades, MOST effectively became scientific dogma with little published research in disagreement, particularly from within the Soviet Union. Instead of challenging it, the research community focused on accurately defining constants and relationships between parameters, particularly K [50]. Through notable experiments conducted across the world; for example in Australia [57], the Netherlands [58] and the USA “The Kansas Experiment” [18], MOST has been proven a reliable method of predicting average wind speeds in the SL. However, since the wind industry is moving offshore and now requires atmospheric profiles extending above the logarithmic MSL, attempts have been made to extend the theory up to 300m [19], and whilst alternative theories have been published [59], they have had little impact on the popularity of MOST.

2.4.1 Calculating L using the Flux Method

The most ‘true-to-original’ way to measure L in field experiments is with the use of sonic anemometers as they are able to measure air temperature as well as wind speed in three components (x , y and z) at very high frequencies. Thus the friction velocity can be calculated using the eddy-correlation equation 2.3 and the turbulent heat flux can be obtained with the following equation:

$$\overline{w'T'} = \frac{q}{c_p \rho} \quad 2.11$$

where T is the air temperature. Caution should be applied when calculating both equations 2.3 and 2.11 as explained by [17], yet this is the only method which includes the friction velocity in the calculation of L , as shown in the common flux form:

$$L = -\frac{u_*^3}{K \frac{g}{T_0} \overline{w'T'}} \quad 2.12$$

2.4.2 Calculating L using the Bulk Method

If there are no sonic anemometers measurements available, the bulk method (verified for the marine environment by [60]) can be applied with readings from a single cup anemometer and suitable temperature measurements at that height and the surface respectively. The Obukhov length can then be calculated via equations 2.13 and 2.14 below, where ΔT is the difference in temperature between air and surface and Ri_B is the bulk Richardson number relating to reference height, z' .

$$Ri_B(z') = \frac{g}{T_0} \frac{z \Delta T}{u^2} \quad 2.13$$

$$L = \begin{cases} \frac{z'}{10Ri_B} & Ri_B < 0 \\ \frac{z'(1 - 5Ri_B)}{10Ri_B} & Ri_B > 0 \end{cases} \quad 2.14$$

When applying the bulk method, it is important that the surface temperature is indeed the temperature of the surface and the only way to achieve this is with remote sensors. Offshore, it is rare to take measurements of the actual sea surface due partially to the cost of placing the equipment in such a hostile environment but also since the waves would compromise accuracy. Instead, temperature measurements are taken roughly 2m below the sea surface. This produces complex systematic errors from the cool-skin and warm-layer effects as mentioned by [61]. Whilst [32] investigated the effects of tides on surface roughness, there has been no work

(known to the author) investigating the effects of tides on atmospheric stability calculated via the bulk method.

2.4.3 Calculating L using the Gradient Method

According to [51], the gradient method is the most successful at representing the atmospheric processors involved in turbulent mixing. Similar to the bulk method, high frequency measurements are not required whilst both temperature measurements are taken above the surface and thus a wind speed is also required at both heights rather than assuming $u = 0$ at the surface as in equation 2.13. Various versions of the equation 2.15 have been suggested [17] [51]. There has also been significant debate about equation 2.16, specifically whether a critical Richardson gradient number $Ri_{Gcrit} = 1/\beta$ exists [62], [63] and whether MOST is relevant for such values where the flow is laminar rather than turbulent. Here, equation 2.16 includes an option where $Ri_G > Ri_{Gcrit}$ for completeness as used by [51]. Most frequently β is assigned a value of 5.

$$Ri_G(z') = \frac{g}{T_0} \frac{(\frac{\Delta T}{\Delta z})}{(\frac{\Delta u}{\Delta z})^2} \quad 2.15$$

$$L = \begin{cases} \frac{z'}{Ri_G} & Ri_G \leq 0 \\ \frac{z'(1 - \beta Ri_G)}{Ri_G} & Ri_G > 0 > Ri_{Gcrit} \\ \frac{1}{2Ri_G} & Ri_G \geq Ri_{Gcrit} \end{cases} \quad 2.16$$

2.5 Appropriate Measurements

As the offshore wind industry has grown rapidly in the last two decades, with each new technological advance enabling bigger machines to be installed further from shore, appropriate meteorological measurements are required from each new location to assist with reducing the financial investment risk. As such, offshore wind speed measurements near development areas have a high commercial value

meaning datasets are rarely shared between developers. There is also a lack of standardisation in terms of what is measured and measurement height at each mast, besides hub height wind speed. On tall offshore masts, wind speeds are typically measured at hub height and at a height just above the mast's working platform. Additional heights instrumented often correlate either with significant heights for the rotor design or significant multiples of 10m. Air temperature is normally measured at the same height as the lowest anemometer and near the top of the mast; additional heights are sometimes included but significantly fewer than for wind speed. Atmospheric pressure is measured (if at all) at platform height and occasionally near the mast top. Any measurements of humidity again tend to be split between the platform and near mast top, occasionally with additional measurements near thermometer heights. Examples of mast locations and their meteorological instrument configurations can be found below. Locations A, B and C are research grade masts sponsored by the German government and as such they are the most instrumented sites, including measurements of many variables of little direct use to wind resource assessment and so not included in Table 2.3.

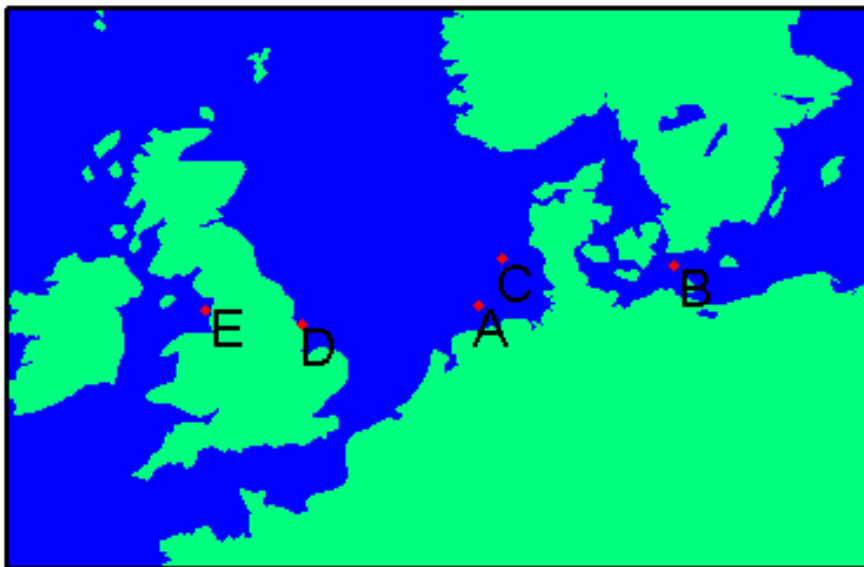


Figure 2.3 Locations of offshore meteorological masts which supplied atmospheric data for this work, not associated to any fully-commissioned wind farm. A=FINO1, B=FINO2, C=FINO3, D=Humber Gateway, E=Shell Flats. Note there are two masts at the Shell Flats site, but on account of their close proximity to each other, they are shown here with only one marker.

Table 2.3. Comparison of offshore met masts and their installed instrumentation. Additional instruments (such as rain gauges) are present at some masts, although these have been left out of this table as their measurements were not used as part of this work. Data availability is not always uninterrupted between dates and contains sections of erroneous recordings.

	FINO1	FINO2	FINO3	Humber Gateway	Shell Flats	
					Mast 1	Mast 2
Nationality	German	German	German	British	British	
Water Body	North Sea	Baltic Sea	North Sea	North Sea	Irish Sea	
Distance From Shore (km)	40	40	80	10	10	
Mast Height (m)	100	102	106	88	82	52
Data Availability	01/2004 to 06/2007	03/2008 to 09/2011	09/2009 to 10/2011	10/2009 to 07/2011	06/2002 to 12/2003	
Heights (m) of Cup Anemometers	33, 40, 50, 60, 70, 80, 90, 100	32, 42, 52, 62, 72, 82, 92, 102	30, 40, 50, 60, 70, 80, 90, 106	34, 52, 70, 88	20, 30, 50, 70, 82	20, 30, 40, 52
Heights (m) of Sonic Anemometers	40, 60, 80	42, 62, 82	60, 100	N/A	80	50
Heights (m) of Wind Vanes	33, 40, 50, 60, 70, 80, 90	31, 51, 71, 91	28, 100	68, 86	20, 30, 50, 70, 82	20, 30, 40, 50
Heights (m) of Thermometers	30, 40, 50, 70, 100	30, 40, 50, 70, 99	29, 55, 95	19, 52, 88	12, 80	12
Heights (m) of Hygrometers	33, 50, 90	30, 50, 99	29, 55, 95	52, 88	12, 80	12
Heights (m) of Barometers	20, 90	30, 90	23, 94	52, 88	12, 80	12

Whilst pressure and humidity do not feature directly in equation 2.10, reference is made to them with c_p and air density, which, alongside temperature, act as stores of potential energy in the atmosphere. Therefore, there have been many attempts to quantify and incorporate the effects of humidity as it affects the thermal profile [64]. Where field instrumentation is highly limited, it is possible to calculate L using absolute temperature values, as shown in section 2.4. However, the additional availability of pressure measurements on the met mast (preferably measured at the same heights as the measurements of absolute temperature), facilitates the implementation of the potential temperature:

$$\theta = T \left(\frac{P_0}{P} \right)^{R/c_p} \quad 2.17$$

Where P is atmospheric pressure, P_0 is the reference pressure and R is the gas constant of air. This is useful as in a neutrally stratified, dry atmosphere, the potential temperature gradient with height ($\Delta\theta/\Delta z$) is zero, becoming positive or negative for stable or unstable atmospheric conditions respectively. If measurements of atmospheric humidity are available (preferably measured at the same heights as the measurements of absolute temperature), the effects of water vapour content can be incorporated into the atmospheric stability analysis via an artificial parameter, the virtual temperature:

$$T_v = T \left(1 + \frac{1 - \epsilon}{\epsilon} q_v \right) \approx T(1 + 0.608q_v) \quad 2.18$$

Where q_v is the specific humidity and ϵ is the ratio between the dry and water vapour gas constants ($\epsilon = R/R_v = 0.622$). Thus as moisture decreases the air density, and increases the virtual temperature, a moist air parcel is theoretically warmer than a dry parcel at an equivalent absolute temperature. The equation above for the inclusion of moisture in stability calculations assumes it is entirely in the vapour state with zero liquid content and is thus not representative of common meteorological conditions such as fog or rain. It is therefore advised that events where measurements of relative humidity (RH) exceed 95% are treated with caution. For high quality datasets, where measurements of T , P and RH exist at suitable heights, the Obukhov length may be calculated using the virtual potential temperature:

$$\theta_v = T_v \left(\frac{P_0}{P} \right)^{R/c_p} \quad 2.19$$

Sonic anemometers are sometimes installed at multiple heights, although rarely at significant heights such as the top of the mast or beside other instrumentation for calibration or comparison studies. Remote locations, combined with limited space and power available for equipment on an offshore mast platform have resulted in an industry standard practice of only recording data in ten minute intervals. Whilst this is a reasonable time frame for statistics such as the mean and variance from cup anemometer measurements it nullifies the benefits of installing rapid frequency equipment such as sonic anemometers.

The inconsistency of measurement height between farms combined with scarcity of available data makes inter-site comparisons difficult without the assumptions that all three calculation methods give the same results and that L is constant with height, which requires that the ratio between temperature gradient and velocity gradient must be constant. Studies using well instrumented masts [52] and [17]) show the three methods do not produce similar results, thus raising the important question, which is most suitable for the wind industry? To answer this, first let us assume we had a hypothetical mast with sufficient instrumentation for all three options. Then let us remember that MOST was not derived with turbines in mind, thus the flux method in effect finds the value of L at a point (even if it is assumed constant through the SL) whilst both the bulk and gradient methods utilise measurements across a profile before relating it back to a point. Other aspects of the wind industry work in the same manner, for example, it is the shear across the whole rotor that apparently causes additional power generation and fatigue yet the controls rely only on wind speed at hub height.

Choosing between the bulk and gradient methods comes down to the relevance of the surface. It is the surface, whether land or sea, which defines the friction velocity and heat fluxes and so including it via the bulk method, would seem logical when calculating stability. However, turbines are progressively being built with higher hub heights to capture higher wind speeds aloft; therefore the area swept out by the rotor is moving away from the surface, making its effects less important. For farms built in coastal waters, the developing MABL as influenced by the surface conditions may not have grown to sufficient heights to significantly affect the winds powering each turbine. In such cases the gradient method using velocity and temperature measurements at rotor bottom and top or bottom and hub would be more suitable to describe the likely behaviour of upstream profile and downstream wakes.

Even having chosen to use the gradient method to calculate L , choosing which measurement heights to use for the calculations can be tricky. As [26] shows, using different heights results in different values of L . Even the FINO masts, which are each equipped with numerous cup anemometers, have very few thermometers, restricting selection options to just three which produce very different results. For

example, [26] shows the use of lower measurements result in more unstable events whilst using just upper measurements produce more stable events from the same dataset. This results from a non-linear thermal profile, which would not have been apparent if only two temperature measurement heights were available. The wind profiles at FINO³ are similar, with variations away from the smooth profile expected which again would not have been apparent without the high number of anemometers. So the moral is: if ever given the chance to decide what heights to measure at for ABL experiments, measure at as many heights as possible.

2.6 The Significance of Atmospheric Stability for Wind Energy

Offshore windfarms are usually much larger than those built onshore (at least in Europe), both in individual turbine size as well as the number of turbines. In addition, the lack of surface terrain irregularity usually results in farms constructed in regular arrays. As a result, whilst onshore resource assessment is concerned about upstream terrain features affecting inflow speeds, the emphasis in offshore wind farm resource assessment is placed on calculating wake losses which are heavily dependent on z_0 and L . Since all offshore locations can be considered to have identical surface roughness conditions, atmospheric stability, becomes the driving influence determining wind farm yield through the effects of turbulence and stratification on wake characteristics such as dissipation rates.

Turbine wakes are characterised by regions of lower than average wind speeds and elevated TI . Therefore, any turbine situated in the wake of another will be less productive and potentially suffer higher levels of fatigue [65], both of which increase the overall cost per megawatt. Ideally, turbines would be located far enough apart for the wind profile to return to its free-stream value before reaching the next turbine, however this would dramatically increase the area of sea surface required to build a farm as well as the cost of connecting cables and power losses within said cables. Thus the key to designing an offshore farm for the optimum ratio of cost verses generation is an accurate prediction of the future wake behaviour on site. The behaviour of each individual wake is dependent on ambient values of speed and TI as well as turbine blade lengths and turbine thrust characteristics. Whilst the turbine characteristics can be optimised by the choice of the developer, the speed and

turbulence at an offshore location are both functions of atmospheric stability, as is the distance behind each turbine required for wake recovery [66].

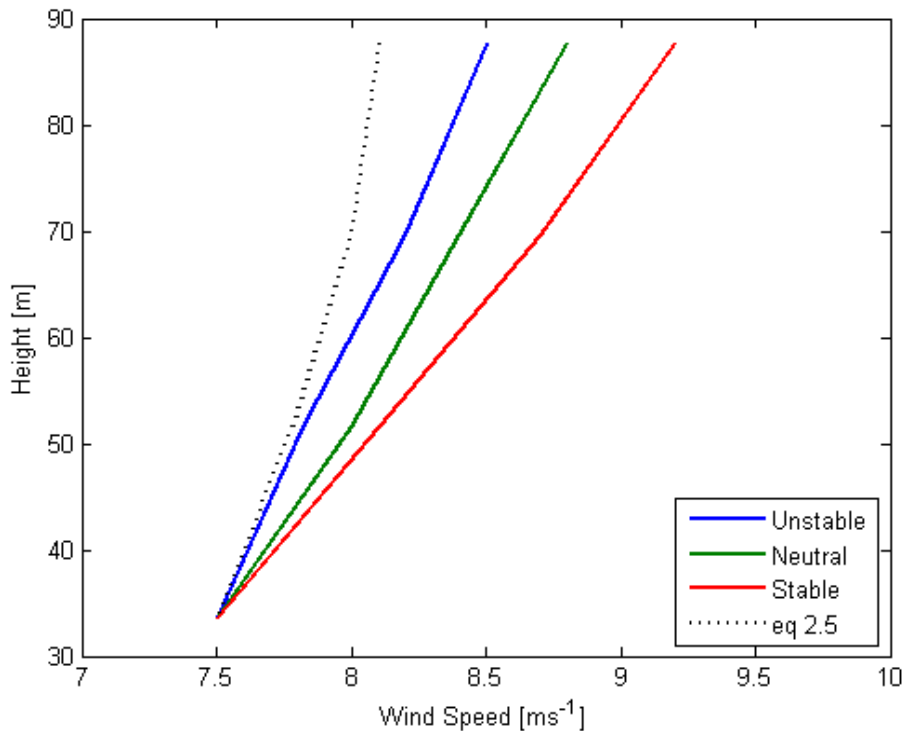


Figure 2.4 Averaged wind profiles from the Humber Gateway offshore mast under various stability conditions, given a wind speed of 7.5ms^{-1} at 33m . Data has been filtered to only include marine fetches and events which satisfy the steady state homogeneous atmospheric assumptions required by MOST, see reference [17]. For reference, a neutral log profile using equation 2.5 assuming a constant value of u_* is also shown.

As mentioned previously, stability plays a significant role in determining the height of the ABL, i.e. stable conditions produce relatively shallow boundary layers whilst unstable conditions extend the layer higher than average. Since the geostrophic wind speed is independent of surface stability and flow must become stationary at the surface, the height of the ABL (defined by stability) forces the gradient of wind shear, particularly in the SL. Figure 2.4 above uses MOST to filter for three scenarios in the SL. Whilst they are very similar lower down, by the top, there is a significant difference in speed between scenarios and this will carry through to variations in electricity generation [67]. These effects of thermally influenced shear on the offshore velocity profile are greater than those onshore on account of differences in mechanically generated turbulence [36]. Figure 2.4 also clearly displays how stability is significant for rotor fatigue, with modern diameters well over 100m . For example, the differences in wind speed between the top and bottom of the rotor under stable conditions are considerable, where [5] finds differences of 5m/s to be common. Thus the assumption of neutral stability with a constant wind speed across the turbine

rotor may be misleading at best, especially since [34] calculated near neutral conditions only exist for 33% of the time while [48] calculated roughly 15% neutral conditions for the data analysed.

Since atmospheric stability is influenced by thermal processes, it is possible to have two scenarios with different values for L but identical average wind speeds across the rotor blades. Under such scenarios, a turbine in an unstable SL may generate as much electricity as a turbine in neutral or stable scenarios, (although fatigue from variations in turbulence and shear will affect the turbine's life expectancy). However, the behaviour of its wake will be significantly different. Wake losses, defined by equation 2.20, which have been studied across large offshore farms [34] and [68], consistently show that if the ambient SL is stable then overall production is lower than equivalent neutral ambient conditions, which themselves are less productive than unstable environments.

$$\text{Wake Loss Ratio} = 1 - \frac{\text{Power generated by turbine}}{\text{Power generated by turbine in free stream}} \quad 2.20$$

Currently there are few offshore farms old enough, well instrumented enough, and with operators willing to provide the commercially sensitive data required for such studies. Thus the majority of offshore wake analysis is based on just two farms, Horns Rev in the Danish North Sea and Nysted in the Danish Baltic Sea [69]. Contributions from other farms such as Egmond aan Zee [35] and Middelgrunden [33] further confirm the importance of stability for the wind industry. Yet despite this evidence, there currently is no industry standard practice for how to instrument a met mast suitably for assessing stability.

Whilst the Nysted offshore wind farm has been well equipped with masts, others such as the Scroby Sands farm in the North Sea ceased to collect meteorological data after the farm was constructed. Another example is the Robin Rigg wind farm in the Irish Sea where the mast was replaced by a Doppler LiDAR after initial resource assessment. Even farms where meteorological measurements were maintained or increased after commissioning seldom measure parameters at identical heights to other farms. This is significant as the top of a resource assessment mast is often

below the proposed turbine hub height, either to save cost or because the choice of optimal turbine has yet to be made. For example, the top of the initial mast (called M2) used at Horns Rev was 62m asl, whilst the installed turbine hub height is 70m asl. Therefore, it is often required to extrapolate measured wind speeds to the likely hub heights and to the top of the rotor heights. This is usually done with the variation of equation 2.9 shown below where subscript 1 refers to the measured speed and height whilst subscript 2 refers to the extrapolated speed and height, for which knowledge of atmospheric stability is required.

$$u_2 = u_1 \frac{\left[\ln \left(\frac{z_2}{z_0} \right) - \psi_m \left(\frac{z_2}{L} \right) \right]}{\left[\ln \left(\frac{z_1}{z_0} \right) - \psi_m \left(\frac{z_1}{L} \right) \right]} \quad 2.21$$

Significantly, for equation 2.21 to work, both heights are assumed to be within the SL, and the assumption made by [45] that the turbulent shear stress and heat flux are independent of height must also be true, despite [13] suggesting fluxes in the SL may vary by up to 10% of their value. If L is truly independent of height in the SL, the height at which measurements are taken is irrelevant. However, [70] gives an empirical relation for converting $\overline{w'T'}$ between heights within the SL and [26] investigating measurements from FINO1 and FINO3 reports distinctly different velocity profiles depending on the measurement heights for L . Studies which show MOST to reliably predict speeds up to 100m, for example [71], tend to consider only neutral and unstable cases without applying semi-empirical extensions and are often utilising onshore datasets. When using offshore data, [26] and [54] both encounter abrupt changes in profiles at heights around 50m, which on account of appearing in both unstable and stable conditions, are usually explained as coastal effects, despite [26] specifically filtering the data to include only very long fetches. It is therefore currently uncertain how far MOST can be used to extrapolate low-level winds in truly marine conditions or whether the cost of installing very tall masts has lower financial risk than making mistakes in assessing the resource and stability across the turbine rotors.

There is a great art in selling the wind

- **Spanish Proverb**

Chapter 3. Analysis of North Sea Data

3.1 Calculating Atmospheric Stability from Wind Speed Alone

As shown by [35] and [66], atmospheric stability has a significant influence on the levels of electrical generation from large offshore wind farms as it dictates the rate of wake dissipation. However standard methods of describing stability through the use of the Obukhov length rely on available knowledge of thermal parameters, preferably at multiple heights. Ref. [52] recommends measuring at least to the proposed turbine hub height. However, obtaining such data offshore from meteorological masts is very costly owing to their unique construction requirements, hostile environmental conditions and on-going maintenance and calibration of instruments. To reduce costs, some developers are now turning to remote instrumentation such as Doppler LiDAR (Light Detection And Range) or Doppler SoDAR (Sound Detection And Range), for example [47]. These can provide measurements of wind speed and direction, suitable for free-stream calculations, as well as taking measurements capable of showing turbine wake behaviour above standard mast heights [72].

It is generally known that the height of the Atmospheric Boundary Layer (ABL) varies with atmospheric stability [13], becoming significantly lower under more stable conditions. For the offshore wind industry, as the ABL height reduces under very stable conditions, it can approach heights relevant to large turbines, resulting in higher levels of potentially hazardous wind shear. Therefore, this study looks at data from two offshore masts in the North Sea in order to assess alternative ways of inferring atmospheric stability, with emphasis on gradients within the vertical wind profile and levels of turbulence intensity.

3.2 Data Sets

For this study, data from two offshore met masts will be used: Humber Gateway (10km from the UK coastline) and FINO1 (40km from the German coastline). To ensure measurements represent the offshore environment, data have been filtered to include wind directions with a minimum of 300km fetch, corresponding to between 350° and 130° for Humber Gateway and between 204° and 015° for FINO1. There

are one and three years of data from Humber Gateway and FINO1 respectively from before the construction of nearby wind farms.

In order to assess the potential for describing atmospheric stability conditions without thermal parameters, a basic study of the two sites using MOST must first be conducted. Whilst there are numerous wind speed measurement heights at both locations, there are only two heights on the Humber Gateway mast with both wind speed and temperature measurements, thus the stability parameter L is calculated via a version of the gradient Richardson number method utilising θ_v as in equation 3.1 with data from heights 88m and 52m.

$$Ri_G = \frac{\frac{g}{T_0} \left(\frac{\Delta\theta_v}{\Delta z} \right)}{\left(\frac{\Delta u}{\Delta z} \right)^2} \quad 3.1$$

The FINO1 mast on the other hand, has no individual height where wind speed, temperature, humidity, and pressure are all measured. Therefore, as [26] and [52] both highlight the variability of L based on height of measurements, the gradient Richardson number is calculated using equation 2.15 across three height intervals: 50m-70m, 40m-70m and 40m-50m. Whilst speed and temperature are also both measured at the mast top (100m), values from the anemometer are suspected to be systematically erroneous due to mast structure effects and are therefore excluded. For consistency between sites, equation 2.15 is also applied to the Humber Gateway dataset. Richardson numbers are then converted to relevant values of L via equation **Error! Reference source not found.**2.16. The measurement heights used in each dataset are shown in Table 3.1.

Table 3.1 Relevant measurement heights for each case study

Method		Measurement Height [m]		Ri_G Ref. Height (z') [m]	Thermal Parameter
		Lower	Upper		
Humber Gateway	Case A	52	88	68.4	θ_v
	Case B	52	88	68.4	T
FINO1	Case C	50	70	59.4	T
	Case D	40	70	53.6	T
	Case E	40	50	44.8	T

3.3 Stability Categorisation and Frequency

As mentioned earlier, the literature contains numerous variations on how to categorise stability and the defining values of L often appear to have been chosen arbitrarily or with little explanation. To account for this, and assess the suitability of approximating L without thermal parameters, two separate distributions within each measurement method will be analysed; one with five categories symmetric around neutral (Table 3.2) and one with seven asymmetric categories (Table 3.3). It should be noted that Table 3.3 does not include the most extreme stability cases where values of L are closest to zero and therefore its utilisation will not only reduce the data sample size on which this study is based but also bias the frequency distributions towards neutral stability.

Table 3.2 Atmospheric stability defined as five symmetric categories

Obukhov Length [m]	Stability Category	Abbreviation
$-200 < L < 0$	Very Unstable	VU ₅
$-1000 < L < -200$	Unstable	U ₅
$1000 < L $	Neutral	N ₅
$200 < L < 1000$	Stable	S ₅
$0 < L < 200$	Very Stable	VS ₅

Table 3.3 Atmospheric stability defined as seven asymmetric categories

Obukhov Length [m]	Stability Category	Abbreviation
$-100 < L < -50$	Very Unstable	VU ₇
$-200 < L < -100$	Unstable	U ₇
$-500 < L < -200$	Near Unstable	NU ₇
$500 < L $	Neutral	N ₇
$200 < L < 500$	Near Stable	NS ₇
$50 < L < 200$	Stable	S ₇
$10 < L < 50$	Very Stable	VS ₇

The stability class frequency distributions across each dataset are shown in Table 3.4 and displayed visually in Figure 3.1 and Figure 3.2. The proportion of events not included in Table 3.3 where L is between -50m and 10m has been included in Table 3.4 for clarity although not in Figure 3.2 as they would mask the distributions of other events.

Table 3.4 Frequency of each stability category depending on assessment method (%)

Stability Category	Humber Gateway		FINO1		
	Case A	Case B	Case C	Case D	Case E
VU ₅	47.7	77.4	80.4	65.6	65.7
U ₅	9.4	12.0	11.9	3.7	2.4
N ₅	8.9	3.4	4.0	0.6	0.4
S ₅	5.1	1.1	1.4	0.4	0.4
VS ₅	28.9	6.1	2.4	29.7	31.1
VU ₇	7.3	8.2	12.3	4.6	6.2
U ₇	6.1	8.5	11.0	3.5	4.3
NU ₇	6.2	8.4	8.6	2.9	2.0
N ₇	14.1	7.5	8.0	1.5	1.0
NS ₇	3.2	0.6	0.7	0.2	0.2
S ₇	3.4	0.6	0.5	0.2	0.2
VS ₇	1.6	0.3	0.2	0.1	0.1
-50m < L < 10m	58.3	66.0	58.8	86.9	85.9

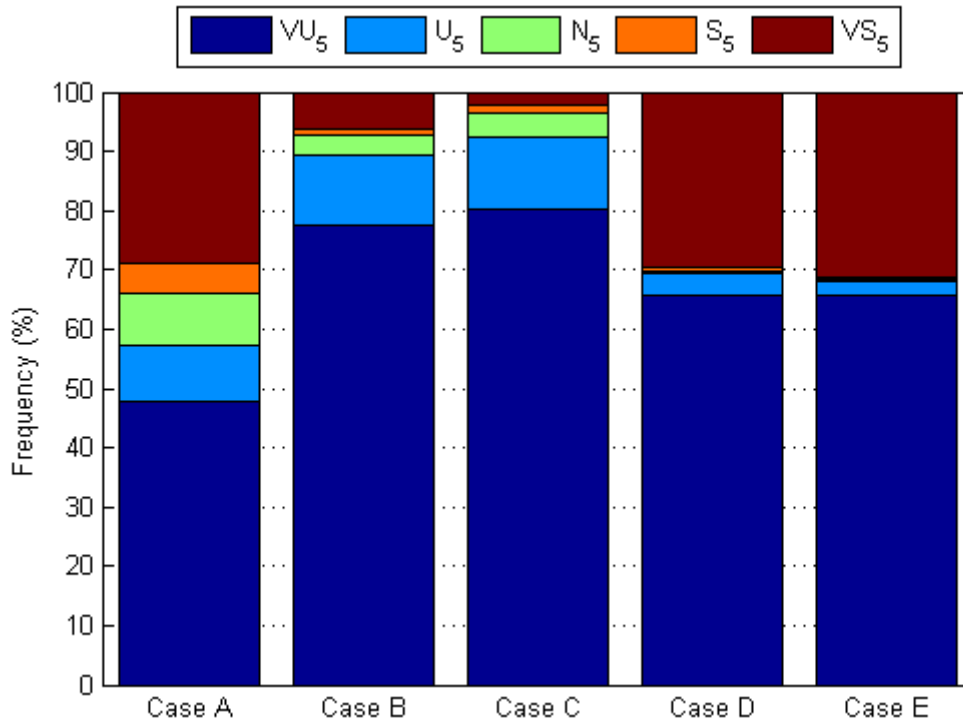


Figure 3.1 Frequency distribution of atmospheric stability split into 5 categories

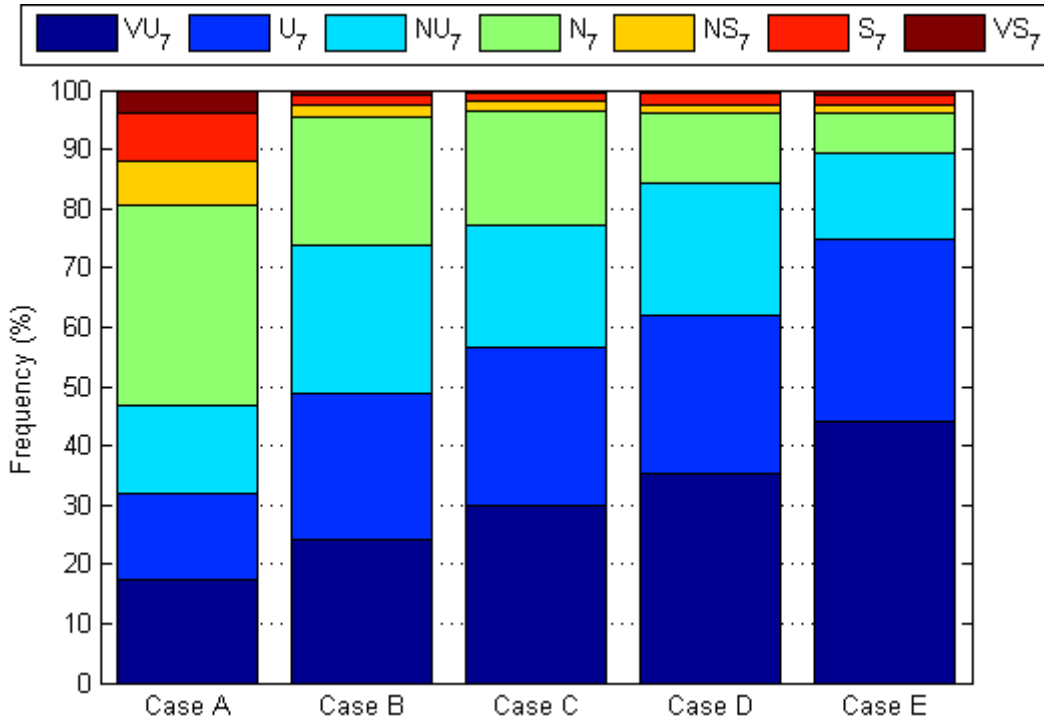


Figure 3.2 Frequency distribution of atmospheric stability split into 7 categories

Both the above graphs show the North Sea to have predominantly negative values of L , although Figure 3.2 suggests a more even distribution, whilst Figure 3.1 implies the offshore atmosphere exhibits either Very Unstable or Very Stable conditions, with little in between. The greater frequency of Very Stable cases using the 5 class method compared with the 7 class method is related to the concept of the critical Richardson number (Ri_{Gcrit}), above which the atmospheric flow does not generate additional turbulence although may maintain existing turbulence for Ri values above but close to Ri_{Gcrit} . In previous work, [17], [48] authors have filtered these events to enable closer analysis of the atmospheric turbulence conditions described by MOST and which affect wind turbine wakes. The 7 class categorization method still applies this filter although one step later, when classifying L rather than calculating it. By also filtering the most unstable events where $0 > L > -50$, all remaining events categorised by Table 3.3 are within the range $|Ri_G| < 0.2$ (if z' is assumed to be the World Meteorological Organisation's standard value of 10m). This suggests that Ri_{Gcrit} is not exclusive to positive values, although a negative Ri_{Gcrit} is more likely to reflect a lack of wind shear between measurement heights than an overbearing thermal gradient.

In Figure 3.1; Case D and Case E display very similar distributions, despite 20m difference between the heights of their respective upper measurements; this contrasts with the third data set from FINO1, where Case C reports Very Unstable events occurring over 80% of the time whilst Very Stable events occur at a rate of less than 3%. Since each case study was processed in the same way and each use overlapping data in their analysis, it can be concluded that the height at which the lower of the two measurements is made is significant in describing local atmospheric stability conditions. This hypothesis is supported by Humber Gateway Case B which uses a lower measurement height just two metres different to those at Case C and reports a similar stability distribution. This hypothesis was also the major finding of [26] and implied by [52]. The inclusion of humidity in calculating L for Case A shifted the distribution significantly towards more stable categories, a result which can also be seen between Case A and B in Figure 3.2 which emphasises the less extreme stability categories. The 7 category method also supports the link between measurement heights and stability category. The four case studies which use T rather than θ_v each show an increase in Very Unstable events and a decrease in Neutral events with each decrease in their z' value shown in Table 3.1, although there is little variation in the frequency of more stable categories, despite differences in location and data collection times between the Humber Gateway and FINO1 masts. There does appear to be some correlation between the frequency of category VU_5 with the combined frequencies of VU_7 , U_7 and NU_7 (where $-200 < L < 0$ and $-500 < L < -50$ respectively) in cases A, B and C. This is considered coincidental however partially because the bin sizes are different, but also as according to Table 3.4, the filtering of events where $-50 < L < 10$ in Figure 3.2, shows that more than 58% of the data in each case has been filtered. That so many extreme data events can be filtered out and still maintain the rough proportions stability distribution emphasises how rarely the offshore atmosphere is neutrally stratified. For cases D and E which have smaller values of z' on the FINO1 mast, removing events where $L < 10$ almost entirely removes the contribution of more stable events as shown in Table 3.4.

3.4 Wind Profile Gradient Analysis

To test whether the atmospheric stability can be obtained without data from thermal measurements, Figure 3.3 and Figure 3.4 below show the average wind speed ratios between upper and lower measuring heights. Data for Figure 3.3 is filtered by the five categories in Table 3.2 whilst data for Figure 3.4 is filtered by the seven categories in Table 3.3. They show that as the atmosphere becomes more stable, the level of wind shear generally increases. This is clearer when using the seven stability categories rather than only using five.

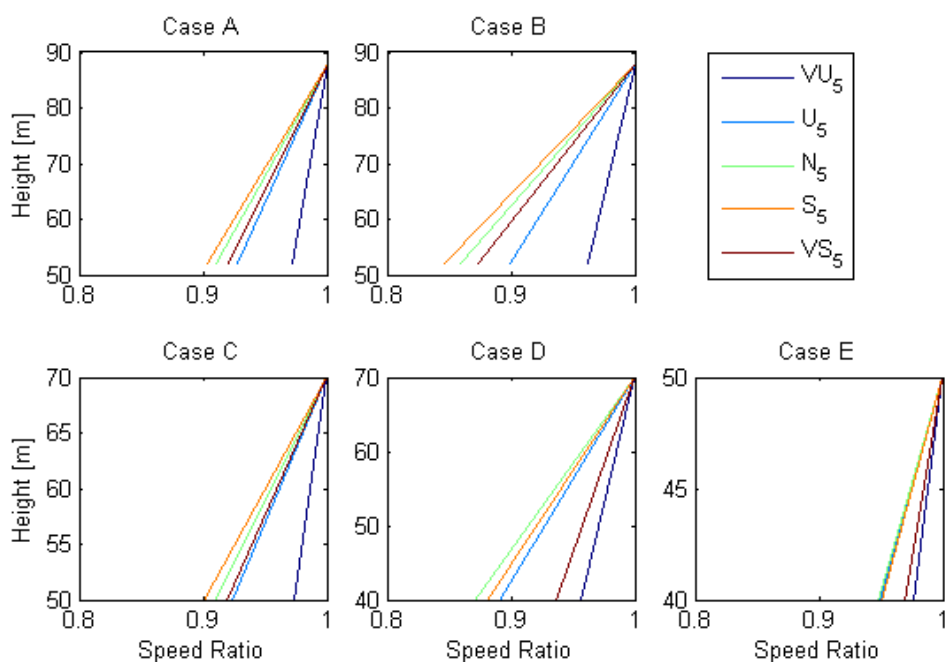


Figure 3.3 Wind shear for the five case studies filtered by five stability categories

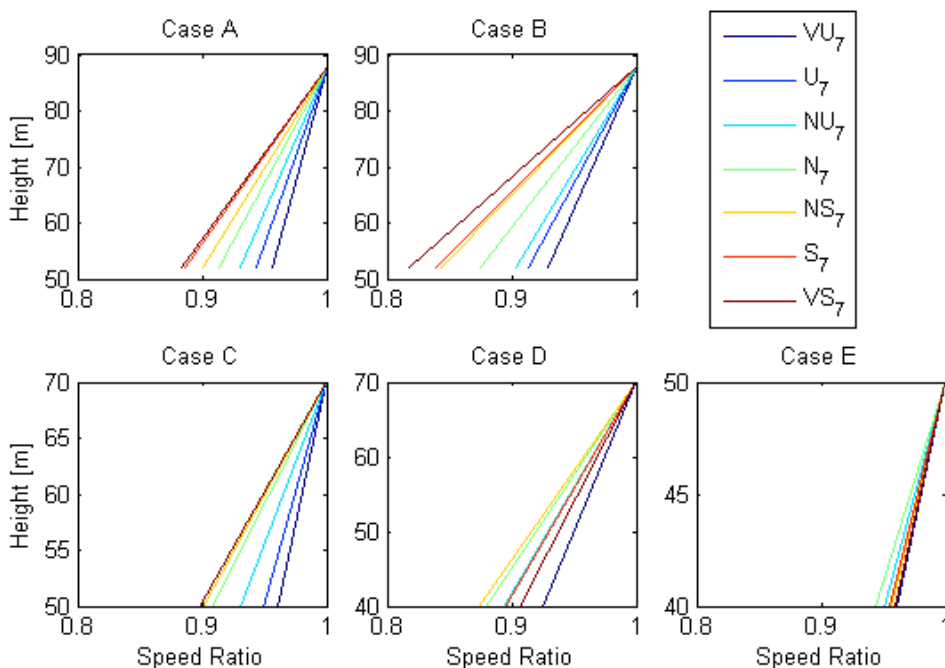


Figure 3.4 Wind shear for the five case studies filtered by seven stability categories

There is significant difference in shear levels between Case A and B; all categories show various levels of decreased shear when incorporating atmospheric humidity and pressure, which combined with the distributions shown in Figure 3.1 suggest opting to utilise either θ_v or T amounts to an arbitrary choice whether to favour turbulence or wind shear in the definition of L . The differences in shear between Case A and B are visible for both the 5 and 7 stability classification methods, supporting the idea in that incorporating humidity produces lower shear factors (greater changes in Speed Ratio with height). With both the 5 and 7 group categorising methods, the choice of thermal parameter does not alter the order in which stability categories are shown to exhibit wind shear, merely the spread of the distribution. Category VS_5 appears to defy the correlation between $1/L$ and shear with values occurring between those of N_5 and U_5 ; this may be a result of failing to filter the events where $|Ri_G| > 0.2$ as the VU_5 shear values also appear proportionally low, for each plot in Figure 3.3 but not in Figure 3.4 where filtering is in effect.

Using the results from the FINO1 it is clear that similar to the results shown by [26], the height of measurement is significant in determining the levels of shear relative to atmospheric stability. Similar to the results from the Humber Gateway mast, there is a general correlation between $1/L$ and wind shear, although not as strong in Cases D_5 and E_5 . Using the seven stability category system appears to be superior in this respect as the level of shear in each category more closely relates to $1/L$. However, that this is not a perfect correlation is shown for Case E_7 where neutral events exhibit the most shear, and Case D_7 where shear values for S_7 and VS_7 are both below that of NS_7 . Thus, atmospheric stability may not be calculated on the basis of mean wind speeds alone, although it should be remembered that Figure 3.2 shows a very small proportion of events exist where $10 < L < 500$ at FINO1 and the sample size may not be sufficient for reliable statistical analysis. Also to be considered is the depth and location of the layer over which shear is calculated, for example Case E (measurement height difference of 10m) is unlikely to achieve the same shear levels as Case C (measurement height difference of 20m). The location is important as it may include features of hidden thermal internal boundary layers; [26] reported the existence of such a layer at roughly 50m at FINO1, irrespective of wind direction,

which although irrelevant for measurement of individual shear events, may be significant for categorisation of stability categories.

3.5 Turbulence Intensity

Using the gradient method to calculate L utilises the Richardson number, a non-dimensional ratio between potential and kinetic energy, representing the buoyancy and shear aspects of turbulence production across a fixed depth of atmosphere as shown below in equation 3.2.

$$Ri = \frac{\text{potential energy}}{\text{kinetic energy}} \quad 3.2$$

Comparing this to equation 2.15 or equation 3.1 implies the kinetic energy equation is only partially implemented when using time averaged wind speeds measured on site, since the speed at any particular moment comprises of the time averaged mean value and a deviation from said mean as shown in equation 3.3:

$$u = \bar{u} + u' \quad 3.3$$

Therefore since changes in offshore ambient TI vary with atmospheric stability, and with [66] linking it to variable turbine wake dissipation rates, it is reasonable to assume variations in the u' parameter with L are at least partially causing the unexpected shear values for some stability categories in Figure 3.3 and Figure 3.4. Therefore, Figure 3.5 below shows values of TI averaged for each case study by stability category, using measurements from the higher anemometer in each case. While TI in Case B significantly reduces with increased stability, there is a less dramatic effect in Case A in both the five category and seven category distributions, suggesting again that choice of thermal parameter directly alters the significance of other contributing parameters when calculating Ri_G . Results from the three FINO1 cases show a decrease of TI as stability approaches neutrality from either end of the stability range, with the exception of Case C using the 7 stability classifications, which shows a general decrease in TI with each increase in stability. The importance of the lower measurement height is again highlighted in that despite TI being

calculated at 70m on the FINO1 mast for both Cases C and D, and at 50m for Case E; TI values for Case D are closer to those for Case E than for Case C for five of the seven categories. This suggests that, similar to the results found by [26], the measurements taken from the lower height are more significant in defining L than the measurements taken from the higher instruments.

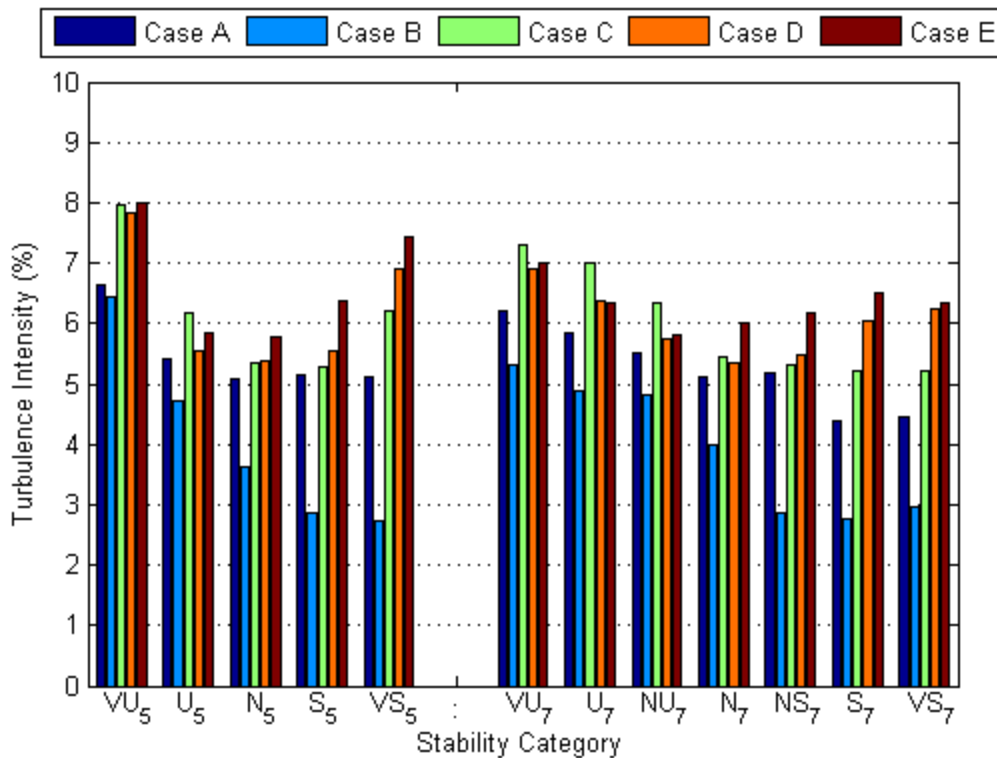


Figure 3.5 Turbulence intensity filtered by stability category

For comparison purposes, [73] reports ‘typical’ values for offshore TI at hub height are 6-8% whilst [33] suggests that it is 10-12% over land on average. Whilst most of the bars in Figure 3.5 show TI rates below 6%, since the majority of pre-filtered events are categorised as VU₅ which are all above 6%, it is a fair assumption that Figure 3.5 supports the findings of [73].

3.6 Combining Shear with Turbulence

Considering how values of TI in Figure 3.5 vary with $1/L$ in a non-trivial fashion, TI alone cannot be used to approximate L in the same way that Figure 3.3 and Figure 3.4 show mean wind shear alone is not enough. Therefore, Figure 3.6 shows TI against wind shear as represented by α where the events have been filtered into three simplified categories of Stable (red), Neutral (green) and Unstable (blue) events according to their Obukhov length.

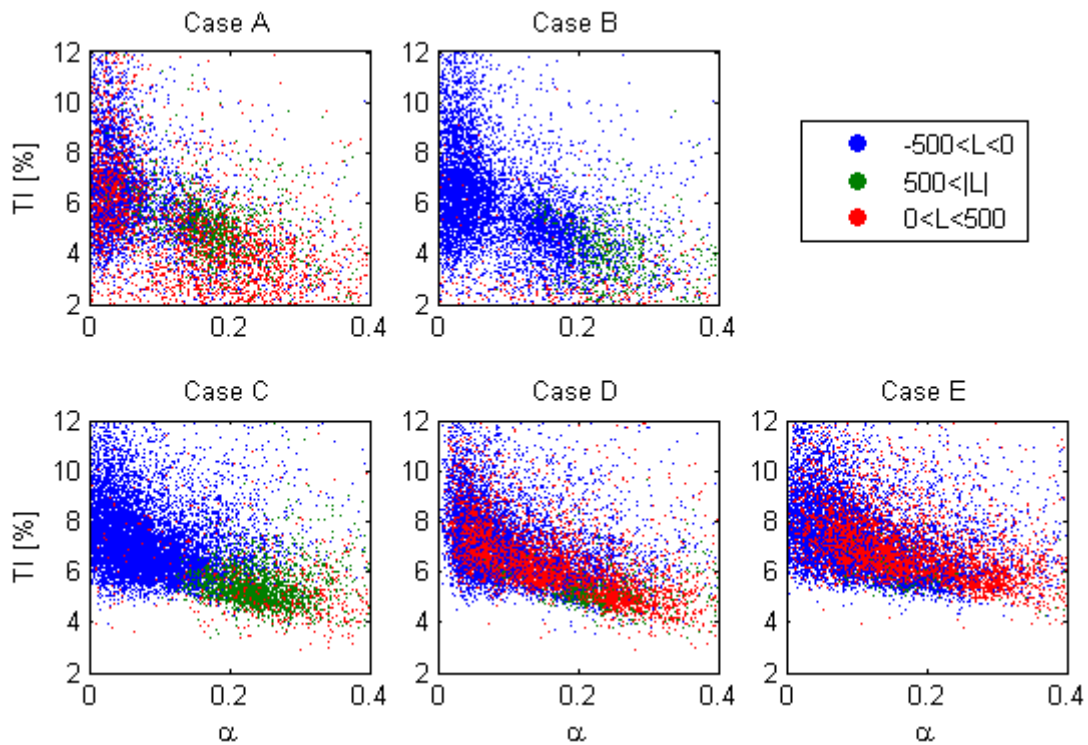


Figure 3.6 Correlations between TI , α and L

Differences between Cases A and B in Figure 3.6 show the inclusion of humidity and pressure in the thermal variable shifts values of L in the positive direction (as also suggested by previous graphs). Although clearer in some cases than others, all five data sets show Unstable events exhibit lower values of α than Neutral events. It is also clear that the often common assumption of Stable events being associated with lower average levels of TI than either Neutral or Unstable events is inaccurate, as overlapping between regions of both TI and α exist in all cases. The plots representing data from FINO1 (cases C, D and E) suggest a natural TI minimum which decreases as α increases. This minimum, whilst generally supported by the plots for the Humber Gateway mast (cases A and B), is not as clear amongst the more widely scattered data points. It is feasible that the lack of a defined minimum TI value in Cases A and B stem from the mast's proximity to the coast; even though data were filtered for steady marine directional flow, the mast is only 10km from a coastline to the west compared with FINO1 which is located 40km north of the nearest coast. The difference in coastal direction and proximity is significant as low pressure weather systems in the North Sea primarily approach from the west, causing them to be filtered out of the Humber Gateway datasets whilst included in the FINO1 sets. It is also notable that the neutral stability events cluster at roughly 5%

TI and between 0.2 and 0.3 α , although using θ_v , shifts it towards lower values of α in Case A. It should also be noted that Case E shows consistency with [74] in that the 50m ambient offshore turbulence is typically between 6% and 8% although at locations close to shore such as Middelgrunden, average TI values are around 13% [33].

A similar plot was made by [75] when analysing wind measurements from the U.S. Great Plains. Rather than filter the data by stability as in Figure 3.6, they filtered by day and night, which considering the large influence of short term solar radiation in continental locations, can be approximated to unstable and stable conditions respectively. They found two distinct clusters with the day (unstable) events grouping below $\alpha = 0.1$ and above $TI = 7\%$ while night (stable) events clustered between TI values of 2 and 8% with shear exponent values between 0.1 and 0.5. Both the North Sea masts show lower variability in TI and also less extreme shear exponent values than at the onshore location analysed by [75] while the FINO1 events seamlessly merge unstable with stable, however, both the onshore mast and Humber Gateway mast exhibit two clear clusters of events. These differences between mast results are assumed to be the result of high marine thermal capacity, with the Humber Gateway mast in coastal waters only partially experiencing this dampening effect on the daily cycle.

Since offshore wind farms are devoid of any external complicating flow effects such as difficult terrain or forest canopies, their overall power output is primarily dependent on the effects of atmospheric stability on each turbine wake throughout the farm. Therefore, using only one parameter (L) to describe the governing relation between TI and α is not sufficient, as shown in Figure 3.6. Therefore, as [75] showed clear distinctions between night and day (stable and unstable) for an onshore location, this suggests that one should let offshore stability be defined, not as a function of L , but as a function of TI and α . Using evidence based empirical judgement with Figure 3.6 and the work by [75], the atmospheric stability is categorised according to

Table 3.5 and visualised in Figure 3.7 below.

Table 3.5 Atmospheric stability defined by TI and α

Stability Category	Parameter Range		Colour Code in Figure 3.7
	TI	α	
Stable	<6%	>0.1	Cyan
Unstable	>6%	<0.1	Yellow
Other (Neutral)	>6%	>0.1	White
	<6%	<0.1	

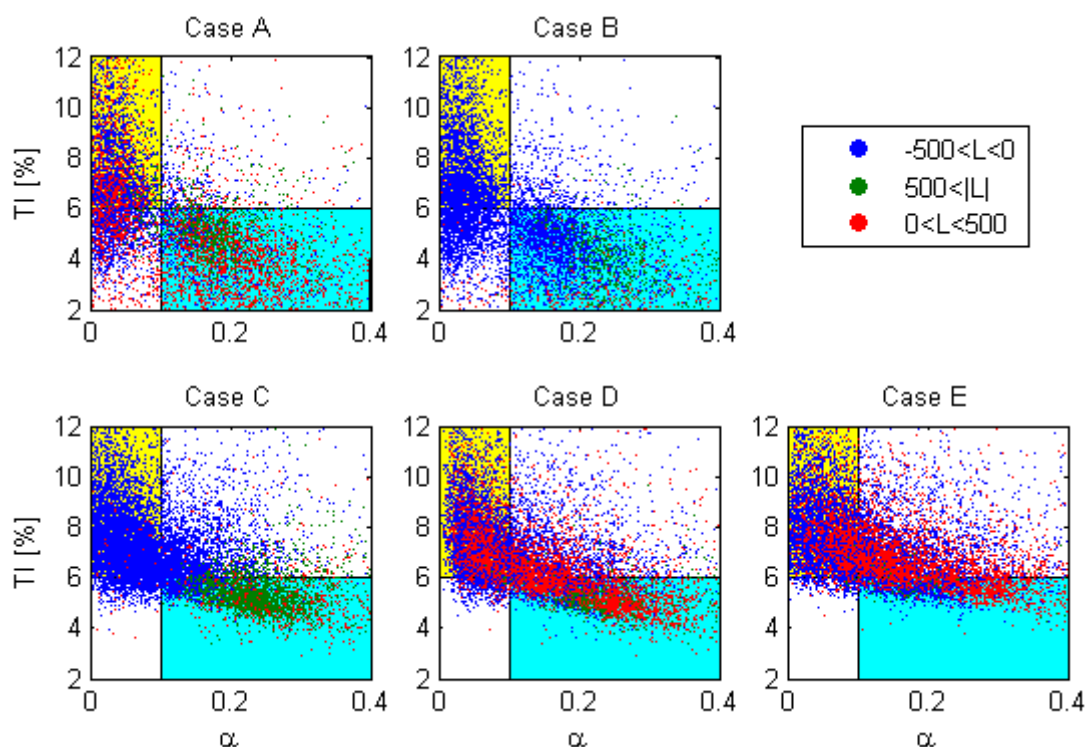


Figure 3.7 Correlations between TI , α and L with new stability regions highlighted

Whilst Figure 3.7 shows the majority of events where $|L| > 500$ occur within the stable region (cyan), Figure 3.8 shows the new proportional distributions for each case study are more heavily weighted stable than in Figure 3.2 using the traditional seven category method. Significantly, Figure 3.8 shows the incorporation of alternative thermal parameters does not change the stability distribution as temperature is not considered in the calculation; allowing future met masts with restrictive recording limitations to focus on wind measurements at multiple heights rather than measuring multiple parameters at each height. Therefore this technique may be used to assess potential wake losses without the required measurements for calculating Ri_G , making it ideal for datasets collected via remote sensing instruments such as LiDAR. Since the critical values of TI and α were chosen empirically (TI_c and α_c respectively), there is scope to alter them based on further study of other

most data or to align the distribution in Figure 3.8 with those in Figure 3.1 or Figure 3.2. For example, if TI_c was decreased to 5%, a significant number of currently stable events would be reclassified as neutral whilst a smaller number of currently neutral events would be reclassified as unstable, thus making a location's stability distribution appear increasingly neutral.

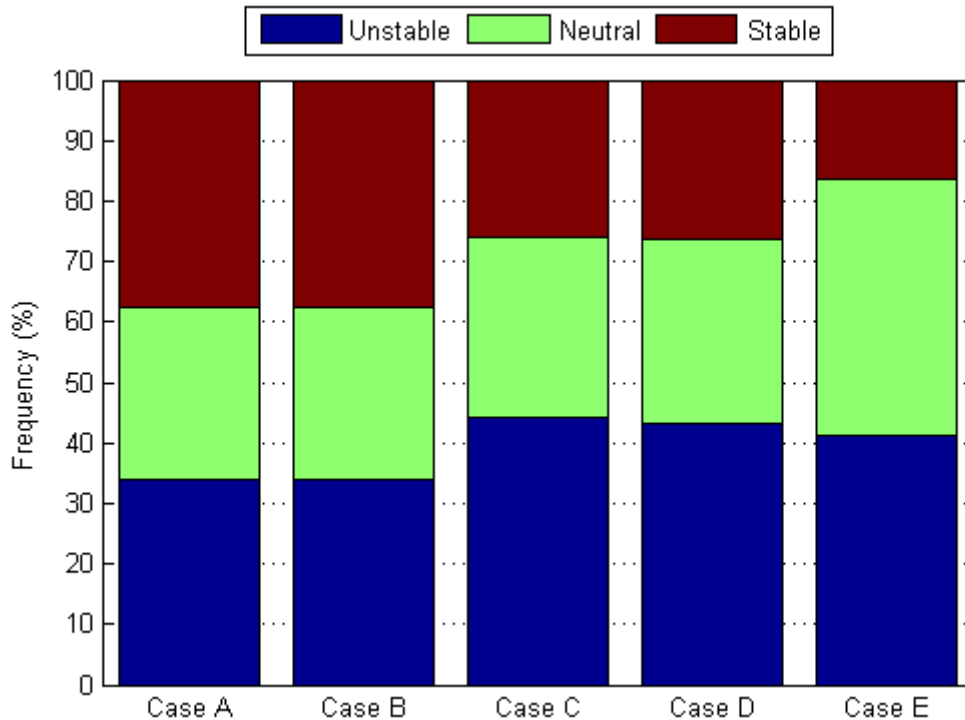


Figure 3.8 Frequency distribution of atmospheric stability split by defining parameters in Table 3.5

For the purposes of Computational Fluid Dynamics (CFD) modelling input conditions, it is suggested the three regimes be represented by the parameters in Table 3.6 and shown in Figure 3.9 as these are not only key locations based on TI_c , α_c and data clustering, but are also representative of values reported by [73] and [75]. Whilst the values of these suggested input parameters stay constant in Figure 3.9, their suitability to describe each dataset once again strongly depends on the measurement height. For example, they are more representative of the measured data in the cases where TI and α are calculated for measured data above 50m (Cases A to D), further evidence that the height of atmospheric measurement is key to its value within the industry.

Table 3.6 Suggested input parameters for simulations

Stability Category	TI Value	α Value
Stable	5%	0.2
Neutral	6%	0.1

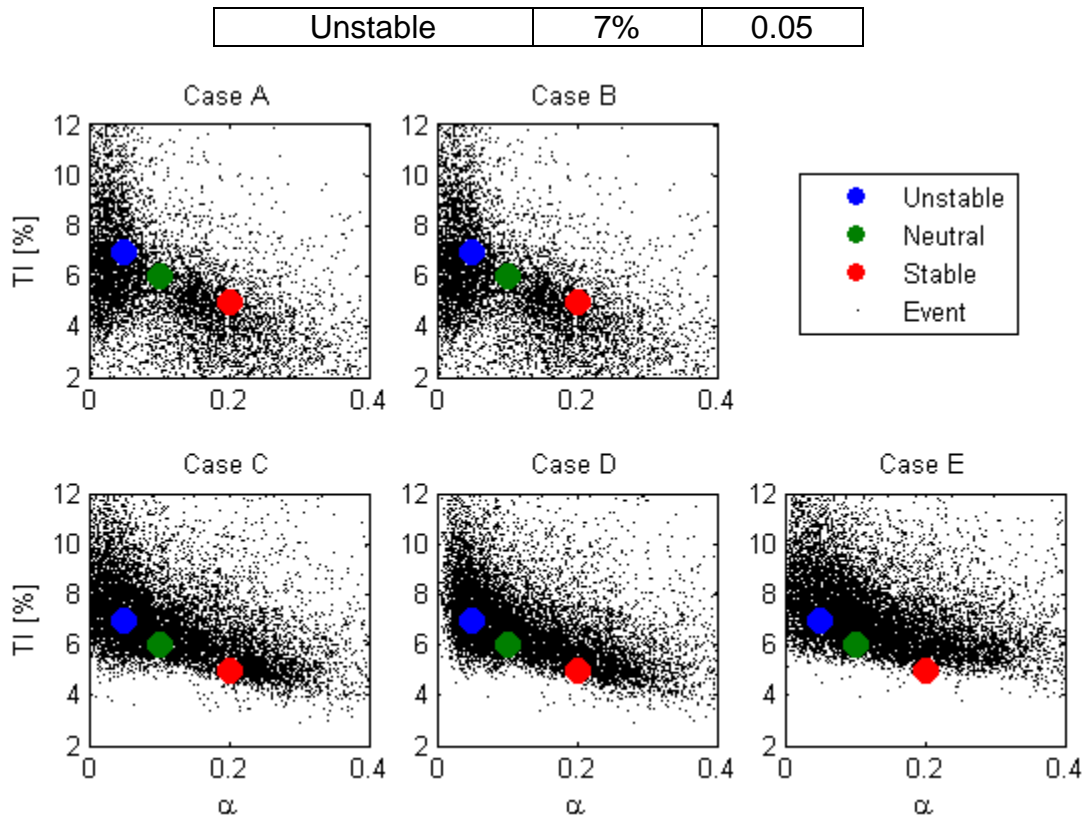


Figure 3.9 Locations of suggested simulation values in Table 3.6 with measured events.

3.7 Study Conclusions

Using the gradient method of calculating L , data from two offshore met masts in the North Sea have been used to assess two different methods of classifying atmospheric stability between five and seven classes. Whilst neither method filtered the datasets to remove events where $|Ri_G| > Ri_{Gcrit}$, the seven classification distribution method filtered them indirectly by not including events where $-50m < L < 10m$. Without filtering for events where $|Ri_G| > 0.2$, graphs comparing average shear against L indicate relations too complex for simple modelling assumptions beyond “increased levels of stability generally increases average wind shear”. Similarly, just comparing TI against L revealed little use as TI decreased with increasing L at the FINO1 mast whilst decreasing with increasing $1/L$ at the Humber Gateway mast. Therefore, as no conclusive correlation with L was revealed from either TI or wind shear alone, and only limited regions of discrete clustering formed when comparing L against both TI and shear, it is concluded that in situations without thermal measurements, atmospheric conditions should be described by the arbitrary values selected through empirical research. For use with offshore wind farm resource analysis, further research should be conducted to determine whether the

shear and background TI are solely responsible for variations in wake behaviour, or if thermal buoyancy effects are significant enough to warrant the extra expense required to measure them.

Who spits against the wind spits in his own face.

- **French Proverb**

Chapter 4. Benchmarking CFD Models of Large Wind Farms in the Neutrally Stratified Offshore Atmosphere

4.1 Introduction

Developing an offshore wind farm is expensive, often requiring co-operation between multiple large utilities or financiers to manage the upfront costs and share any potential risk. To convince potential investors that the planned farm is a financially sound project with attractive returns, computer models at many scales [76] are used to simulate likely wind conditions the farm will experience and thus calculate the expected power losses due to turbine wakes (depending on turbine spacing 5%-25% [69] [77]) and thus the overall asset value. In addition to predicting the expected generation levels of the final design, models of various complexities are used iteratively throughout the design process. First, an initial resource assessment is conducted using any of the eight methods described by [78] depending on available data. Then specialised models for the optimization of turbine layout such as described by [79] or [80] are run before fast linear models based on [81] such as WAsP [82] or WindFarmer [83] are run for a general overview of expected farm performance given any wind speed and direction. Output from the linear models also highlight areas requiring further investigation such as regions of flow separation in complex terrain or specific flow scenarios with significant wake losses (especially for offshore farms) where more powerful models are required to reduce investment risks. These are typically computational fluid dynamics (CFD) models for example [84] [85]; as they utilise detailed flow models including complex turbulence closure equations or very high resolution meshes, CFD models are very time consuming and therefore are only run for a few key scenarios where accuracy is paramount. Since for large offshore farms, it is well known that turbine wakes are the prominent source of power loss, specialist offshore models may have to be developed to cope with lower ambient turbulence or wakes from other farms [86].

4.2 Wake Modelling Review

Every simulation ever made, no matter what the field of interest, requires assumptions which allow it to operate within its limitations. Most commonly in the wind industry, the restricting limitation is a lack of sufficient computational resources. Despite ever more powerful computers, it remains unlikely that science will ever produce a completely accurate computer model capable of matching the exact variations in the micro-scale, random turbulence characteristic of the ABL, particularly over the vast volumes which modern offshore farms occupy. Therefore, each modelling technique has its own definition of accuracy and the term “good enough”. Often this is determined by the five limitations: the affordable calculation window, the available computational resources, the maximum scale and resolutions of the intended simulation and the number of simulated scenarios required.

Early approaches to wake modelling focused on co-flowing jets, symmetric regions of low momentum with constant expansion and decay expressions behind a single turbine [87] calibrated against measurements from wind tunnels [88] or turbines [89] [90] and the theoretical effects of their superposition within a farm [91] [92]. However, linear superposition of wakes can lead to the amusing but unhelpful prediction of negative velocities when simulating very large farms; [90] attempted to avoid this by assuming wake superposition based on a power law of flow deficits which gave smaller cumulative wakes than the linear alternative and thus a more accurate prediction. In general, any system for calculating farm deficits based solely on single wake multiplications will fail as the rate at which each wake dissipates is a function of the surrounding atmosphere which in turn is affected by the wakes of upstream turbines and therefore will not be constant throughout the farm. This was experimentally shown by [93] when the velocity deficit from a downstream turbine recovered faster than the upstream turbine’s wake at the same relative distance behind the rotor. Analysis of wind tunnel results [94] and farms [69] [95] suggest there may be an equilibrium value for generated wake turbulence levels and thus wake deficit, dependent on turbine spacing and thrust for any particular wind speed although this does not account for observed deep-array effects [96]. The inclusion of ground effects causes further problems for kinematic models, especially for large wind farm arrays when assuming axial symmetry. Whilst [91] observed the ground

reflection could be treated as a symmetrical boundary between two adjacent turbines, this does not appreciate drag losses caused by friction, thus [97] concludes the only proper treatment of ground effects are to use 3D models.

An alternative approach was developed for large farms where models assume infinite arrays of turbines behave as regions with higher surface roughness values, thus modifying the ambient atmospheric flow [98] [99]. Whilst producing satisfactory results [100], these boundary layer models do not explicitly simulate the turbine or wakes, and their wind profiles tend to result in smooth logarithmic functions rather than regions of rapid shear and high turbulence through the rotor height. To counter this [101] developed a model with one logarithmic wind profile beneath and a separate profile above hub height, thus whilst acknowledging the deviation from a non-wake profile, the model effectively consigns the wake to an infinitely thin layer between the two profiles and ignores lateral variation. Such roughness length models are shown by [102] to be all based on two common equations whilst the additional assumptions made to close these equations can produce significantly different results. A comprehensive review of these early techniques and their validation with wind tunnel data is given by [103]. The continuous advancement of available computational power has now led to more complex models for risk assessments of large projects, especially as the more simplistic models which consider the spatially averaged effects of increased surface roughness, struggle to portray atmospheric stability or the near wake [104]. They could be useful however, as modules within large climatic models observing the alterations caused by modern offshore farms at lower resolutions [105].

Modern computer models of wind farms attempt to solve the differential equations governing the flow, allowing the components associated with ambient stability to be more accurately considered [106]. Their varying levels of accuracy are often linked to their resolution and choice of turbulence modelling closures such as $k-\varepsilon$ (described in section 4.3 below). Prominent pioneers with these techniques include [88] [107] [108] and their models have been the basis of many such as FLaP [109], EVFARM [110] and UPMWAKE [111] which has recently received major upgrades to its turbulence resolution [112]. CFD models can be categorised by three main types (often with many sub-categories) based primarily on their mesh resolution of

calculation points. Generally, a higher mesh resolution leads to a greater accuracy of turbulence calculations but also greater requirements of computational resources, so the choice of grid design is often based on user experience, cost requirements and computational availability. There are three main types, the coarsest of which are Reynolds-Averaged Navier-Stokes (RANS) models which utilise time averaged variables and is chosen when the mean flow velocities are the simulation priority with turbulence acting as a modifying factor. This is useful when calculating long-term expected farm outputs but less so when analysing how events develop through time, particularly the turbulence within the near-wake region [113]. Direct numerical simulation (DNS) by comparison fully resolves the mean flow and all its turbulent fluctuations through time. The high mesh resolution is sufficiently fine that the unsteady Navier-Stokes equations are resolved down to the scale of energy dissipation, the Kolmogorov length. Large Eddy Simulation (LES) is a cross-breed method between RANS and DNS which uses space filtering processes to track and directly resolve the largest eddies whilst applying RANS-type averaging to the smallest, enabling higher resolution and greater accuracy than RANS whilst remaining more economical than DNS.

On account of its extreme computational requirements for even a basic flow, DNS is currently only used for small simulation domains containing flows of low Reynolds numbers around arrays of simple objects [114]. It is currently not logistical to model a whole turbine at rated wind speed, let alone a whole farm. Currently, the only use for DNS to wind resource assessment is to investigate and calibrate the assumptions required by LES models [115], although wind tunnels are often capable of this in a fraction of the time. Likewise, because LES models require fine meshes to resolve the larger eddies, they are more expensive than RANS and so uneconomical to simulate whole wind farms, although the use of sub-grid scale models for features smaller than the controllable grid scale (about 10m [116]) and variable mesh resolutions throughout the domain reduces complexity [117] enabling domains to contain around 5 turbines [118]. As such, large farms can only be simulated at reasonable costs via the use of periodic domain boundaries [119] although recent simulations are getting bigger [120]. Therefore, LES simulations tend to focus on investigating the generation, transportation and dissipation of turbulence behind individual turbines [112] since [97] highlights lesser models are unable to deal with

the non-isotropic ambient turbulence integrated with wake turbulence. Other uses include simulating the higher resolution flow patterns around each turbine [121] to control the wake direction and maximise farm output [122] or investigating assumptions such as the actuator disc (AD) method described in section 4.3.1 [123] [120] – work which would otherwise be restricted to models in wind tunnels [124] [125] with complex scale conversions. Although wake meandering from large eddies has been approximated by previous models [126]; LES models produce time-variable results, which can be used to directly observe the effects of wake meandering [123]. These observations can then be applied as averages in RANS models or provide statistics on likelihood of damaging gusts from large eddy superposition under different stability conditions.

Currently, whilst ‘industry standard’ wake models are typically eddy viscosity models named after their pioneer as ‘Ainslie’ type designs [88] such as those within Windfarmer, the optimum method for modelling whole offshore farms in detail is via RANS CFD. The sheer scale of these wind farms renders the detailed results of LES too expensive. Whilst fast ‘Ainslie’ models are able to assess many scenarios and provide good comparison with measured power data [109] [127], they are unable to provide detail about the flow characteristics and often require empirical corrections or user experience to cope with larger arrays or neighbouring farms [86] [128] [129]. It is the CFD capability to calculate turbulence (either with model closure equations or modelled directly) that enables it to forego such tuning requirements. After the incident wind speed defining the turbine thrust coefficient and so initial wake strength, the secondary factor controlling wake behaviour is the level of ambient turbulence [65] which, offshore, is strongly linked to both atmospheric stability and wind speed [96] [73]. Thus, for a CFD simulation to be worth the extra cost to run, it needs a reliable turbulence closure scheme which responds to changes in speed and stability, particularly for offshore farms where mechanical terrain generated turbulence is relatively low. This is highlighted by the “Deep Array Effect” characterised by larger than expected wake losses from turbines located far from the free stream atmospheric flow and thus are subjected to flow conditions generated within the wind farm itself and are significantly different from ambient conditions. Current difficulties in validating offshore models stem from relatively few quality datasets and most are compared to data from either Horns Rev or Nysted farms [69] however, as more

farms come online and their developers become willing to share data, problems such as inhomogeneous fetch conditions [38] will be better understood. Although normally still classed as a 'research' tool, CFD is gaining popularity and there are a range of available options such as WAKEFARM, NTUA, RGU [100], PHOENICS [130] and Ansys CFX/Fluent/Windmodeller [131].

As the main problem with CFD models is the computational time required even when using RANS, assumptions and approximations are made to either simplify the flow or the structures within the domain. A common example of this is the AD concept which acts as a momentum sink averaged across the turbine rotor plane rather than requiring the vast number of extra computational cells to accurately simulate the rotor area [117]. Whilst this saves considerable time for large farm simulations and detailed turbine geometry often is not available, the compromise is a loss of wake rotation and misrepresentation of turbulence from tip-vortices [132] which, combined with the assumption of a homogeneous inflow, could impact on the very reason to use CFD detailed wake loss calculations. However, [133] reports AD methods give reliable wake descriptions when further than three diameter lengths downstream – the distance shown by [124] as where differences between wakes behind porous disks and rotating models are indistinguishable as wake rotation and tip vortex structure had ceased effectively to exist and AD methods appear acceptable even in conditions with low ambient turbulence. Therefore, whilst fully resolved turbine models may be required when developing new blades, modelling at farm scale, where the main attention is on wake models and turbines are far enough apart that they only ever experience the far-wake of other turbines, the AD method is used to save cost without loss of significant accuracy. However, despite [84] using a three dimensional AD method to demonstrate the existence of positive interference between turbines (venturi effects), [117] urges caution when implementing standard AD methods within RANS models utilising the standard $k-\varepsilon$ turbulence model [134] as other authors have shown it to under-predict near-wake effects [135] [104]. According to [136], this exaggerated wake dissipation is a result of different turbulence scales relative to individual disks and blades. Since the dissipation rate is largely empirical and often based on constants proposed by [108] suitable for the neutral ABL, applying further empirical modifications often yields greater results [85]. Alternatives to the AD concept include the actuator line (AL) concept where the

turbine blades are each represented by a line rotating around the hub and interacting with the flow [137]. Since these 'blades' require the higher resolution of LES and fail to significantly improve on near-wake results from rotating AD methods [118] they are seldom used for simulating whole farms. As turbine rotor diameters continue to increase however, [138] notes the IEC standard of one point measurement will no longer be representative across the whole blades, particularly in high shear conditions and AL may need to be embraced as standard by modelling software with detailed research models based on full rotor computations [139], assuming continued growth in computational processing power.

In Chapter 2, it was described how atmospheric stability can impact the productivity of a large wind farm by either prolonging or dispersing turbine wakes and so reducing or enhancing the wind resource respectively. Therefore, any simulation involving turbines, particularly offshore, where farms are large and wake losses significant, should include such stability effects. For LES, [140] shows the model coefficients to be highly sensitive to atmospheric stability whilst the averaging aspects of RANS simulations make them more forgiving [67]. Based on a scale of $1/L$, the median atmospheric condition is neutral, although after applying the filters required to account for the assumptions made by MOST, offshore conditions appear more frequently unstable. It has become common practice to assume neutral atmospheric conditions for CFD simulations as this gives the simplest velocity profile and as the median it is often assumed most suitable when simulations are limited to a single run. An alternative reason is that wind turbines are rated at higher than average wind speeds, where the stability tends to neutrality (see equations 2.13, 2.14) and so making this assumption gives a more consistent assessment. Although [36] points out that stability conditions have greatest effect on wind speeds and thus are most important between typical cut-in and rated wind speeds, and since wake assessments often simulate speeds where the turbine thrust coefficient is at its maximum, stability should be included in resource assessment simulations. Past experiments have been conducted using AD and AL techniques to model the effects of atmospheric stability on a single turbine wake both with RANS and LES [67] [141]. Until recently, there has been little research into modelling the whole farm in non-neutral conditions.

Finally, there is the problem of direction bin size. Ideally, there would be sufficient data from numerous offshore farms to investigate flow from any direction at any speed and stability. However, as there are only a few large operational farms willing to share data, and they have only been running a few years, after filtering for erroneous and missing data, there are very few data left (if any) for every scenario. To cope with this, events with similar incident wind directions are often banded together in 'direction bins' whilst wind speeds are often grouped to an accuracy of $\pm 0.5 \text{ms}^{-1}$ or lower. Stability events are grouped most loosely as described in Chapter 2. Naturally the bin sizes impact the accuracy of any subsequent results, for example, the more wind speeds that are grouped together, the more variation there will be in respect to each turbine thrust and so wake development. The direction bin size is even more important since not only is stability often related to direction [66], a wind direction 'down the line' of turbines will result in each turbine being subject to the wakes of upwind turbines, whilst depending on turbine spacing as the wind direction moves further from 'down the line', the second turbine will become more subject to free stream flow or even some venturi effects as shown by [68]. It is possible that deep-array effects may be a consequence of direction bin size and turbine spacing, although there are not enough large farms to validate this idea. As the power output of a large farm is dependent on wind direction, it should be incorporated accordingly in any simulation. Models such as WAsP operate with wide direction bins (30°) whilst for CFD models, each simulation is an individual direction and matching measurement bin sizes requires multiple simulations and thus a considerable cost increase. Results from [67] indicate that generally CFD models over-predict wake losses in the narrow sectors, while non-CFD models tend to under-predict wake losses unless their coefficients are adjusted to match the observations.

4.3 An Overview of CFD

CFD is a virtual research tool, comparable to physical tools such as wind tunnels. As with all experimental practises, CFD simulations are subject to a range of assumptions and compromises that allow complex real-world events to be assessed at different temporal or physical scales before full-scale production on site. This is particularly valuable for large offshore wind farms, where any construction requires hiring expensive equipment (such as jack-up vessels) and calm weather (in locations

selected for their regularly high wind speeds). Simulations consider fluid-flows to be a continuum and only analyse the macro-scale events, ignoring individual molecular structure or motions. Whilst this reduces the required processing power, it maintains the ability to solve the flow governing equations anywhere within the domain. Thus, unprecedented quantities of detailed output data are obtainable without risk of altering the flow patterns, which might occur when simultaneously using multiple hot-wire anemometers in a wind tunnel scale model. Although the virtual environment does not need specialised hardware to be built and calibrated for each simulation, suitably powerful computers and a limited supply of experienced engineers cause alternative resource limitations. To help mitigate this, commercial CFD packages can be run with parallel processing units with the software split into three user-friendly components: a pre-processor, a solver and a post-processor.

The pre-processor uses clear graphical interfaces such as drop-down menus and 3D viewers to define:

- The domain: the region of simulation including scale, boundary conditions and the locations of physical structures such as turbines or masts.
- The mesh: the multiple, non-overlapping, sub-domains dividing the domain into smaller control volumes, also called cells.
- The fluid properties: the physical and thermal characteristics prompting the simulation to be conducted.

The solver uses numerical algorithms to calculate the flow solution corresponding to the defined input data from the pre-processor and sends it to the post-processor. Assuming the well-established “finite volume method” is applied, the governing fluid equations are integrated across every cell in the domain, converted into a system of algebraic equations and then solved via an iterative process.

The post-processor uses appropriate display features such as graphs, tables and 3D viewers to interpret the simulation results. Whilst this is often semi-automated to provide faster access to commonly required features, such as turbine power outputs or wind speed at mast locations, additional manual, fully-customisable features such

as colour surface plots and particle tracking, provide further analysis of the simulation results.

According to [142], more than half of the time spent conducting industrial CFD research is allocated to the definition of domain and grid generation, although this statistic is probably biased by work with complex objects such as vehicle engines or aerodynamics. Domains for simulating large offshore wind farms by comparison, are devoid of complex geometry, with shorelines often beyond the domain boundary, waves consolidated into the value of z_0 and turbine structures either ignored or simplified. This, combined with a non-uniform mesh (coarser further away from the sea surface) and options for automated mesh refinement around areas of rapid flow variations (such as wind turbines), significantly reduces simulation cost, for both individual solution calculation and operator training times. However, the solution accuracy is strongly governed by the size and number of cells throughout the domain, with smaller cells leading to greater accuracy. Since there is no way to assess the suitability of complex physics models within a CFD code, other than to compare simulation results against multiple real-world events, the operator must always judge whether the results are 'good enough' or if the solution must be recalculated with alterations to either flow boundary conditions or mesh resolution. For reference, in this work the solver was considered to have iteratively converged on an acceptable solution when the momentum, mass and turbulence residuals (normalised by the residual value at their respective first iterations) of said iteration process were below 0.00001. Lesser levels of convergence can be considered acceptable with suitable operational experience of similar simulations.

The CFD governing equations which determine the simulation results are built upon the three physical laws of conservation: the conservation of fluid mass, the conservation of momentum (Newton's second law of motion) and the conservation of energy (the first law of thermodynamics). This means the conservation of a flow variable, such as a velocity component, within each cell is expressed mathematically through a combination of convection, diffusion and creation. For example, adopting the common Cartesian co-ordinate conventions, if a cubic volume of fluid has sides of lengths δx , δy and δz , then the flow of an incompressible liquid (or air at low wind speeds) through the volume can be described by the equation below.

$$\frac{\partial u}{\partial x} + \frac{\partial v}{\partial y} + \frac{\partial w}{\partial z} = 0 \quad 4.1$$

This can be extrapolated for any parameter, for example, below is a function describing the total rate of work done on a fluid particle by surface stresses:

$$\left[\frac{\partial(u\tau_{xx}) + \partial(v\tau_{xy}) + \partial(w\tau_{xz})}{\partial x} + \frac{\partial(u\tau_{yx}) + \partial(v\tau_{yy}) + \partial(w\tau_{yz})}{\partial y} + \frac{\partial(u\tau_{zx}) + \partial(v\tau_{zy}) + \partial(w\tau_{zz})}{\partial z} \right] - \left[\frac{\partial(uP)}{\partial x} + \frac{\partial(vP)}{\partial y} + \frac{\partial(wP)}{\partial z} \right] \quad 4.2$$

Where τ is the shear stress on the surface of the cell with the associated suffix notation indicating the stress direction. The field can be solved with approximation to mass conservation and momentum equations only. If the simulation involves heat transfer, such as non-neutral atmospheric stability, then the Ideal Gas Law and energy equation (below) also need to be solved.

$$\rho \frac{DE}{Dt} = \left[\frac{\partial(u\tau_{xx}) + \partial(v\tau_{xy}) + \partial(w\tau_{xz})}{\partial x} + \frac{\partial(u\tau_{yx}) + \partial(v\tau_{yy}) + \partial(w\tau_{yz})}{\partial y} + \frac{\partial(u\tau_{zx}) + \partial(v\tau_{zy}) + \partial(w\tau_{zz})}{\partial z} \right] - \left[\frac{\partial(uP)}{\partial x} + \frac{\partial(vP)}{\partial y} + \frac{\partial(wP)}{\partial z} \right] - \left[\frac{\partial q_x}{\partial x} + \frac{\partial q_y}{\partial y} + \frac{\partial q_z}{\partial z} \right] + S_E \quad 4.3$$

Where E is the sum of thermal (internal) and kinetic energy, S_E is defined as a source of energy per unit volume per unit time, while q_x , q_y and q_z are directional components of heat flux vector \mathbf{q} .

As this section is presented as an overview of general CFD techniques; the considerable algebra required to convert the above theory into the well-known Navier-Stokes equations (below) is not explored in detail. For a more in-depth description of the algebra, descriptions of symbols and the process of converting them into solvable computer expressions, the author recommends reference [142].

$$\text{Continuity} \quad \frac{\partial \rho}{\partial t} + \text{div}(\rho \mathbf{u}) = 0 \quad 4.4$$

$$\text{x-momentum} \quad \frac{\partial(\rho u)}{\partial t} + \text{div}(\rho u \mathbf{u}) = -\frac{\partial P}{\partial x} + \text{div}(\mu \text{grad } u) + S_{Mx} \quad 4.5$$

$$\text{y-momentum} \quad \frac{\partial(\rho v)}{\partial t} + \text{div}(\rho v \mathbf{u}) = -\frac{\partial P}{\partial y} + \text{div}(\mu \text{grad } v) + S_{My} \quad 4.6$$

$$\text{z-momentum} \quad \frac{\partial(\rho w)}{\partial t} + \text{div}(\rho w \mathbf{u}) = -\frac{\partial P}{\partial z} + \text{div}(\mu \text{grad } w) + S_{Mz} \quad 4.7$$

$$\text{Energy} \quad \frac{\partial(\rho i)}{\partial t} + \text{div}(\rho i \mathbf{u}) = -P \text{div } \mathbf{u} + \text{div}(k \text{grad } T) + \phi + S_i \quad 4.8$$

$$\text{Equations of State} \quad P = \rho R T \quad 4.9$$

$$i = C_v T \quad 4.10$$

Where S_{MX} , S_{MY} and S_{MZ} are momentum sources in the three respective Cartesian directions, μ is the dynamic viscosity, ϕ is the dissipation function, i is the specific internal (thermal) energy and S_i is its source term.

4.3.1 Actuator Disc Theory

As briefly mentioned in section 4.2, the Actuator Disc Theory is a means of approximating the effects of a wind turbine on the atmospheric flow. Flow effects around the turbine nacelle and tower structure are assumed to be negligible in comparison to those through the blade swept area, and are therefore ignored. The AD is considered a flat circular disc, perpendicular to the flow of an incompressible fluid, and acts as a momentum sink. As the mass of air does not change as it passes through the disc, its velocity must decrease. It follows that on account of the air parcel behaving as an incompressible fluid, it must expand radially and occupy a hypothetical cylinder with a larger diameter than the disc itself. This can be described by the equation below:

$$\rho a_{Upstream} u_{Upstream} = \rho a_{AD} u_{AD} = \rho a_{Downstream} u_{Downstream} \quad 4.11$$

Where $a_{Upstream}$ and $u_{Upstream}$ are the circular cross-sectional area and perpendicular velocity respectively of the cylindrical parcel of air upstream of the disc,

whilst a_{AD} and u_{AD} are the respective values at the disc and $a_{Downstream}$ and $u_{Downstream}$ are the respective parameters downstream of the AD. The combined effect of induced radial motion and decrease in streamwise velocity relative to neighbouring air parcels, is the generation of turbulence at the wake edge. Assuming the effects of the turbine blades are spread evenly across the swept out area, the energy extracted by a wind turbine in a unit of time can be simplified as the force acting to retard the flow multiplied by the incident velocity. Since the incompressible fluid parcel must always maintain some velocity, the AD will never extract all the available power in the wind passing through a , described below:

$$power = \frac{1}{2} \rho a u^3 \quad 4.12$$

If u_a is defined as an axial flow induction factor, the power extracted by a wind turbine, assuming AD theory, is:

$$power = 2 \rho a u^3 u_a (1 - u_a)^2 \quad 4.13$$

Naturally, the accuracy of representing a wind turbine in simulations as an AD is subject to the suitability of each assumption required by the theory. A problematic assumption required by AD theory relates to levels of wind shear. Originally conceived for rotors with small diameters in a uniform flow; the incident velocity at the centre of the disc was representative of the whole flow. However, modern wind turbines span much larger areas and are placed in flow regimes with significant vertical shear, as well as having potential for significant horizontal or directional shear across the largest machines. It is reasonable to assume that for a large AD located in a non-uniform flow, equation 4.13 will not perfectly simulate the productivity of each turbine, especially since the reference value of u used in equation 4.13 is taken at the disc's centre and is thus likely to be the mean value. Equation 4.12 shows there is significantly more power available in regions of higher flow, thus the mean value of potential power is located above the location of mean wind speed. This may affect how efficiently an AD is able to represent an operating turbine when considering atmospheric stability as wind shear increases in a non-linear manner with $1/L$ (see section 3.4). Through experimental comparison between

detailed wind tunnel investigations and CFD models utilising LES techniques, it has been shown [118] that the AD wind turbine approximation produces reasonable results in the far wake. However, in the near wake region, the central wake velocity is higher and blade tip turbulence lower, than wind tunnel measurements report. To obtain greater accuracy in the near wake region, [118] recommends using the AL method, although this can reasonably be approximated (to reduce computational requirements) by an AD that incorporates a source of rotational momentum.

4.3.2 Introduction to Windmodeller

There is now a wide selection of computational models used to conduct wind resource assessment and wake effects in the literature. As offshore wind farms get larger and more susceptible to significant wake losses, the costs involved with CFD become more acceptable when balanced against the potential savings from wake mitigation, both in power generation output as well as fatigue management relating to turbulence prediction. Whilst numerous CFD models have been developed, most are still research grade tools used by universities or independent consultancy organisations. If such models are going to become widespread throughout the wind industry, they need to be convenient to learn and quick to use. Therefore, a commercially available set of tools, Windmodeller, which drive the Ansys CFD software [131] has been chosen as an acceptable base to develop.

Rather than the basic cuboidal domain used by most other CFD software, Windmodeller generates a standard cylindrical domain divided into a 5-block hexahedral mesh topology with a horizontally homogeneous square centre mesh block from which a ring of four trapezoid mesh blocks extend with curved outer edges to form a circle. An optional extra four mesh blocks may then be included beyond this inner ring as shown in Figure 4.1 for assistance with smoothing boundary conditions over complex terrain features. The circular shape allows various flow directions to be modelled using the same mesh without need to rotate the locations of terrain, obstacles or proposed turbine layout. For simulations of offshore farms where the terrain is flat with constant surface roughness and no vegetation, cost savings are made by excluding the mesh extension. Further savings are made via mesh horizontal expansion with distance from the centre block and a vertical

mesh expansion away from the surface. Wind turbines are simulated via the AD method which unless specified, automatically orientate perpendicular to the flow and utilises adaptive meshing [131] (see Appendix B for examples) to ensure both disc and wakes are well resolved.

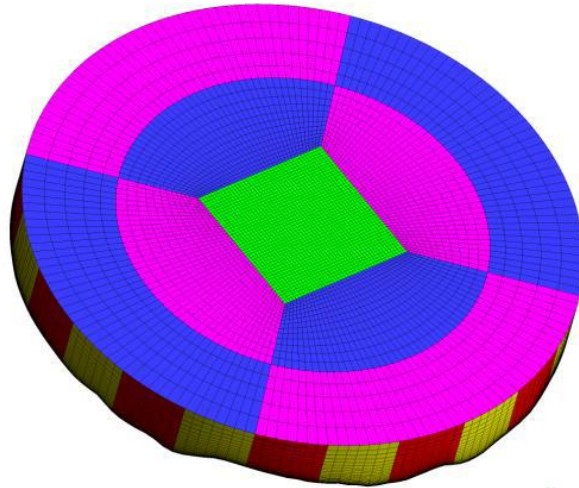


Figure 4.1 Mesh geometry showing both inner and outer mesh blocks

Windmodeller uses the Ansys CFX solver to close the Navier-Stokes equations assuming air is an incompressible fluid and a process known as Reynolds Averaging which splits each of the flow variables into a temporal mean (bar) and instantaneous fluctuation (prime) as indicated below:

$$\gamma = \bar{\gamma} + \gamma' \quad 4.14$$

This reduces the governing equations 4.4 – 4.10 into the RANS equations below:

$$\text{Continuity} \quad \text{div } \bar{\mathbf{u}} = 0 \quad 4.15$$

$$\text{x-momentum} \quad \frac{\partial \bar{u}}{\partial t} + \text{div}(\bar{u}\bar{\mathbf{u}}) = -\frac{1}{\rho} \frac{\partial \bar{P}}{\partial x} + \nu \text{div}(\text{grad } \bar{u}) - \text{div}(\overline{u'\mathbf{u}'}) \quad 4.16$$

$$\text{y-momentum} \quad \frac{\partial \bar{v}}{\partial t} + \text{div}(\bar{v}\bar{\mathbf{u}}) = -\frac{1}{\rho} \frac{\partial \bar{P}}{\partial y} + \nu \text{div}(\text{grad } \bar{v}) - \text{div}(\overline{v'\mathbf{u}'}) \quad 4.17$$

$$\text{z-momentum} \quad \frac{\partial \bar{w}}{\partial t} + \text{div}(\bar{w}\bar{\mathbf{u}}) = -\frac{1}{\rho} \frac{\partial \bar{P}}{\partial z} + \nu \text{div}(\text{grad } \bar{w}) - \text{div}(\overline{w'\mathbf{u}'}) \quad 4.18$$

By time-averaging the Navier-Stokes equations, additional stress terms appear in the three momentum equations (4.16 to 4.18) known as Reynolds stresses and must be

modelled with additional equation sets known as turbulence models. For Windmodeller, the default option is the Shear Stress Transport (SST) model [143] which benefits from the best of the standard k - ω model near flow boundaries and areas of adverse pressure gradients, switching to the k - ε model in the free-stream where the ω -equation becomes highly sensitive [144]. Whilst twenty years old and primarily intended for aeronautic design [145], the SST model is now finding new life with flow modelling through wind farms, particularly those in or near forestry [146]. Alternatively, Windmodeller can be run with just the k - ε turbulence model as widely used by other CFD models. Although it may suffer in the very near wake as mentioned previously, offshore turbines are generally widely spaced and thus simulations of whole farms are primarily interested in the far wake, where the k - ε performs well. The k - ε model's lower accuracy in the near wake region may result in less accurate simulations of turbine wake generation in non-neutral stability conditions as properties of the far wake are dependent on their generation and propagation within the near wake region. Its two equations, used to solve the additional stresses in the RANS equations are shown below:

$$k = \frac{u_*^2}{C_\mu^{1/2}} \quad 4.19$$

$$\varepsilon = \frac{u_*^3}{Kz} \quad 4.20$$

Where k is the turbulent kinetic energy, C_μ is a constant of the turbulence model (typically 0.09 [142]) and ε is the rate of dissipation of k per unit mass, also known as the eddy dissipation rate. Both assume an isotropic turbulent viscosity, i.e. the ratio between the Reynolds stress terms and the rate of deformation is the same in all three Cartesian directions. This assumption is acceptable for many simulated flow scenarios, but may fail under more stable atmospheric conditions where vertical movement is suppressed.

As Windmodeller simulates high Reynolds number scenarios, where flows are turbulent and dominated by inertia rather than viscous forces, it is unnecessary to fully integrate the model equations against the sea surface. Instead, simulation cost

savings are made by applying universal near-wall approximated conditions, giving the flow a logarithmic profile representative of a neutral ABL with a constant shear stress as appropriate for MOST and are described by equation 2.5. Simulations are implemented in standard Ansys CFX Expression Language with pre-processing data passed to the model via ASCII files (.csv format) and the solution phase is fully parallelised to run on multi-core and clustered systems for more economical modelling.

4.4 Benchmarking Windmodeller

As with any new simulation, results must be validated against actual real life measurements and before progress in applying atmospheric stability can be accurately confirmed, a set of standard results from current or previous methods must be compared. Since CFD is not yet 'industry standard' and production data suitable for validation are highly commercially sensitive, there are few peer-reviewed articles for cross reference, and what little exists in conference papers [131] [147] [148] supply graphs of insufficient resolution to be accurate sources. Therefore, the remainder of this chapter shall be given over to testing and benchmarking four different Windmodeller options. The domain and mesh will not be changed between simulations, ensuring an effective blind test. Results will be compared against production data from the Danish farms Horns Rev and Nysted and against the British farms Robin Rigg and Scroby Sands whose locations are shown below.

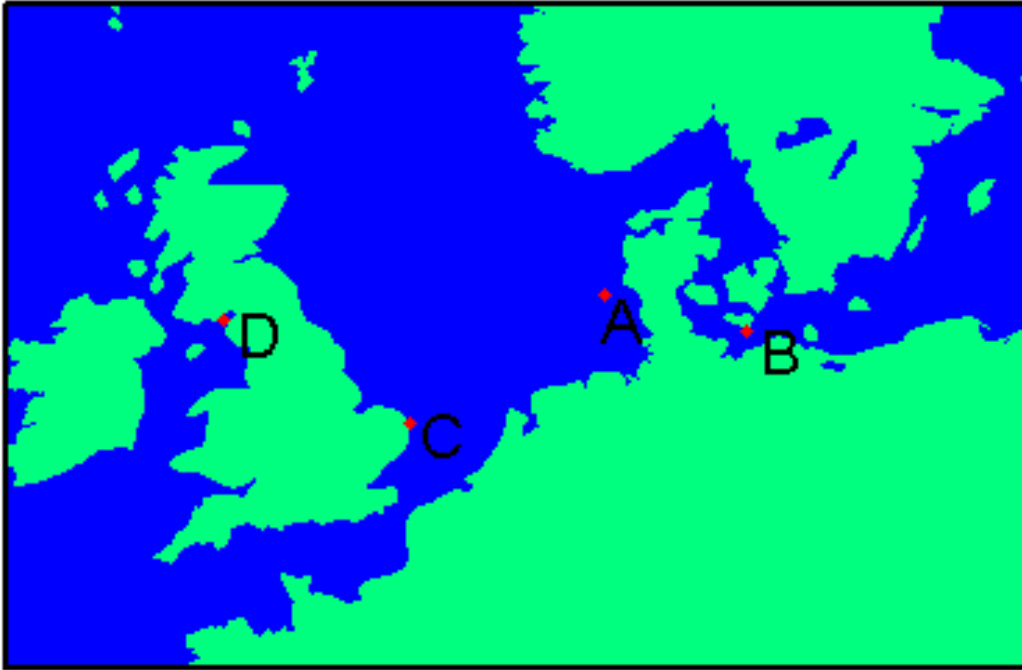


Figure 4.2 Locations offshore wind farms which supplied production data for this work. A=Horns Rev, B=Nysted, C=Scroby Sands, D=Robin Rigg.

Every farm location has a different environment. Despite z_0 effectively remaining constant between offshore locations, conditions on the sea bed, local marine activities, distance from shore as well as conditions of the coastal area where the export cables make landfall can all play a part in dictating farm layout. This can be seen clearest in Figure 4.3 with the Scroby Sands layout, where gaps and extra turbines in an otherwise regular pattern of three columns of turbines betray locations of sea bed unsuitable for turbine foundations. The Robin Rigg layout by comparison was constrained by shipping lanes and water depth. The Danish farms are regular in a parallelogram layout but with different orientation and separations. On account of each farm having differing layouts, conducting typical 'down the line' assessments are not always possible. This can be viewed as a problem for simulation validation as cross-farm comparison is harder, but it can also be viewed positively since Figure 4.3 shows offshore farms are not always in regular arrays and averaging power production across numerous turbines may hide unusual or unexpected events. Within these four farms there are three types of turbine design with varying rotor diameters and thrust curves. This further complicates analysis which can no longer be based on turbine spacing and meteorological conditions alone. As ever, there is always a need for more farms to contribute data towards model validation.

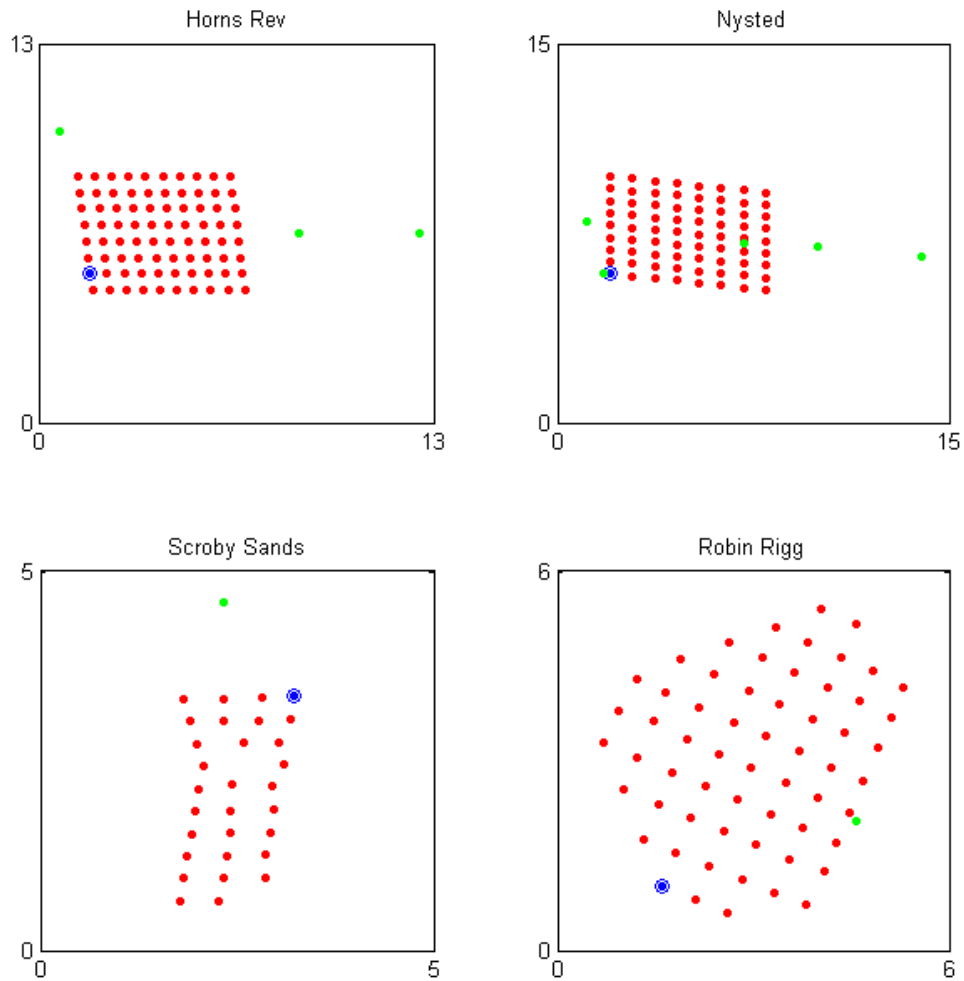


Figure 4.3 Layout of turbines (red dots) and meteorological masts/LiDAR (green dots) at each of the four offshore wind farms which supplied production data for this work. The 'key turbine' used as a reference for free-stream wind direction and speed is highlighted by a blue circle. All dots are the same size and do not represent the scale of object they symbolise. Objects are located at the centre of a dot and distances between objects are indicated by the scale (in km) on the diagram edges. In all four plots, North is to the top of the image.

Each of the four farms shown above has at least one location where meteorological measurements are taken. Information about what is measured at each location is shown below in Table 4.1. Note that not all of the met masts were fully maintained after farm construction was complete and therefore there are often periods of missing or erroneous data.

Table 4.1. Comparison of met masts associated with wind farms and their installed instrumentation. Additional instruments (such as rain gauges) are present at some masts, although these have been left out of this table as their measurements were not used as part of this work.

	Horns Rev			Scroby Sands	Robin Rigg LiDAR Platform
	M2	M6	M7		
Nationality	Danish			British	British
Water Body	North Sea			North Sea	Irish Sea
Mast Height (m)	62	70	70	51	10 (platform)
Heights (m) of Cup Anemometers	15, 30 45, 72	20, 30, 40, 50, 60, 70	20, 30, 40, 50, 60, 70	33, 51	10, 14, 58, 102, 114 (LiDAR)
Heights (m) of Wind Vanes	28, 43, 60	28, 68	28, 68	33, 51	10, 14, 58, 102, 114 (LiDAR)
Heights (m) of Thermometers	13, 55	16, 64	16, 64	19, 47	10 (platform)
Heights (m) of Hygrometers	13	N/A	N/A	N/A	10 (platform)
Heights (m) of Barometers	55	N/A	N/A	14	10 (platform)
Depth (m) of Sea Thermometer	4	4	4	N/A	N/A

	Nysted				
	Mast1	Mast2	Mast3	Mast4	Mast5
Nationality	Danish				
Water Body	Baltic Sea				
Mast Height (m)	68	68	68	68	25
Heights (m) of Cup Anemometers	10, 25, 40, 55, 65, 68	10, 25, 40, 55, 65, 68	10, 25, 40, 55, 65, 68	10, 25, 40, 55, 68	10, 25
Heights (m) of Wind Vanes	68	68	68	68	N/A
Heights (m) of Thermometers	10, 65	10, 65	10, 65	10	10
Heights (m) of Hygrometers	10	N/A	N/A	N/A	N/A
Heights (m) of Barometers	10	10	10	N/A	10
Depth (m) of Sea Thermometer	N/A	2	2	N/A	N/A

In addition to each wind farm being unique in its turbine layout, the actual turbines installed are different in each farm as well. This is mainly due to the variations in farm age, although local planning regulations also play a part. This can be seen in Table 4.2 and Figure 4.4 below by comparing the Horns Rev and Scroby Sands farms where both use the same turbine model although the British farm has a lower hub height to reduce visibility from shore. The Robin Rigg farm by comparison, is made up from a more recent and thus larger model designed by the same company.

Table 4.2. Comparison of wind turbines installed at each of the four offshore wind farms.

	Horns Rev	Nysted	Scroby Sands	Robin Rigg
Model	Vestas V80	Bonus 2.3	Vestas V80	Vestas V90
Rated Power	2MW	2.3MW	2MW	3MW
Hub Height	70m	68.8m	60m	80m
Diameter	80m	82.4m	80m	90m
Cut-in Wind Speed	4ms ⁻¹	3ms ⁻¹	4ms ⁻¹	3.5ms ⁻¹
Cut-out Wind Speed	25ms ⁻¹	25ms ⁻¹	25ms ⁻¹	25ms ⁻¹
No. of Turbines	80	72	30	60

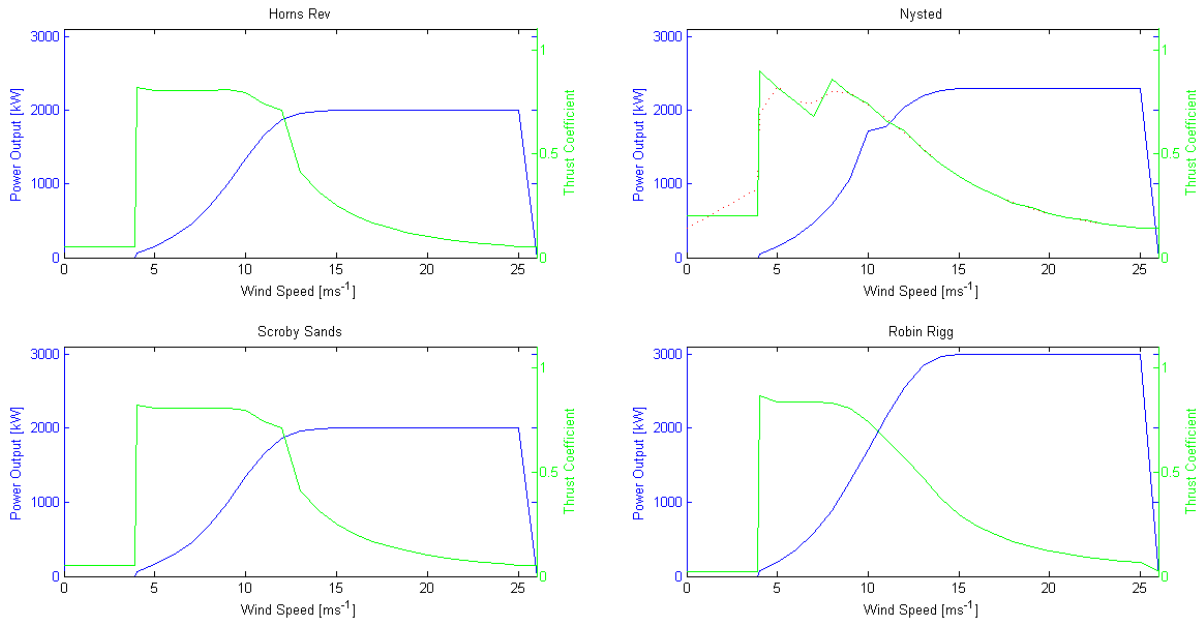


Figure 4.4. Plots of wind turbine power curves (blue) and their corresponding thrust coefficients (green) according to wind speed. Since Windmodeller struggled to converge any simulation using the sharp variations in thrust coefficient for turbines at the Nysted wind farm, so an alternative, smoothed curve (red dots) was used as an acceptable substitute.

As large offshore wind farms by definition have many components that may require maintenance at any particular time, causing an individual or group of turbines to remain stationary, it is a rare event where all turbines are fully operational whilst the atmospheric conditions are also within boundaries set by a case study. Therefore, at the three largest farms, measured values from each turbine were only considered when every machine along that line of turbines was fully operational. Then these filtered values were averaged across turbine lines so that each of the free-stream turbine outputs were averaged together, all the output values from the second turbines in line were averaged together, and so on. Whilst this means stationary turbines in neighbouring lines may not be contributing to losses from horizontal wake expansion, the number of suitable validation events was significantly increased. To assist with clarity for the staggered Robin Rigg layout, Figure 4.5 below shows how

the definition of each turbine position in a line is calculated for this work. As each individual wind turbine has a blocking effect on wind flow and air at low speeds may be considered incompressible, regions between turbines often report flow velocity increases above the free-stream value, known as the venturi effect. The inclusion of some venturi effected turbines within the free-stream category should not bias the work significantly as they are not directly within the wake of another turbine and are consistent for both simulation and validation datasets. They may however be a topic for future investigation, to discover whether such venturi effects alter the rate of wake dissipation within large offshore farms and whether such findings can be used to develop more productive wind farms.

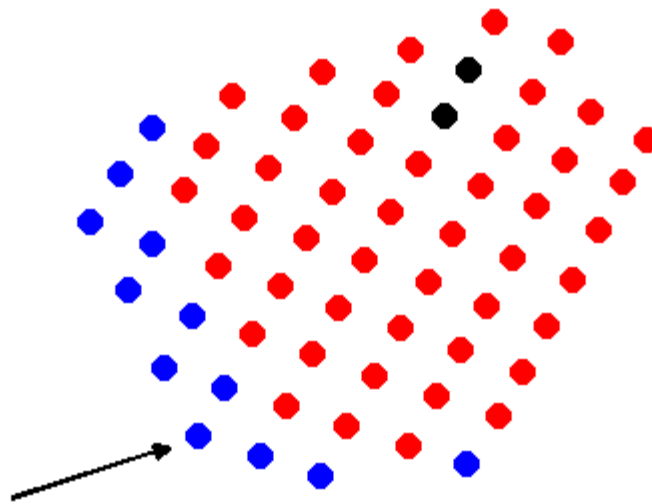


Figure 4.5 Layout of turbines at the Robin Rigg offshore wind farm. Highlighted (black) are the turbines B2 and C3 which had significantly fewer events suitable for validation purposes and so were excluded from the analysis along with the turbines downstream of them. Highlighted (blue) are the free-stream turbines for case studies with wind direction 249° (indicated by arrow) showing that whilst they are not directly in the wake of an upstream machine, at least three turbines are likely to be effected by venturi processes as air flows between two other turbines. There are also five turbines which may be partially affected in this way as they are located diagonally behind at least one other machine.

A major assumption of this work is that any CFD model suitable for mass deployment throughout the wind industry must combine both the flexibility to adjust simulation parameters by experienced users and give acceptable results when used as a 'black box' technique by less experienced users or developers without time to conduct calibration tests. For example the mesh resolution affects both the simulation accuracy and the computational cost. Windmodeller's default setting (before automated mesh refinement takes place) is for a 100m horizontal mesh within the centre block and an average vertical resolution of 80m throughout a 2km deep domain. Although this seems large, each mesh layer is defaulted to 15%

deeper than the one below it. Therefore, at an 80m hub height this would result in mesh roughly 16m deep. After automated re-meshing takes place, the resolution around each turbine is considerably finer enabling it to model the blockage effect and shear generated turbulence generated by the disc. The sensitivity study conducted by [149] systematically varied mesh input parameters in isolation of others; finding solution accuracy and cost were most sensitive to horizontal resolution and the domain radius, although trends were dependent on wind direction relative to the mesh angle. Their recommendations for domain depth were just less than 1km with initial horizontal and average vertical mesh resolutions of 0.4 and 0.35 times the rotor diameter (D) respectively, although having only conducted tests on one farm it is uncertain whether these are site specific, if the scales depend on the size of D or are general RANS rules of thumb. When comparing four CFD models, [150] states that spatial resolution must be roughly 50m or better which roughly correlates to that suggested by [149].

Each of the benchmark simulations were conducted using the same initial mesh geometries although the automated process of re-meshing around turbines and the ADs positioned facing the flow may cause each individual case study to have slightly different mesh qualities. However, they are all initiated as a 1km deep cylinder with a 10km radius. Horizontal resolution was set at a generic 50m while average vertical resolution measured 45m. To account for variability in production data wind direction, a bin size of five degrees was allotted to each case, with the modelled production being the average of three runs, one in the centre and one at each direction extreme. Table 4.3 below lists the seven case studies along with the colour plotted in the figures.

Table 4.3 List of seven validation case studies for benchmarking

Wind Farm	Wind Direction	Case Name	Colour
Horns Rev	270±2.5°	HR270	Red
Nysted	180±2.5°	N180	Blue
Nysted	278±2.5°	N278	Red
Scroby Sands	77±2.5°	SS77	Blue
Scroby Sands	90±2.5°	SS90	Red
Robin Rigg	204±2.5°	RR204	Red
Robin Rigg	249±2.5°	RR249	Blue

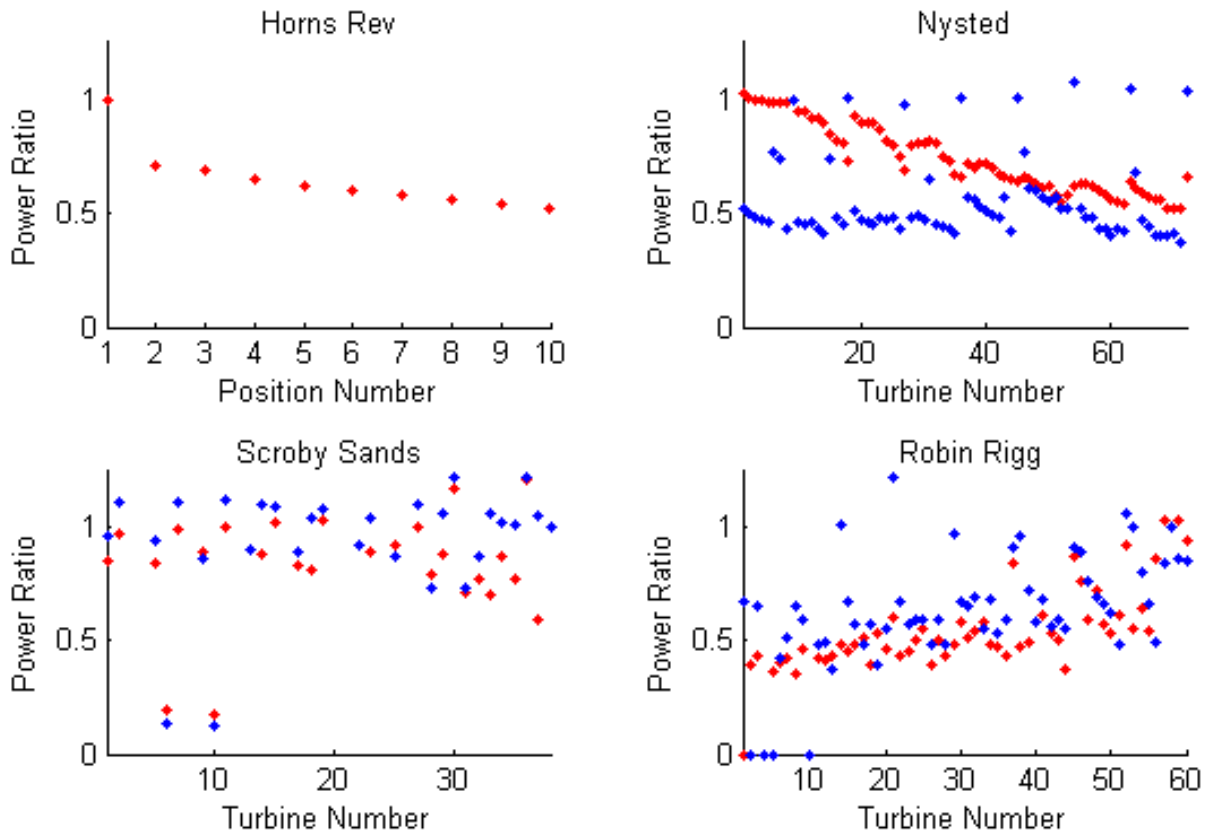


Figure 4.6 Plots showing measured power generated by each turbine normalised by the power generated by a turbine in the free-stream. Top left shows production data averaged across turbines in the six central rows at Horns Rev for case HR270 with the position number referring to each turbine's position in the 'down the line' row with position one being the free-stream turbine, Top right shows production data from Nysted case N180 in blue and N278 in red. Bottom left shown production data from Scroby Sands case SS77 in blue and SS90 in red. Bottom right shows production data from Robin Rigg case RR204 in red and RR249 in blue.

Figure 4.6 above shows the measured production levels for individual turbines to be used as validation data for each case study, except for the top left plot corresponding to HR270, where each point represents the average measured production of the central six rows unaffected by the farm edge. Relating each turbine number in the figure above to its position in the farm according to Figure 4.3 is not immediately clear, especially for the farms Nysted and Robin Rigg, which would also benefit from similar treatment to help display their wake-losses as a function of turbine position within a row. However, displaying each turbine separately reveals some interesting phenomena such as the 'power cascade' in case N278; indicating whilst each column deeper in the farm generates less power than the previous column (sometimes referred to as the deep-array effect), not all turbines in the column generate the same amount of power, despite the column being orientated perpendicular to the wind direction. Indeed, there appears to be a clear north-south gradient where turbines closer to the north farm edge generate more power than

those closer to the south in the same column, and often generate more than those close to the south edge of the previous column as well. Since the wind direction is assumed to be uniformly distributed with the average in this case study being 278° , it must be concluded the northern turbines were not overly benefiting from biased event frequencies within the directional bin any more than the southern turbines. It is possible that since the northern turbines are closer to shore roughly 10km away, they may be benefitting from higher levels of background turbulence and thus faster wake dissipation rates. However, since there is some evidence of a similar cascade effect in the eastern turbines for case N180, coastal proximity may not be the only cause, with Coriolis turning possibly also being significant across the length scales of an offshore wind farm.

From the numbering system used for Robin Rigg in Figure 4.6 it is difficult to observe any patterns as a result of 'down the line' sampling. However there is a general trend for both RR204 and RR249 that turbines located towards the backs of rows, so for these examples located to the north-east with lower turbine numbers, generate less power than those towards the front of rows, as would be expected. Due to missing data or turbine downtime, there were no suitable generation events for either turbine B2 or C3 (numbered 4 and 10 on Figure 4.6). Therefore their points and the turbines directly behind them (turbines A1 numbered 1 for case RR204 and turbines A2 and B3 numbered 2 and 5 for case RR249) are shown as zero and will not be included in the analysis.

Scroby Sands is a relatively small farm with only thirty turbines (confusingly numbered from one to thirty-eight), which are not in strict lines characterised by the other three farms. Therefore, turbines will not be averaged together as for the other farms in Figure 4.7, rather the accuracy of modelling Scroby Sands will be considered at a farm level, whilst ignoring turbines 6, 10 and 21 as outliers resulting from a very small data sample and turbine downtime. However, production from the downstream turbines 5 and 9 are not ignored as they do not appear to be affected and it is therefore assumed the problems with turbines 6 and 10 are related to data collection rather than turbine downtime. Turbine 21 consistently registered SCADA data wind speeds and directions significantly different to other turbines and so was ignored with assumed data collection errors.

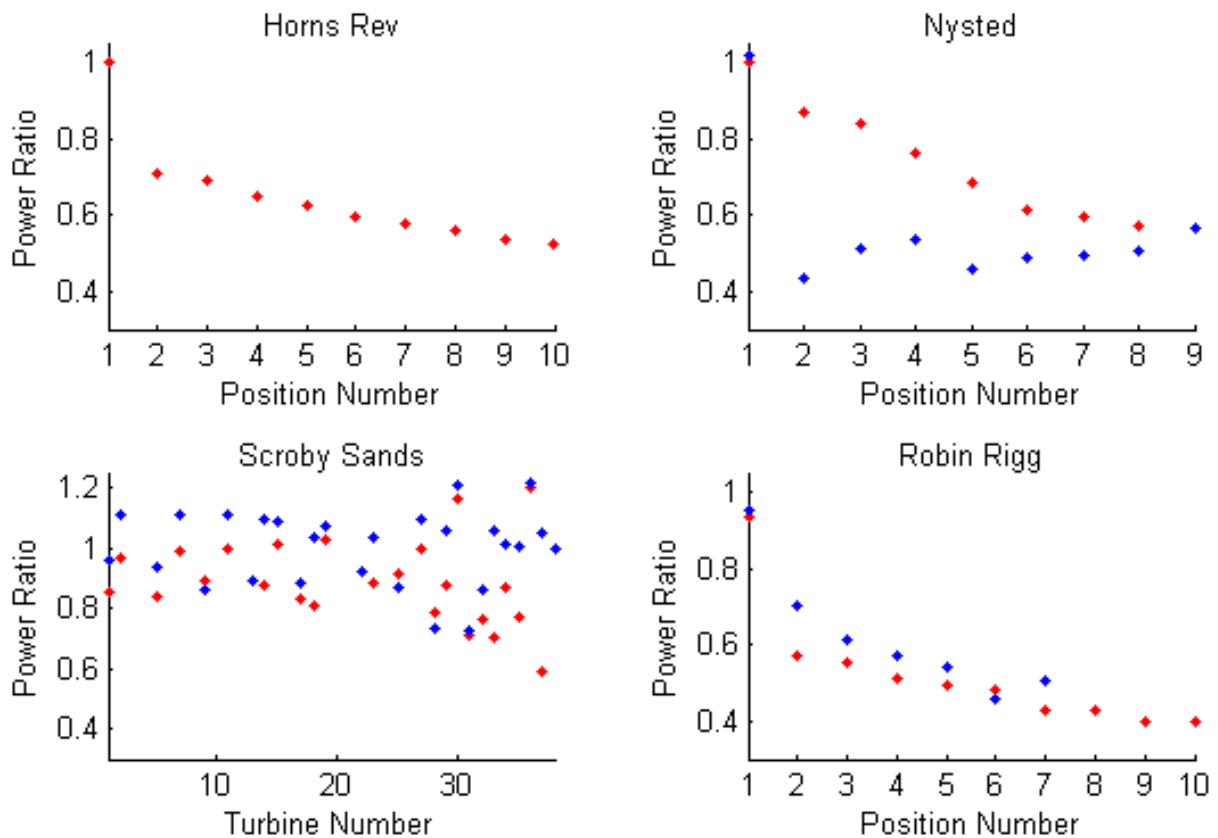


Figure 4.7 Plots of averaged power ratios through the farm. Edge effects are assumed to be negligible, considering the 5° direction bin and it dramatically simplifies calculations for Robin Rigg with its non-parallelogram boundary and two erroneous turbines. Position number referring to each turbine's position in the 'down the line' row with position one being the free-stream turbine. Due to farm layout, free-stream turbines for RR249 may experience some venturi effects as suggested in Figure 4.5.

Having plotted the turbine power output as averaged by its position in line, four out of five large-farm case studies imply some level of deep-array effects. Case N180 is the exception, showing varying levels of generalised wake recovery between turbines; other than after the first and fourth turbine, each machine generates more power than the machine upstream of it. This is possibly a result of relatively close turbine proximity ($5.8D$ separation), combined with a complex relationship between inlet wind speed and the thrust coefficient curve indicated by Figure 4.4. Case N278 shows the same turbines, for the same incident wind speed but different direction, generate more electricity per turbine when arranged with a larger distance between them ($10.5D$). However, the difference in generation between comparable turbine position numbers decreases further into the farm. This relation between turbine separation and productivity is again seen with the Robin Rigg data, although to a lesser degree. Case RR204 (separation $5.3D$) has less initial wake loss than case RR249 (separation $4.3D$), although the difference in turbine separation distance is less relevant further into the farm. Taken together, this suggests future farms may

benefit from layouts with turbines separated by variable amounts depending on distance between turbine and the prevailing free-stream farm edge.

4.4.1 SST RANS

As described in section 4.3, SST is the default turbulence closure scheme for Windmodeller. Figure 4.8 shows four plots comparing power generated at each wind farm against model output. Production data has not been filtered by stability category to help test the common assumption that simulations representing neutral stability are representative of average conditions. Incident hub height inflow is 8ms^{-1} at the key turbine (as indicated in Figure 4.3) and modelled generated power has been normalised against measured power generated by said key turbine.

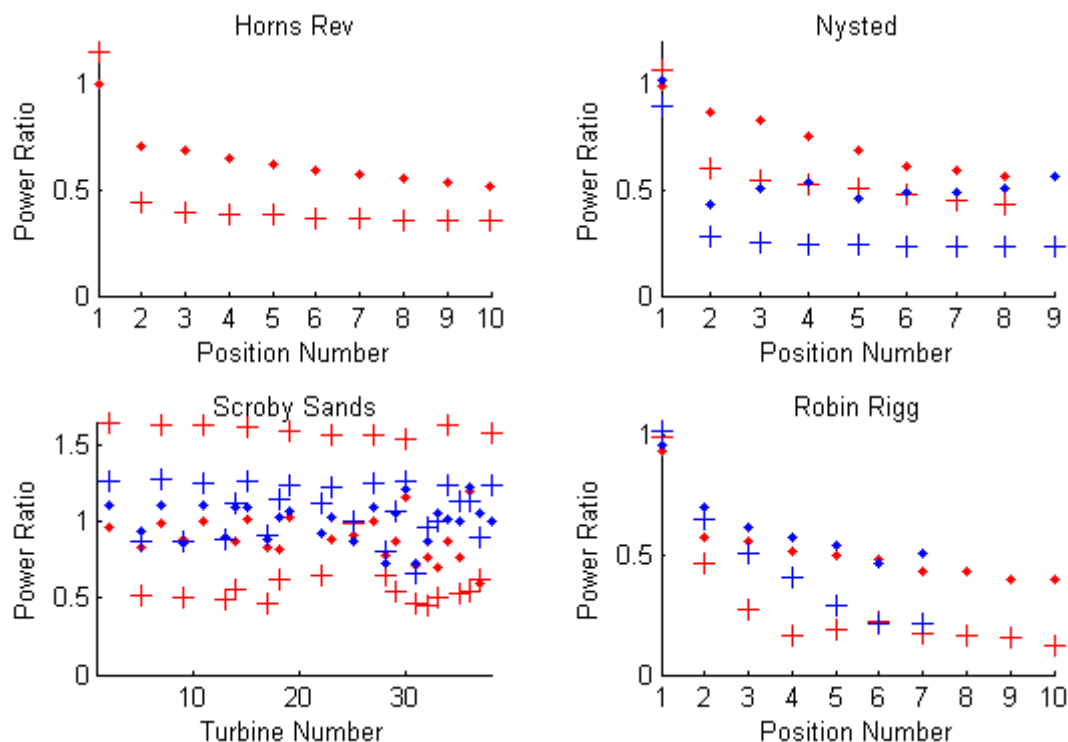


Figure 4.8 Results from SST simulations of the four farms marked as “+” symbols while dots denote the measured values for each farm. Top left shows Horns Rev for case HR270, top right shows Nysted case N180 in blue and N278 in red, bottom left shown Scroby Sands case SS77 in blue and SS90 in red and bottom right shows Robin Rigg case RR204 in red and RR249 in blue.

With exception of N180, each plot in Figure 4.8 shows a slight over prediction of power generation for any turbine in the free-stream, while they all over estimate wake losses in downstream turbines. For both Horns Rev and Nysted, Windmodeller predicts a large initial drop in production between the first and second turbine with little additional loss through the farm. However, for Robin Rigg, Windmodeller predicts lower initial losses with a sharp decline in generation with depth into the

farm before levelling out to a near constant wake loss. Whilst the predicted wake loss in the top two graphs follow similar patterns, the difference in simulation results for the Robin Rigg farm may partially be a factor of turbine size; 50% more rated power than either of the Danish farms, leads to different levels of thrust and incident wake effects associated with each AD. Although a wind direction of 77° at Scroby Sands results in some wake losses (quite accurately modelled), the initial free-stream generation is systematically over predicted. This over prediction is worse for case SS90, with modelled free-stream generation roughly 50% larger than measured. The modelled wake affected generation by contrast is nearly 50% than measured values, so whilst the predicted overall farm generation may be close to reality, modelling of wakes and individual turbine behaviour is far from it.

4.4.2 k - ϵ RANS

As an alternative to the default SST model, Windmodeller can run simulations using the k - ϵ model as utilised by many other CFD models such as [151]. Although it has been shown to be lacking in the near wake [104], where the AD theory also struggles, the minimum separation within the four farms is greater than three diameters, the key distance indicated by [124] and [133]. Figure 4.9 below shows the results of benchmarking simulations identical to those used to create Figure 4.8 except with the use of the k - ϵ turbulence model.

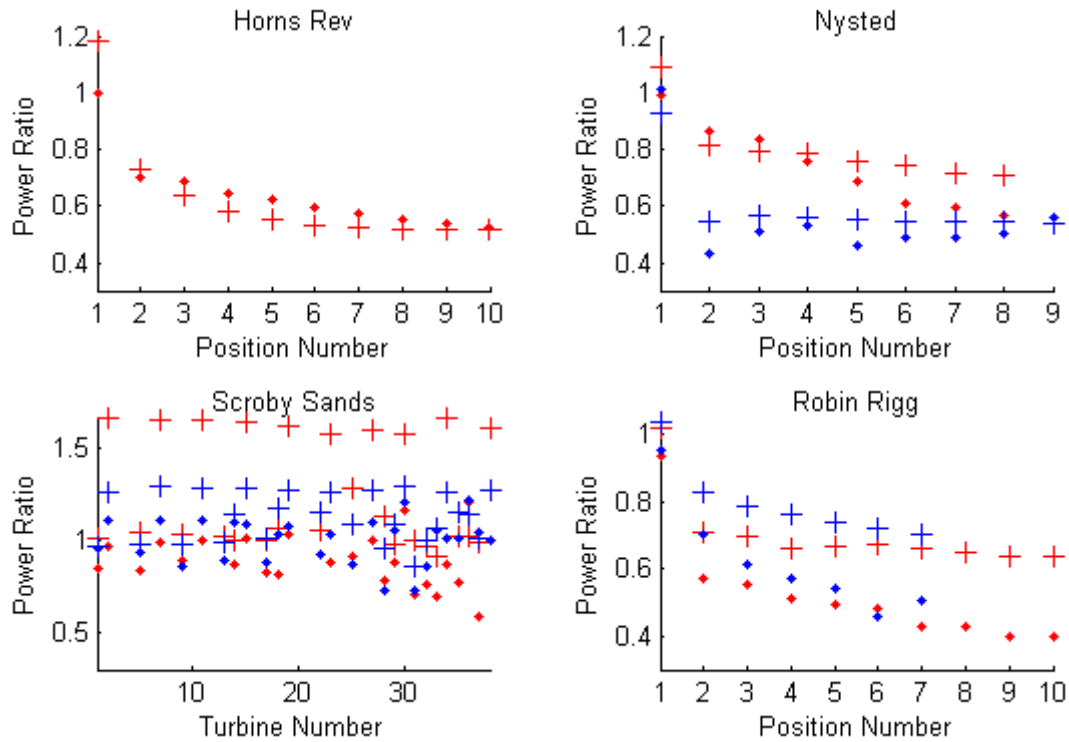


Figure 4.9 Results from initial $k-\varepsilon$ simulations of the four farms marked as “+” symbols while dots denote the measured values for each farm. Top left shows Horns Rev for case HR270, top right shows Nysted case N180 in blue and N278 in red, bottom left shown Scroby Sands case SS77 in blue and SS90 in red and bottom right shows Robin Rigg case RR204 in red and RR249 in blue.

As for the SST results, for each simulation except N180, production at the free-stream turbine has been over predicted, most significantly for SS90. With the Horns Rev and Nysted simulations, the $k-\varepsilon$ turbulence model results fit the validation data better than the SST option, although it significantly under predicts the wake losses at Robin Rigg. Whilst the $k-\varepsilon$ model maintains reasonable accuracy for the first few wake affected turbines in the top two farms, it appears not to match the deep-array effects seen clearest in case N278. Prediction of further additional wake losses with depth into the farm does not occur, causing a plateau appearance whilst measured generation continues to drop for all three large farms. The variation in measured generation for case N180 implies a potential recovery from maximum wake losses whilst the simulation predicts a general plateau. Overall, modelled output using the $k-\varepsilon$ turbulence model appears greater than that of the SST model as the power ratio values are larger, yet the over prediction at free-stream and deep-array turbines suggest the $k-\varepsilon$ model is less accurate near flow boundaries and regions of strong adverse pressure gradients such as ADs. As indicated by [145] these boundary problems were the reason for the original development of the SST model, although it is not clear if the SST model is better at modelling the deep array effect than the $k-\varepsilon$.

4.4.3 Modified $k-\varepsilon$ RANS

The third Windmodeller turbulence model to benchmark is a modified version of the $k-\varepsilon$ where the constant C_μ from equation 4.19 is altered from 0.09 to 0.03. Originally performed by [147], this resulted in modelled power ratios comparable to those measured at the Horns Rev and North Hoyle farms, though the near-wake recovery process was suspected of being too fast, leading to the over prediction of generated power at farms with closely spaced turbines. Figure 4.10 below shows the results of benchmarking simulations identical to those used to create Figure 4.8 and Figure 4.9 except with the use of the Modified $k-\varepsilon$ turbulence model.

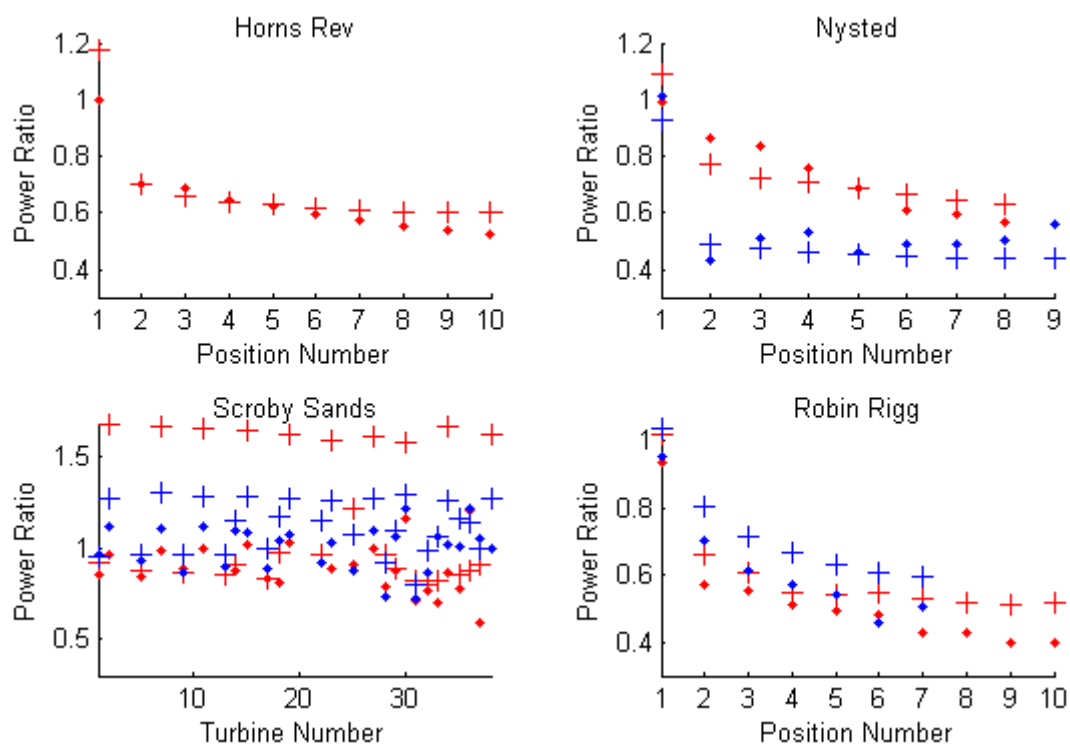


Figure 4.10 Results from the Modified $k-\varepsilon$ simulations of the four farms marked as “+” symbols while dots denote the measured values for each farm. Top left shows Horns Rev for case HR270, top right shows Nysted case N180 in blue and N278 in red, bottom left shown Scroby Sands case SS77 in blue and SS90 in red and bottom right shows Robin Rigg case RR204 in red and RR249 in blue.

By comparing Figure 4.9 with Figure 4.10 it can be seen that modifying the C_μ constant results in dramatically better wake loss predictions for Robin Rigg with case simulation RR249 almost perfect except for a systematic power overestimation at every turbine. Measured production at position six is suspected of being abnormally low however, as it does not fit the smooth curve formed by either the other validation data points or the curve of simulation results. For case RR204, the Modified $k-\varepsilon$ turbulence model provides fair prediction throughout the early farm although fails to replicate the deep-array affect indiscernible for RR249 on account of farm design

and performs better than both SST and the normal $k-\varepsilon$ model at this farm. There is little significant improvement from modifying C_μ for either the Horns Rev or Nysted farms. Neither of the $k-\varepsilon$ models capture the deep-array affect for HR270 and just predict an effective wake-loss limit, although Modified $k-\varepsilon$ returns higher total yield predictions than the basic $k-\varepsilon$ model, and both predict greater yields than SST. Results from both simulations SS77 and SS90 give a better fit to the data for wake affected turbines with the Modified $k-\varepsilon$ model while N278 and N180 are inconclusive.

4.4.4 URANS

The fourth model to benchmark is significantly different from the others in that the previous three were all RANS model runs computed in steady-state with a disregard for thermal variations based on the neutral atmospheric assumption. The URANS model (Unsteady Reynolds-Averaged Navier-Stokes) by comparison is not run in steady-state and is therefore more computationally expensive than RANS, although unlike LES, URANS still uses the cost saving averaging of turbulence values across all scales. Whilst there is additional cost to be paid in terms of computational time required for each simulation compared to basic RANS models, URANS benefits from the inclusion of a prognostic equation for potential temperature based on [152]. Although the ABL is often assumed to exhibit neutral stability, as indicated in Figure 2.2, above Z_{ABL} there is a steady increase in θ_v with height, resulting in a stably stratified layer. With the inclusion of the prognostic equation for potential temperature in URANS, it is possible to incorporate a layer at the top of the domain which varies in θ with height. Thus, if a simulated air parcel moves into this region, its expansion and resultant cooling due to the lower pressure will force it to sink again, effectively ‘capping’ the simulation and helping to prevent uncontrolled model divergence. The strength and height at which this simulated free atmosphere region begins may be significant as it likely effects the expansion (and thus diffusion) of wakes behind each AD. Since Z_{ABL} is known to vary significantly under different stability conditions, the height and strength of the marine free atmosphere’s thermal inversion should be the subject of future field investigation and is outside the scope of this work. For the purpose of URANS simulations which incorporate a free atmosphere thermal gradient, we shall assume it matches the dry adiabatic lapse rate and begins at a

height determined by a variation of equation 2.4 approximated using work by [153], whilst the simulated ABL itself remains neutrally stratified.

A further benefit of a transient simulation is it allows for the inclusion of the Coriolis effect which not only controls the Ekman spiral [149] but may also produce significant farm edge effects over the large areas proposed for development in the North Sea [154]. The inclusion of the Coriolis effect does change the model set-up process however. For a RANS model, the required wind speed and direction are specified for a specific reference height and equation 2.5 ensures a suitable profile is generated across the domain inlet. Simulations which include the Coriolis effect generate the inlet wind profile using a user-defined free-stream (geostrophic) flow speed above the ABL (and subsequently above the Ekman spiral), from which Windmodeller then computes the wind speeds down to z_0 using the geostrophic drag law, equation 2.1. The flow direction undergoes a similar process to ensure the Ekman spiral is accurately modelled based on the user-defined geostrophic flow direction. This can significantly increase cost as a process of trial and error must be carried out to obtain the correct meteorological conditions at hub height.

In order to observe the effects of the URANS components, results from four URANS simulations of case N278, described in Table 4.4, are shown below.

Table 4.4 List of four URANS configuration options

Option Name	Coriolis Parameter	Free Atmosphere Thermal Gradient	Colour
Option 1	Off	Off	Blue
Option 2	Off	On	Green
Option 3	On	Off	Orange
Option 4	On	On	Red

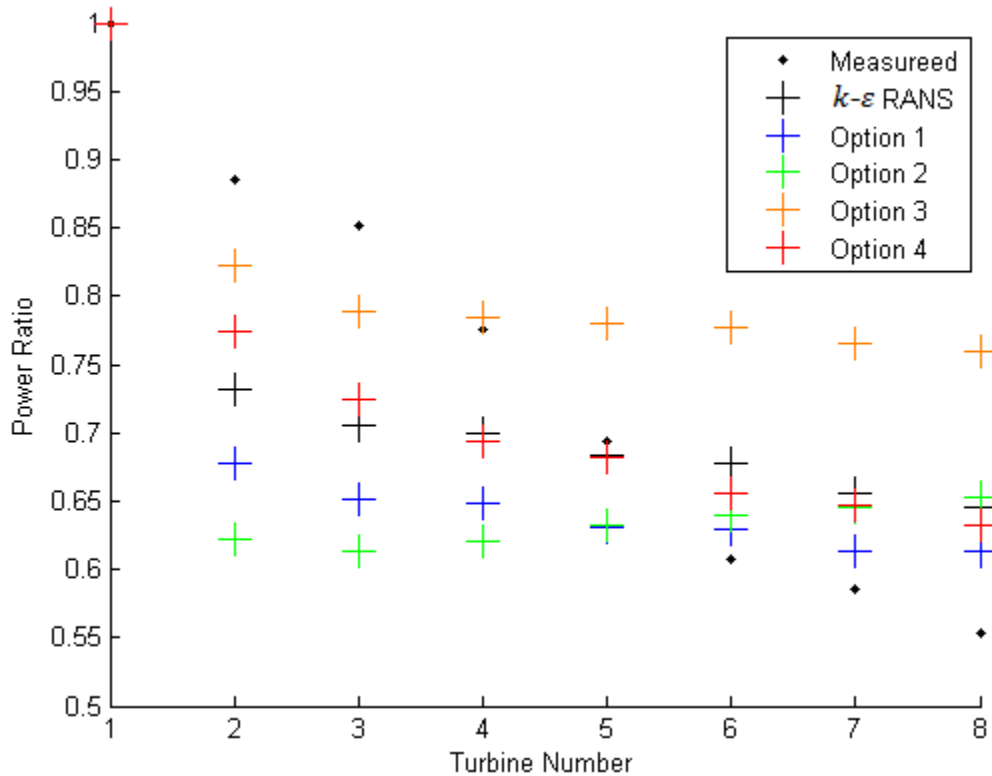


Figure 4.11 Results from the different options for URANS model simulations of case N278 (“+” symbols) using the colours described in Table 4.4. Measured values from the Nysted wind farm are shown as black dots. For comparison, the results from the standard $k-\epsilon$ RANS simulations from section 4.4.2 are also displayed (black “+” symbols).

The results in Figure 4.11 above show significant variation in simulated power ratios at each turbine location within case N278 dependent on which aspects of the full URANS model are included. For example, Option 3 and Option 4, which both include the Coriolis parameter, return significantly higher power ratios at the second turbine position, making their results closer to the measured values. Higher power ratios are recorded throughout the farm for models including the Coriolis parameter compared to models without the parameter, suggesting the wakes are being at least partially directed away from downstream ADs. In addition, the application of a non-neutral thermal gradient representing the free atmosphere in the upper domain appears to affect the wake recovery process despite starting hundreds of metres above the turbines, with results from Option 4 displaying a much greater deep-array effect than an otherwise identical Option 3. It is also noted that whilst the inclusion of a thermal gradient in a Coriolis effected simulation appears to strengthen the deep array effect, its inclusion in a model which excludes the Coriolis parameter appears to weaken it and even aid wake recovery. These results indicate that both the Coriolis parameter and a non-neutral thermal gradient in the free atmosphere should be incorporated in

URANS models. Therefore, any subsequent mention to the URANS turbulence model throughout this work will refer to Option 4. However, caution should be applied during the set-up and interpretation of URANS simulation results. For example, since the Coriolis parameter changes with global location, simulations of wind farms in equatorial regions may suffer from inaccurate wind speed profiles as a function of equation 2.1. Whilst comparisons of results from Options 3 and 4 above in Figure 4.11 imply the inclusion of a simulated stable free atmosphere may influence modelled deep array effects, its height is based on the assumption of neutral stability conditions in the ABL. More fieldwork needs to be conducted to determine its exact height under various conditions and how its fluctuations influence the wake losses in large farms.

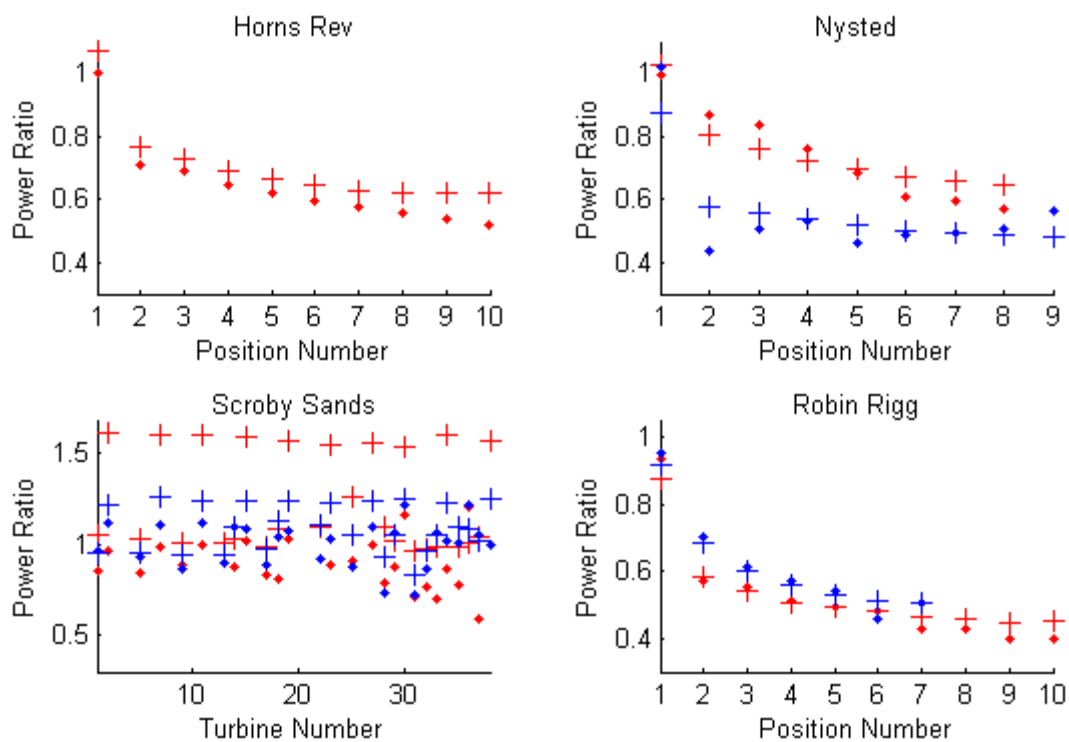


Figure 4.12 Results from the URANS simulations of the four farms marked as “+” symbols while dots denote the measured values for each farm. Top left shows Horns Rev for case HR270, top right shows Nysted case N180 in blue and N278 in red, bottom left shown Scroby Sands case SS77 in blue and SS90 in red and bottom right shows Robin Rigg case RR204 in red and RR249 in blue.

Results from the URANS simulations show clear improvements over other models for the Robin Rigg simulations. However, there is little other improvement with URANS obtaining similar or worse results than the Modified $k-\epsilon$ turbulence model. For the Horns Rev farm, the shape of the graph is similar to that of the Modified $k-\epsilon$, but with the exception of the free-stream turbine, the URANS predictions are constantly about 0.05 higher than reality. The same can be said of N278 while

URANS predicts a slight deep-array effect rather than the gentle recovery seen in N180. Observing the Scroby Sands graph suggests slightly worse power predictions than the Modified $k-\varepsilon$ results for wake-affected turbines although each individual machine is modelled well. Across all seven case studies, URANS predicts lower power generation for turbines in the free-stream than any of the other three models with N180, RR204 and RR249 all under-performing the measured data. Combining the decrease in free-stream production with the increase in wake-affected production for URANS suggests the Coriolis force plays a significant role in farm efficiency. Whilst maintaining a constant hub height wind speed for each key turbine, the Coriolis caused Ekman spiral will alter the vertical wind speed shear over each AD. While the increase in production deep into N278 and RR204 could be attributed to farm edge effects with changing wind directions, this explanation is shown to be false by HR270 where data from turbines on the farm sides were discarded both in measured data and simulations.

4.4.5 Comparison of Models

As can be seen from the figures in the previous sections that there are considerable differences between predicted generated electricity modelled for the four benchmark options. It is also clear that new models need to be verified against a greater number of farms than previously available. For example, while the $k-\varepsilon$ model performed well with the Horns Rev and Nysted farms, it did less well with the Robin Rigg farm. This may be a due to differences in wind farm layout, turbine size or even the technique used to measure meteorological conditions, variables which are hard to investigate using field data from just the two Danish farms and particularly flow directions 270 degrees and 278 degrees respectively. Similarly, there was variation in accuracy for each model within each farm, specifically Scroby Sands where all four models were more accurate at predicting SS77 than SS90. To help assess the results, Figure 4.13 and Figure 4.14 show the Root Mean Squared (RMS) errors and the standard deviation (σ) of prediction accuracy for each of the seven case studies. Case RR249 provided an unusual comparison as turbines from this direction are staggered and so spaced roughly one diameter further apart downstream than case 204, with turbines located in the gap between previous turbines in neighbouring rows (see Figure 4.5). This allows the turbine rows to be considered in numerous ways, yet since both

measured and predicted generation data were averaged using the same method, simulations produced results directly comparable with reality, with the URANS model the most accurate.

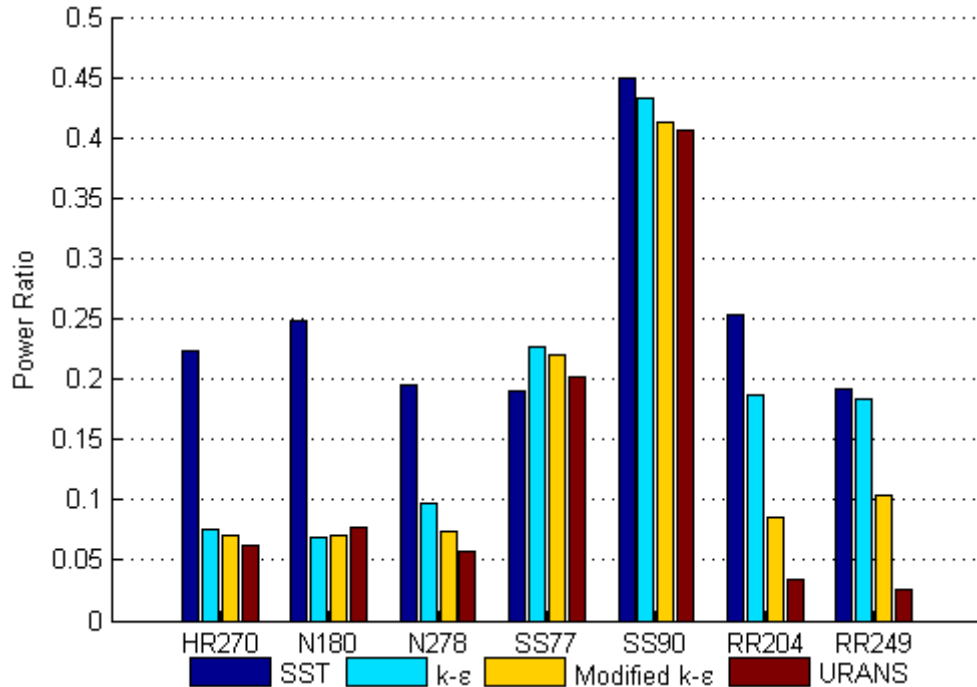


Figure 4.13 Root Mean Squared (RMS) error for each of the seven cases in Figure 4.8 to Figure 4.12

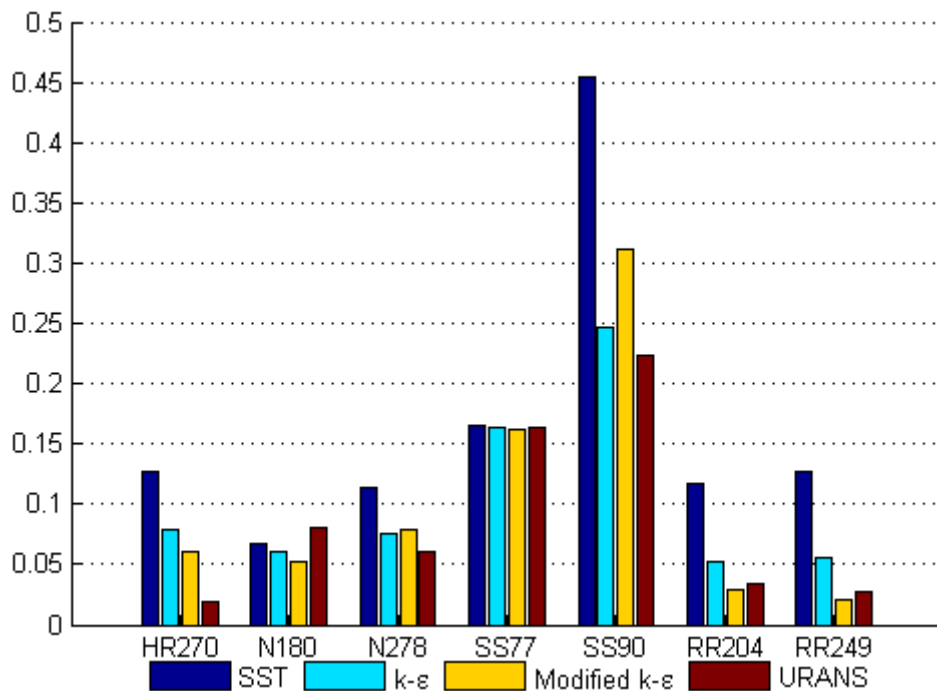


Figure 4.14 Standard Deviation (σ) for each of the seven cases in Figure 4.8 to Figure 4.12

Despite being Windmodeller's default turbulence closure for wake modelling, the two figures above show the SST option as the least accurate overall, as well as having the most variability within individual farms. There is little separating the other three models for greatest RMS accuracy if only the usual industry test cases are considered, (HR270 and N180) however, the URANS runs resulted in greatest accuracy in five of the seven case studies with similar RMS values to the most accurate model for the other two cases. URANS also achieved lowest σ values in three cases, only being surpassed by the Modified $k-\varepsilon$ model which achieved the lowest σ values in four cases (where the URANS values for σ were very similar).

It should be reiterated here that because Scroby Sands only contains 30 turbines in a non-regular layout, results from individual turbines at this farm were not averaged together based on their position in a line. It is therefore reasonable to expect higher RMS error values as shown by Figure 4.13 for SS90 and SS77 than the other case studies. However, attention is drawn to SS77 where the SST model not only performs best out of the four (lowest RMS error with near identical σ values), but also is more accurate here than in any other case study. The reason for this success is not clear, as for the other case at that farm, case SS90, the SST model is again the worst performing and its large σ value showing variability even within itself.

4.4.6 Comparison using Neutral Stability Filtered Data

So far in this chapter atmospheric stability has been ignored. All four models assume neutral stability in the ABL (although the URANS model includes a stably stratified layer at the top of the domain representing the free atmosphere above the ABL), and production data were filtered based on wind speed and direction only. These could be considered fair assumptions, especially as not every development monitors suitable meteorological conditions required to calculate stability via any of the favoured methods in Chapter 2. For example, at the Robin Rigg farm a met mast was erected for preconstruction resource assessment but was since removed and replaced with a Doppler LiDAR. Similarly, the Scroby Sands mast was retired after farm construction and there are very few simultaneous measurements of power generated and meteorological conditions. Horns Rev however, has since construction been further instrumented for scientific research. Therefore production

data from the Danish farm has been filtered by L , calculated using the Bulk Richardson number (equation 2.13) at mast M6 (provided by the UpWind project [51]). On account of diminishing sample sizes, the direction bin has been extended from $\pm 2.5^\circ$ to $\pm 5^\circ$.

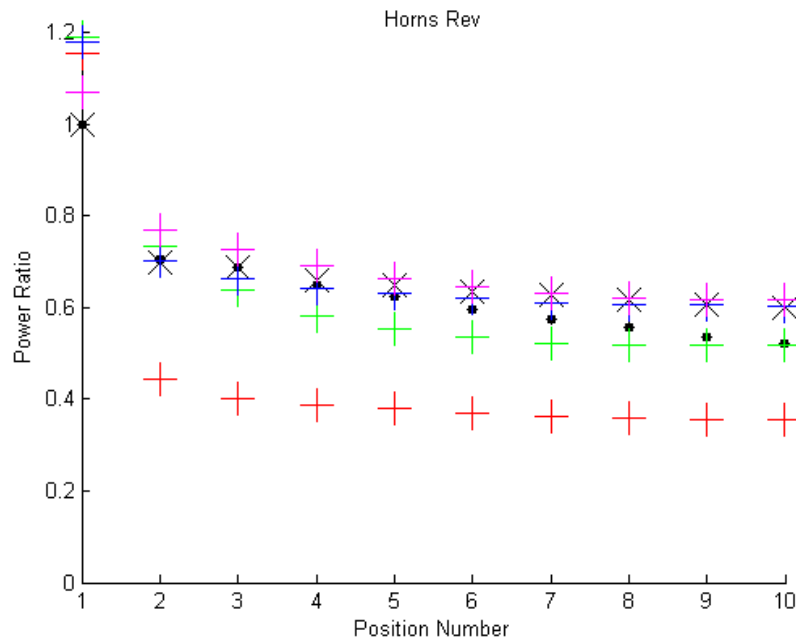


Figure 4.15 Comparison of the four models against Horns Rev production data both unfiltered and filtered for neutral stability. Unfiltered measurements are represented by black dots whilst measurements filtered to ensure neutral stability are shown as black 'X' symbols. Model results are represented by '+' symbols, SST in red, $k-\epsilon$ in green, Modified $k-\epsilon$ in blue and URANS in magenta.

Figure 4.15 above shows a poor fit for either Horns Rev data set using the SST model. The $k-\epsilon$ model does well deep within the farm against the unfiltered data as seen before in Figure 4.9. However, both the Modified $k-\epsilon$ model and URANS predict the filtered production data better than the unfiltered data. On this basis, combined with the benefit of the URANS model already incorporating a potential temperature variable, it is this model which will be considered for development in future chapters to incorporate atmospheric stability rather than being forced to assume neutral conditions.

One cannot fight against the wind.

- **Hungarian Proverb**

Chapter 5. Modelling of Large Offshore Wind Farms under Various Stability Conditions

5.1 Introduction

In the previous chapter, four separate CFD models were compared against measured power generated at four offshore wind farms. Building on the previous conclusion that the URANS model was consistently the most accurate, with its more complete representation of governing equations (such as the inclusion of the Coriolis Effect and an approximation for potential temperature), it lends itself towards the modelling of non-neutral atmospheric conditions. URANS is therefore the basis for simulations in section 5.3 which aim to predict farm productivity whilst replicating atmospheric stability via parameter L in addition to the required wind speed and directions. Whereas in section 5.4, the basic $k-\varepsilon$ RANS model is developed for modelling wind farm productivity under different atmospheric stability conditions with reference to TI and wind shear rather than to L .

5.2 Review

Whilst it is still standard practice for the industry to assume neutral conditions when conducting resource assessment, popular linearised models such as WAsP are capable of incorporating atmospheric stability with variations in the vertical wind speed profile [23]. This is particularly relevant at sites far from shore where there are no trees or relief to degrade linear solutions by generating flow separation and stability is a more significant factor in wake-loss calculations. Despite its popularity, WAsP's limitations for calculating wake losses both on- and off-shore are reflected in the number of CFD models being showcased at each European annual conference [147] [155] [156].

When models such as WAsP were first created in the late '80s, the average wind turbine was a lot smaller, with hub heights typically around 30m. This was well within expected onshore SL depths and so using MOST to define stability conditions was

considered appropriate. Modern offshore turbines on the other hand, with their hub heights approaching 100m and locations far from shore where the MABL is shallower, are unlikely to be fully submerged within the SL. Since one of MOST's assumptions is that its measurements and height transformations occur within the surface layer, its use is not technically valid in many offshore resource assessment simulations. Despite this, it continues to form the basis of our knowledge of the MABL and is often assumed to be applicable for regions in which turbines operate. Therefore, the ability of MOST to replicate stability conditions within CFD simulations is an important assumption which is investigated below, while alternative methods of incorporating stability into CFD similar to those used for linear models are investigated in section 5.4.

5.3 Modelling Using Variable Values of L

Despite studies analysing the offshore environment showing the MOST assumptions result in the theory only being relevant for less than 20% of the time [52] and its dubious applicability at modern turbine heights, it remains the popular method to describe atmospheric stability. Therefore, since the URANS model includes a parameter for potential temperature, allowing L to be calculated at any point in the domain, MOST appears the logical way to model the effects of stability on wake losses in large offshore farms.

In chapter 4 the URANS model required model calibration runs to ensure the correct free-stream wind speed and direction at key locations. Stipulating specific values of L increases the boundary condition complexity by increasing the number of variables being tuned during calibration. Put plainly, including stability in URANS simulations increases the cost of modelling each case study. This is because Windmodeller's URANS model is transient in nature with wind and thermal profiles developing with time through the modelled domain. Each parameter interacts with and is dependent on the others. For example, incorporating a surface heat flux changes the local air density and fluid viscosity and thus the simulated wind speeds, leading to different turbulent mixing rates, which in turn effect how quickly the surface heat flux influences different levels in the domain. Thus by requiring specific L and therefore thermal values at specific locations, the initial model inlet conditions have to be

obtained via a process of trial and error. Through experience, a user can minimise this process by setting inlet conditions similar to previous simulations, though each domain set-up (mesh and turbine characteristics) and meteorological scenario (stability, wind speed and direction) will require individual calibration. Multiple simulations are run for each case study with identical mesh and turbine layouts but with small perturbations to the inlet conditions until modelled output at the required locations match the measured meteorological data for each case study. This is a costly process and if adopted by developers, the creation of a reference table listing input and output conditions is advisable to reduce costs of future studies.

5.3.1 Validation Data

In order to validate results from models simulating specific values of L , the relevant field data must include measurements of not only wind speed, direction and turbine power generation, but also the thermal atmospheric conditions. Since it is not possible to calculate $\overline{w'T'}$ from standard mast records, absolute temperature measurements at multiple heights are the basic minimum requirements. Measurements of sea surface temperature are also required for use of the bulk method (equations 2.13, 2.14). In addition, measurements of atmospheric pressure and humidity allow for calculations including θ , T_v or θ_v , providing greater detail and are thus desirable. Ideally, these extra measurements are made at the same heights as the absolute temperature measurements (see Chapter 2). Out of the four available wind farms simulated in Chapter 4, only the two Danish farms provide concurrent atmospheric data suitable for MOST calculations alongside power generation. The Scroby Sands farm stopped collecting meteorological data after the farm was commissioned whilst the Robin Rigg farm measures wind speed and direction via a LiDAR system, thus lacking the required thermal data. A further validation constraint is the limited data from the Horns Rev farm, as this dataset was made available as part of the IEA Wind Task 31 “Wakebench” program and has been externally processed using the Bulk stability calculation method. It should therefore be used with caution for validation of alternative calculation methods. By contrast, the Nysted farm is well instrumented with five met masts and therefore provides the majority of subsequent validation data. This is unfortunate as Chapter 2 suggested too much reliance on data from just Horns Rev and Nysted may result in

models becoming unwittingly tailored to their specifications and thus less able to cope with non-regular arrays such as the Scroby Sands farm design.

As the data from Horns Rev were externally processed, they define the values of L to be modelled. Events were placed in three groups by combining ranges used in the asymmetric seven category system in Table 2.2 as shown below in Table 5.1. Similar to how variations in measured wind directions were accounted for in Chapter 4, in this chapter, each non-neutral category is simulated for three values of L and results averaged before being validated against measured field data. Since the Neutral category is open-ended and discontinuous, four representative values of L are modelled and their results combined.

Table 5.1 Range and representative Obukhov lengths of stability groups for simulation

Stability Category	Range of L (m)	Modelled Values of L (m)
Stable	$10 < L < 200$	10, 105, 200
Neutral	$ L > 200$	$\pm 200, \pm 1000$
Unstable	$-200 < L < -50$	-200, -125, -50

A summary of case studies simulated using L to describe atmospheric stability is shown below in Table 5.2. Whereas the events used for validation in Chapter 4 were not filtered for stability, the events used for the validation processes in this chapter are. As a consequence, each case study contains fewer corresponding events, and so the directional bin size has been increased from 5° to 10° to help ensure significant sample sizes. However, increasing the bin width also decreases the significance of wake losses as events not strictly ‘down the line’ are included in the samples. Therefore, whilst three simulations were run with their results averaged for each case study in Chapter 4, each simulation in this chapter shall be run for five individual wind directions (the listed simulation direction as well as $\pm 2.5^\circ$ and $\pm 5^\circ$) with the results averaged for comparison against the field data.

Table 5.2 List of nine case studies for comparison

Wind Farm	Wind Direction	Stability Condition	Case Name	Colour
Horns Rev	270±5°	Stable	HR270S	Red
Horns Rev	270±5°	Neutral	HR270N	Green
Horns Rev	270±5°	Unstable	HR270U	Blue
Nysted	278±5°	Stable	N278S	Red
Nysted	278±5°	Neutral	N278N	Green
Nysted	278±5°	Unstable	N278U	Blue
Nysted	180±5°	Stable	N180S	Red
Nysted	180±5°	Neutral	N180N	Green
Nysted	180±5°	Unstable	N180U	Blue

Atmospheric stability at the Horns Rev farm was calculated at met mast M7 located 6km east of the farm using wind speed measured at 20m, absolute temperature at 16m and the sea water temperature as described in [157]. Whilst M7 is directly downstream of the farm, the free-stream mast, M2, has only been in partial operation after completion of farm installation. Data from M7 is assumed to be a more appropriate approximation for the free-stream conditions than those from mast M6 which is only 2km downstream and thus more heavily affected by turbine wakes.

Meteorological data were available from all five met masts at the Nysted farm with varying parameters measured at each mast (see Table 4.1). A simple comparison between the frequencies at which the three stability categories in Table 5.1 occur is conducted below.

The bulk method for calculating L is analysed first in Figure 5.1 using wind speed and air temperature from 10m above sea level combined with sea temperature measured at 2m below the surface from met masts 2 and 3. Sea temperature is assumed to be equivalent to the surface temperature despite [61] indicating it is not. The comparison between masts shows little difference between stability distributions measured using data from masts upstream or downstream of a wind farm (direction 278±5°). Southern sector results from mast 3 show a similar distribution to that of the western sector, whilst those from mast 2 report a complete lack of Neutral events and a much greater frequency of Stable events than for the other three cases. Therefore, the required measurements for calculating L via the bulk method at the Nysted farm should come from met mast 3, enabling simulation case N180N a chance to be validated against production data. This maintains consistency with both

the Horns Rev farm, where meteorological measurements were taken downstream of the farm, and within the Nysted validation datasets as case studies from both flow directions can be compared against data from the same mast.

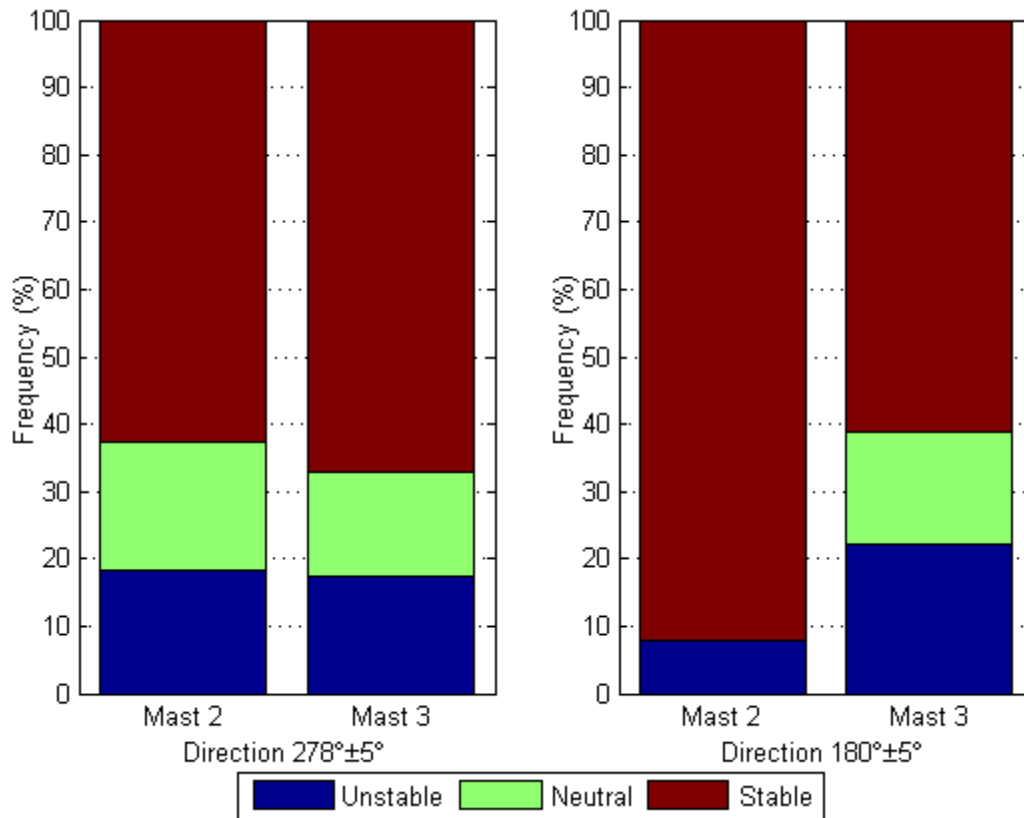


Figure 5.1 Comparison of bulk stability calculated at masts 2 and 3 at the Nysted farm

However, low availability of sea temperature measurements combined with filtering by wind directions and L result in very small atmospheric stability datasets, such that Figure 5.1 shows only 472 events in its most populous column (Mast 2 direction $278\pm 5^\circ$) and 54 in its least (Mast 3 direction $180\pm 5^\circ$). With such small sample sizes, it is perhaps surprising that Figure 5.1 displays consistent stability distributions across three columns. By comparison, stability distributions from the gradient method are displayed below in Figure 5.2 using data from heights 10m to 65m at met masts 1 and 2. The mast selection has been changed to ensure stability is calculated in the free-stream flow, before it interacts with the farm, as the gradient method required hub height measurements and therefore would risk significant wake effects at downstream locations. It was not possible to calculate stability at mast 1 via the bulk method as sea temperature measurements do not exist at that location.

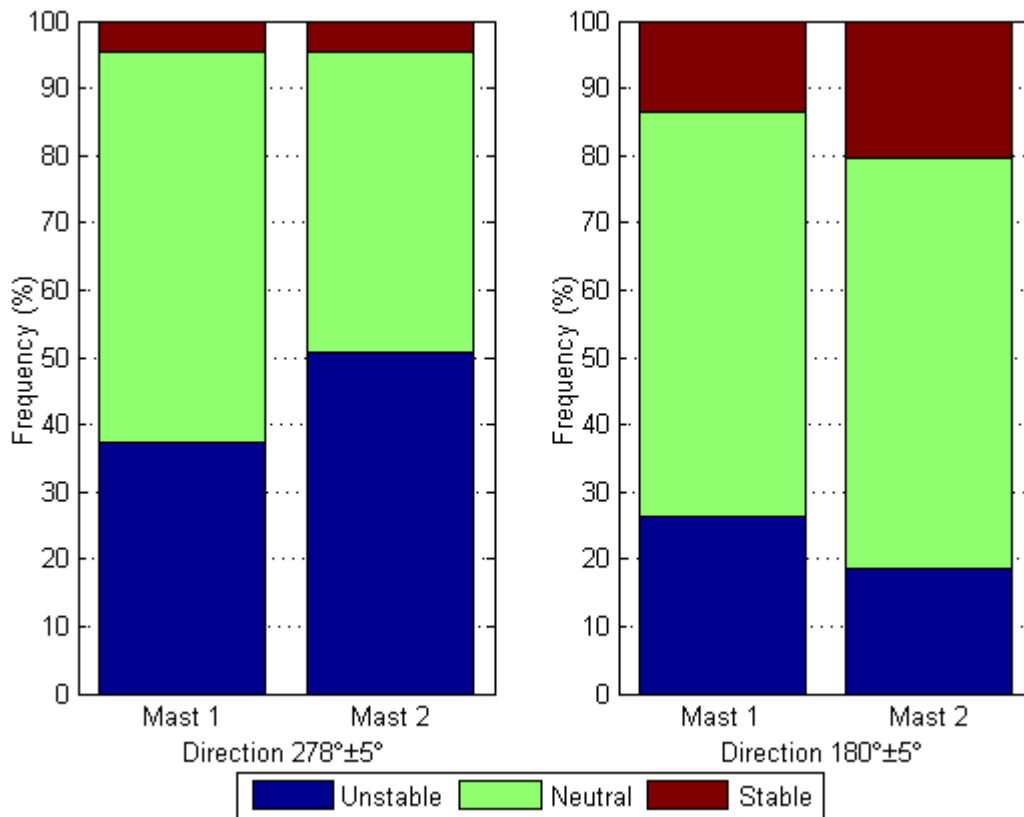


Figure 5.2 Comparison of gradient stability calculated at masts 1 and 2 at the Nysted farm

Stability distributions resulting from the gradient method of calculation, shown in Figure 5.2, contrast greatly with those from the bulk method in Figure 5.1. Primarily, the gradient method reports significantly greater proportions of Neutral and Unstable events than the bulk method which could be a result of ignoring the cold Baltic waters. It is, however, unlikely to have resulted from using measurements higher up each mast as [52] and [26] both show stability increases with height, nor can turbulence from turbine wakes be blamed as both masts 1 and 2 are upstream of the farm for both wind directions.

Using the gradient method, there is a greater variety in distributions between masts and wind directions than shown with the bulk method. Whilst the proportion of stable events is considerably reduced compared to Figure 5.1, each bar is overall more populous and so contains a greater number of Stable events. It follows that a greater number of Neutral and Unstable events also result from the gradient method. Therefore, the calculation of L in this chapter's model validations for the Nysted farm is calculated using the gradient method, differing from the analysis at the Horns Rev farm which uses the bulk method. Whilst this may produce some discrepancy, it is considered preferable to extending the directional bin size to achieve significant

dataset sample sizes. The closer proximity of mast 1 to the farm makes its measurements more relevant and shall provide stability information in the following sections.

5.3.2 Production Variability due to Stability

In Chapter 2, the effects of atmospheric stability on wind farm productivity were detailed in reference to other studies with the corresponding theory explained. In Chapter 4, results from numerous CFD simulations were compared against production data irrespective of concurrent stability conditions. Therefore, before the results of simulations incorporating stability are explored, Figure 5.3 displays the variability of electrical generation at the two Danish farms corresponding to changing stability conditions. The free-stream inlet speed remains unchanged from Chapter 4 at $8\pm 0.5\text{ms}^{-1}$.

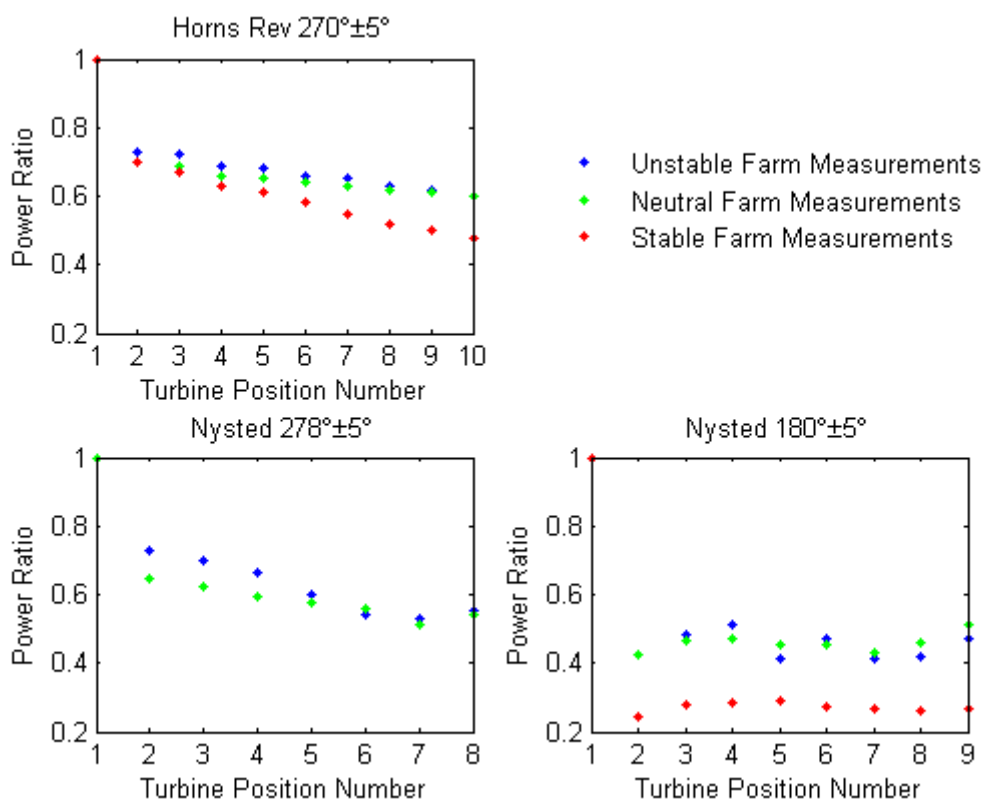


Figure 5.3 Plots of averaged power ratios through the farms, similar to those in Chapter 4. Production from turbines on the farm edges have been ignored to remove edge effects. Turbine position number refers to the location of each turbine in the ‘down the line’ row with position one being the free-stream turbine. There is no plot of N278S as there were no events coinciding within the set limits of incident wind speed, direction and stability without occurrences of individual turbine downtime.

From the three graphs above it is clear that a stably stratified atmosphere decreases overall power production, whilst an unstable atmosphere may slightly increase it,

relative to production levels in neutral conditions. The similarity between production levels during unstable and neutral events, combined with the stability distributions shown in Figure 5.2 suggest there may not be much reason to include stability in CFD simulations, but these are just power expectations and do not include the added operation and maintenance costs involved. Regions where stable events are more dominant would clearly benefit from stability modelling however, as shown by the large difference in wake losses for case N180S and HR270S by the end of the farm.

Figure 5.3 shows turbine wakes in stable events take longer to dissipate and in large farms, accumulate to cause higher wake losses than with other stabilities. By comparison, the initial wake effect between turbine 1 and 2 for cases HR270U and N278U are less than those experienced in neutral conditions, implying a higher measure of wake recovery already occurs before the second turbine in more unstable conditions. This is not shown for case N180U however, suggesting the closer proximity between turbines negates the benefits of the more unstable atmosphere. Deep array effects are seen with varying severity for all three stability categories at the Horns Rev farm and the majority of the westerly events for the Nysted farm, with some possible wake recovery at the last turbine. They are not observable however for any of the case studies with a southerly wind direction at the Nysted farm. This is hypothesized to be a result of the Nysted turbines being of two-speed design and therefore capable of a higher power generation at lower wind speeds. Thus the data referring to the southerly events may depict the changing of turbine rotation speeds rather than true wake recovery. The dual-speed turbine may also be the reason behind apparent wake recovery deep in the array in cases N278N and N278U when combined wakes from upstream turbines have reduced the resource enough for the end turbines to operate with different gear ratios. The smaller distances between turbine rows than columns cause this dual-speed effect to manifest sooner into the farm for southerly winds than westerly winds at identical inlet speeds. It is therefore important for simulations to be able to accurately reproduce where this change in gear ratio will happen within a large farm to accurately predict whole farm generation levels, and therefore financial investment risk.

5.3.3 Modelling Stability via Domain Surface Parameters

Despite being a transient model rather than a time averaged simulation, URANS does not have sufficient time resolution to calculate $\overline{w'T'}$ at any location in the domain. However, the model may be initiated with a constant heat flux value as a boundary condition across the domain base. This, combined with a variant of equation 2.11 shown below as equation 5.1, enables an approximate calculation of L via the flux method using the bulk Richardson number. Whilst calculating L using a heat flux instead of the Richardson number is more representative of the original MOST format, describing the kinetic and potential atmospheric energy balance in terms of thermal fluxes and mechanical forcings [158], this cross-breed of techniques may not be too useful since surface fluxes are not standard offshore measurements.

$$H_s = c_p \rho \overline{w'\theta'_v} = c_p \rho u (T_{sea} - T_{air}) \quad 5.1$$

Whilst the equation above is convenient for converting between heat flux and bulk methods, it requires some additional assumptions. For example, it is assumed that the bulk sea temperature (T_{sea}) inevitably measured two metres below the surface, is an acceptable approximation of the surface temperature. Similarly, wind speeds are normally assumed to equal zero at rough flow boundaries, which according to equation 5.1 would result in a zero heat flux. Therefore, the air speed and temperature (T_{air}) are measured at the common meteorological height of 10m. Conveniently, this matches the measurement heights used at the Horns Rev farm.

The calculation of Ri_B as shown in equation 2.13 requires a single wind speed measurement and two thermal measurements, one of the air and one of the sea surface. As described in Chapter 4 URANS defines the velocity profile based on an initial free-atmosphere input value above the Ekman Spiral, which controls the wind's velocity at lower heights via the geostrophic drag law (equation 2.1). This means the inlet parameters can only be tuned to specify a wind speed at one height per simulation, with other heights conforming to the drag law to ensure smooth profiles meeting the condition of 0ms^{-1} at z_0 . As such, it is unlikely that wind speeds of events measured at the relevant mast heights at the Danish farms, filtered by the required hub height speed ($8\pm 0.5\text{ms}^{-1}$), will match those at equivalent heights within each

simulation. It follows therefore, that as the measured and modelled velocities are not identical, in order to simulate specific values of L , the required simulated thermal gradient value, ΔT , will also be different to those measured by the met masts.

By default, URANS includes a thermal profile with a constant potential temperature throughout the ABL and a constant stable gradient with height above. There is no default value for the sea surface temperature as Windmodeller simulations typically only interact with the domain base through mechanical forcings such as the surface roughness value. However, an appropriate value can be incorporated, calculated by rearranging equations 2.13 and 2.14 and substituting wind and air temperature values produced as by-products from URANS simulations in Chapter 4. Owing to feedback effects between thermal and mechanical processes, a further process of trial and error is required with all input variables to ensure the correct meteorological conditions are simulated. This adds further cost to those already mentioned in previous chapters. Results from using Ri_B to calculate L via both the surface heat flux and sea temperature method are shown in the following subsections 5.3.3.1 and 5.3.3.2 respectively.

5.3.3.1 Surface Heat Flux

Although the URANS model is a transient simulation and therefore theoretically capable of producing a value of L using the flux method (equation 2.12), the resolution required to obtain suitable values of $\overline{w'T'}$ would compromise the cost savings of RANS-based simulations and approach LES complexity, thus making it unsuitable for simulating large wind farms with currently available resources. It is possible however, to define a constant heat flux through the bottom of the domain (here representing the sea surface) and substituting values in equation 2.11 to calculate L near the sea surface. Although the validity of this method deteriorates further from the surface and has little connection to flow speed, it could be useful for simulating offshore sites without met masts. Figure 5.4 below compares measured production data against simulation results using a surface heat flux to control the value of L at the relevant met mast location.

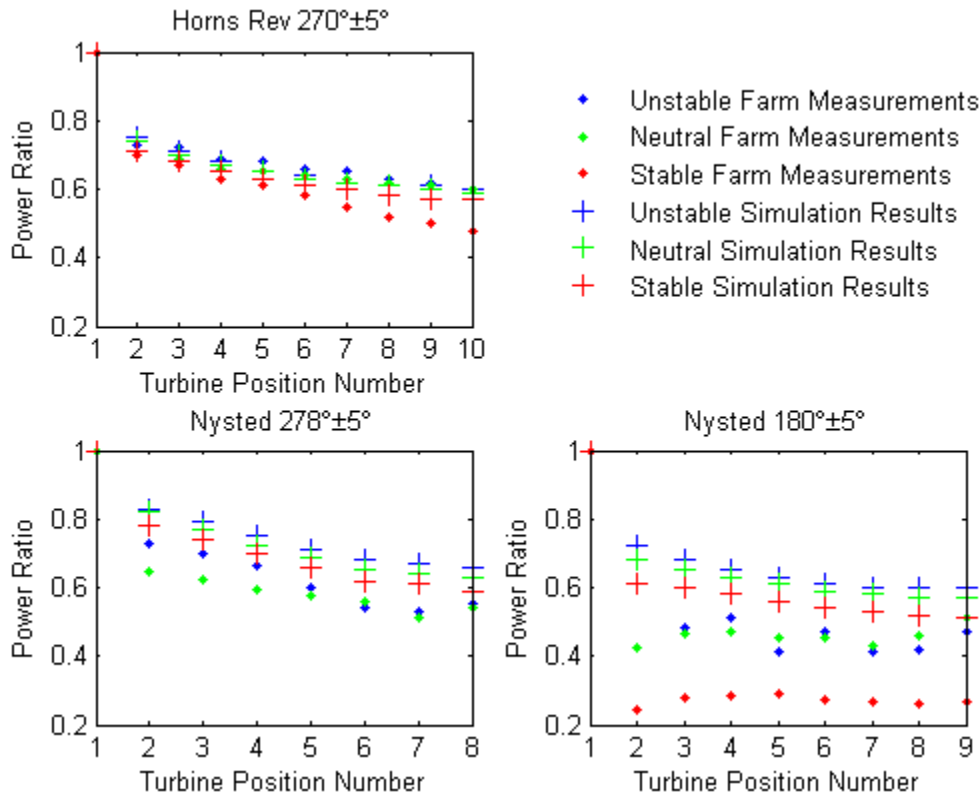


Figure 5.4 Comparison of measured production data against with simulations using a surface heat flux to generate three Obukhov lengths for the Stable (red, $L = 105\text{m}$), Neutral (green, $L = \pm 1000\text{m}$) and Unstable (blue, $L = -125\text{m}$) atmospheres as measured at the relevant mast locations.

Results from the heat flux simulations show small variations in production levels relative to L . It is hypothesized that this difference is only small because the heat flux calculation of L is not directly inclusive of wind speed, favouring instead the friction velocity. It is clear the variations between stability categories are caused by variations in L however, as the incident hub height wind speeds are the same for each flow direction. This is supported by all three Unstable cases being more productive than the three Neutral cases, which in turn are more productive than the three Stable simulations.

The general accuracy of each simulation result shown in Figure 5.4 is dependent on the accurate capture of the initial wake loss experienced by the second row turbine. This is shown for cases HR270N and HR270U which both capture the first wake and then closely match subsequent losses. Cases N278N and N278U both under-predict the initial wake loss, but then capture subsequent additional losses, thus systematically under-predicting the total wake losses across the farm. Whilst the simulation of case HR270S reflects both the initial wake loss and subsequent losses in the farm front half, it fails to display the deep array effect shown by the later

turbines and instead follows the loss curve from the other two case studies. As there were no suitable field data for comparison with N278S, no conclusive statements can be made, other than the simulation has predicted a lower farm output than for the other stability cases on that graph. For all three westerly stability categories at Nysted, there is some indication of wake recovery rather than deep array effects at the later turbines; however, this may result from the previously mentioned issue of turbines with dual-speed gearing or unusually wide turbine spacing. Results from southerly flow simulations are less accurate than other case studies, symptomatic of a poor analysis of initial wake losses. In this case, all three models assuming higher flow speeds penetrating through the farm than reality and thus over-predicting subsequent turbine generation and failing to capture the features of dual-speed gearing at low incident wind speeds. This is likely to be a combined result of closer turbine spacing and model assumptions of the near wake region caused by using the actuator disc approach.

5.3.3.2 Sea Surface Temperature

In the previous section, stability was inferred by a domain boundary condition flux. In reality, however, this flux is inferred by the thermal difference between two touching bodies. Therefore, in this section, results from simulations are discussed with L defined via Ri_B , created by replacing the surface heat flux from the previous section with a suitable constant temperature across the domain bottom, representing the sea surface temperature. This should create a more realistic simulation, although a number of additional assumptions are required. For example, it is assumed that the thermal capacity of a significant water body is great enough that the surface will remain at a constant temperature across the whole domain, whereas in reality, the skin temperature will converge with the air temperature directly above it [61]. Furthermore, as the air inlet potential temperature throughout the boundary layer is modelled as a constant value independent of height, separate to the value assigned to sea surface temperature, this method implies the advection of air from a location just beyond the domain with a different surface temperature rather than a very long marine fetch, else the surface air temperature could be expected to match the sea temperature. As the simulated atmospheric thermal profile will develop through the domain in response to the defined constant sea temperature, it is also assumed that

the flow will have developed a realistic and steady temperature profile before reaching the simulated turbines. For reference, Figure 5.5 below shows the difference between air and sea temperatures at the Nysted meteorological mast 2, for the different stability categories in Table 5.1, calculated using Ri_B (left) and Ri_G (right), filtered for relevant wind speed and directions to this study.

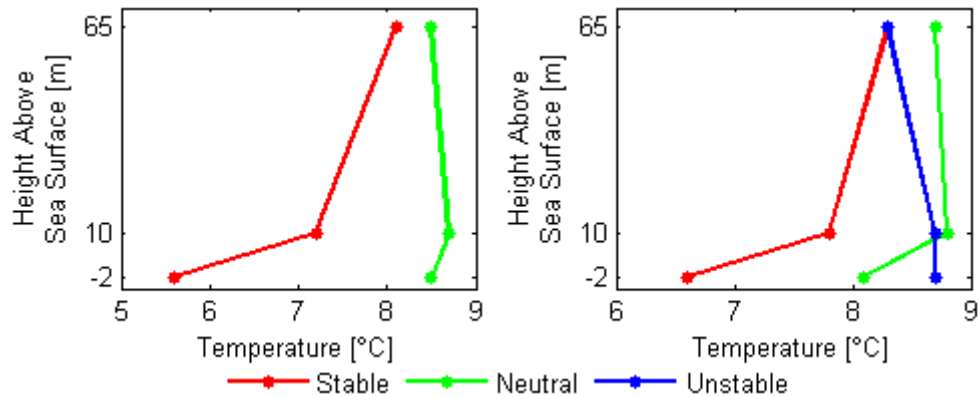


Figure 5.5 Temperature profiles at the Nysted met mast 2 showing non-linearity between air temperature (measured at 10m and 65m) and sea temperature (measured at -2m). Left shows profiles with L calculated via the Bulk method whilst Right shows profiles with L calculated via the Gradient method. Event profiles have been filtered to include only wind directions $180\pm 5^\circ$ and $278\pm 5^\circ$ with hub height wind speeds $8\pm 0.5\text{ms}^{-1}$ and are displayed according to their values of L . Red=Stable ($L = 105\text{m}$), Green=Neutral ($L = \pm 1000\text{m}$) Blue=Unstable ($L = -125\text{m}$). Note, there were no Unstable events with required wind speed and directions using the Bulk method.

Figure 5.5 shows non-linear profiles of temperature from air to sea with either rapid change in the lowest atmospheric 10m or highest marine 2m, particularly for stable conditions. Both calculation methods show air absolute temperature slightly increases near the surface in neutral conditions, despite a cooler water surface. Whilst Unstable events calculated using the gradient method show equality between sea temperature and lower air temperatures. It is of note that despite a 2°C difference in sea temperature, the averaged values for Stable and Unstable air temperature at 65m height are the same, suggesting the thermal effects of variable surface forcings do not penetrate far through the atmosphere, although further temperature measurement heights would be required to confirm this. Figure 5.5 suggests that above the surface layer, the horizontal advection of air masses from one regime to another are a more significant driver of atmospheric stability conditions than differences between surface and atmospheric temperatures. Alternately, Figure 5.5 suggests that a relatively warm sea results in an equally warm layer of air above it, whilst a relatively cold sea only partially cools the air above it. This was also observed in the URANS simulations using sea surface temperature to determine stability via Ri_B : simulated air temperature was insensitive towards colder

sea temperatures, resulting in $L = 10m$ from a $8^{\circ}C$ surface temperature, whilst the simulated air temperature would rise significantly with warmer sea temperatures. As such, it was not possible to simulate the most extreme cases where $L = -50m$ without stipulating sea temperatures in excess of $50^{\circ}C$, clearly an unrealistic value of sea temperature anywhere. Therefore, for simulations using the bulk method to calculate stability, Unstable events are represented by only the central value of L shown in Table 5.1, which is $L = -125m$.

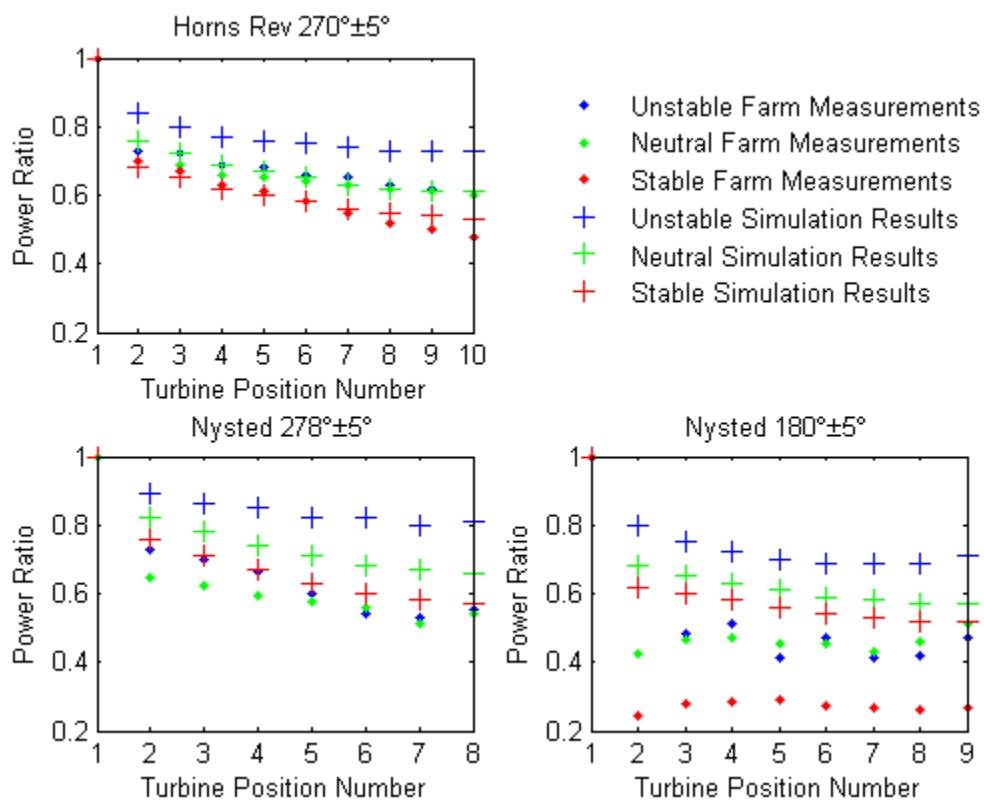


Figure 5.6 Results from simulations using a sea surface temperature to replicate Obukhov lengths for the Stable (red, $L = 105m$), Neutral (green, $L = \pm 1000m$) and Unstable (blue, $L = -125m$) atmospheres as measured at the relevant mast locations.

Despite all simulations being initiated so that the free-stream turbines are exposed to hub height wind speeds of $8ms^{-1}$, Figure 5.6 clearly shows how variations in stability affect the significance of wake losses, even by the second turbine. For example, in each of the three graphs above, the simulated results for Unstable conditions show significantly greater farm output than for Neutral conditions. This suggests the warmer sea, and hence warmer atmosphere, result in greater levels of turbulence which dilute the wake effects with faster moving flow from either above or below rotor height. With the domain base providing a continuous source of thermal energy

available for assisting wake recovery, simulated wake effects deep in each farm are less than those measured in real life, and even include suggestions of significant wake recovery such as deep in case N180U.

Unsurprisingly, the small variation in sea temperature from the input air temperature required to simulate all four neutral values of L result in little difference between neutral simulation outputs using sea temperatures or surface fluxes as in section 5.3.3.1. Using cool sea temperatures to define Stable events, however, has resulted in greater initial wake loss than defining stability via heat fluxes. For case HR270S, this has resulted in the under-prediction of generated power in the front half of the farm, although as each subsequent wake effect between turbines is under-predicted, by the second half of the farm, cumulative simulated wake losses are less than in reality. Thus, whilst the simulation of overall farm production in Stable events is closer to reality using sea temperatures than heat fluxes, the model has deteriorated in its capture of the wake effect. Whilst there are no Stable measurements to compare case N278S against, the simulated results show lower power generation across the farm than in Neutral events. Interestingly, case N278S does well at matching the measured results for the Unstable events, though this is purely coincidental. In a similar manner, the simulation of case N180S predicts less generated power than N180N, although all three simulations from this direction fail to capture the dramatic wake losses between the free-stream and subsequent turbines. Beyond the initial wake effect, the simulations for case N180S suggest small further wake losses between each turbine. Therefore, simulation production values neither reflect the actual values from the corresponding real turbine or appropriate individual wake losses between turbines within the farm. It is again suggested this is a result of using actuator discs in close proximity, possibly within the near wake region.

5.3.4 Modelling via Gradient Richardson Numbers

Previously, in section 5.3.3, atmospheric stability was included in wind farm simulations by defining suitable parameters across the bottom of the simulation domain. However, this method results in neutral atmospheric inlet conditions with stability expected to develop throughout the domain, culminating in the desired value of L at the key mast location. Thus for cases with more extreme values of $1/L$, larger

stability gradients are created horizontally across the domain ($\Delta L/\Delta x$ or $\Delta L/\Delta y$), such that the horizontally homogeneously stratified assumption of MOST will not be met as theoretical values of L at mast locations will vary from that at the turbine locations. Whilst it is likely in the real world that L will vary laterally across large wind farms, a simulated domain where stability conditions vary from Neutral at the inlet to either Very Stable or Very Unstable at mast locations are not supported by Figure 5.1 and Figure 5.2 which suggest little variation in atmospheric stability across such distances. It was also previously noted that the advection of different air masses from other thermal regimes (particularly near the coast) likely plays a significant role in defining the Obukhov length for particular location. Therefore, in this section, results are discussed from simulations of the Horns Rev and Nysted farms where simulation inlet conditions define a non-constant thermal profile in the boundary layer, building on the work of [159]. Thus, this section analyses simulated stability using Ri_G .

As the gradient method of calculating stability requires wind speed and temperature measurements at two heights, the validation data used in previous sections for the Nysted farm is appropriate for use here. The data from Horns Rev however, was analysed externally for use with bulk method simulations. Therefore, two heights located at the simulated Horns Rev mast M7 were selected from which modelled values of L correspond with those measured at the farm; heights 15.7m and 25m result in a value of z' equal to that representative of the bulk method data used to validate results. As temperatures at only two heights are required to calculate L via Ri_G , there are no other thermal requirements the simulations must include within the SL. Thus for simplicity, the simulated boundary layer, normally at constant temperature with height, is split into two sub layers, each with a constant inlet temperature with height as shown in Figure 5.7. The upper sub-layer (θ_{upper}) retains its thermal inlet value of 288K (15°C), whilst the inlet temperature of the lower sub-layer (θ_{lower}) is varied to control the simulated stability value. As the simulation progresses, the two sub-layers interact and the discreet inlet profile develops into a gentler gradient before the flow reaches either the simulated turbines or mast, more akin to field measurements. To prevent the temperature gradient dissipating too rapidly, the sea temperature is defined as a constant value equal to the inlet value of

θ_{lower} , despite Figure 5.5 showing significant differences between temperatures of the sea and lower SL for both Stable and Neutral stability events. This method of controlling the atmospheric stability by varying input temperatures of the lower SL is supported by the findings in [26] which suggests a narrow sub-layer next to the sea surface acts to dampen any surface forcing causing the air above to be less susceptible to strong gradients of θ .

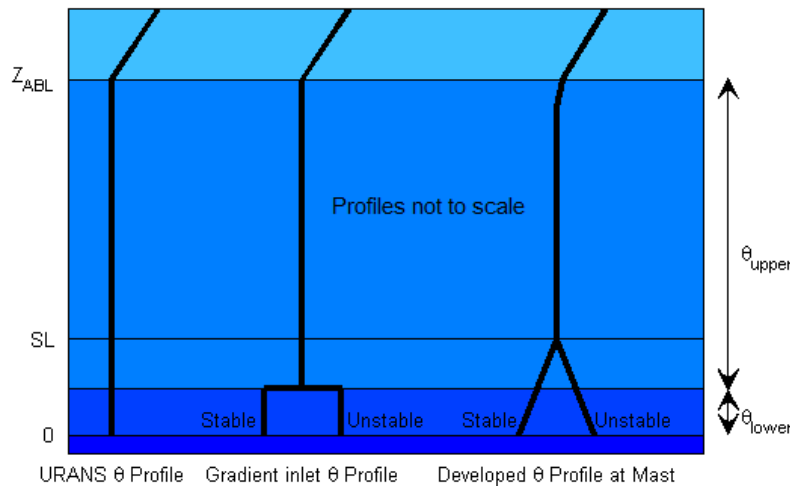


Figure 5.7 Illustration of the thermal inlet profile for a default URANS simulation (left) and the modified profile for simulations using the gradient method of calculating L (centre) where a constant value of θ is defined in the θ_{upper} region above a separate constant value of θ defined in the θ_{lower} region. As the simulated flow progresses through the domain, the different values of θ in the two sub-layers interact and merge into smooth gradients (right) before reaching the mast where stability is classified. The vertical axis is not to scale.

Similar to the bulk methods in the previous section, each simulation using the gradient method required a number of calibration runs in order to obtain the desired values of L at mast locations whilst maintaining the correct values of wind speed and direction at the key turbines. During these calibration runs, it was noticed that the values of L at each mast were highly sensitive to the input temperature value of the θ_{lower} sub-layer, particularly for modelling stable conditions. This suggests there was more turbulence with greater mixing between sub-layers for unstable events whilst the colder θ_{lower} sub-layer in stable events suppressed turbulence, reducing mixing and thus becoming self-propagating through the domain. It can be concluded that by extrapolating this process through the rest of the SL, the higher turbulence caused by warmer air near the sea surface results in a greater mixing of air throughout the height of a wind turbine, not only decreasing wind shear but also increasing wake recovery behind each turbine as faster moving air is mixed into the slower wake

region. However, the results shown below in Figure 5.8 only partially support this idea.

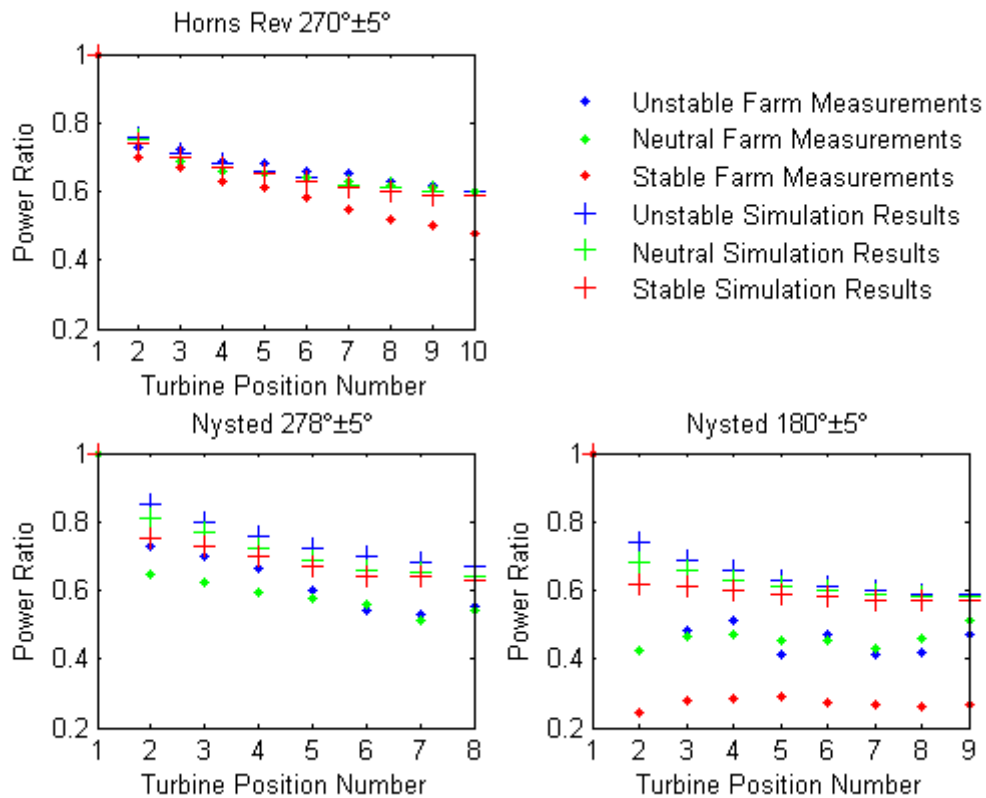


Figure 5.8 Results from simulations using variations in air inlet temperatures to generate three Obukhov lengths for the Stable (red, $L = 105\text{m}$), Neutral (green, $L = \pm 1000\text{m}$) and Unstable (blue, $L = -125\text{m}$) atmospheres.

Results from the Horns Rev simulations show no statistically significant difference between each stability category. Each modelled turbine generates less power than the turbine before it, although with smaller losses amongst the later turbines and no real evidence for significant deep-array affects. A similar result is shown for westerly flow simulations of the Nysted farm, although there are clear differences in wake losses towards the front of the farm with case N278U generating more than case N278N which in turn generates more than case N278S. Both Unstable and Neutral simulations predict a greater power output than actually measured at the farm. As with the other methods of simulating atmospheric stability, the gradient method simulations of southerly flow through the Nysted farm dramatically under-predict the wake losses after the first turbine and thus any comparison further into the farm is irrelevant. Although, it is useful to note that simulation N180U predicts lower power losses than N180N or N180S near the front of the farm whilst at the back, all three simulations predict similar values of power generation. This suggests that whilst the

problems with actuator disks producing accurate near wake effects prevent accurate production simulations for narrow distributions between turbines, there are still some visible effects of atmospheric stability on the strength of turbine wakes.

5.3.5 Comparison of Richardson Number Methods

Having simulated active wind farms using three separate methods of incorporating atmospheric stability, a visual comparison of model accuracy is given below in Figure 5.9 where the overall accuracy of each method of incorporating stability is calculated using equation 5.2.

$$\text{Simulation Error} = \frac{\text{Simulated Power} - \text{Measured Power}}{\text{Measured Power}} \quad 5.2$$

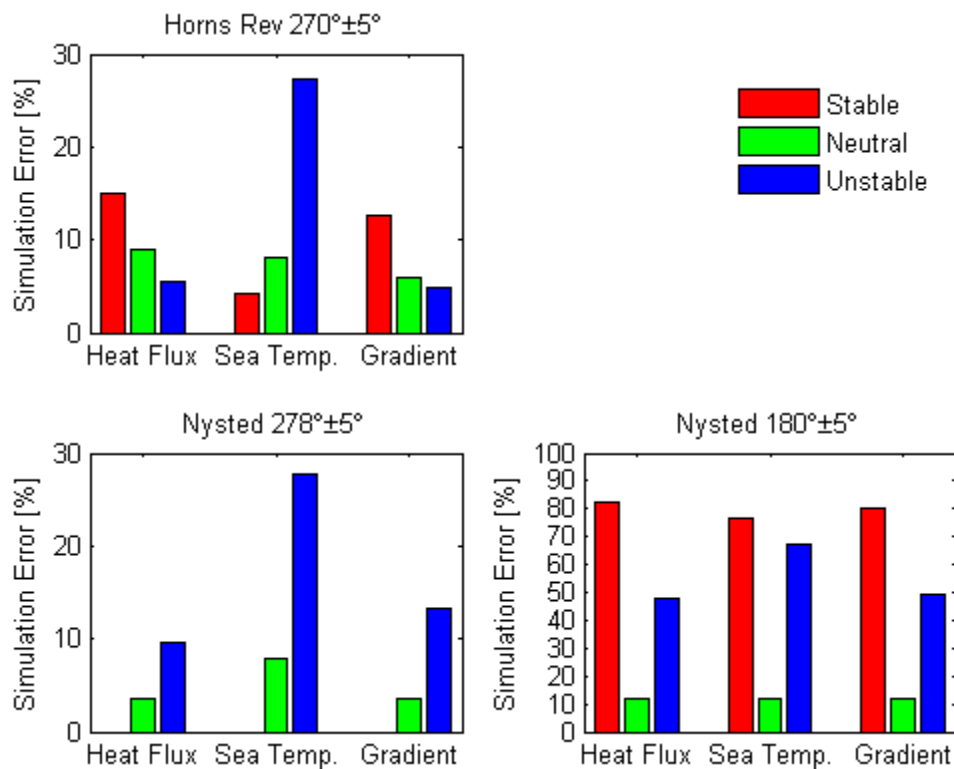


Figure 5.9 Combined results from the three Richardson Number simulation techniques showing the accuracy as a function of measured power generation at each farm using equation 5.2. Note there are no error statistics for case N278S as there were no measured events suitable for comparison.

The comparison of results shown in Figure 5.9 show mixed results. Whilst all three stability methods show high levels of simulation error with both stable and unstable events for southerly flow at the Nysted farm, there is little difference in the accuracy of their relevant neutral simulations. This is partially unsurprising as the simulations of neutral stability are each very similar to the default URANS model which assumes

neutral conditions. It does follow however, that if simulation accuracy problems with cases N180U and N180S stem from the close proximity of turbines (as suggested previously), then there should be high Simulation Error in all three stability categories. This apparent inconsistency is a direct consequence of the results shown in the three Figure 5.4, Figure 5.6 and Figure 5.8 having been normalised by the production of the free-stream turbine whilst data used in Figure 5.9 are not normalised. From this, it appears that although Windmodeller, using all three stability calculation methods, struggles to replicate initial wake losses between narrowly spaced turbines, the overall greater measured production in Neutral events result in significantly less Simulation Error.

Simulations of the Nysted farm with westerly flow are more accurate than for southerly flow. This is primarily assumed to be a result of greater turbine spacing, and whilst there are no available measured data from Stable events, both the Neutral and Unstable simulations show more relative variability between stability calculation techniques. For example, the method outlined in section 5.3.3.2 using sea temperatures to control atmospheric stability is clearly the least accurate method, with Simulation Error more than twice that of the others. There is little separating the Heat Flux and Gradient methods for Neutral events whilst the Gradient simulation of Unstable conditions is less accurate than the Heat Flux version.

Simulations of the Horns Rev farm show mixed levels of accuracy across the three methods. For example, Figure 5.9 shows while the Sea Temperature method is clearly the best at simulating the Stable events, it is also clearly the worst at simulating the Unstable events (as with the Nysted case studies). Simulations of the Neutral events suggest the Gradient method is most accurate, although the range between results is small. Similarly, whilst the Gradient method returns the smallest errors for simulations of Unstable events, there is only marginal improvement on the Heat Flux method.

The variation shown here could be a result of how turbulence is formed and works to mix the air across different layers in the atmosphere. Stable atmospheric stability is characterised by low levels of turbulence, causing little mixing with height, and a strong thermal gradient near the surface. Thus it is unsurprising that the Sea

Temperature method produced more accurate Stable simulations than the Heat Flux method, as a flux by definition requires vertical mixing to transport a characteristic whilst a cold surface temperature just saps the thermal energy from the lowest regions without relying on kinetic processes. This, however, does not explain why the result from the Gradient Stable simulation is comparably poor as it too uses a sea temperature and even accelerates the cooling affect with a layer of cool air. The reverse is beneficial for the simulating the Unstable cases. It was found that using a warm sea temperature resulted in the lower SL warming very quickly with distance into the domain, such that excessive sea temperatures were required in order to ensure the correct temperature gradient existed at the mast location. Use of such high temperature values are unrealistic of real sea measurements in Northern Europe, yet could not be avoided on account of fixed velocity requirements at hub height and a lack of control over the wind profile.

The results from the Horns Rev Gradient method simulations are much closer to the Heat Flux method than the Sea Temperature method, with Stable simulations returning with the highest errors and Unstable simulations the lowest. The relative amount of simulation error for each stability category is also very similar. To help determine which is more helpful for resource assessment and farm planning, Figure 5.10 below shows the standard deviations of simulation error at each individual turbine in the farm.

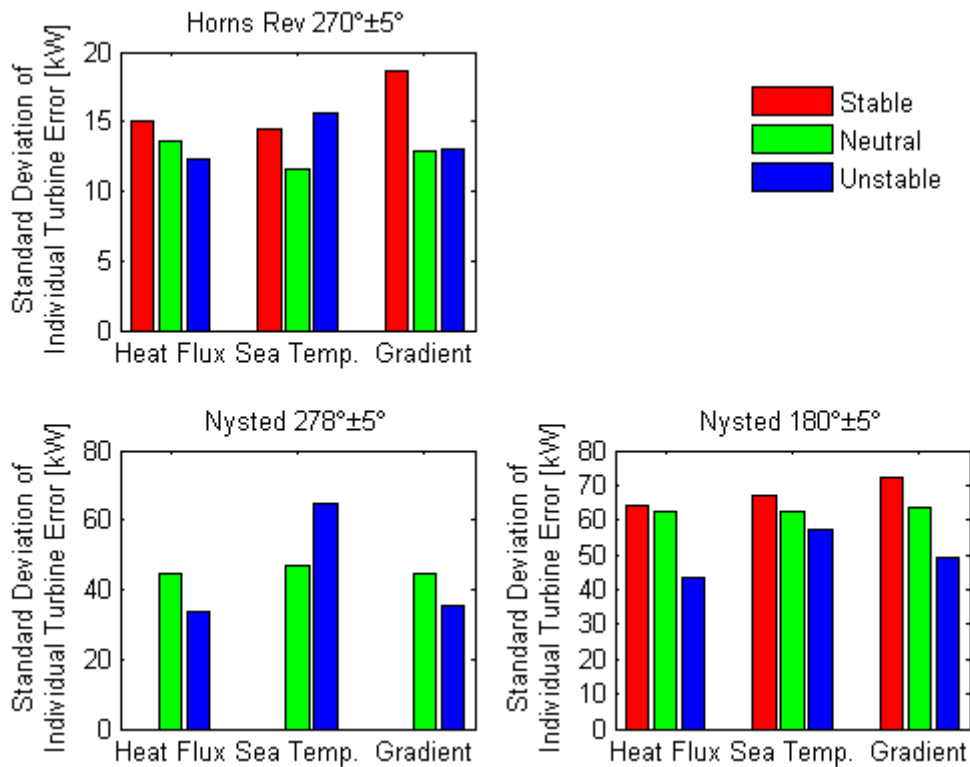


Figure 5.10 Combined results from the three Richardson Number simulation techniques showing the total standard deviation between the simulated and measured power generated by each turbine. Note there are no statistics for case N278S as there were no measured events available for comparison.

The standard deviations of modelling error shown above indicate a significant difference in confidence between modelling the Nysted and Horns Rev farms. This is particularly shown for westerly flow where the average Horns Rev value is between 10-15kW whilst the average for the Nysted farm is more than double at around 40kW. Whilst the graph showing results from the Nysted farm with southerly flow have been included for completeness; the quantity of Simulation Error shown before in Figure 5.9 mean the individual values for Stable and Unstable stability conditions are of little interest. However, it is worth noting that despite the Neutral simulation events returning similar levels of Simulation Error to some westerly flow simulations, the standard deviation of error for case N180N is much higher than most of the westerly flow scenarios. The difference in absolute values for westerly flow between the two farms is likely to be a result of the difference in turbine used as the turbines are located closer together at Horns Rev then at Nysted for these flow directions (turbine separations of 560m and 857m respectively). Windmodeller struggled to simulate the more complex thrust curve required by the Nysted turbines, particularly as the low free-stream hub height speed of 8ms^{-1} is inconveniently located in the thrust curve such that downstream actuator discs are required to manage the rapid changes in thrust co-efficient.

In the same way that Figure 5.9 showed the Heat Flux method to be better than the Sea Temperature method as a way to define the stability conditions within a simulation, Figure 5.10 reinforces this as the standard deviation of error is lower in simulations of Stable conditions for the Sea Temperature method, but lower in Unstable conditions for the Heat Flux method. Unlike results with the Simulation Error, however, the Gradient method results in the highest standard deviation of accuracy for Stable simulations and no significant improvement on the Heat Flux method for either Neutral or Unstable events. Therefore it is unclear which of the three ways of simulating atmospheric stability is best without suitable validation data from other offshore wind farms.

5.3.6 Comparison of Model Accuracy With and Without Stability

At the end of Chapter 4, simulated power ratios from the four turbulence model options were compared against two measurement sets from the Horns Rev wind farm, one filtered for neutral stability and one not. It is now appropriate to compare whether the inclusion of stability in the simulations has had a significant impact on model accuracy. For this, it is important to understand the differences in assumptions required between the two simulation categories. Of primary importance is the difference in directional bin sizes, which were twice as wide for simulations including stability than simulations assuming neutral conditions. Whilst this succeeded in increasing the number of events available for model validation, thus making time-averaged simulations more comparable, it degraded the quality of wake measurements associated with studies of flow along a line of turbines. In addition, each CFD run simulated a single wind speed and direction case rather than the range of values used by the validation data. Whilst this was partially accounted for by averaging the results from multiple simulations across the directional gate range, no attempt was made to reproduce the variability of measured free-stream wind speeds, $\pm 0.5\text{ms}^{-1}$.

5.3.6.1 Possible Over Stipulation of Meteorological Conditions within Case Study Validation Data

With every meteorological requirement of the validation data, be it the primary concerns of wind speed and direction or secondary issues such as atmospheric stability or background levels of TI , the resulting filtering process inevitably leads to a smaller dataset suitable for model validation. The graphs below show the importance of comparing a CFD simulation reporting time averaged results against validation data averaged across a significant number of events. The graph on the left of Figure 5.11, reporting production values from a single line of turbines, shows significant variation in power ratio between individual turbines along the row for both measured events. Whilst the right-hand graph of Figure 5.11 displaying the average power ratio values across multiple rows of turbines within the farm, indicates a steady decline with depth into the farm. This is because despite both graphs displaying the same two ten-minute events, averaging across each line of turbines in the farm effectively multiplies the number of events, whilst maintaining very similar meteorological inflow conditions. Validation data from a single line of turbines during an individual event will be subject to the effects of turbulent eddies moving through the farm during the event. Although the other turbine rows may also experience the same or other eddies, over a sufficient number of rows, or with sufficient separation between rows, the effects of eddies on turbine wakes average out similarly to when production data is averaged across several individual events.

Table 5.3 Details of two ten-minute measured events, randomly selected from the Nysted validation data used in previous sections, displayed in Figure 5.11 below.

Event	Hub Height Wind Speed	Hub Height Wind Direction	Obukhov Length	No. of fully operational non-edge rows of turbines
Event 1	8.0ms^{-1}	277°	-352m	3 out of a possible 7
Event 2	8.1ms^{-1}	281°	-127m	5 out of a possible 7

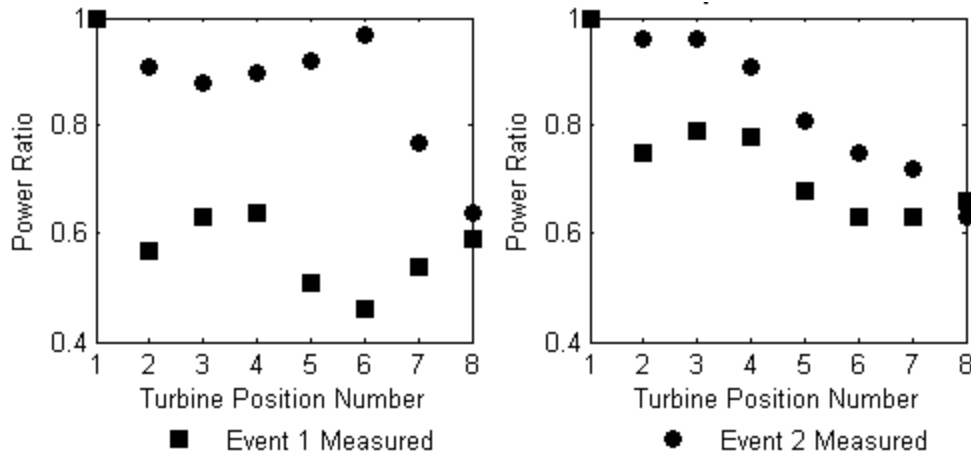


Figure 5.11 Power ratios measured at the Nysted wind farm during each of the ten-minute stability case study events with a wind direction of $278 \pm 5^\circ$. The graph on the left shows measurements from row 5 (the centre of the farm) whilst the right graph shows power ratios averaged across all fully operational turbine rows (excluding the turbines on the farm's edges parallel to the wind direction) during the same two events.

Excluding the turbines on the farm edges parallel to wind direction, only three rows of turbines were fully operational during Event 1 and five fully operational during Event 2 for the two events used in Figure 5.11. Although the variation in magnitude between turbine power ratios decreases when values are averaged across multiple rows, there are still some fluctuations which may in previous sections have been suggestive of wake recovery or variations in turbine thrust curves. Based on the comparison between the graphs in Figure 5.11, this is more likely to be due to an insufficient quantity of events being combined to eliminate the effects of prominent eddies. (There is likely no clear definition of what classifies as a sufficient quantity which could be transferred from one large wind farm to another, though strong relations to turbine size, lateral separation and meteorological conditions are possible.) By comparison, results from time-averaged based simulations such as URANS, do not exhibit any fluctuation in power generation resulting from eddies in the atmospheric flow. This is highlighted in the figure below where the production data from the previous figure has been shown alongside output from simulations using the gradient method approach in previous sections, with useful simulation information shown in Table 5.4. The left graph only displays simulated results from the farm's central turbine row, the row used for the measured data, while the right graph displays the average across all seven internal turbine rows, as is consistent with the power ratio graphs in previous sections. By comparing the two graphs in Figure 5.12, it is clear that for this example there are no significant differences in time averaged simulation results between one row and the average of internal rows

of turbines. This strengthens the suggestion that the differences between the graphs in Figure 5.11 may be the result of eddies moving through the farm and the spatial aggregation of such effects across multiple rows of turbines, rather than fluctuations in wake generation and recovery related to the complex nature of the turbines' thrust coefficient profile. Hypothetically, it might therefore be possible to use this aspect of temporally averaged modelling to simulate very large farms with only a few rows of ADs, so long as the number of turbines in each row is maintained. This would reduce the number of required mesh cells and thus the simulation computational time. However, this is not advised as such methods may result in errors from insufficient flow blockage effects and wake interactions, particularly in stable conditions where the wakes are forced to expand horizontally by strong vertical buoyancy gradients. Nor would such a simulation reflect the subtle variation in meteorological inlet conditions likely across the scale of such farms.

Table 5.4 Details of the two simulations compared below.

Event	Hub Height	Wind Speed	Hub Height	Wind Direction	Obukhov Length
Event 1		8.0ms ⁻¹		278°	-254m
Event 2		8.0ms ⁻¹		281°	-141m

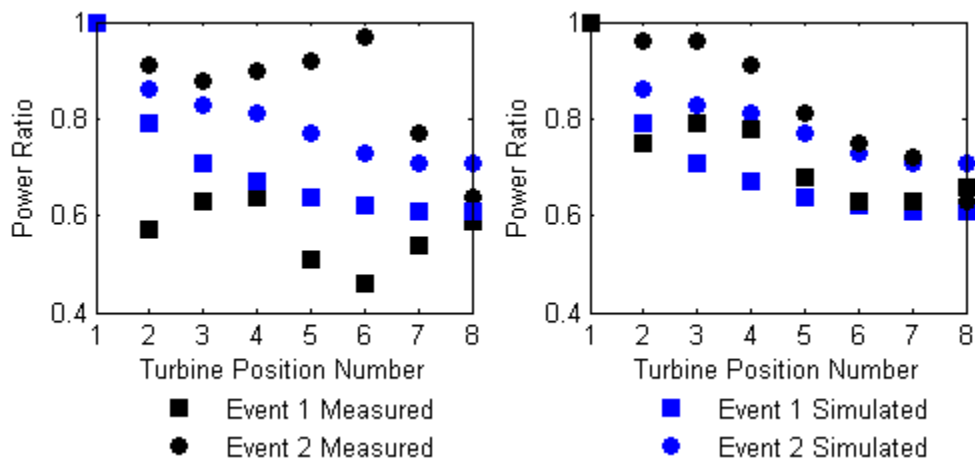


Figure 5.12 Simulated power ratios (blue) for the Nysted wind farm for both of the ten-minute stability case study events. The graph on the left shows results from row 5 (the centre of the farm) whilst the right graph shows results averaged across the rows used to calculate the corresponding validation data (black).

The modelled results in the right hand graph of Figure 5.12 show a much better fit to the validation data than in previous sections, particularly in the later regions of the farm. This factor is attributed to matching the simulation boundary conditions to a single event (with averages taken across the farm to reduce effects from eddies) rather than comparing a large range of events to a few simulations with

representative conditions. This suggests assessments of wake losses at future wind farms using CFD would need to incorporate a much greater number of stability scenarios than just “Stable”, “Neutral” and “Unstable”, each with a much narrower range of L and would therefore be subject to greater time costs.

Although the measured incident hub height wind speeds and directions for both events are reproduced appropriately by the simulations, the values for L differ between simulation and reality. To investigate this further, Figure 5.13 below compares the profiles of wind speed and temperature as measured and simulated at Nysted met mast M1 located in the free-stream flow nearby (see Figure 4.3). It is clear that for both events, the measured profiles differ from their simulated equivalents, although there is very little difference between the two events themselves. Despite the simulated wind speeds at turbine hub height being 8ms^{-1} , at the location of met mast M1 it is only 7.7ms^{-1} , whilst the measured speeds at hub height for each event are 8ms^{-1} at both mast and turbines. The standard deviations of measurements however are sufficient to suggest that there is no statistical difference between measured and simulated values over the 10 minute period of each event. Further down the mast, however, there is divergence between the profiles, with both the measured events showing a relatively constant rate of shear across the mast heights whilst both simulations return a more logarithmic profile. This results in statistically significant differences in wind speeds between the measurements and simulations at 10m, which is important as the 10m wind speed is used in the gradient method calculation of the Richardson number. As the URANS model operates by defining an inlet wind speed for the free atmosphere and a boundary condition of 0ms^{-1} at height z_0 with speeds at intermediate heights defined according to the geostrophic drag law, the shape of a URANS speed profile in the MABL does not fluctuate as much as those measured by offshore met masts. As described earlier, this requires the simulated thermal gradient to also differ from measured values in order to maintain the required ratio of buoyancy to mechanical mixing processes known as the Richardson number.

Figure 5.13 also shows the thermal profiles at the met mast location revealing that although the simulations utilise temperatures roughly 10° warmer than those

measured, the difference in the change in temperature with height is small. Statistically, the two measured wind speed profiles are the same (ignoring the measurement at 55m); however, the variance in air temperature during each of the events is small enough that the average values are statistically different from each other. As there is less than half a degree difference over 55m between the two rates of temperature change with height, it is possible that the difference in L is defined more by the temperature gradient with respect to T_o than by the actual temperature gradient itself. This would also explain why the two simulations result in significantly different values of L despite portraying identical wind speed profiles and temperature gradients separated by less than 0.1° over 55m. Put another way, with reference to equation 2.15; the URANS model results in a value of $\Delta u/\Delta z$ that is smaller than the field measurements, so $(g/T_o) * (\Delta T/\Delta z)$ must also be smaller in order to maintain the same ratio. Since the simulated values of T_o are significantly greater than the measured values, the simulated values of $\Delta T/\Delta z$ can be very small and still result in the desired stability classification. Therefore, for simulations using the URANS model, it is possible to suggest that since variations in temperature between the two simulations of less than a tenth of a degree have here altered the value of L by over 100m, resulting in a difference in stability classification, further study should be conducted into how temperature gradients interact and change through a wind farm. Conversely, since this high sensitivity to temperature gradients directly results from the inflexibility of the simulated free-stream wind speed profile, future effort should be directed towards ensuring the simulated wind profiles more accurately represent field measurements. It is also worth comparing the two measured temperature profiles below against the Unstable and Neutral profiles shown in the left graph of Figure 5.5 which also uses the gradient method to calculate L . As Events 1 and 2 are both colder than the local average, the difference between measured temperatures and the default simulated temperature will normally be smaller than shown those below. However for events where the difference between the default simulation temperature (15°C) and measured validation data is smaller; in order to generate the correct Ri value, the simulation will be highly sensitive to the value of $\Delta T/\Delta z$ potentially resulting in a long and frustrating trial-and-error process to simulate the desired value of L .

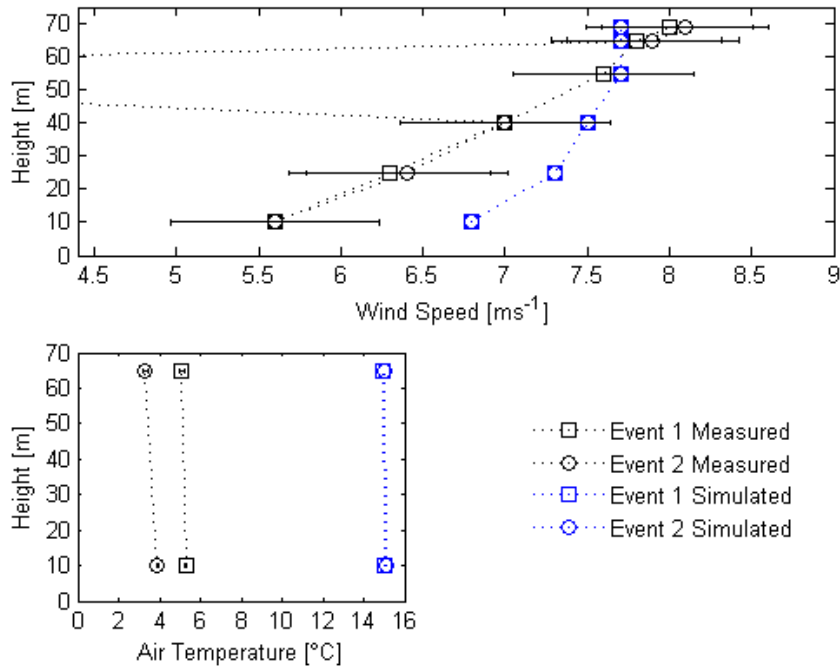


Figure 5.13 Comparison of measured (black) and simulated (blue) wind speed (top) and temperature (bottom) profiles for both events. The standard deviations of measurements taken during the ten minute intervals are also shown for reference, although the variance in temperature is small. Note that the 55m wind speed measurement for event 2 was 0.3ms^{-1} with a variance of 0ms^{-1} , suggesting a fault with the instrument.

Having seen that there is little difference between the simulated profiles for both events despite a difference in L of over 100m, a comparison shall now be made between these simulations and the turbulence models used in Chapter 4. As a note of caution however, both the values of L for Events 1 and 2 are negative and thus in a region of the stability distribution normally associated with low levels of shear. As it is not currently possible to control the simulated wind speed profile below hub height, simulations of more stable conditions are likely to result in greater discrepancies between measured and simulated profiles thus further increasing the sensitivity of simulated L values to variations in $\Delta T/\Delta z$ and T_0 .

As discussed earlier, directly comparing results from only one ten-minute event against time-averaged simulation results is not appropriate on account of eddies moving through the farm, even with the strict filtering required by MOST to ensure atmospheric homogeneity. As eddies are not associated with a homogeneous atmosphere, it is hypothesised that for use with large offshore farms the number of ten-minute events from which meteorological parameters are analysed during homogeneous testing should be related to the size of the farm. Typically, averaged parameters from each ten-minute event are compared against those from the

previous two events and the one immediately following it, resulting in a rolling period of 40 minutes where atmospheric conditions are relatively constant, although no consideration is made to the variance within each ten-minute period which may result in the differences between graphs in Figure 5.11. In addition to this, it theoretically takes an air parcel travelling at 8ms^{-1} , 12.5 minutes to cover the 6km between the first and last turbine in a row at the Nysted offshore farm, meaning not all the turbines will be subject to the same air parcel during the ten-minute period. In reality as the parcel encounters each turbine's wake it will be temporarily slowed, resulting in it taking longer to reach the last turbine while the distance between the met mast and free-stream turbine will add further travel time. Ideally time-averaged simulations of the Nysted farm would be validated against the average of a large number of ten-minute events with very similar meteorological conditions. However, despite the available production data set spanning 16 months, after filtering for quality control, wind speed, direction and atmospheric homogeneity, there were very few ten-minute periods remaining and none with comparable values of L . Therefore the simulation results shown below are each only compared against a single ten-minute period and assume the atmospheric conditions before and after the period are constant.

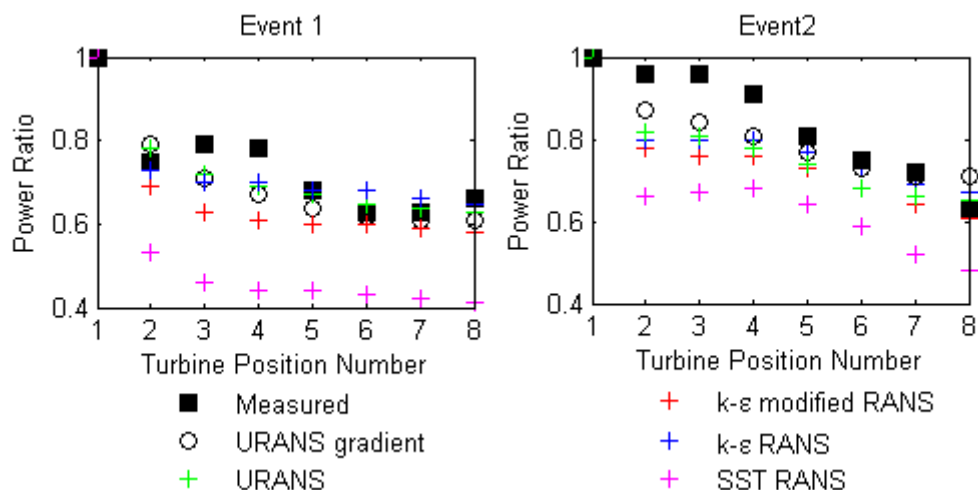


Figure 5.14 Comparison of measured power ratios (black filled squares) against five different simulation configurations: the 'URANS gradient' simulation (black open circles) are the same simulations used earlier this section using the gradient method of calculating L , the other simulation results (various coloured plus symbols) show results from models used in Chapter 4 with assumed neutral stability. Simulation results have been filtered to only include the rows of ADs which represent the operational turbine rows in the farm during each ten-minute period.

Although the measured values in Figure 5.14 are not reliable as long-term averages, they have been included as a reference to suggest where the average values may

occur. It is clear from the Event 1 graph (left) that the SST model consistently predicts significantly greater wake losses than the other models, a result also found in Chapter 3 and repeated to a lesser extent above in the graph for Event 2 (right). Each of the other models by comparison appears to be within a power ratio of about 0.1 of the other three. There does appear to be some differences between results from the URANS model between when neutral stability is assumed and when the gradient method is used to replicate stability conditions. Significantly this is more apparent for Event 2 than Event 1 (Unstable/Very Unstable and Neutral/Unstable conditions respectively, according to the 7 and 5 stability class systems), although whether the differences are significant and which model is closer to replicating the reality of a long-term average is unclear. The most notable outcome from the three RANS models is the different patterns in where the losses occur; with Event 1, all three models report decreasing power ratios from the initial turbine before a plateau appears deeper in the farm. This differs from Event 2 which displays an apparent plateau for turbines 2-4 before the power ratios decline in accordance to the deep-array effect. This is likely a result of wind direction relative to the turbine layout. The turbine rows at the Nysted farm are positioned such that the 'down the line' wind direction from west to east is 278° , so the measured conditions for Event 1 are only one degree off this whilst Event 2 is three degrees off in a clockwise direction. Although this difference does not seem significant, it is enough to change which simulation results are the most relevant to display in Figure 5.14: the left graph used results from simulations configured for 278° flow whilst for the right graph, the simulations with 280° were a closer comparison. Although this may result in reduced wake losses in the earlier part of the farm, turbines deeper in the farm are more likely to encounter interference from wakes relating to other rows of turbines.

The limited number of ten-minute time periods suitable for validation purposes could be considered a good thing as it means the Nysted wind farm was constructed in a manner which minimises the frequency of these worst-case scenario 'down the line' events. However, the lack of suitable validation data is also strongly linked to the classification of what is and is not suitable in terms of the requirements for MOST and the variability of L . Whilst useful for offshore farms with a regular layout, the approach used here of artificially multiplying event frequencies by averaging power ratios across multiple rows of turbines will not be suitable for farms with inconsistent

distances between turbines, such as with the Scroby Sands offshore farm. Since the main purpose of using CFD to simulate an offshore wind farm is to assess the turbine wakes and associated generation losses, it makes more sense to simulate frequently occurring events where wake losses and structure fatigue cumulated across the multiple events are a greater financial risk than more severe events which may only happen once a year. Furthermore, since Figure 5.14 suggests there is only a small difference between the output from models which include atmospheric stability via thermal gradients compared to those which just assume neutral stability, at least with negative values of L , the extra time required to calibrate the very small variations in thermal conditions shown in Figure 5.13 appears to yield little benefit. It is therefore suggested that an alternative to MOST, one which considers a much larger proportion of all possible meteorological conditions, should be used to describe atmospheric conditions, specifically the characteristics of the wind flow at the locations of planned offshore wind farms.

Using the mean and standard deviation of hub height measurements from the meteorological mast M1 at the Nysted farm, a Weibull distribution of long-term expected wind speeds suggests roughly 8.4% of events should have hub-height wind speeds in the range used in this work for validation, $8 \pm 0.5 \text{ms}^{-1}$. Combining this with the theoretical number of ten-minute events within the observed period and assuming an evenly distributed wind rose (divided into regular directional bins of 5° to correspond with the validation data from Chapter 4); there should theoretically be 64 validation events for each direction. Naturally, for a directional bin size of 10° as used in earlier sections of this chapter, the expected number of validation events would double to 128, although this is then subdivided according to atmospheric stability distributions. According to the stability distributions in Figure 5.2, this should result in 47, 73 and 6 events for westerly flow and 34, 76 and 18 events for southerly flow under Unstable, Neutral and Stable atmospheric stabilities conditions respectively. It can therefore be suggested that the significant differences between these expected quantities of events and those measured suitable for validating this work is a combined result of the filtering required by MOST and periods of turbine down-time. Although the even distribution of wind directions simplifies the calculation, the wind rose reported by [96] suggests a higher frequency of events from the westerly direction and a lower frequency from the south. This may partially explain

why there are fewer suitable measured events with southerly flow than expected, though it further emphasises the amount of valuable data removed by the MOST filtering requirements as it is reasonable to assume turbine downtime is not expressly linked to wind direction.

5.3.6.2 Model Results Comparison

The simulations replicating atmospheric stability conditions so far throughout this chapter have all been variations on the URANS model from Chapter 4, with all the additional calibration complexities and filtering requirements for validation described in the previous section. So has simulating offshore events according to their stability categories individually increased or decreased the accuracy of the results? By not filtering according to Obukhov Length, there are a theoretically greater number of events contributing to the validation process of each individual simulation, allowing the width of each direction bin to be narrower. However, this also means there is a greater variability in stability conditions within the validation data, leading to greater variation in turbine wake behaviour. By comparison, filtering on atmospheric stability helps focus on specific wake behaviour patterns, although the low frequencies of such events results in the requirement for wider directional bins in order to incorporate events with suitable stability conditions, and this changes the multiple wake interaction patterns. There may be occurrences where theoretically desired validation measurements do not exist as in the case for Stable conditions under westerly flow at the Nysted farm, while scenarios with insufficient validation measured events can lead to misleading long-term expectations. Dividing the simulation analysis by atmospheric stability also increases the amount of time required to calibrate each model whilst reducing the occurrence frequency of events for which the results are relevant, effectively increasing the cost whilst reducing the general usability of simulation results. However, while CFD remains a research tool, primarily used for investigating worst-case scenarios rather than providing a generalised resource estimate like other methods described in section 4.2, the increased cost of simulating a specific stability event may be financially acceptable if it reduces the perceived risk surrounding worst-case conditions. Therefore, power ratios from the URANS model in Chapter 4 (assuming neutral stability) and its variations earlier this chapter (modelling stability via the gradient method) are now

plotted together below. For reference purposes, the appropriate validation measurements are also shown.

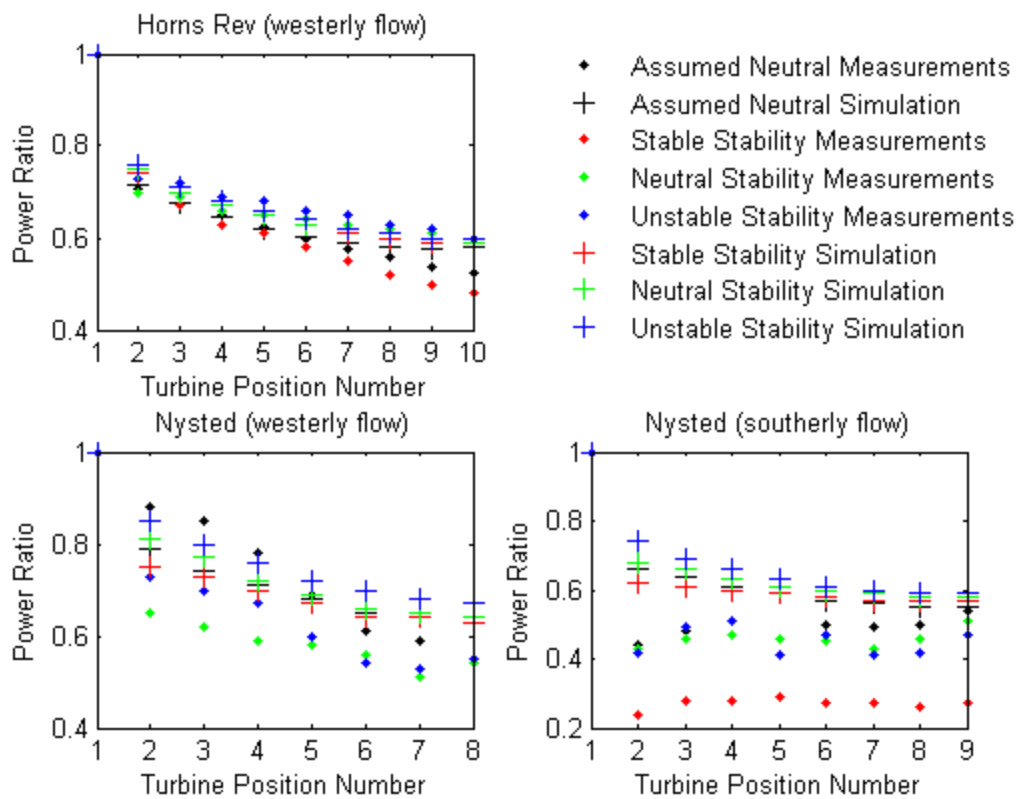


Figure 5.15 Three graphs showing the power ratio results of the URANS model from Chapter 4 alongside the stability simulations from earlier in this chapter utilising the gradient approach. The relevant validation data for each simulation are also plotted for reference. Anticlockwise from top: westerly flow at the Horns Rev offshore wind farm, westerly flow at the Nysted offshore wind farm, southerly flow at the Nysted offshore wind farm.

The differences between the results from each at individual AD positions shown above are often small. Therefore, the table below displays the overall error levels of each model, defined as the average difference between measured and simulated power ratio and displayed as a percentage of the relevant power generation from the free-stream turbine. The average overall error across the stability categories simulated using the gradient method has also been included, suggesting that the simulations which include atmospheric stability are less accurate than the basic URANS model from Chapter 4, although they are being compared against different subsets of validation data. For clarity on where the most significant of these simulation errors occur within the lines of turbines, Figure 5.6 plots the differences between measured and simulated values at each individual turbine position.

Table 5.5 Comparison of simulation accuracy defined as: the average of each turbine position's measured power ratio minus its simulated power ratio. Thus a positive value means the simulation over predicted the farm's output whilst a negative value shows an over prediction of wake losses.

	Results from using the gradient method in Chapter 4				Chapter 3
	Neutral Stability	Stable Stability	Unstable Stability	Average	URANS
HR270	-0.40%	-5.54%	0.97%	-1.65%	-1.37%
N278	-11.04%		-10.69%	-10.87%	1.38%
N180	-14.13%	-28.20%	-16.80%	-19.71%	-9.16%

Table 5.5 shows for each direction for the Nysted farm, the most accurate simulations are those from Chapter 4 which assume neutral stability rather than attempt to model it. The Horns Rev results by comparison show that incorporating atmospheric stability into the simulations via the gradient method increase accuracy for the neutral and unstable events. However, the lower simulation accuracy when modelling the stable event category is sufficient for the more basic simulations from Chapter 4 to be more accurate on average. The superior accuracy of the models which do not include stability may be in part down to the distribution of stability events at each wind farm. For example, [66] shows that stable events occur roughly a quarter of the time for westerly winds at the Horns Rev farm whilst the average error value for the farm in Table 5.5 assumes their frequency is a third. If the average error value is recalculated with the percentage bias reported by [66], the resulting average error for simulations including atmospheric stability reduces to only -1.05%, which is smaller than the basic URANS error from Chapter 4. The same technique does not, however, help improve the results from the Nysted farm simulations. Calculating the weighted average for southerly flow at the Nysted farm, using stability distribution data from Figure 5.2 results in an average simulation error of -16.79%, which although smaller than the unweighted average, is still larger than the error from the basic URANS model. The lack of suitable validation data for westerly stable conditions at the Nysted wind farm prevent the calculation of a similar weighted average; although the relatively large errors from Neutral and Unstable simulations in comparison to those from the Chapter 4 simulation, suggest it is unlikely that the inclusion of atmospheric stability via the gradient method has led to a more accurate modelling solution.

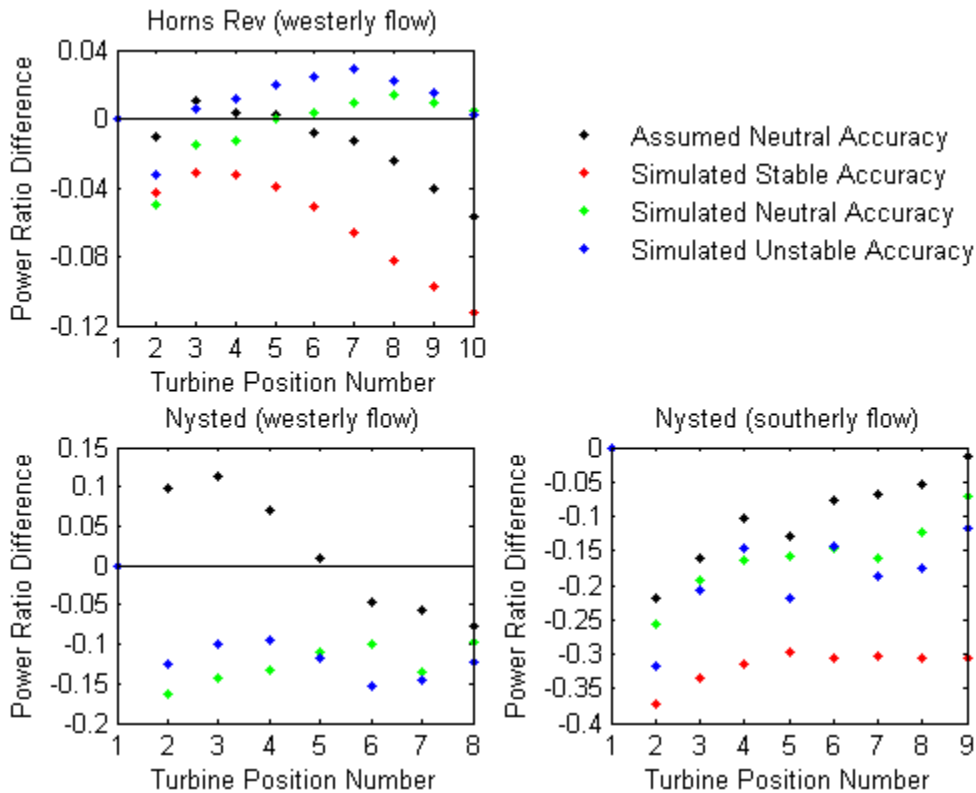


Figure 5.16 To increase clarity, these three graphs show the difference in power ratios between simulated events and their corresponding validation data where positive values indicate the simulation predicted greater than measured wake losses while negative values indicate where the simulation under-predicted the wake losses. Anticlockwise from top: westerly flow at the Horns Rev offshore wind farm, westerly flow at the Nysted offshore wind farm, southerly flow at the Nysted offshore wind farm.

It is unclear according to Figure 5.16, whether a turbine's position within a row is related to the level of accuracy to which its power production can be simulated. It can be hypothesised that each turbine should be harder to simulate than the machine immediately upstream, simply on account of the existence of an additional wake interacting with previous wakes and background conditions. This idea is supported by the results for the Horns Rev farm where the Stable stability simulation results (red) and those from the basic URANS model (black), both show deterioration in accuracy with depth into the farm. The results relating to southerly flow at the Nysted farm contrast with this however, as the basic URANS model generally increases in accuracy with depth into the farm while the simulation of Stable conditions shows initial improvement with depth but plateaus out half way through the farm. By comparing the general patterns in data points between Figure 5.15 and Figure 5.16, it is clear that this improvement with depth within the Nysted farm is a direct result of each simulation significantly under-predicting the initial wake losses at turbine position two. As each model reports greater wake losses with depth through the farm while measured values remain steady, the overall effect is that of improved accuracy

with depth. Across all three scenarios, there is generally a much smaller difference between the accuracy of results from Neutral and Unstable simulations and between the Stable simulations and any of the others. This is hypothesised to be caused by the lower variation in wind shear for negative values of L compared to Stable atmospheric conditions, especially as the AD theory relies on non-sheared flow across the disc to calculate the expected generated power. It follows that the accuracy of the simulations assuming neutral conditions from Chapter 4 are similar to those of Neutral and Unstable conditions, as the average atmospheric conditions at the two farms are rarely Stable. The difference in power generation at the Horns Rev farm under Stable compared to both Neutral and Unstable conditions is large enough to have a significant impact on accuracy of the basic URANS model from Chapter 4. Similarly, for simulations of westerly flow at the Nysted farm where Figure 5.2 shows Stable events are rare, the basic URANS model overestimates the wake losses in the front half of the farm. This suggests the fixed stability conditions used by the basic URANS model are ‘Neutral’ in the sense that ‘Neutral’ is the long-term average stability condition in a scale of $1/L$. Therefore, the basic URANS model may be sufficient for resource analysis at locations where the local stability is suitably distributed, but if the location being modelled has a significantly different long-term stability distribution, the basic URANS model will appear more erroneous and the inclusion of stability within the model more favourable.

5.4 Modelling Atmospheric Stability Without Using L

In section 5.3, atmospheric stability was simulated using three different techniques, each relying on the single parameter L to define the state of the atmosphere. However, studies such as [26] show the value of L measured at offshore locations is highly dependent on factors such as measurement height and [52] shows restrictions imposed by the availability of onsite temperature data greatly affect the value of L for each event. Its usefulness for describing average wind shear and turbulence is also dependent on large amounts of data filtering and averaging over time. Therefore this section shall investigate ways of modelling the symptoms of different atmospheric stability conditions without relying on the Obukhov Length, and is based on the findings of Chapter 3. This freedom to model variations in atmospheric stability without using MOST also has a greater value to a wider range of heights. Whereas

[19] indicates MOST combined with SL scaling is only valid for the lowest 80m, and lower in more stable events, modelling stability based on measured values of shear and turbulence can be scaled to any height where measurements are available. Only preliminary results from simulations using RANS $k-\varepsilon$ models are available for comparison with field data at this time. Although the use of the URANS model, including the Coriolis force and thermal gradient effects may be investigated in future work, the RANS model with $k-\varepsilon$ turbulence closure requires less calibration and is therefore more appropriate for initial trials.

5.4.1 Validation Data

Unlike the previous stability simulations involving calculations of L , validation datasets from wind farms in this section do not require the inclusion of thermal parameters. This means offshore farms which measure the wind resource with Doppler LiDAR, such as Robin Rigg, are suitable as model validation datasets, thus increasing and diversifying the case studies available whilst moving the industry away from dependence on the two classic Danish farms. However, as the data from the Horns Rev farm was externally processed and made available as part of an alternative project, it does not include the required information for this study.

Following the work in Chapter 3, the simulations incorporating atmospheric stability in this section do so by varying the inlet flow conditions of mechanical processes only. Variations in wind profile are described by the shear factor:

$$\alpha = \frac{\ln(u_{z_1}/u_{z_2})}{\ln(z_1/z_2)} \quad 5.3$$

The steady state nature of a RANS simulation requires an approximation to the definition of TI , shown below on the left side is the meteorological definition, whilst the definition used by CFD codes is on the right:

$$\frac{\sigma_u}{\bar{u}} = TI = \frac{\sqrt{\left(\frac{2}{3}k\right)}}{\bar{u}} \quad 5.4$$

Where σ_u and \bar{u} are respectively the standard deviation and mean of the wind speed during a set period of data collection. Suitable values of both α and TI for three typical atmospheric events are shown in the table below:

Table 5.6 Values of meteorological parameters defining the three stability categories (without using L to define atmospheric conditions) and the range of values in measured field data they represent.

Atmospheric Stability Category	Simulation TI Value	Simulation α Value	Field Data TI Range	Field Data α Range
Stable	5%	0.2	$4\% < TI < 5.5\%$	$0.125 < \alpha < 0.275$
Neutral	6%	0.1	$5.5\% < TI < 6.5\%$	$0.075 < \alpha < 0.125$
Unstable	7%	0.05	$6.5\% < TI < 9\%$	$0.025 < \alpha < 0.075$

Where validation data have been collected from a met mast in the free-stream flow, (the Nysted wind farm), TI is calculated using wind speed measurements taken from hub height as this corresponds to the top of the mast. Likewise for α , z_1 is the hub height whilst z_2 is a suitable significant height, the height closest to the bottom of the rotor. At Nysted these wind measurement heights are 68.8m and 25m respectively and all meteorological measurements shall be sourced from meteorological mast M1 as it is suitably close to the farm whilst remaining in a free-stream environment for both wind directions investigated.

Where validation data have been collected from LiDAR measurements, (the Robin Rigg wind farm), atmospheric measurements directly at hub height (80m) were not available. However, measurements were available corresponding to heights of 58m and 102m. Using these heights for calculations of α , will evaluate the wind shear across the central half of the turbine rotor, and are comparable to more traditional point measurements on meteorological masts at the hub height. Values of TI are calculated at hub height via linear interpolation between measurements taken at 58m and 102m. Wind direction measurements are also linearly interpreted between 58m and 102m as the case study direction of 204° will not cause errors across the $360^\circ/0^\circ$ numerical discontinuation. Whilst in Chapter 3, events from the Robin Rigg wind farm were simulated for two wind directions using only data from the turbines, the farm LiDAR is located to the southeast of the farm, within the turbulent wake of multiple up-stream turbines for events with wind direction 249° . In addition, it is noted that as the location of the LiDAR is beside, rather than in front of the farm for the 204° flow direction, it may not be sufficiently separated from the farm to be considered as a source of free-stream measurements, especially when large directional bin sizes and

horizontal wake expansion are considered. However, owing to the farm’s location in the Solway Firth, there are no alternative directions where the LiDAR can safely be assumed to be measuring free-stream marine conditions. Thus it is assumed the LiDAR is outside the wake region for events with wind directions in the sector $204\pm5^\circ$ in order that simulations of the farm may provide a comparative scenario alongside simulations of the Nysted wind farm in this experiment.

A summary of case studies simulating atmospheric stability without reference to L is shown below in Table 5.7. Similar to the events used for validation in section 5.3, the events used for the validation processes in this section incorporate a directional bin size of 10° to help ensure significant sample sizes.

Table 5.7 List of nine case studies for comparison

Wind Farm	Wind Direction	Stability Condition	Case Name	Colour
Robin Rigg	$204\pm5^\circ$	Stable	RR204S	Red
Robin Rigg	$204\pm5^\circ$	Neutral	RR204N	Green
Robin Rigg	$204\pm5^\circ$	Unstable	RR204U	Blue
Nysted	$278\pm5^\circ$	Stable	N278S	Red
Nysted	$278\pm5^\circ$	Neutral	N278N	Green
Nysted	$278\pm5^\circ$	Unstable	N278U	Blue
Nysted	$180\pm5^\circ$	Stable	N180S	Red
Nysted	$180\pm5^\circ$	Neutral	N180N	Green
Nysted	$180\pm5^\circ$	Unstable	N180U	Blue

5.4.2 Simulating Stability by Varying Only the Wind Shear

The data analysis in Chapter 3 indicates a complex relationship between wind shear and L . However, using the three atmospheric stability categories described in Table 5.6, the effects of wind shear on wind farm power yield are shown below, where Unstable events exhibit least wind shear across the turbine rotor, while Stable events exhibit the most. Since Windmodeller utilises the AD method described in section 4.3.1, varying the shear whilst maintaining the hub height velocity will not alter an individual simulated turbine’s power output, although it should change the wake dissipation rate downstream, thus effecting output from subsequent turbines. Figure 5.17 below shows measured productivity for each of the nine case studies when describing atmospheric stability by wind shear alone, averaged by turbine row position within the farm and neglecting turbines at the sides of the farms:

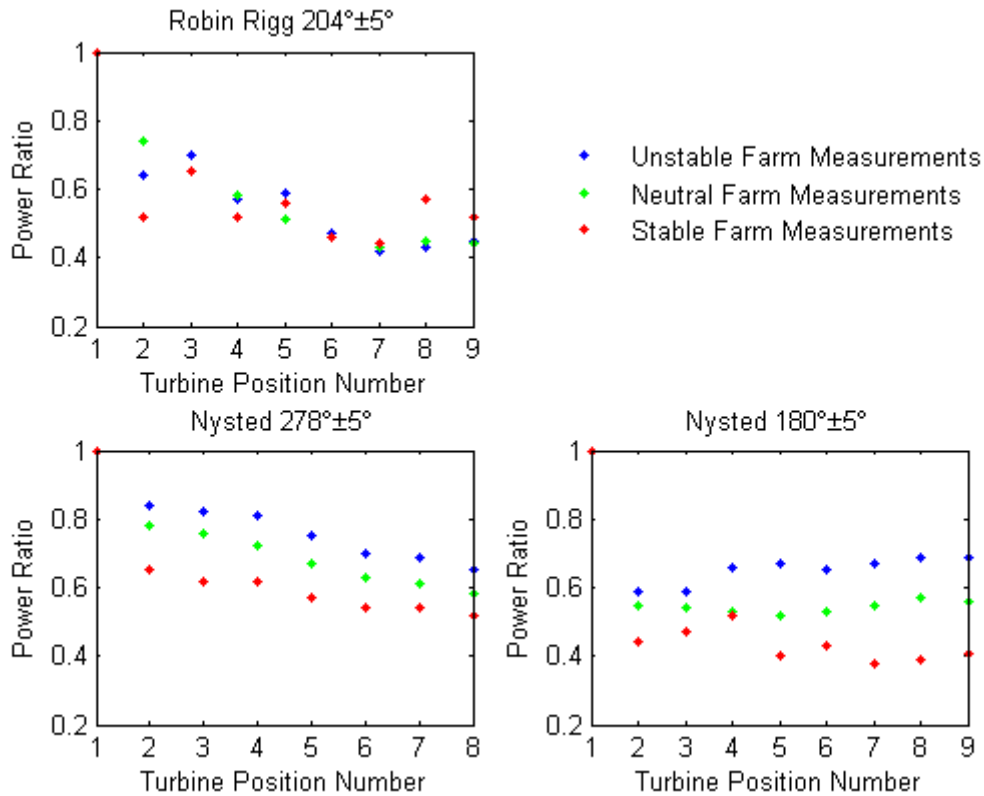


Figure 5.17 Normalised power production at the Robin Rigg and Nysted Wind farms, filtered by free-stream wind shear as indicated by atmospheric stability category: Stable (red, $\alpha = 0.2$), Neutral (green, $\alpha = 0.1$) and Unstable (blue, $\alpha = 0.05$).

Both the graphs showing production at the Nysted farm in Figure 5.17 show a clear relation between atmospheric stability (defined by wind shear) and farm yield. Unstable events, with low wind shear values, display higher farm productivity than either Neutral (medium shear) or Stable (high shear) events, despite all events experiencing a free-stream inflow at hub height of 8 ± 0.5 m/s. It is hypothesized that events with low shear are the result of high levels of ambient turbulence, resulting in increased wake dissipation rates while events with higher shear have less ambient vertical air movement and result in lower rates of wake dissipation. The higher rates of wake dissipation behind each turbine allow higher flow speeds to occur at subsequent turbines downstream.

The difference in wind direction between the two Nysted graphs results in significantly different farm generation efficiencies. This is directly linked to the difference in turbine spacing, $10.5D$ vs. $5.8D$ for the westerly and southerly directions respectively. There is more time for wake recovery processes between turbines with westerly flow, hence their higher values of Power Ratio. There is some evidence for

deep array effects for westerly flow as each turbine generates less power than the turbine immediately upstream of it. However, there is no such evidence with southerly flow events. This is possibly a function of the turbines' complex thrust curve at low speeds (see Figure 4.4), which despite complicating the Turbine Position Number to Power Ratio relation, does not hide the inverse relation between shear and power generation across the farm.

The inconsistency in clarity between the Nysted results and those from Robin Rigg is likely to be caused by the less-regular shape of the Robin Rigg farm, and subsequent complexities with defining turbine position numbers. This is exaggerated by a relative lack of events at Robin Rigg with both suitable wind conditions and operating turbines. Although not as significant as for the Robin Rigg farm, there are also fewer events than desired for southerly flow at the Nysted farm. Westerly flow events however, are plentiful at the Nysted farm, for all three stability categories, which has resulted in a smooth distribution of data points, emphasising the need for field data sets which span long time frames of many years.

Therefore, inspired by the work by [101], simulations were run with inlet wind profiles defined as separate logarithmic regions above and below the heights swept through by turbine rotors, with the required vertical wind shear connecting the two, maintaining the required 8ms^{-1} velocity at hub height. However, although it is possible with CFD models to define specific wind profiles at the domain's inlet boundary, RANS simulations of high Reynolds Number flows are subject to the log-law. This corresponds to equation 2.5 in real-world atmospheric flow. Therefore, between the inlet boundary and the simulated farm's location, the turbulence characteristics within the flow acted to return the flow profile towards its logarithmic default profile described by equation 2.5, resulting in α values around 0.08. Whilst it may be possible to define an inlet profile such that some of the required wind shear is achieved as the flow reaches the simulated met mast (or LiDAR), such profiles are unrealistic and therefore not suitable for simulation purposes. If CFD simulations are to match variable wind shear conditions, the vertical profile of turbulence is required to be changed such that it does not act to deteriorate said specified wind profile. Preliminary experiments exploring how to achieve this were unsuccessful. Experiments with variations in the k and ε definitions (equations 4.19 and 4.20) to

make them variable with height as well as variations in default values of viscosity and constants $C_{1\varepsilon}$ and $C_{2\varepsilon}$ (which control the production and destruction of k and ε) have had little effect on the value of α by the time the flow reaches the simulated farm. It is hypothesised that the inability to vary α is a function of using RANS models to simulate atmospheric flow as the alternative definition of k is:

$$k = \frac{1}{2}(\overline{u'^2} + \overline{v'^2} + \overline{w'^2}) \quad 5.5$$

In this definition, it is assumed that a third of k is allocated to each of the normal stress components to ensure their sum has the physically correct value for Boussinesq's proposal that the Reynolds stresses are proportional to the mean rate of flow deformation in an isothermal incompressible flow. Indeed, the RANS method of conducting simulations of flow fields is entirely focused on the mean flow, only considering turbulence by its effects on the mean flow properties. As such, RANS is deemed an insufficient technique for simulating atmospheric stability via variations in wind shear alone. It may be that URANS provides a suitable alternative, as variations in its customisable thermal profile as investigated in section 5.3, resulted in small perturbations in the respective wind speed profiles through changes in flow viscosity. Using a more expensive simulation method, such as LES, would allow for greater control over flow turbulence, such as biasing turbulence to favour horizontal flow perturbation and thus reducing vertical mixing and prolonging the non-logarithmic inlet conditions. Such investigations have not been attempted in this study.

5.4.3 Simulating Stability by Varying Only the TI

The case studies in Chapter 3 indicate a complex relationship between TI and atmospheric stability. According to the literature, there is a clear correlation between ambient TI and farm efficiency [96] as higher ambient turbulence acts to mix each turbine wake with the surrounding flow, reducing its significance on turbines downstream. This is not clear from the results below in Figure 5.18 which reveals its effects on wake losses as measured at the Robin Rigg and Nysted wind farms.

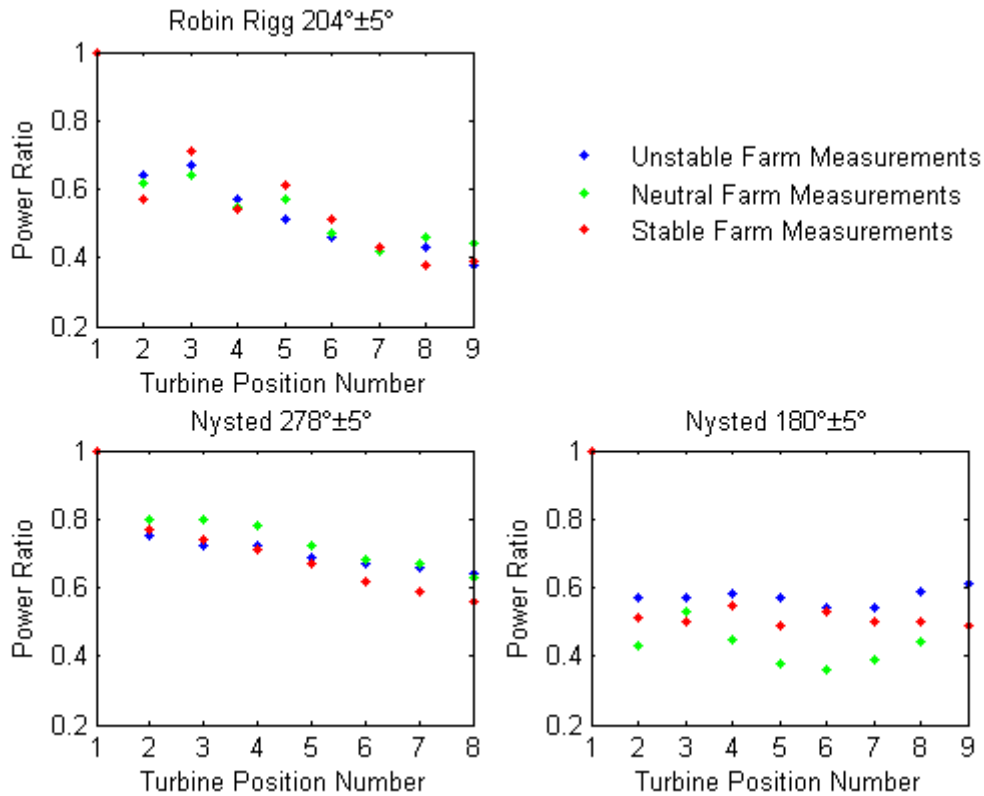


Figure 5.18 Normalised power production at the Robin Rigg and Nysted Wind farms, averaged by free-stream turbulence intensity as indicated by atmospheric stability categories: Stable (red, $TI = 5\%$), Neutral (green, $TI = 6\%$) and Unstable (blue, $TI = 7\%$).

The graph showing Robin Rigg data is complicated by the turbine layout, and most of the available data events correspond to the rows of turbines far from the location of the LiDAR. There is some indication of varying TI levels effecting initial wake dissipation rates after the first turbine, but the differences may not be statistically significant and do not appear to continue as expected beyond the second turbine. Although these results do not support findings in the literature, there is a general consensus of deep-array effects across all three stability scenarios.

The major differences between the graphs for westerly and southerly flow at the Nysted farm are caused by the difference in turbine separation. As the turbines are separated by nearly twice the distance for westerly flow, it is unsurprising that there are greater wake losses associated with the southerly direction. As each turbine in Unstable flow for the southerly direction reports higher Power Ratio than either the Neutral or Stable events, whilst only reporting average values for the westerly flow, we can hypothesise the strength of ambient TI is most significant in the near wake region – before much of the wake has dissipated into and increased the surrounding

turbulence. However, the levels of ambient TI for the wider spaced turbines in the westerly flow may act to control the levels of deep-array effect, in that the Unstable data points track the Stable data points until turbine position 5 before tracking the Neutral data points deeper within the farm and registering the highest power ratio (although not statistically different to the Neutral value) by the 8th turbine. This could be the reason for other studies claiming wind farms are more efficient in environments with higher turbulence [96]; although Figure 5.18 suggests high TI may only be a significant factor in farm efficiency for offshore wind farms constructed with large numbers of turbines located far apart (to combat deep array effects) or close together (to reduce losses in the near wake).

Windmodeller is capable of manipulating the inlet boundary conditions to specify a specific TI flow value whilst maintaining the standard mean flow logarithmic profile. This is done by imparting a step-change in z_0 at the domain boundary similar to flow across a coastal boundary, so that within the domain z_0 , is representative of offshore conditions, whilst the flow retains the properties of the upstream flow regime. Whilst this means an internal boundary layer will develop through the simulation as described in section 2.3.2, the domain's value of z_0 is small enough that it develops very slowly and is unlikely to be significant at the farm's location. However, the flow above the developing boundary layer, having been defined with a separate z_0 value, has a slightly different logarithmic profile than normal offshore Windmodeller simulations. Whilst this results in different shear values and thus may indirectly affect the simulated wake losses, hub height wind speed is still 8ms^{-1} and considering there is insufficient raw data to authoritatively define a 'correct' offshore profile, this is acceptable. It is also worth considering that both farms are near the coast in certain directions and so a small step change in z_0 at the domain boundary is fairly representative of reality. The results of the nine simulated scenarios using values of TI as defined by Table 5.6 are shown below in Figure 5.19:

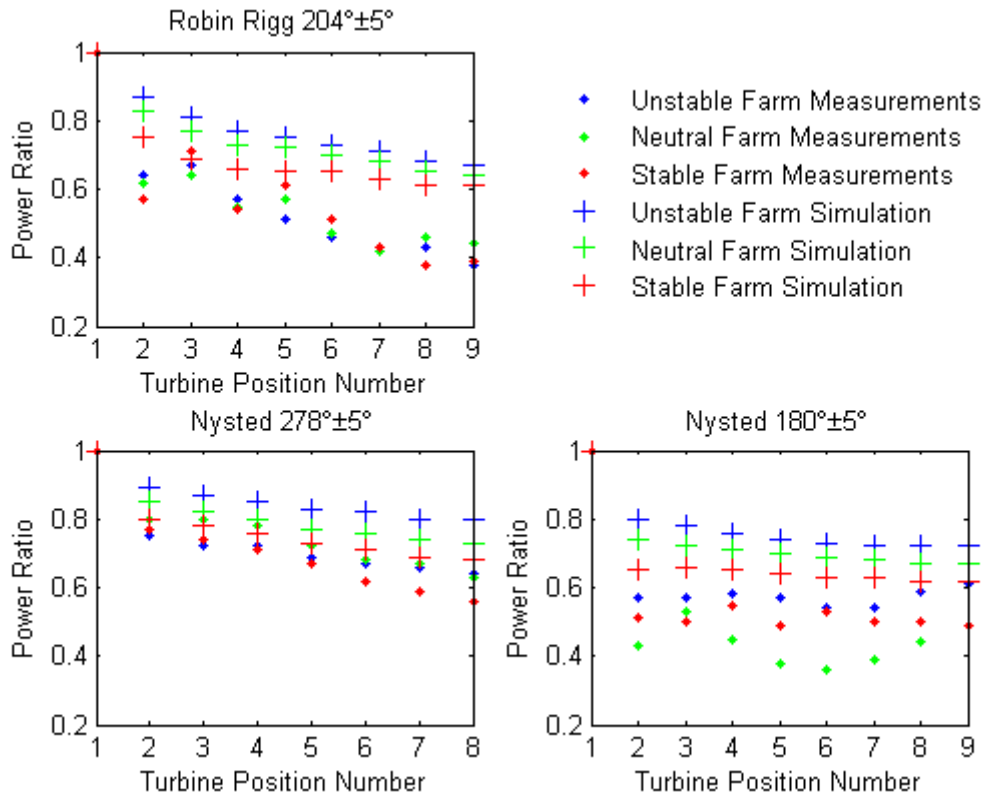


Figure 5.19 Normalised power production at the Robin Rigg and Nysted Wind farms, averaged by free-stream turbulence intensity as indicated by atmospheric stability categories: Stable (red, $TI = 5\%$), Neutral (green, $TI = 6\%$) and Unstable (blue, $TI = 7\%$). Results from $k - \epsilon$ simulations are shown as plus (+) symbols whilst real-world measurements are shown as dots.

Without defining the upstream TI , a RANS $k - \epsilon$ Windmodeller offshore simulation with hub height speed of 8ms^{-1} results in an ambient TI values of 4.5% , which is less than that used for stable conditions. Therefore, whilst Figure 5.19 shows a clear correlation between ambient TI and Power Ratio, each of the above results predicts higher levels of electrical generation than Windmodeller's default setting. It is perhaps unsurprising (based on results from simulations in Chapter 4) therefore that every one of the nine scenarios investigated in this section over predicts the electricity production, although this is primarily a result of Windmodeller failing to fully capture the initial wake loss behind the free-stream turbine.

After the second wind turbine at Nysted, there is little additional wake loss between subsequent turbines, and there is little to differentiate either between ambient atmospheric stability or wind direction. Therefore, based on this evidence, the spacing of turbines is of less consequence to an AD in a RANS simulation than to a real wind turbine in atmospheric flow. Results from the Robin Rigg simulations offer contrasting evidence, however, despite showing a simulated absolute difference in

Power Ratio at the second turbine of 0.12, whereas the difference between stability simulations at position nine is halved at 0.06. This suggests TI effects the wake behind an AD similarly to wake behind real turbines, although the underestimation of the initial wake loss, indicates that whilst the AD technique can cope and adjust to ambient turbulence, the technique may lack accuracy in the generation of turbulence behind the first turbine, supporting the findings of [160].

5.4.4 Combining Shear and TI Changes

Analysis in Chapter 3 shows atmospheric stability is best described by a combination of shear and TI . Therefore it is desirable for CFD simulations to investigate the effects of stability by replicating both α and TI values at the same time. However, as it was previously described that Windmodeller seems currently incapable of maintaining an altered parameter α over required distances, it is not currently possible to simulate events with specified shear and turbulence in a RANS $k-\varepsilon$ environment.

The modelling of wind shear is not the only barrier to modelling wind farm productivity in varying stability conditions. There is also very little data with which to validate models against. For example, after searching 2.5 years of measurements from the Robin Rigg farm, there were no events with operational turbines corresponding to LiDAR measurements with the wind parameters α and TI matching those described in Table 5.6 along with the desired speed and direction. However, with just 1.5 years of measurements from the Nysted farm, there were some events suitable for model validation. The majority of qualifying events for both southerly and westerly flow measured at Nysted meteorological mast 1 were Stable with just two Neutral events for each wind direction and only one Unstable event for southerly flow. These events, whilst plotted below in Figure 5.20, should be treated with caution as their small sample size could bias findings and might be considered statistical outliers in a larger dataset.

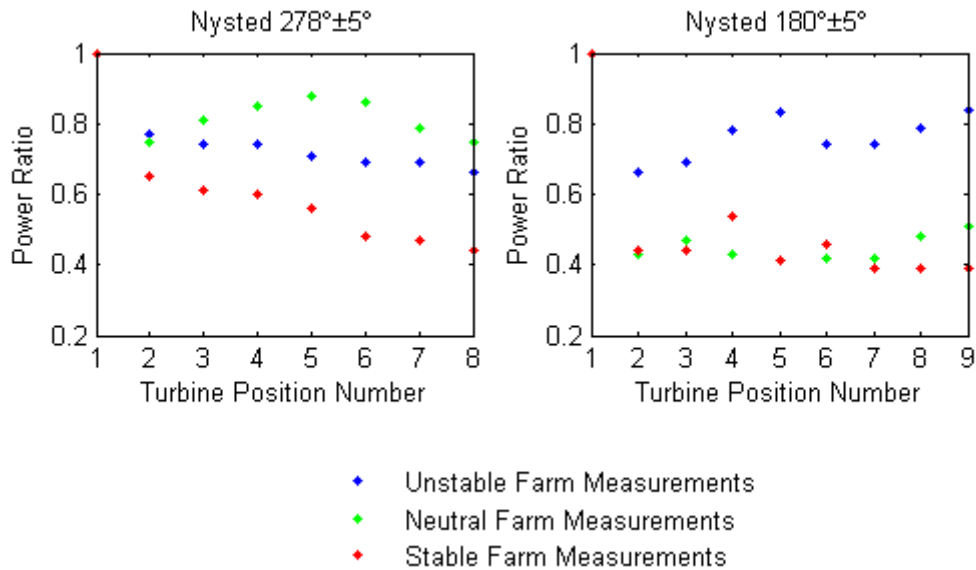


Figure 5.20 Measurements of Power Ratio from the Nysted offshore wind farm where events are filtered by both α and TI to generate the three stability categories according to Table 5.6.

As previously shown in section 5.4.2, there is a significant difference in farm wake losses between Stable and Unstable events for westerly flow at Nysted. The plot of Neutral events is significantly different to both the other stability classes and the neutral events in Figure 5.17, with rapidly diminishing wake losses within the front of the farm. After closer inspection of this case study, it was found that this rapid recovery is a combined result of a very small data sample (two events), wide directional bins and distance from point of measurement. Whilst the parameters recorded at the met mast were within experimental limits, the SCADA data recorded by the free-stream turbine in each case shows a wind direction of 272° . Although only one degree beyond the bin limit, this shows how meteorological parameters vary perpendicularly to the mean flow (also shown by [95], [154]) and indicates how perception of farm wake loss patterns can be altered by choice of limits to directional bin size. Similar events may occur within the other case study datasets, although they are less significant in larger sample sizes.

Analysis of these small dataset sample sizes adds little to our knowledge of farm efficiency under varying stability conditions. Although results from Chapter 3 suggests both α and TI are important factors in describing offshore flow conditions, it is impractical to filter field datasets to such a degree while also requiring large wind farms to be fully operational. The earlier results of various URANS model options in Figure 4.11 also suggest that factors above the ABL, such as a thermal capping

layer, may prove important for limiting wake dissipation and should be the subject of further investigation. Especially as smaller values of Z_{ABL} are often linked to Stable conditions, when wind shear is greatest. Figure 5.17 shows there is little to be gained from the resulting small samples, whilst the two filtered datasets of reasonable size show similar findings to Figure 5.17 which did not consider TI .

If a wind blows, ride it.

- **Arabic Proverb**

Chapter 6. Summary and Conclusion

6.1 Summary of Chapters 2 and 3

For over a hundred years, people have been studying fluid flow near boundaries. Theoretical physicists and engineers refer to it as the 'law of the wall' while in the real world, meteorologists call it 'boundary-layer meteorology'. Whatever its name, understanding of the SL is key for wind farm resource analysis. With ever growing turbine sizes and new farms located further from shore, how this region interacts with the lesser studied conditions directly above it, is also a rapidly growing field of study. However, it is generally assumed in CFD simulations (for historical and simplicity reasons) that the turbines reside well within the SL and in the absence of measurements, the wind profile can be approximated by equation 2.5. More detailed models require knowledge of the local balance between buoyancy and mechanical forcings, referred to as Monin-Obukhov Similarity Theory (MOST). Although since there is no standardised method of calculating L or even an agreement as to which parameters are required for doing so, any hypothetical wind profile generated via equation 2.9 is subject to a number of simplifying assumptions. Filtering a measurement dataset to accommodate these assumptions, for the purposes of validating such a profile, often removes 80-90% of the original data. Thus it is reasonable to claim MOST does not describe the average offshore atmospheric conditions, rather, a simplified approximation based on idealised small scale fluid flow and field experiments at homogeneous onshore sites, such as south-western Kansas [18]. However, since it has long been established amongst meteorologists, the wind industry has adopted the theory and attempted to extend it to describe conditions at ever increasing heights above its strict limit of applicability.

Seemingly unwilling to move on from describing wind conditions in terms of L , the wind industry now uses three main methods to calculate it. However, all require direct measurements of the wind speed at at least one height. Met masts are usually installed to provide these (and other) measurements on site, although having gone to the great expense of installing the mast, it appears financial concerns often limit the number of (comparatively inexpensive) instruments connected. While developers

often favour the Bulk Richardson method, thus making financial savings with fewer measurements on a shorter mast, academic researchers favour the Gradient Richardson method as a more complete description of the atmospheric conditions. Either way, the required wind profile is often interpolated between sparse measurement heights or extrapolated above the mast without information about features such as developing boundary layers in coastal waters or low level jets. With the high cost of installing masts far from shore, poor utilisation of their data collection opportunities and limited resolution of results, there is greater incentive to exploit newer technology such as LiDAR. Although unable to measure temperature, humidity or pressure remotely, measurements of wind speed and direction from a LiDAR, extending well above normal mast heights, are enough to calculate wind shear, turbulence intensity and the prevailing wind directions. Combined, these variables should be enough to calculate the available free-stream power potential and design a farm layout with minimum interaction between individual turbines and wakes from upstream machines for multiple wind directions. However, measurements of stability through buoyancy may be required to predict complex wake expansion patterns, and increased meteorological instrumentation from within large wind farms is always desirable for greater understanding of wake interaction.

6.2 Summary of Chapter 4

There is currently a wide range of models available to assess the productivity (and thus value) of a future wind farm. Ranging from kinematic simulations with assumptions designed to provide fast estimates of wake losses but struggle with the multiple wake interactions fundamental in large farms, to CFD using LES codes to individually resolve the larger turbulent flow eddies, requiring intensive computational resources. Although unable to cope with integrating non-isotropic ambient turbulence with turbine wakes or instantaneous snapshots of turbulence structure, less complex CFD methods such as RANS provide a higher standard of physical accuracy than eddy viscosity models while able to obtain time-averaged results at the farm scale within a reasonable time-frame. Whilst the growth of wind turbine blade lengths have pushed the AD theory in terms of the location of turbulence creation (the majority of which being at the blade tips rather than uniform across the disk), its low cost makes

it still the best way to represent wind turbines in large array simulations outside of the near-wake region.

As offshore farm production data has a high commercial value, limited data were available from only four farms, with the Horns Rev wind farm only supplying pre-processed production averaged statistics from event categories frequently discussed in the literature. By analysing data from the Nysted and Robin Rigg offshore wind farms in a similar fashion, evidence for deep array effects became clear in four out of five case studies, with turbine separation strongly influencing the rate of production loss. With its non-regular turbine array, it was not possible to use data from the Scroby Sands farm to conduct 'down the line' analysis of wake losses. However, using time-averaged production data from individual turbines revealed some venturi effects as turbines located in-between the wakes from two other turbines reported higher than expected free-stream values of electrical generation.

Windmodeller's default SST turbulence model over-predicts both free-stream production and wake losses, especially for the Scroby Sands farm. The difference in results for the turbines towards the front of the Robin Rigg farm is possibly due to the staggered farm layout causing an uneven flow across the free-stream turbines and those in staggered positions, with some effected by venturi effects. Substituting the $k-\varepsilon$ turbulence model instead of the SST default, results in similar over-prediction of generation by free-stream turbines. However, the expected electrical generation from wake affected turbines is higher, which more accurately follows the measured production. The exception is the Robin Rigg farm where simulations significantly over-predict electrical generation at each turbine and fail to match the rate of increased loss with progression through the farm. By modifying the C_μ constant, the Modified $k-\varepsilon$ RANS turbulence model does little to change the absolute accuracy of simulated Power Ratio compared to measurements from the Danish farms, but does change the region where simulation accuracy is greatest. For example, whilst the standard $k-\varepsilon$ RANS turbulence model (using a value of $C_\mu = 0.09$) predicts the later turbines at Horns Rev well, the modified version (using a value of $C_\mu = 0.03$) has greater accuracy over the first half but fails to follow the deep-array effects. The simulation accuracy of westerly flow at the Nysted farm however is the opposite, with

the $k-\varepsilon$ model performing better towards the front of the farm while the Modified $k-\varepsilon$ model gives lower predictions of Power Ratio for each turbine and so achieves greater accuracy deeper in the farm. This decreased Power Ratio result is also true for the Robin Rigg case studies; the Modified $k-\varepsilon$ model predicts greater wake losses between turbines than the conventional $k-\varepsilon$ model, thus achieving better accuracy for the early turbines. Finally, the URANS model, with its inclusion of the Coriolis Effect results in reduced production levels at the free-stream turbines compared to other models. Whilst there may be general improvements in absolute RMS error, it is the location of where these improvements are made that is important. For example, the $k-\varepsilon$ RANS model achieves acceptable accuracy of the Horns Rev farm productivity but does not accurately show the progressively lower production at each turbine down a line, whereas the URANS model systematically matches it (with a small over-prediction at each turbine) up to the seventh turbine. Much better simulation results are achieved for the Robin Rigg farm, where even the measured slight variations in the Power Ratio curve deeper in the array are modelled to some degree.

Considering the results from simulating the two Danish wind farms, the SST model is the least accurate according to RMS errors while the other models produce similar levels of accuracy. However, results from the Robin Rigg simulations alone show the URANS model to be the most accurate, with RMS values half that of the nearest alternative. Since the standard deviation values add little information to separate the model outcomes, it was concluded that the URANS model is worth developing further, with a view to incorporate effects of non-neutral atmospheric stability. The unsteady aspect of the simulation in itself may not increase the accuracy of simulation results; however it does enable the inclusion of the Coriolis parameter which helps reproduce the measured wake asymmetry in large offshore farms [154]. The incorporation of a simulated thermal capping layer in the free atmosphere above the ABL was also shown to have a positive effect on model accuracy, particularly in replicating deep array effects. As many of the free-stream turbines are predicted to generate significantly more power than measured in reality despite consistent hub height wind speeds, the AD method of calculating productivity for large turbines when combined with the complexities of calculating a turbine power curve, may introduce a source of error. However it provides considerable cost savings, is a

constant assumption across the models and the literature has shown it results in acceptable wake patterns beyond the near-wake region. Therefore, whilst the AD method is not likely to cause of significant model error across these experiments, a suitable replacement should be found for future work with turbulence modelling in the near-wake region.

6.3 Summary of Chapter 5

Simulations of wind farm productivity under various atmospheric stability conditions were tested. First, the two Danish wind farms were modelled using the URANS technique using a varying Obukhov Length to describe atmospheric conditions in the surface layer, via three different methods. Validation was conducted against Bulk and Gradient Richardson filtered measurements from the Horns Rev and Nysted farms respectively with data showing both farms are most productive under Unstable stability conditions and least productive under Stable conditions, with deep-array effects visible for westerly flow events at both farms. It was observed that after filtering observed meteorological data appropriately for the homogeneous requirements of MOST, often removing the vast majority of events, the remaining corresponding production dataset is too small to suitably validate computational models that output time-averaged results, such as the URANS model. This is because the filtering process does not account for eddies in the atmospheric flow with lengths which fully pass the met mast within the ten-minute averaging period, yet the same eddies can be responsible for significant variations in the output from individual turbines. The effects of these eddies are hidden when the validation dataset is large enough for long-term averages such as when atmospheric stability is not considered, but when stability is considered the resulting datasets are often too small to suitably validate time-averaged simulation results. Preliminary results were discussed from experiments using the $k-\varepsilon$ RANS model with adjusted boundary conditions which attempted to model various atmospheric conditions assuming neutral buoyancy conditions. The validation data for these models came from the Nysted and Robin Rigg offshore wind farms. Whilst measurements from the Danish farm showed a clear link between wind shear and wake losses, its relation to turbulence intensity was less clear. By comparison, although the analysis from the

British farm was complicated by farm layout, LiDAR location and dataset size, there were indications of deep-array effects.

Results from each of the heat flux simulations suggest a significant wake loss for the second turbine, followed by additional losses for subsequent turbines, each smaller than for the previous turbine. This pattern was not significantly different for changes in farm, wind direction or atmospheric stability. The only difference between results from each case study appeared to be the size of initial wake loss modelled at the second turbine in line, where there was significant variation between farm and flow direction and small variation according to L . The simulations incorporating the effect of sea surface temperature by comparison show clear variations in the level of wake losses between stability case studies. Using a constant sea temperature significantly higher than the atmospheric inflow value to create Unstable conditions results in very little additional production loss after the fourth turbine and some indication that electrical production rates may even start to recover in extreme cases. The differences between Neutral and Stably stratified simulations are more subtle, resulting from the lower difference in sea temperature required to vary L towards more Stable values. Again though, the most significant difference between the three stability category models is the initial wake loss incurred by the second turbine, with southerly flow simulations of the Nysted wind farm significantly underestimating losses in all three case studies. Considering the results from using the Gradient method to simulate stability for the Horns Rev farm, both the Unstable and Neutral events appear to suggest using Ri_G is an accurate technique to simulate atmospheric stability through large wind farms; however, the Stable simulation results for the same farm are not significantly different to the others, despite strong variation in measured generation. Similar results are seen to the Bulk method: values for initial wake loss at the second turbine in each of the Nysted farm Ri_G case studies are underestimated, leading to systematic wake-loss errors along each row of turbines with differences between simulated and measured Power Ratio at each turbine.

Comparisons between individual model Simulation Error for each case study show consistently accurate results for all simulations of Neutral stability whilst Stable and

Unstable events vary significantly between the different methods of simulating atmospheric stability. For westerly flow simulations of the Danish farms, the normalised difference between simulation and measurement is generally less than 10% whilst the southerly flow varies between 10% and 80%. The associated standard deviation of error at individual turbines for each simulation appear closely related to the farm being modelled, in that the Horns Rev wind farm case studies all have significantly lower variability in accuracy than the Nysted wind farm case studies. This could imply a relation between the accuracy of a model and the complexity of a turbine thrust coefficient curve; the similar range of variance within simulations of the Nysted farm irrespective of direction suggest the turbine separation may be of lower importance. However, the measured Power Ratio plot from the Horns Rev farm has for a long time been the primary source of model validation data and the seminal work by which developments to each wake model are assessed to be improvements or not. Thus it is unsurprising that errors and variance are smallest for simulations of this farm as measurements from different farms will deviate from it in multiple ways, with each deviation requiring capture in the model, increasing the complexity of modelling that scenario. Whilst Windmodeller has not been deliberately tuned towards conditions at the Horns Rev site, lack of available offshore data suitable for providing a variety for validation case studies may have had an unintentional effect on model parameters. However, these differences are consistent between simulations, small and probably within the boundaries of experimental error. Alternative hypotheses for failing to capture the southerly flow patterns for the Nysted farm could be proposed, such as the separation between turbines may be too small, such that downstream ADs are each within the complex near-wake region of another AD, where modelled turbulence conditions are known to be less accurate. The values of L may also vary across the domain; but without significant new measurement field campaigns, data from new farms being made available or high cost and large scale LES simulations, these theories are hard to test.

Alternative methods of simulating atmospheric stability by varying the wind shear and levels of ambient turbulence according to work in Chapter 3 were tested using variations on the basic $k-\varepsilon$ RANS model. The ambient TI was controlled via defining

the inflow velocity profile with reference to a theoretical alternative value of z_0 which although providing the TI value, also resulted in a developing boundary layer through the domain similar to those at a coastal location. Simulation results show clear differences in expected electrical generation between stability categories, with Stable events returning higher wake losses at each turbine than Neutral events, which in turn have higher losses than Unstable events. However, while the simulations indicate this basic relationship between TI and wake losses, its interaction between various ambient turbulent conditions and the wakes behind each AD are insufficiently represented by the $k-\varepsilon$ RANS model, leading to significant over-prediction of electrical power generation. Most significantly, there is a large difference between modelled and measured wake losses deep in the Robin Rigg array and the initial wake loss experienced by the second turbine for southerly flow at the Nysted farm. Despite significantly altering the inlet velocity profile as well as turbulence model parameters and constants, the basic $k-\varepsilon$ RANS model was unable to maintain the defined flow shear required at turbine heights to simulate stability conditions through variations in wind shear alone. This means there are no model results to compare against the validation data for either the wind shear method or the combined method, which was unfortunate as the validation data filtered for wind shear at the Nysted farm clearly shows its significance for variations in wake losses across large farms.

Comparing the measured production data from the Danish wind farms used in chapter 5 (with the relevant graphs repeated below in Figure 6.1 for convenience); it can be hypothesised that for events with equivalent hub height wind speeds, the wind shear incident to the free-stream turbine is primarily responsible for the variation in its wake strength and behaviour. It follows that the thermal buoyancy component of atmospheric stability is then primarily responsible for the wake recovery time, since the initial flow shear structure has been compromised by the rotating turbine blades, and thus how significantly the combined wakes of multiple upstream turbines affect the turbines located further into the farm, the deep-array effect. This combination of effects from variations in both wind and thermal shear is why academic researchers favour the Gradient Richardson method of calculating L and leads to the recommendation that met masts should measure conditions well above the turbine hub height, preferably above the rotor top. Then simulations will

have suitable boundary conditions for initiation and would be able to replicate a deeper layer of the SL with appropriate thermal buoyancy. As it is, with measurements extending only to the turbine hub height, any simulation incorporating the Gradient method of calculating L either has to estimate buoyancy conditions for the remainder of the ABL above this level or assume neutral conditions as in this work. Since in more stable conditions where the buoyancy limits the vertical wake expansion and dissipation, deep-array effects become more significant, if L remains the basis of assessing atmospheric stability, the accuracy of future simulations may become dependent on the heights to which meteorological datasets extend.

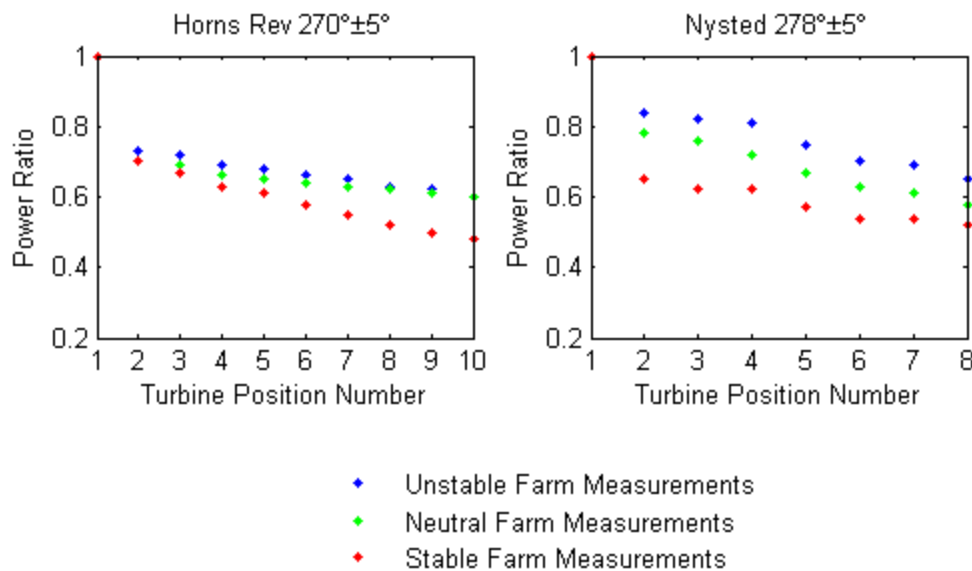


Figure 6.1 Comparison between stability classification techniques. The left graph shows measured Power Ratio for westerly flow at the Horns Rev wind farm with events filtered by L as described in section 5.3.2. The right graph shows measured Power Ratio for westerly flow at the Nysted wind farm with events filtered by both α and TI as described in section 5.4.2.

6.4 Conclusion

To simulate any flow accurately, of primary concern is to reproduce the effects of the flow boundary on the rest of the flow-field. In atmospheric simulations, this flow boundary is the planetary surface and whether land or sea, it exerts a retarding effect on the ABL. Even ignoring the effects of weather systems, planetary shape and rotation, creating an accurate model of how the wind in the lower atmosphere reduces to zero in proximity to the earth is a complex problem, made harder by the infrequency of measureable real world events which match particular conditions suitable for model validation such as hub height wind speed. This has historically

lead to atmospheric models being developed from scale experiments in laboratories relying on suitable approximations and assumptions before adjustments are made based on data from more expensive field experiments. As a result, many of the older descriptions of atmospheric conditions in the boundary layer are based on the assumption of neutral stability, i.e. that within the flow field, mechanically induced features are always more significant than those of a thermal buoyancy nature. It follows, therefore, that CFD models are now quite accurate at predicting wake losses experienced by large farms under the following conditions: the turbines are regularly spaced in rows, turbine output is averaged across turbines in similar row positions excluding those at the farm edge, the model assumes neutral stability conditions whilst site measurements are not filtered for stability and turbines are located beyond the region of near wake conditions created by upstream machines. Out of the four turbulence models compared under the assumption of neutral conditions, the three variants on the traditional $k-\varepsilon$ turbulence model produced results of very similar accuracy levels, whilst the SST alternative model was significantly less accurate when modelling the Danish farms and four times less accurate in terms of the RMS error of Power Ratio than the most successful at simulating the Robin Rigg farm. This is believed to be a direct result of the assumptions made by each of the models as the process of Reynolds averaging the Navier-Stokes equations relies on the fluid being non-compressible and thus by continuity, the flow must be neutrally stratified and conforms to the standard velocity profile. The URANS model by comparison, whilst built on the RANS principles (and thus assumes flow incompressibility required for theories such as AD and Rossby-Montgomery), contains additional equations to represent the compressible nature of a non-isothermal flow but still generates only neutral stability wind profiles.

Experiments using the URANS model to simulate non-neutral atmospheric flow through the Danish farms by varying the flow's thermal properties near the domain bottom to match required values of L resulted in small changes to the velocity profile. During the model calibration process, it was found that by maintaining a hub height speed of 8ms^{-1} and increasing the flow temperature below hub height, the SL wind profile became less sheared through the rotor heights whilst decreasing the inlet flow temperature below hub height increased vertical wind shear. This increased the time requirements for simulating each complete case study as a greater number of

calibration runs were required to obtain suitable boundary conditions. For the more extreme case studies, it also required modelled flow and boundary conditions unlikely to occur in reality, which combined with the scarcity of suitable offshore measurements of temperature at a suitable range of heights, introduces more flow assumptions into the model which are difficult to validate and justify. Furthermore, since the hub height velocity was a fixed requirement with no control over the rest of the flow profile, each simulation required thermal values inconsistent with those measured at the farms in order to maintain the correct ratio of influence between buoyancy and mechanical processes defined by L . As each method of calculating L required a different relationship, the levels of flow shear varied from simulation to simulation, despite identical values of L . Since there were no changes in the definition of TI at the domain inlet, it is assumed the variations in initial wake loss at the second turbine in each row are a result of variations in flow shear as it interacts with the free-stream AD and the resulting region of lower velocity behind it. Thus the flow shear affects the overall Simulation Error despite each free-stream AD using consistent single point wind speed measurements (each 8ms^{-1}) to calculate the momentum sink created by the first turbine in each row.

The idea that wind shear is the most important flow consideration (after hub height speed and direction) for modelling wake losses towards the front of large offshore farms was emphasised by the preliminary work into modelling atmospheric stability without reference to L , primarily by the validation data from the Nysted farm. The significant difference in wake losses between cases with different incidental wind shear was much greater than between events with different incidental levels of TI or L , although both TI and L appear to influence the deep-array effect to a greater extent, significantly for Stable events. Therefore, since preliminary attempts to alter the flow shear in a $k-\varepsilon$ RANS model were unsuccessful, it is suggested research is undertaken to further explore the thermal variability and geostrophic drag law in the URANS model, with an interest to obtain a better control over maintaining non-neutral wind speed shear profiles. It is also recommended that research be conducted to determine if the AD method accurately portrays power and wake generation under conditions of high wind shear. The buoyancy aspect of MOST (and thus L) in simulations should be considered of secondary importance until significant

quantities of measurements of both wind speed and temperatures are available at the locations of large offshore wind farms at heights suitably above the turbine rotor tops. However, buoyancy should not be completely neglected as the presence of a thermal capping layer above the ABL has been shown to affect the strength of the deep array effect.

The purpose of this research has been to explore our current understanding and increase CFD modelling accuracy of wind flow through large offshore wind farms. It would be easy to conclude that future simulations should turn to LES codes for more control and accuracy over turbulence and eddies with more control over wind shear in the lower boundary layer, and thus achieve greater simulation accuracy of wake losses. However, despite recent progress in computational hardware, the events developers wish to simulate are also increasing in size. Wind farms with greater numbers of turbines, each with larger blades resulting in more complex interactions between wakes and the ambient flow, would benefit from detailed LES computations but would also be unrealistically costly. Both in the time required to run a single scenario and the computational resources monopolised to solve the problem. A RANS (or RANS based) model is currently the only CFD option which can feasibly solve such a large and complex problem within acceptable cost parameters. So until technology progresses to allow LES over such scales, URANS should be championed and developed with a focus on controlling wind shear. Most importantly of all however, is the need for time-frame consistency between modelled scenarios and real-world comparisons. If a simulation produces time-averaged results, such as those in this work, then its results can only be legitimately compared against the average of a large long-term dataset, something the filtering processes required by the MOST assumptions make unlikely for specific wind speeds and directions.

Grind with every wind.

- **Latin Proverb**

Appendix A: A Paper Published in the Journal of Wind Engineering and Industrial Aerodynamics

Assessing the Dependence of Surface Layer Atmospheric Stability on Measurement Height at Offshore Locations

P. Argyle ^a, S. J. Watson ^{a*}

^a CREST, School of Electronic, Electrical and Systems Engineering, Loughborough University, Loughborough, UK, LE67 5AH

*Corresponding author. Tel.: +44 1509 635348

E-mail address: s.j.watson@lboro.ac.uk

Abstract

Incorporating atmospheric stability into wind resource assessment modelling is becoming more common. This study investigates some of the challenges associated with calculating stability in the offshore environment. Data are analysed from meteorological masts FINO1 and FINO3 in the German North Sea using measurements at three different heights and results show significant differences in stability assessment depending on which combination of heights are used. All methods show the North Sea to be very unstable for the majority of the time, although by ignoring wind and thermal data from below 50m, the atmosphere appears more stable, indicating the presence of a marine internal boundary layer. Even 80km out to sea, it is suggested FINO3 still feels the effects of land, and it is clear the height of the atmospheric surface layer effects wind speed measurements under certain conditions.

Keywords

Atmospheric stability; Monin-Obukhov similarity theory; FINO1; FINO3

1. Introduction

During the process of resource assessment for a new wind farm, it is common practice to erect at least one meteorological mast extending to proposed turbine hub height to obtain climate information suitable for the prediction of future production yields. Since taller masts are more expensive, wind speeds above this height are estimated using a form of logarithmic profile. It is well documented ([12] and [161]) that atmospheric stability significantly alters the wind shear as well as the height of the surface layer (SL) and therefore accurate predictions of the wind resource above hub height usually depend on the reliability of stability calculations used for equation 1 below, where u_z is velocity at height z above the sea surface, u_* is the friction velocity, k is the von Kármán constant, z_0 is the sea surface roughness and ψ_m is the stability function which depends on height and the Obukhov length L .

$$u_z = \frac{u_*}{k} \left[\ln \left(\frac{z}{z_0} \right) - \psi_m \left(\frac{z}{L} \right) \right] \quad (1)$$

Besides knowledge of a site's wind resource above hub height, the frequency distribution of atmospheric stability is becoming increasingly valuable within large offshore farms as [66] directly links it to the magnitude of power deficits from wake losses. As farms grow in size, the importance of accurate wake loss prediction (and thus analysis of stability conditions) increases. For offshore farms, the cost of a met mast is a significant initial expenditure and therefore, resource modelling is desirable to reduce the number of masts required to obtain velocity profiles throughout a large development area [161] whilst also predicting how turbine wakes will affect production yields. To accommodate the prevailing non-neutral marine atmospheres described in [48] and [20], wake modelling software designers are starting to include basic stability functions, [149] and [162].

To verify the accuracy of models, a high quality source of meteorological data is required, to define the local stability conditions and assess the model results. However, there are many ways to calculate stability, (some of which are compared in [17] and [52]) and studies often use the method effectively dictated to them by available data. This inconsistency not only makes site comparison difficult, but also relies on assumptions made when using the Monin-Obukhov Similarity Theory

(MOST), notably, that the virtual potential temperature (VPT) described by equation 2, follows a linear profile within the SL.

$$\theta_v = \theta(1 + 0.61r - r_L) \quad (2)$$

Where θ is the potential temperature, r is the mixing ratio of water vapour and r_L is the mixing ratio of liquid water in the air. This assumption allows thermal measurements to be taken at any height on a mast and be considered sufficient to determine the stability conditions from the sea surface to the top of the SL. However, the thermal profile is not linear; changes in surface heat capacity (for example land to sea) or the development of internal mixing layers throughout the day can significantly change the profile [13]. Offshore, this is most likely to be caused by thermal differences between air and sea [12].

Whilst [56] shows there is good agreement between stability calculations at three heights using sonic anemometers to calculate the corrected surface heat fluxes of marine fetches at FINO1; sonic anemometers are not standard equipment installed by the wind industry. Remote sensor measurements of the sea skin temperature required for the bulk method of calculating L [60] are rarely available and bulk temperature measurements within 2m of the surface have to be carefully adjusted [61] and calibrated with air measurements. Using the gradient between two air temperatures is not only more representative of physical conditions experienced by turbines; masts are often suitably instrumented at multiple heights and [51] proposes it to be the most promising classification method. Therefore, this study investigates the implications of measurement height in relation to MOST, using the gradient Richardson number (Ri) to infer L , via equations 3 and 4 below:

$$L = \begin{cases} \left(\frac{z'}{Ri} \right) & Ri < 0 \\ \frac{z'(1 - 5Ri)}{Ri} & 0 < Ri < 0.2 \end{cases} \quad (3)$$

$$Ri(z') = \frac{\frac{g}{\bar{T}} \left(\frac{\Delta \bar{\theta}_v}{\Delta z} \right)}{\left(\frac{\Delta \bar{u}}{\Delta z} \right)^2} \quad (4)$$

Where z' is the height where the calculated gradient Richardson number is valid, estimated via $z' = (z_1 - z_2) / \ln(z_1/z_2)$, \bar{T} is a reference atmospheric temperature, $\Delta \bar{\theta}_v$ is the difference in VPT between z_1 and z_2 , g is gravitational acceleration, Δu is the difference in wind speed and Δz is the height difference between the two measurements at heights z_1 and z_2 .

2. Datasets

For this study, data were analysed from the offshore meteorological masts in the German North Sea: FINO1 and FINO3. Table A1 compares the instrumentation at each mast suitable for atmospheric stability analysis.

Table A1 Heights of instruments used to measure the five variables necessary. An asterisk implies the use of a sonic anemometer whilst numbers in brackets imply multiple instruments at specific heights.

Variable measured	Heights at FINO1 [m]	Heights at FINO3 [m]
Wind Speed	33, 40, 40*, 50, 60, 60*, 70, 80, 80*, 90, 100	30, 40, 50(3), 60, 60*, 70(3), 80(2), 90(3), 100, 100*, 106
Wind Direction	33, 40*, 50, 60*, 70, 80*, 90	30, 60, 60*, 80, 100, 100*
Air Temperature	30, 40, 50, 70, 100	29, 55, 95
Air Humidity	33, 50, 90	29, 55, 95
Air Pressure	20, 90	23, 94

Data from the FINO1 mast are from the beginning of January 2004 to the end of December 2007 (before the construction of the nearby wind farm Alpha Ventus), whilst the FINO3 data are from mid-September 2009 to the end of October 2011. Each datum represents the average across a ten minute event. In order to satisfy the assumptions of MOST, both datasets have been filtered to ensure homogeneous atmospheric conditions, although no adjustment has been made to account for the height of the SL. Values of wind speed, direction and temperature at key heights for each event were compared to those for the following event and previous two events; the atmosphere was considered to be in a non-homogeneous state if the wind speed varied by more than 20%, direction by more than 15° or temperature by 0.5°.

Whilst both masts are equipped with sonic anemometers, masts deployed by the wind industry normally rely on cup anemometers as their lower frequency sampling rate is considered sufficient for measuring the mean wind speed. Their greater deployment also provides more options when selecting heights for this study, compared to sonic anemometers, thus providing a more complete picture of the SL. (One conclusion from [56] was that the sonic anemometer heights are not low enough to represent the near surface conditions, particularly in stable conditions). At FINO3 there are varying numbers of cup anemometers at each height. For consistency between heights therefore, only the speed data from instruments located on booms facing direction 345° were used. This also increases the consistency between mast datasets as FINO1 only has one cup anemometer at each height, although it increases the risk of mast shadow effects. To counter this, both datasets were analysed for mast shadow by comparing ratios of speed measurements from the cup and sonic anemometers at 80m and 100m at FINO1 and FINO3 respectively against wind directions at the top of each mast. It was deduced that the cup anemometer booms extend from the masts at 135° and 350° respectively and it is assumed booms at other heights are consistent with these, with mast shadow affected data entries filtered accordingly. A sector of 40° was considered affected by mast shadow at FINO1 in contrast to only a 16° sector at FINO3.

At both locations, atmospheric pressure was measured at two heights. However, because of the low quality of the readings taken at 90m at FINO1 and the two pressure measurements at FINO3 having a correlation coefficient of 0.999 whilst differing by less than one percent of the absolute value; all required values for pressure from FINO1 were assigned those measured at 20m. To maintain consistency between datasets, pressure readings taken at 23m at FINO3 were used accordingly, (thus ignoring the measurements taken at 94m). The data have been split and analysed as six case studies, as shown by Table A2 to show the dependence of L on z' .

Table A2 Height in metres of temperature, humidity and wind speed measurements for each case study.
[†]Temperature at 90m was estimated via linear interpolation between 70m and 100m.

case	Met Mast	z'	Temperature Height		Humidity Height		Wind Speed Height	
			Low	High	Low	High	Low	High
A	FINO1	40.91	30	50	33	50	33	50
B	FINO1	68.05	50	90 [†]	50	90	50	90
C	FINO1	56.81	30	90 [†]	33	90	33	90
D	FINO3	39.15	29	55	29	55	30	50
E	FINO3	68.05	55	95	55	95	50	90
F	FINO3	54.61	29	95	29	95	30	90

3. Results

Having calculated Obukhov lengths for datasets A to F, they were binned by stability class to simplify analysis as shown in Table A3. Whilst the definition of stability bins is often open to interpretation and varying their boundaries could alter results of any analysis, these definitions have been used previously by authors [12], [161] and [48].

Table A3 Classification of atmospheric stability. The abbreviations are used to refer to specific stability conditions in figures throughout this work.

Atmospheric Condition	Definition	Abbreviation
Very Stable	0m<L<200m	VS
Stable	200m<L<1000m	S
Neutral	1000m<L or L<-1000m	N
Unstable	-1000m<L<-200m	U
Very Unstable	-200m<L<0m	VU

Figure A1 shows that the distribution of stability classes is related to the heights at which the measurements are taken. For example, there is a significant difference in stability distribution when comparing cases A and D with cases B and E, indicating that the marine air below 50m is mostly very unstable whilst above 50m, there is greater stability. The difference in distributions above and below 50m suggests an internal boundary layer may be present at both sites, with greater thermal and mechanical mixing processes than in the less turbulent air at potential hub heights. Significantly, FINO1 is located 45km from shore whilst FINO3 is 80km from the nearest shore (although roughly 60km from the farm Horns Rev), so there is a significant fetch for these marine boundary conditions to develop and any coastal effects to dissipate. The distributions for C and F also show a strong bias towards very unstable conditions, similar to that of A and D, indicating that the lower, more unstable atmosphere has greater significance than more stable conditions above, when calculating the overall stability, a result also concluded by [52]. Not shown in Figure A1 is that roughly 40% of analysed data for B and E had to be filtered out as

their corresponding gradient Richardson numbers were larger than the critical value, (taken as 0.2 as in [48], [20] and [17]) and thus removed. Less than 10% of the other datasets suffered this condition implying very stable events with low turbulence intensities are even more common at higher levels than shown for B and E. As a result, any modelling for resource assessment using results from C and F (to benefit from the complete height of the masts) will primarily simulate the prevailing unstable conditions when in fact the future turbine rotors are likely to initially experience the more stable conditions displayed by B and E, although wake rotation and turbulence is likely to increase mixing between the two layers. Caution is urged when attempting to translate these results to other offshore locations as results by [12] show stability distributions from four masts with more neutral and stable conditions. Whilst these differences can partially be explained by proximity to shore, and therefore the averaging effects of stronger diurnal cycles observed by [12], none of their four masts measure parameters more than 50m above the sea surface and so would be closest to Cases A and D in this work.

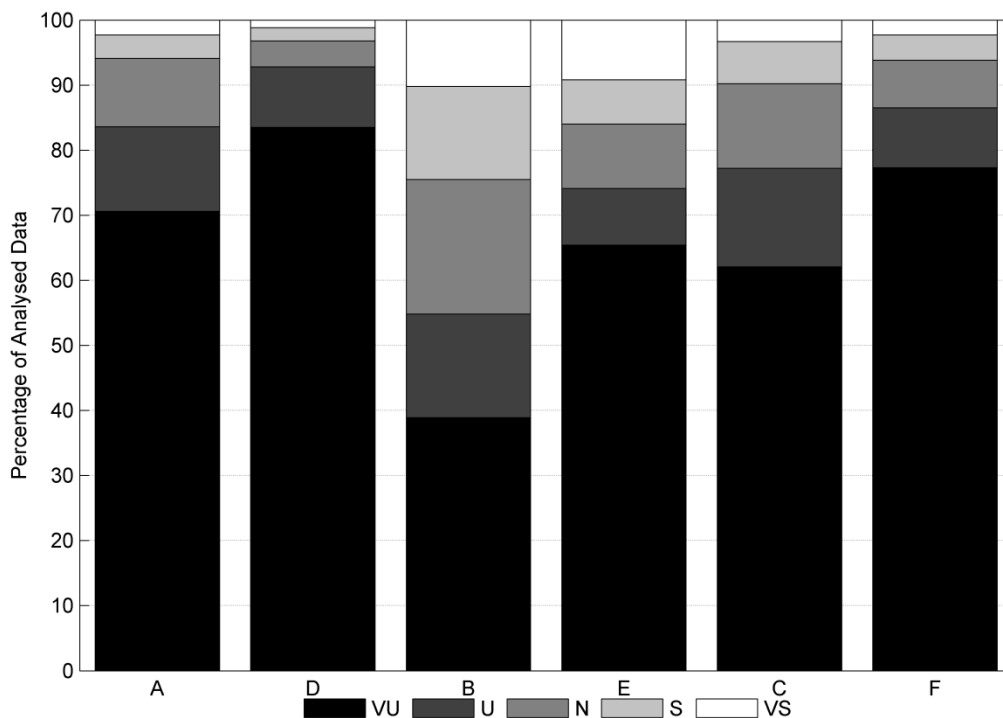


Figure A1 Distribution of stability for each case study dataset.

For the purpose of comparison between alternative methods of calculating the atmospheric stability; Figure A2 below plots the distributions for Cases A, B and C from FINO1 alongside distributions publicised by [56] from the same offshore mast

utilising the sonic anemometers to calculate L via both flux and bulk Richardson number approaches. As the sonic data comes from after the construction of the Alpha Ventus wind farm, it had been filtered by wind direction to avoid wake interference. Therefore, data from Cases A, B and C have been filtered to maintain directional consistency, although the data collection period differs by three years. Comparing the five stability distributions indicates that the gradient method returns greater proportions of VU events than either the flux or bulk methods. However Case B, utilising measurements from the upper mast portion, is in close agreement with the flux method, despite its reference height being located over 25m higher up the mast. By comparison, the distribution of Case A is considerably more unstable than either of the results from [56], despite having a reference height less than a single metre apart. Case C with its reference height 15m higher, also shows a greater frequency of VU events than either of the flux or bulk methods, although its proportion of U and N events is similar to those of the bulk method. The differences between results suggest the height at which measurements are made is more significant to the gradient method than its resulting reference height.

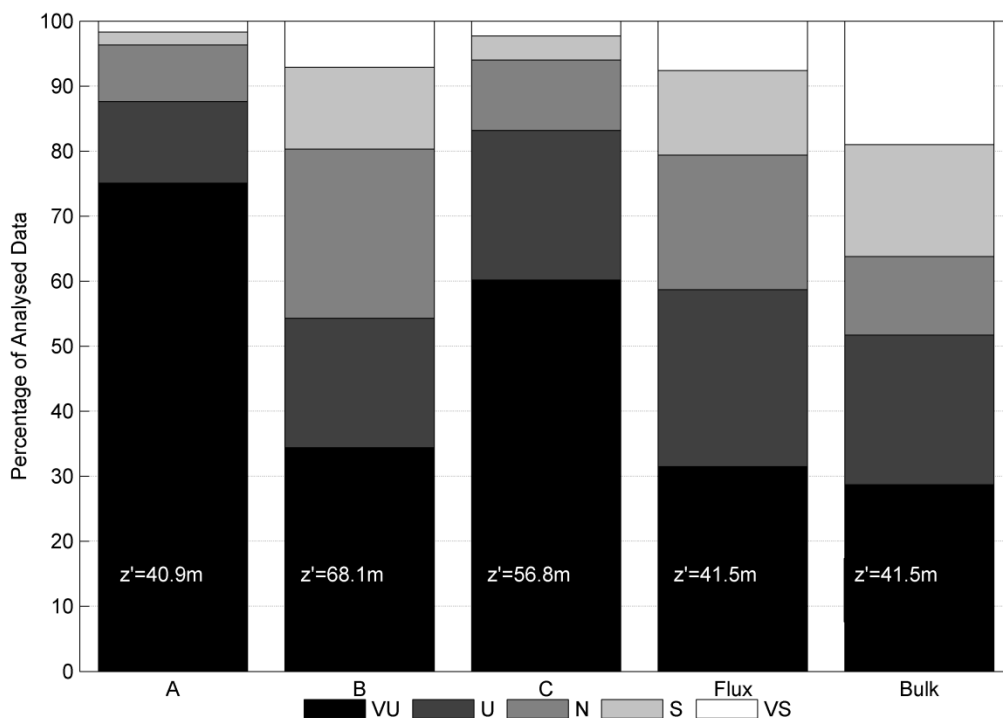


Figure A2 Distribution of stability at FINO1 as calculated via the gradient method, compared alongside results from reference [11] using their flux and bulk methods. For consistency with [11], Cases A, B and C have been filtered by wind direction to only include the sector 240°-360°.

To further investigate this point, Figure A3 shows the mean VPT profiles for each site and as a function of wind direction. Below 50m, the stronger gradients suggest greater instability than above 50m, although seasonal variability and weather systems result in the standard deviations of each sample to be roughly 5 degrees. This means there is no clear statistical confidence that the VPT is non-linear with height, however with only 3 reference points, the height of those reference points is important for our understanding of the local atmospheric stability. For example, if the middle height VPT values were instead derived from measurements just 10m higher up the mast, A and D may show a higher proportion of stable events. Similarly, if the heights of the lowest values were actually 10m lower on the mast, A, D, C and F might all produce more unstable results, assuming the VPT is linear with height below 50m and also above 50m. This is an assumption which is only maintained by the high variance in temperature measurements, despite qualitative indications from distributions and filtering due to high Richardson numbers in Figure A1 suggesting a non-linear profile.

Typically for Western Europe, the northerly and easterly winds are colder than the average, although the difference is significantly greater at FINO3 despite being twice the distance from shore and therefore experiencing a greater influence from the large heat capacity of the sea. Worth noting is the difference in range of VPT by wind direction at each site considering they are roughly 130km apart. Although the large variances mean the differences are not statistically significant; any directional variation that does exist may be partially due to a shorter easterly fetch for FINO3 (and so greater variation from site average). Although following this argument, FINO1 should experience higher temperatures for southerly winds yet Figure A3 does not support this theory. Therefore, it is assumed that variation in absolute VPT between sites is a result of mast data recorded over different time periods.

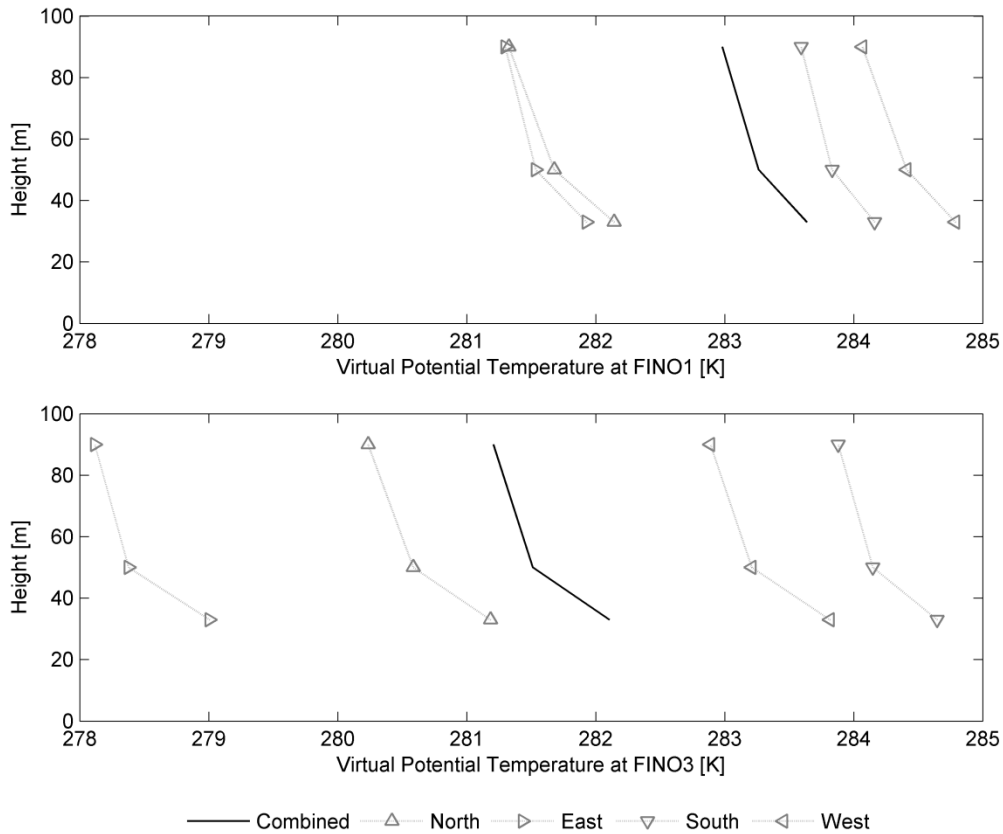


Figure A3 Virtual potential temperatures at FINO1 (top) and FINO3 (bottom) by direction sector.

The variation in temperature shown in Figure A3 suggests a loose relationship to sea surface temperature. Although measured, no water measurements were available for analysis. It is, therefore, hypothesized that water's relatively larger heat capacity would lead to little variation in temperature with wind direction. It appears possible that at heights greater than 30m above the sea, perhaps on account of low surface roughness values, horizontal advection of air parcels from other regions may have a more direct impact on stability than the sea itself. Although beyond the scope of this work, it is worth considering that while higher wind speeds lead to greater sea surface roughness values, both increased roughness and surface temperature will result in increased VPT at lower levels as a result of increased relative humidity.

The results presented in Figure A4 make use of the more extensive absolute temperature measurements at FINO1 to further investigate the nature of temperature in the marine SL. Whilst sample standard deviation values again mean there is no statistical difference between wind direction or measurement height, measurements from all wind directions suggest there may be some atmospheric feature which although requiring more detailed data filtering to decisively prove, may impact any

stability calculations from individual measurements rather than as an average across a large time scale.

If it exists as more than a statistical quirk of a dataset with seasonal variability, the implied difference in temperature profile between 40m and 50m could be caused by a number of reasons, but since the FINO1 project team calibrates and deploys its instruments to a high scientific level [163] it is unlikely to be from systematic measurement errors at either height. Therefore, it is hypothesised that the rapid change in temperature gradient is caused by a persistent internal boundary layer. Comparing profiles for easterly and westerly winds implies that this internal boundary layer height does not change with distance from shore as all directions maintain an average 40m absolute temperature roughly 0.3K greater than at 50m. Since FINO3 only measures temperature at three heights, a plot of absolute temperature profiles is not shown as it would not expand on results from Figure A3. Such indicators of internal boundary layers as shown in Figures A3 and A4 show the significance of additional measurement heights for resource assessment, either to incorporate redundancy, highlight suspicious measurements or reveal atmospheric structures that may contradict the standard modelling assumptions.

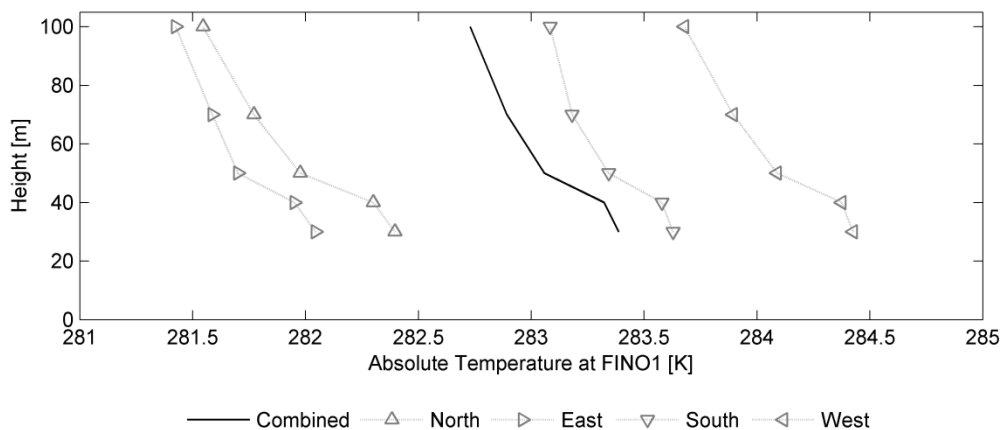


Figure A4 Absolute temperature profiles at FINO1 by direction sector.

The thermal state of the atmosphere will strongly affect the levels of ambient turbulence, and therefore wind turbine wake behaviour, but only under more stable conditions will it significantly affect the wind shear profiles at hub height. Figure A5 shows wind speed profiles for all categories (A-F) under the five stability conditions. In very unstable conditions (as defined individually by each method), the average wind speeds for each mast never vary more than 0.6m/s throughout measured

profile heights. The same is generally true for the unstable cases although B and E both display higher average speeds than the others at lower levels. Ignoring the difference in absolute wind speeds between masts, all six profiles display wind shear characteristics of unstable and very unstable conditions, with negligible shear in the very unstable case and slight shear in unstable conditions. It should be noted that under unstable conditions, E displays a profile sheared less than the others whilst B displays a lower average wind speed at 100m than at 90m.

Under neutral conditions, Figure A4 shows greater variation between A-C and also D-F. Whilst A,C,D and F display similar profiles varying by roughly 1m/s for each mast, B and E display shear profiles more characteristic of an unstable atmosphere. The precise reason for this is unclear although it is likely that as their ratios of thermal to mechanical shear are small enough to result in neutral values of L , and the wind shear is small, it follows that there is a negligible thermal shear. As this is only apparent higher up the mast (Cases B and E), it is reasonable to conclude the upper mast is subject to less variation in air temperature (as shown in Figure A3), possibly with the lower air dampening any effects of variable surface forcing. In stable conditions, all six profiles again show the same shear, but the absolute difference between the A, B and C as well as D, E and F have become significant. For example, at FINO3 under stable conditions, the average wind speed at 30m varies by up to 2.5m/s depending on the height at which stability is calculated, whilst the difference in average wind speeds exceed 3m/s at FINO3 when very stable conditions are considered. The same cannot be said about FINO1 whose averaged profiles always remain within 2m/s of each other and indeed are in greater agreement during very stable than stable conditions.

It should be noted that in very stable conditions, A and D (as well as for D in stable conditions) show a clear decrease in shear at upper levels. It is hypothesised that this is because the SL height decreases in more stable conditions and since these categories do not contain stability data calculated from measurements above 50m, well below the profile anomalies, the upper mast extends significantly above the surface layer. Thus measurement heights used to calculate stability are significant, for calculating expected wind speeds, and also wind shear above hub height which is an important factor in the generation of wake turbulence and wake recovery.

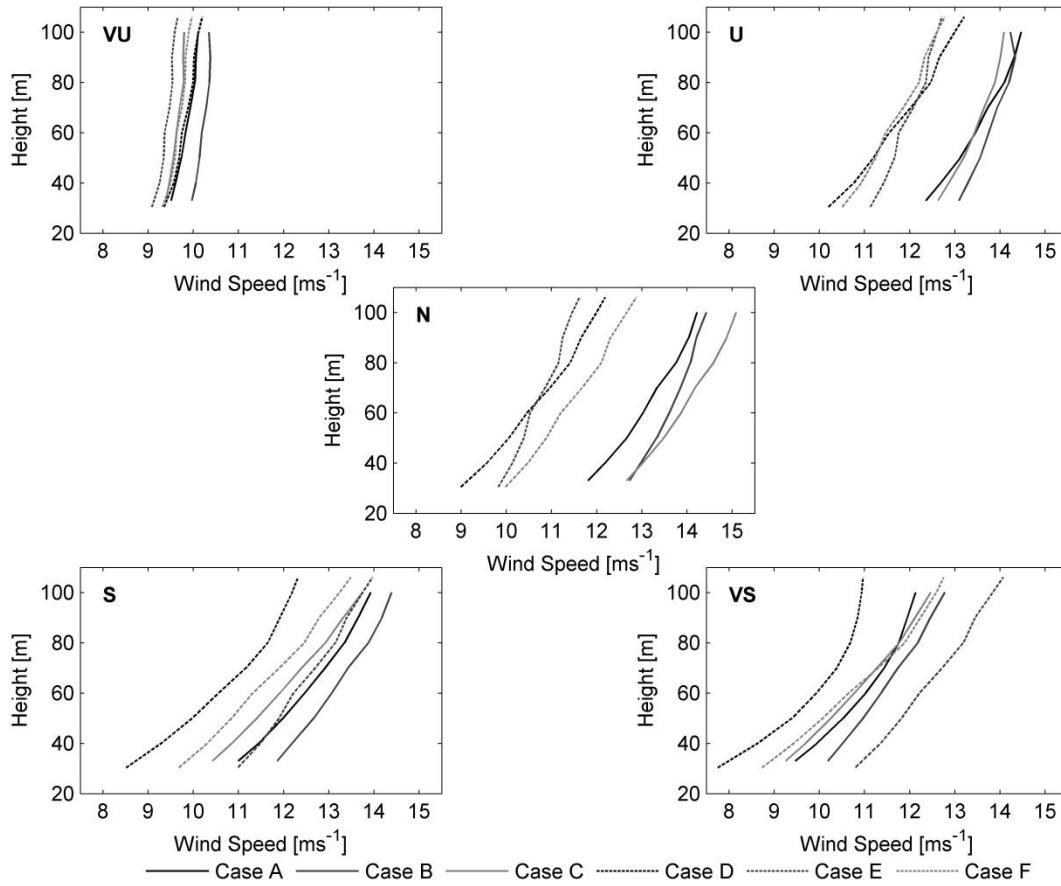


Figure A5 Wind speed profiles under different atmospheric conditions – top left = very unstable, top right = unstable, centre = neutral, bottom left = stable, bottom right = very stable. Solid lines show profiles from FINO1, while dotted lines represent FINO3 profiles.

Having analysed how using different heights can change the distribution of stability and wind profiles in the SL; we also consider how the measured data in each category A-F match the wind speeds predicted by MOST. Expected speed ratios are calculated via equation 5 using the different heights relevant for each Case as a function of stability. Suitable values of $\psi_m(z/L)$ are calculated via the Businger-Dyer formulation [18], with z_0 assumed to be the constant value 0.0002m. Whilst higher wind speeds will result in larger waves leading to greater surface roughness, reference [17] has shown constant values of z_0 to be a close fit to more complex calculation methods and Table A4 shows wind speed ratios calculated using a range of values to be within 5% of the $z_0 = 0.0002\text{m}$ results:

$$\frac{U_1}{U_2} = \frac{\left[\ln \left(\frac{z_1}{z_0} \right) - \psi_m \left(\frac{z_1}{L} \right) \right]}{\left[\ln \left(\frac{z_2}{z_0} \right) - \psi_m \left(\frac{z_2}{L} \right) \right]} \quad (5)$$

Table A4 Variation in vertical wind speed ratio across different stability conditions, as calculated using equation 5, expressed as a percentage difference from values obtained using the standard $z_0 = 0.2\text{mm}$. Values of $10/L$ have been partitioned into bins based on one decimal place.

$10/L$	$z_0 = 0.1\text{mm}$			$z_0 = 1\text{mm}$		
	U_{50}/U_{30}	U_{90}/U_{50}	U_{90}/U_{30}	U_{50}/U_{30}	U_{90}/U_{50}	U_{90}/U_{30}
-0.2	0.1%	0.1%	0.2%	-0.4%	-0.3%	-0.7%
-0.1	0.1%	0.1%	0.3%	-0.4%	-0.4%	-0.8%
0	0.2%	0.2%	0.5%	-0.6%	-0.7%	-1.3%
0.1	0.5%	0.6%	1.1%	-1.4%	-1.8%	-3.1%
0.2	0.6%	0.8%	1.4%	-1.7%	-2.1%	-3.9%

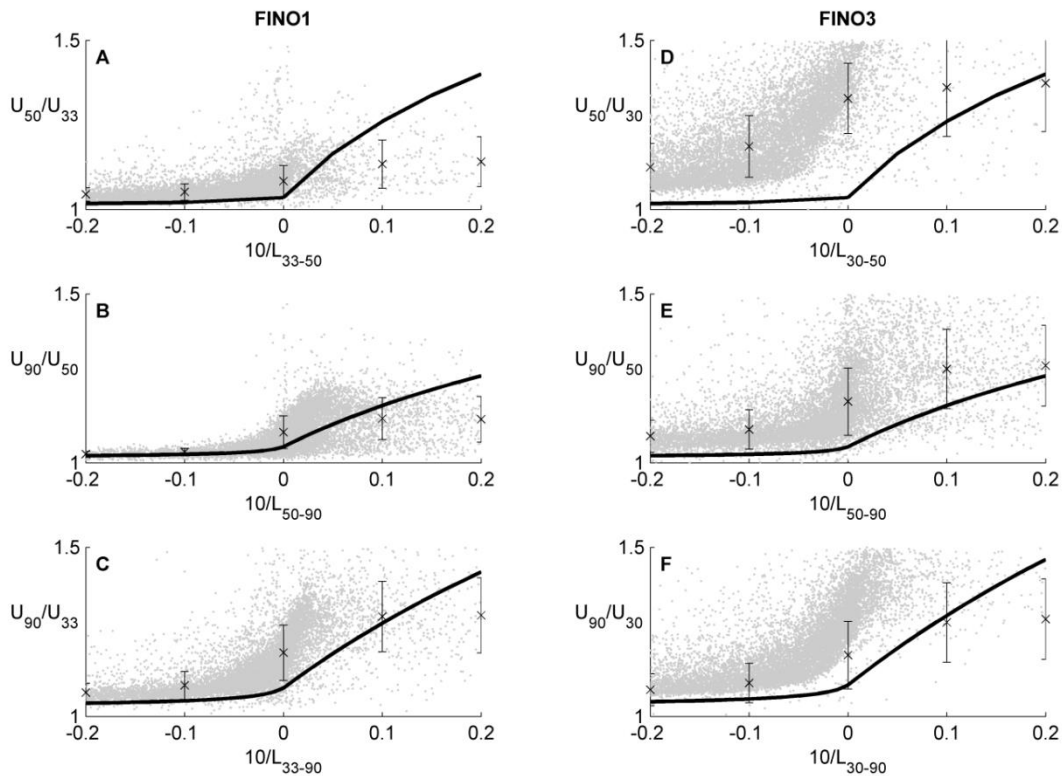


Figure A6 Scatter plots comparing the ratios of wind speeds at FINO1 (left) and FINO3 (right) at heights indicated on the left axis against corresponding predicted ratios (black lines) using equation 5. Binned average values are shown as crosses with error bars signifying ± 1 standard deviation about each bin.

An initial observation from Figure A6 confirms the results in Figure A1 in that there are very few very stable events ($0.05 < 10/L$) with case B displaying a greater percentage than the others. None of the six case studies however can claim that MOST accurately predicts wind shear for the more stable events. Whilst the upper mast cases (B and E) have most events in this category, there is still significant scatter with MOST over predicting shear at FINO1 and under predicting at FINO3. This is due to an increase in shear values measured in each case for negative values of $10/L$, rather than within the expected neutral range around $10/L = 0$, indicating equation 4 may produce absolute values of Ri which are too large in

unstable events and too small in stable events. Neutral shear events at FINO1 are predicted well for case B by MOST, although for cases A and C, the value calculated using MOST reflects measurements more commonly found with Very Unstable events. This slight under-prediction of neutral shear at FINO1 along with clear under-prediction for FINO3, is consistent with the calculation of Ri using equation 4, as the general shape of the measured shear scatter distribution is similar to the expected values, but with higher than expected shear. For very unstable cases ($-0.05 > 10/L$), MOST provides a good prediction of wind shear at FINO1, particularly for case B. However at FINO3, MOST consistently under-predicts the levels of shear, with mast data displaying a wide scatter, especially lower down the mast for case D. Although the structure of availability data (for example no water temperatures) led to this study using the gradient method of calculating L ; it is worth remembering that other methods do exist, though reference [17] for example found similar trends across three separate approaches, the gradient method returned the largest errors but lowest variance within the stable region. As developers frequently use temperature gradients for simplicity to infer stability, their further academic study is recommended, especially comparison with other approaches.

Further investigation into the accuracy of MOST can be conducted by using equation 5 to calculate z_0 for known wind speed gradients across a range of stability values. Having calculated L using equations 3 and 4, Table A5 below shows the mean values for the corresponding values of z_0 across the same stability grouping used in Table 4 and Figure A6. Although the majority of values appear larger than the 0.0002m length used in calculating the expected speed ratios in Figure A6; their corresponding standard deviations (shown in Table A6) range from 0.003m to over 3m, and so only one value of average surface roughness in Table A5 (Case D where $10/L=0$) is statistically different to the assumed value of 0.0002m. Across the data, larger values of z_0 correlate with high wind shear, this is particularly clear for Case D with a correlation coefficient of 0.97. Case A also shows strong correlation with a coefficient of 0.82 suggesting z_0 is very important for creating shear lower down the mast whilst Cases B and E from the upper masts' section have coefficients of 0.35 and 0.70 respectively. Across the whole mast, Cases C and F show some correlation between wind speed ratio and z_0 with coefficients 0.48 and 0.59 respectively.

Table A5 Average values of z_0 (in m) for each Case across the specified stability gates.

10/L	Case A	Case B	Case C	Case D	Case E	Case F
-0.2	0.2577	0.0070	0.0735	1.6589	0.8870	0.2294
-0.1	0.2975	0.0123	0.1372	3.1864	1.3154	0.3955
0	0.5813	0.0963	0.2497	6.5488	2.4637	0.7752
0.1	0.4131	0.0139	0.0269	3.8583	0.7983	0.0647
0.2	0.1221	0.0004	0.0009	2.5375	0.1896	0.0038

Table A6 Standard deviation values of z_0 (in m) for each Case across the specified stability gates.

10/L	Case A	Case B	Case C	Case D	Case E	Case F
-0.2	0.5103	0.0174	0.2377	1.5441	1.2668	0.4645
-0.1	0.6707	0.0361	0.4235	2.2513	1.8647	0.6845
0	1.3008	0.5178	0.5457	2.5845	3.0917	0.7390
0.1	1.0382	0.0869	0.0818	3.5026	1.4467	0.1102
0.2	0.3131	0.0026	0.0029	2.8353	0.5392	0.0070

To help ascertain the cause of the variation in MOST accuracy between FINO1 and FINO3, the data in Figure A6 is filtered by wind speed range. Figure A7 show these filtered data as three wind speed categories, high ($u > 14 \text{ms}^{-1}$), intermediate ($8 < u < 14 \text{ms}^{-1}$) and low ($u < 8 \text{ms}^{-1}$).

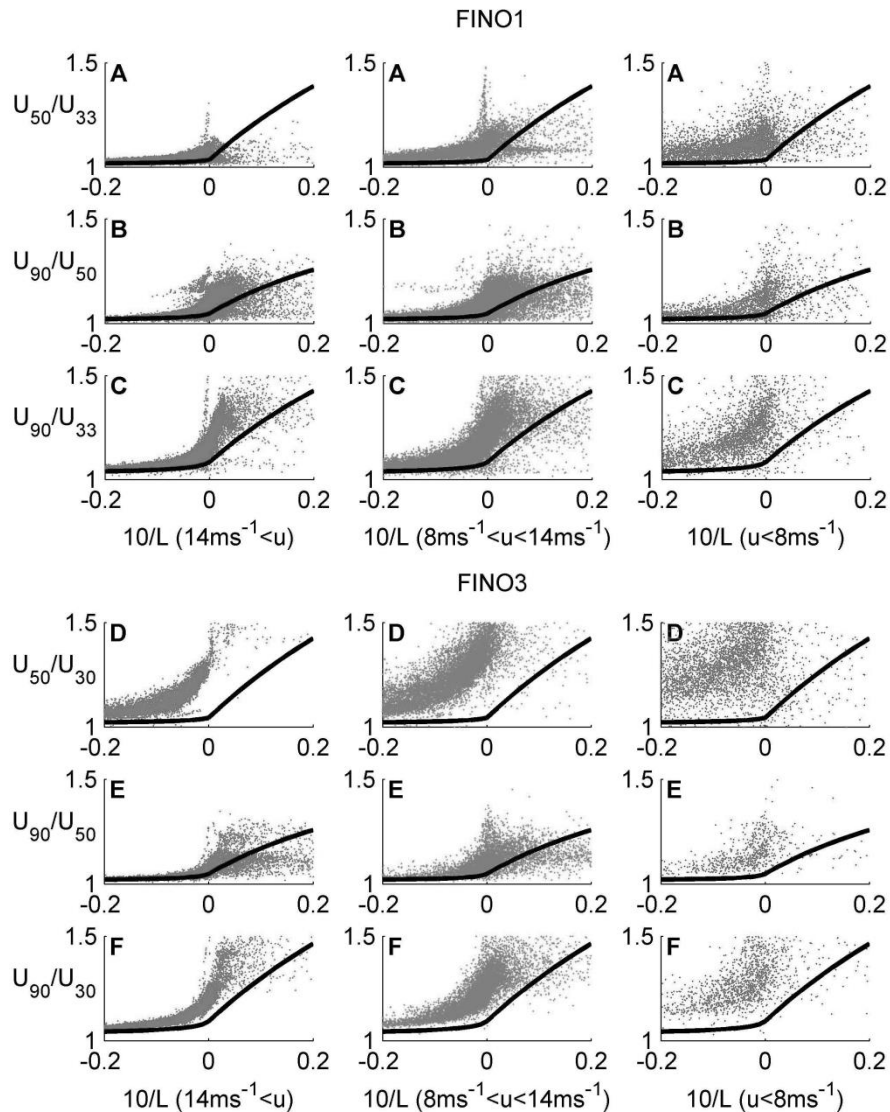


Figure A7 Scatter plots as shown in Figure A6 broken down by wind speeds as measured at the top of the two anemometers, with high wind speed ($u > 14 \text{ms}^{-1}$) events on the left, low ($u < 8 \text{ms}^{-1}$) wind speed events on the right and intermediate wind speed ($8 < u < 14 \text{ms}^{-1}$) events in the centre.

Due to the filtering in Figure A7, the levels of scatter and therefore accuracy of MOST in predicting the wind shear is clearly shown to be directly linked to wind speed. In all six case studies, the events with low wind speeds have higher levels of scatter than those with high wind speeds with intermediate wind speeds resulting in mid-range levels of scatter. At FINO1 (top nine plots in Figure A7), in addition to reducing scatter, comparing higher wind speed events against MOST also results in more accurate predictions of average wind shear values from very unstable (low shear events) to very stable (high shear events). Whilst it is not clear if the same effect occurs with increasing stability for the FINO3 data (bottom nine plots in Figure A7), the higher wind speed measurements show less scatter with mean results closer to MOST predictions. This is particularly clear in case F which displays a clear

gap between plots for MOST and measured data for intermediate wind-speed events where $10/L < 0$; this gap is large for low wind speeds and small for high wind speeds.

The additional filtering applied in Figure A7 reveals a further feature for stable conditions. This is most clearly seen in the high wind speed plot on the left of the figure, although it is also noticeable in some intermediate wind-speed cases. Above a certain value of stability measured by $10/L$, which we denote ζ , there is little correspondence between the shear predicted by MOST and that determined from the measured data. Although ζ varies between cases from 0 to 0.02, the related value of Ri is less than half the critical value of 0.2 where flow becomes laminar [10]. For $10/L > \zeta$, there is little increase in maximum wind shear with increasing stability and it is hypothesised that at $10/L = \zeta$, the SL is the same height as the top wind speed measurement. This would help explain why the phenomena is most prevalent for case studies B and E whilst the effect is less for cases C and F which also use mast upper mast measurements as values of both $10/L$ and shear are moderated via measurements in the less stable atmosphere below. Another result of filtering by wind speed range is the revealing of narrow spikes in shear around neutral stability, seen clearest in case A. This is thought to be related to large variation of Δu at low mast heights in equation 4 as they are clearest when speeds at 33m are used from FINO1.

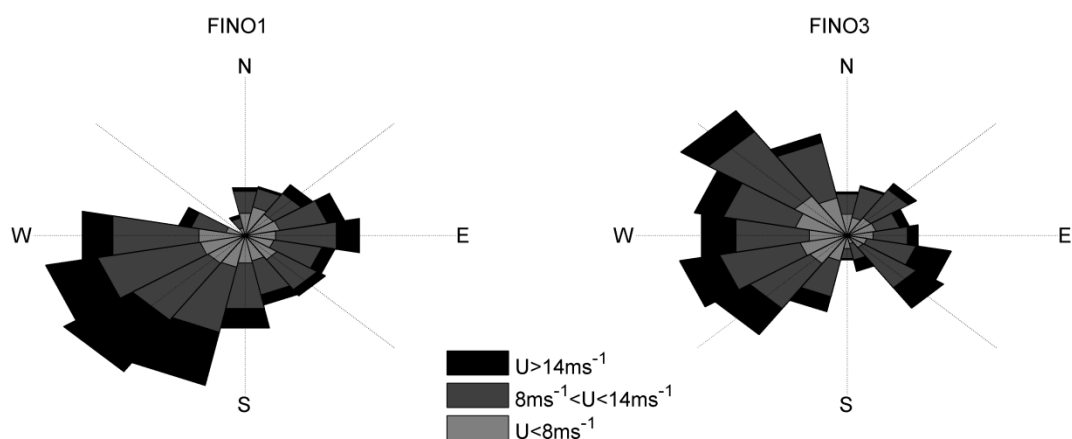
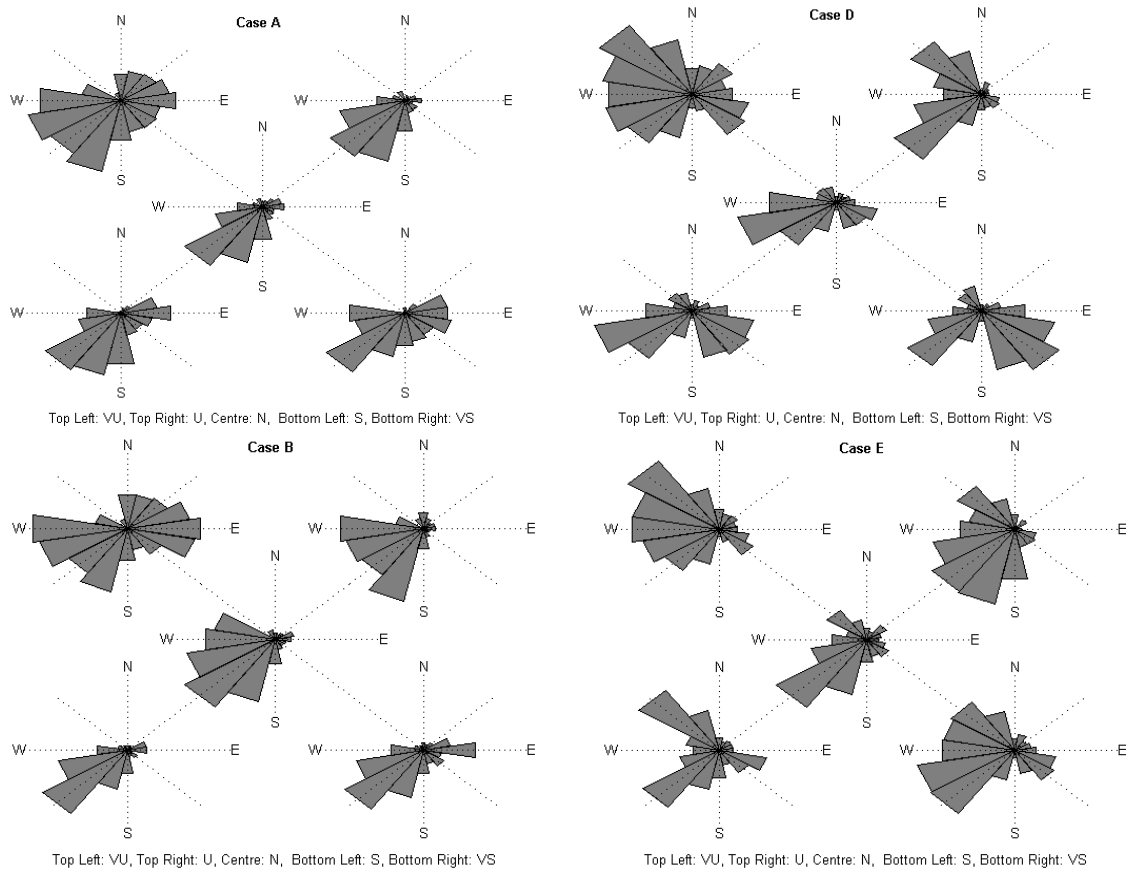


Figure A8 Wind Roses for FINO1 (left) and FINO3 (right). The rose for FINO1 clearly shows the effect of filtering to account for mast shadow over a large sector around 310° whilst the FINO3 rose appears less effected by shadow as the narrow filtering does not occupy a whole segment at 170° .

Figure A8 shows wind roses for the two offshore masts, using directions measured with the highest available wind vane and subdivided with grayscale into the three

speed categories used in Figure A7. Despite being located roughly 130km apart, and using data from different years, the two are similar. Considering the missing sectors for each rose to account for mast shadow, both show a spectrum of wind speeds with no sector disproportionately high or low and the majority of events occurring within the middle speed bin. Both masts show prevailing winds are from a wide westerly sector with the greatest quantity of high speed events, although filtering for mast shadow and different measurement periods hinder absolute comparisons across the distance separating the two masts. As a result of their locations in the North Sea, the majority of measured events at FINO1 are from directions less than 200km from shore whilst events at FINO3 are more strongly distributed towards directions of longer fetches.



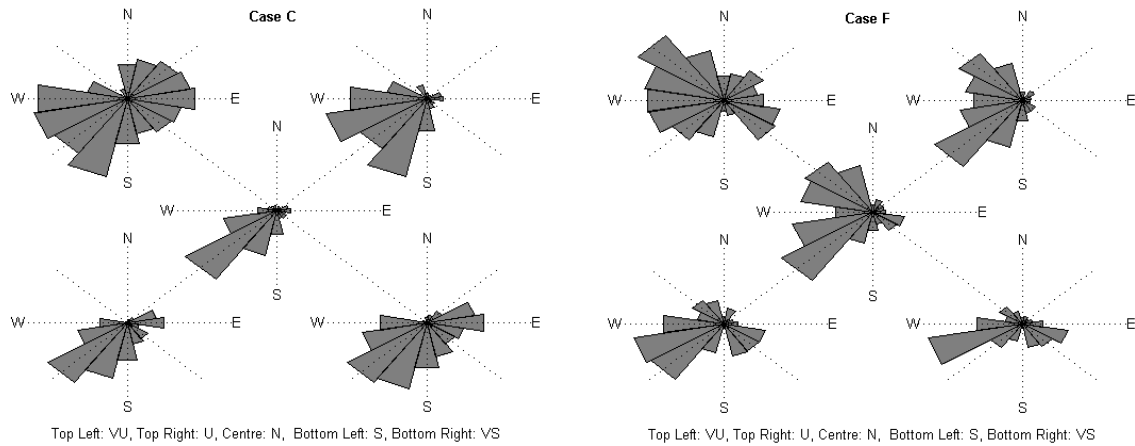


Figure A9 Wind Roses for FINO1 (left) and FINO3 (right) for each of the six case studies split into the five stability categories such that: top left: VU, top right: U, centre: N, bottom left: S, bottom right: VS. Wind directions were measured at 90m and 100m at FINO1 and FINO3 respectively.

Whilst Figure A8 suggests the proportions of North Sea wind speeds below 14ms^{-1} to be evenly distributed relative to directional frequency, Figure A9 shows atmospheric stability to be strongly dependent on wind direction. For example, almost all events at FINO1 from the northerly quarter ($315^\circ > \theta$ or $\theta < 45^\circ$) are very unstable. Another way of analysing the roses shows unstable, neutral and stable events at FINO1 are primarily from the southwest quadrant ($180^\circ < \theta < 270^\circ$) whilst the more extreme stability categories vary more in direction. It is worth noting that neutral events at FINO1 are mostly concentrated in a few direction sectors. Combining observations from FINO1 in Figures 1 and 9 suggest that wind farm developments near FINO1 can assume predominantly very unstable conditions from most directions, particularly with respect to heights below 50m. Also worth noting is how the distribution of mast top wind directions for neutral events changes veer with stability reference height. For example, neutral events for case B using stability measurements from the upper mast shows events occur across a 90° compass sector from SSW to WNW whilst neutral events for case A occur mainly from S to WSW. Similarly, the unstable roses also show veering with height, with compass wind directions in case A ranging from S to WSW whilst the case B rose is weighted between SSW and W. Whilst veering with height is often a result of the Ekman spiral, the difference in stability reference heights between cases A and B is small relative to the boundary layer depth and direction change is small; thus it is more likely the differences in results from FINO1 are caused by the underlying stability reference heights for each Case for calculating L occurring within separate atmospheric sub-layers and the resulting classification by stability. The inclusion of stability

measurements from lower down the mast as in both case A and C result in less variation in wind directions with a greater dominance from the southwest sector. The reverse is true for unstable events; where only stability measurements from the lower mast are considered (case A), the spread of events is concentrated in a fewer direction sectors than for either case B or C where upper mast stability measurements are analysed. It is unclear whether this variability in prominent directions is a direct result of differences in measurement height or a product of variable sample size for each stability category, itself a product of the stability reference height as shown by Figure A1.

The roses displaying results from FINO3 in Figure A9 are less unidirectional than those for FINO1. Although the two roses in Figure A8 are similar, and the three less extreme stability categories are still weighted towards the southwest; some roses show greater influence from wider sectors compared to their FINO1 equivalent. Others show high frequencies from the northwest (where mast shadowing affected FINO1 results). An example of this is the stable rose for case E, while its equivalent for case B is weighted strongly to the southwest. Neither of the other stable events for FINO3 case studies (with stability reference heights lower down the mast) show this directional spike, with each indicating stable events are more commonly occurring with south-easterly winds. Lower stability reference heights on the mast may indeed result in more unstable characteristics as the dominant northwest sector appearing in the stable rose for case E may include the same events as the clear northwest sector for the neutral category for case F or even the unstable rose in case D. The wide sector of west to northwest directions for the very stable category of case E is also missing from the roses categorised using stability measurements from lower heights in cases D and F. Thus, whilst variable sample sizes of each stability category make direct comparisons difficult, variation in stability reference height can significantly change not only the categorising of stability events, but also the significant wind direction, which will have implication for both initial wind resource and wind turbine array wake loss predictions for a proposed offshore wind farm.

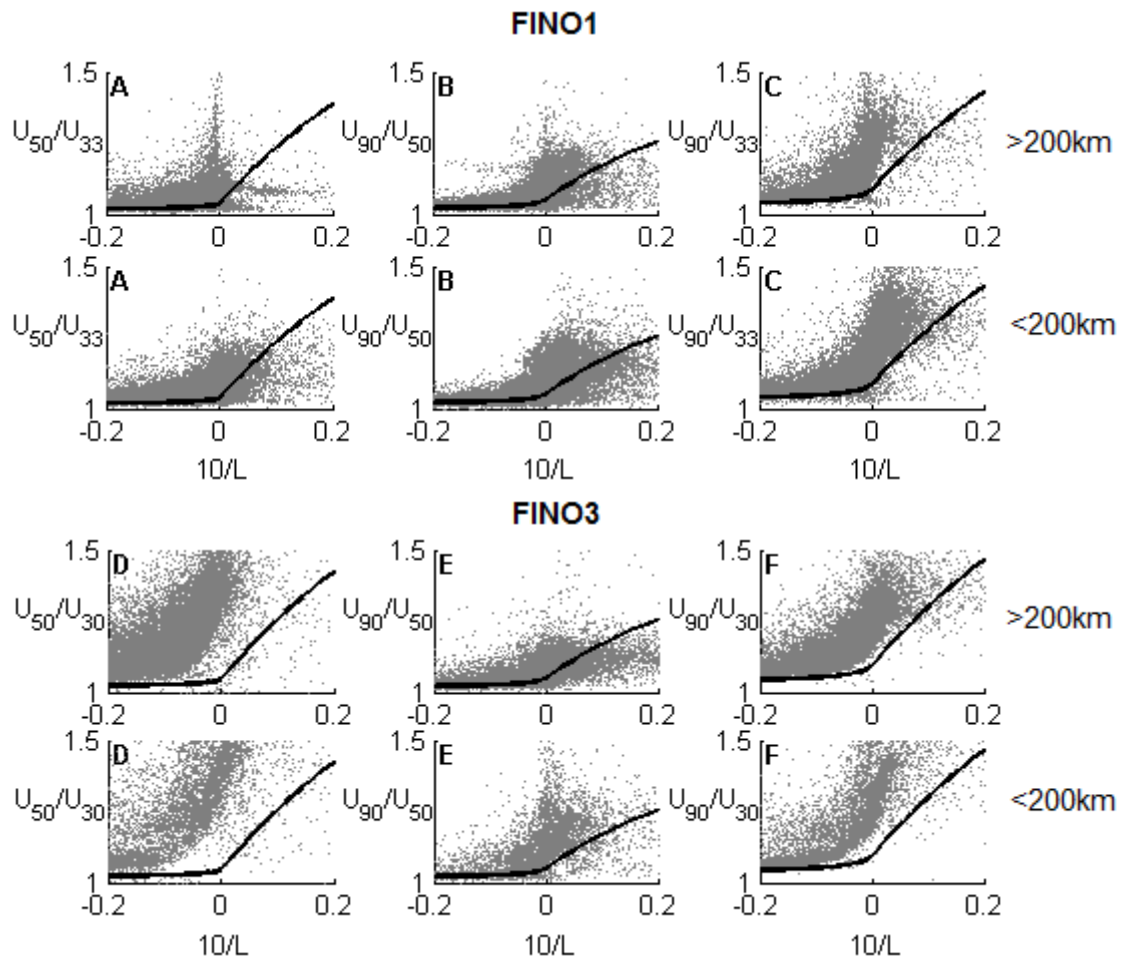


Figure A10 Scatter plots as in Figure A6 split into directions with a longer offshore fetch (>200km) and shorter offshore fetch (<200km) as measured by the wind vanes at the top of each mast. The black lines show the MOST expected shear values.

With the arbitrary definition of a long offshore fetch being greater than 200km, Figure A10 compares measurements from directions with long offshore fetch against directions with shorter fetch. Whilst FINO1 and FINO3 are located 40km and 80km from the nearest shore respectively, there are still some variations in shear depending on fetch. For example, whilst the overall range of shear values measured in case F does not noticeably vary, the dense region of points indicating high frequency is narrower for shorter fetch directions than for the longer marine fetches. This is also seen for case D, although this may be due to the higher frequency of offshore wind cases at FINO3. Possibly due to its closer proximity to shore, the reverse is true at FINO1, where wind direction observations from coastal sectors are more frequent. However, this has not resulted in much variation in fetch dependent scatter for cases A, B or C in Figure A9 except in the region $10/L > \zeta$ as mentioned for Figure A7.

4. Conclusion

This study has applied MOST to two offshore locations and generally found that the theory acceptably predicts wind shear in unstable conditions but that caution is advised when considering stable conditions, particularly for greater heights. The three year data set used from FINO1 generally supports these findings though results from the two year data set from FINO3 are less clear. Differences in results between masts could be due to variation in weather patterns as the data were not from consistent years. Alternatively, location may have played a part since, although the two masts are both in the North Sea, they are roughly 130km apart with the nearest land in different directions, (south for FINO1 and east for FINO3). Despite being far from the coast, and both datasets suggesting the presence of internal boundary layers around 50m, it is seen that temperature profiles, and thus stability are vary with wind direction. This was unexpected considering the high thermal capacity of the sea. It would seem that a fetch of 80km is not enough at FINO3 for the effects of the coast to be completely ignored and, along with the SL height, should be included in the resource assessment considerations for offshore wind farm projects. It is also concluded that offshore advection of air from one region to another may play a more significant role determining hub height stability than the sea surface temperature.

Although less relevant for the wind industry, the analysis reveals another consideration for MOST, i.e. around neutral stability, there is often a spike in wind shear which corresponds to low wind speeds. Therefore, caution is recommended when analysing data with very low velocities and it is hypothesised that an additional filter to remove data entries below a minimum speed could be introduced. This may result in Figure A1 displaying an even lower proportion of neutral cases. Removing low speeds from all analysis altogether is likely to decrease the dominance of very unstable events.

Having analysed the atmospheric stability using measurements from different heights at two high quality research met masts, it is clear that the height at which measurements are made is significant and influences many of the resulting conclusions. Therefore, it is recommended that masts used for resource analysis are

equipped to record temperature and humidity measurements at more than three heights. Although high variance in the data prevented confirmation through statistical tests, the three heights used at FINO3 were enough to suggest that the thermal profile may not be linear as assumed by MOST, but not for showing a detailed atmospheric profile. Whilst FINO1 is equipped with temperature sensors at five heights, humidity is only measured at three, the highest of which is not situated at the same height as any temperature sensor. Multiple sensors indicated that the top of an internal boundary layer may be located between 40m and 50m. Thus informed decisions about which instrument heights are suitable for resource assessment and a more complete picture of the structure of the atmosphere encountered by large turbines can only result from an appropriately detailed measurement campaign.

In terms of absolute shear, Figure A5 shows MOST predicts similar values for very unstable to neutral conditions irrespective of measurement height. However, for positive (stable) values of L , the rate of shear is very dependent on measurement height, with largest values expected lower down the mast. Furthermore, the shear levels over the whole mast are closer to those through the lower mast than the upper mast. This reinforces the finding that stability frequency distributions from the two cases using data from the entire mast height were more similar to distributions using measured data from just the lower mast heights. This would suggest that there is little need to extend mast measurements above 50m as it is the lower boundary layer that appears to dominate profiles averaged across the whole mast up to hub height. However, this assumes that MOST is a reliable theory when predicting wind conditions offshore, an assumption which the variation in Figure A6 shows to be questionable, particularly in more stable conditions. Therefore, not only is it important to make wind speed measurements at least to hub height and preferably beyond, temperature measurements should also be made at multiple similar heights. Even for wind directions with large fetches across the North Sea, results from both masts suggest the possibility of non-linear thermal profiles in the SL, contrary to MOST assumptions. These also highlight the need for multiple measurement heights to provide redundancy and help capture the true nature of the offshore atmospheric boundary layer.

Acknowledgements

The authors would like to thank the BMU (Bundesministerium fuer Umwelt, Federal Ministry for the Environment, Nature Conservation and Nuclear Safety) and the PTJ (Projekttraeger Juelich, project executing organisation) for providing data from the FINO1 and FINO3 meteorological masts. The authors would also like to thank E.ON for sponsoring this research through an EPSRC CASE award and the EPSRC Supergen Wind Energy Technologies consortium (grant number: EP/H018662/1) for additional support.

Appendix B: Simulation Mesh Images

Throughout this work, each simulation was initiated with identical basic mesh structures: a cylindrical domain height and radius of 1km and 10km respectively, with a central square region 10km along each edge. Within the central square, the basic horizontal mesh size was 50m whilst the height of the lowest cell was 2m with each subsequent layer increasing at a constant rate to give an average cell height of 45m. Shown below in Figures B1 and B2 are the final mesh structures in each central square region after Windmodeller has completed its mesh refinement process.

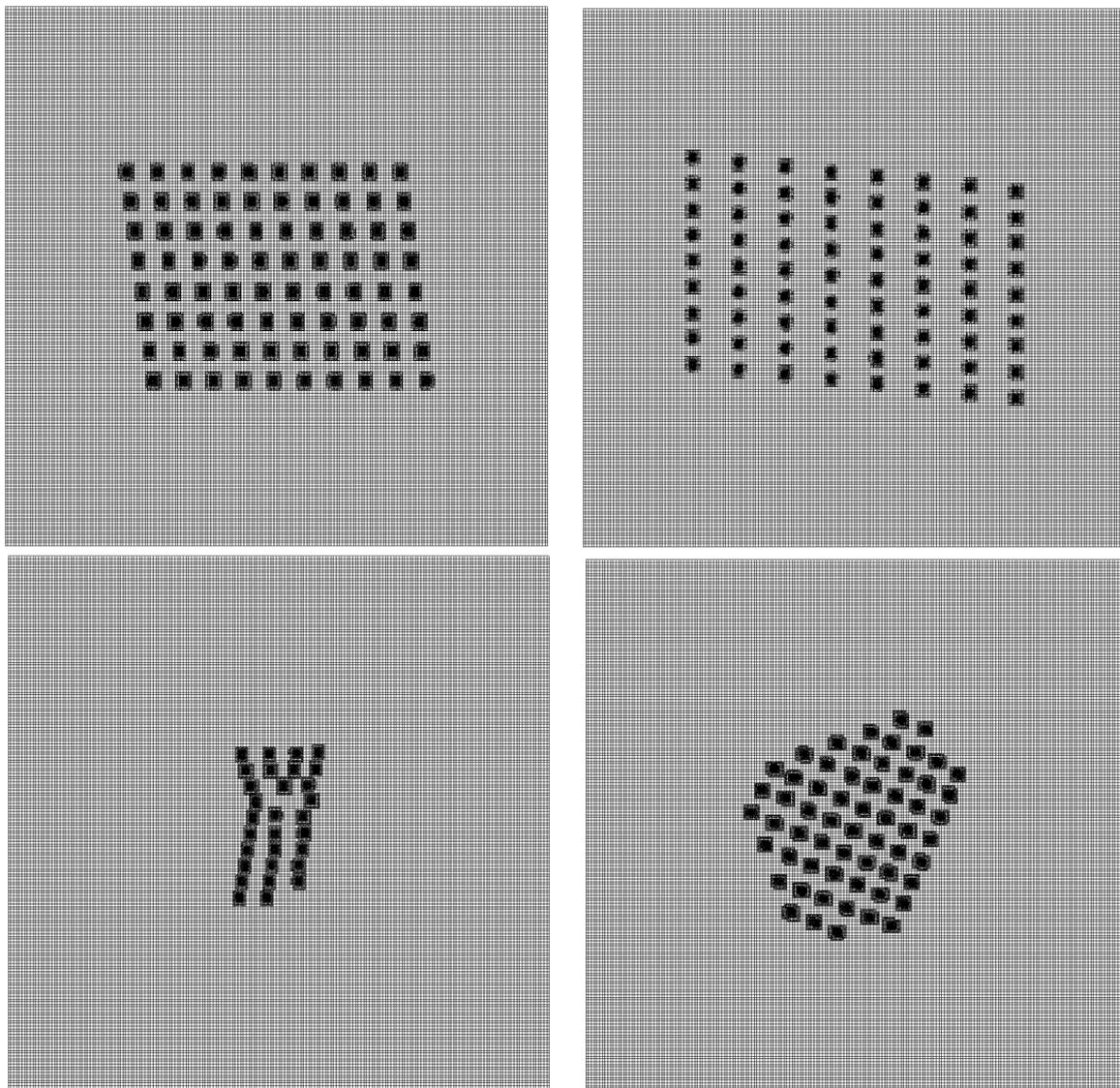


Figure B1 Horizontal mesh structure in the central 10km square region for each of the four wind farms, clockwise from top left: Horns Rev, Nysted, Robin Rigg and Scroby Sands. Due to image scale and resolution, the light gray cell areas are 50m by 50m whilst the dark regions are areas of much higher mesh resolution around each actuator disk as Windmodeller has refined the mesh around each AD. Each mesh is shown at the relevant farm's hub height.

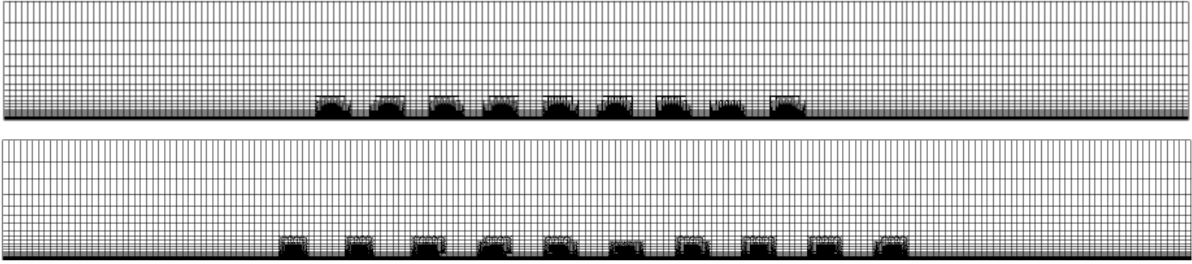


Figure B2 Vertical mesh structure in the central 10km square region. Due to turbine layout complications, cross-sections from only the farms Nysted (top, facing due east) and Horns Rev (bottom, facing due north) are shown. Each mesh is shown as a slice through the centre of a turbine line.

To provide a clearer view of how the mesh refinement process affected the regions close to the ADs, Figures B3 and B4 below show expanded versions of the horizontal and vertical mesh structures respectively.

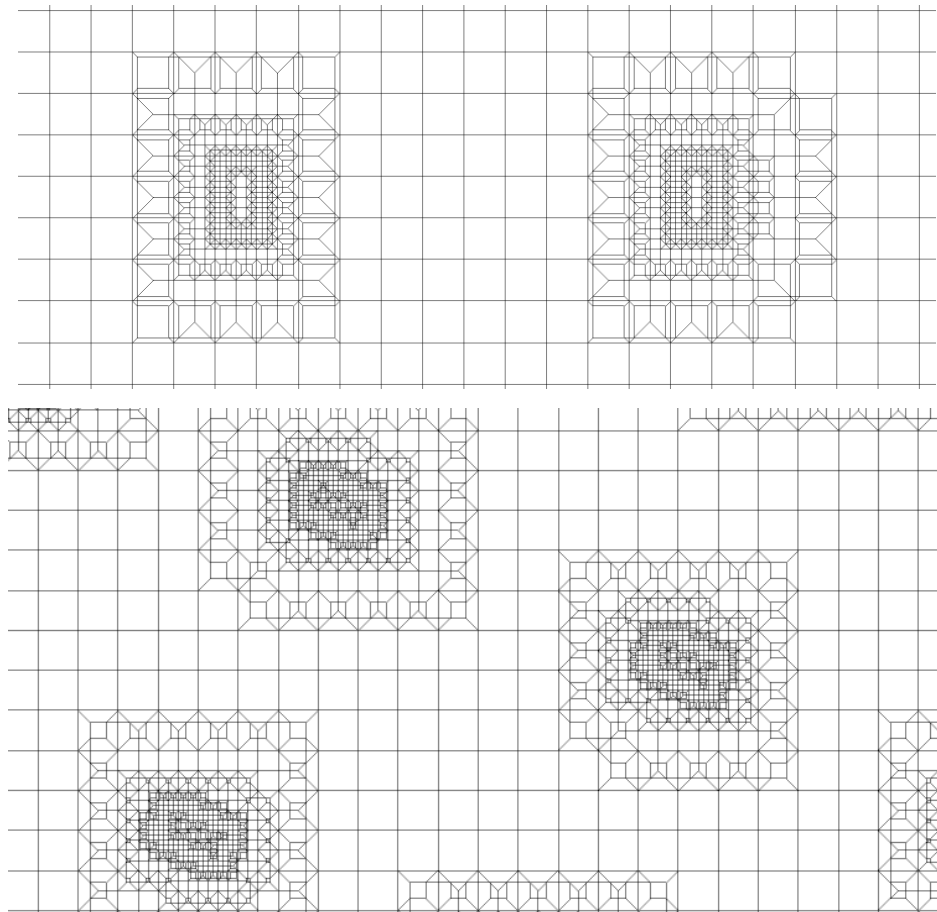


Figure B3 Horizontal mesh structure around actuator disks from the simulations of the Horns Rev (top) and Robin Rigg (bottom) farms. Note that the mesh refinement process does not always result in symmetrical mesh structures around each disk owing to flow direction and complexity. For reference, the larger squares are 50m in length along each edge.

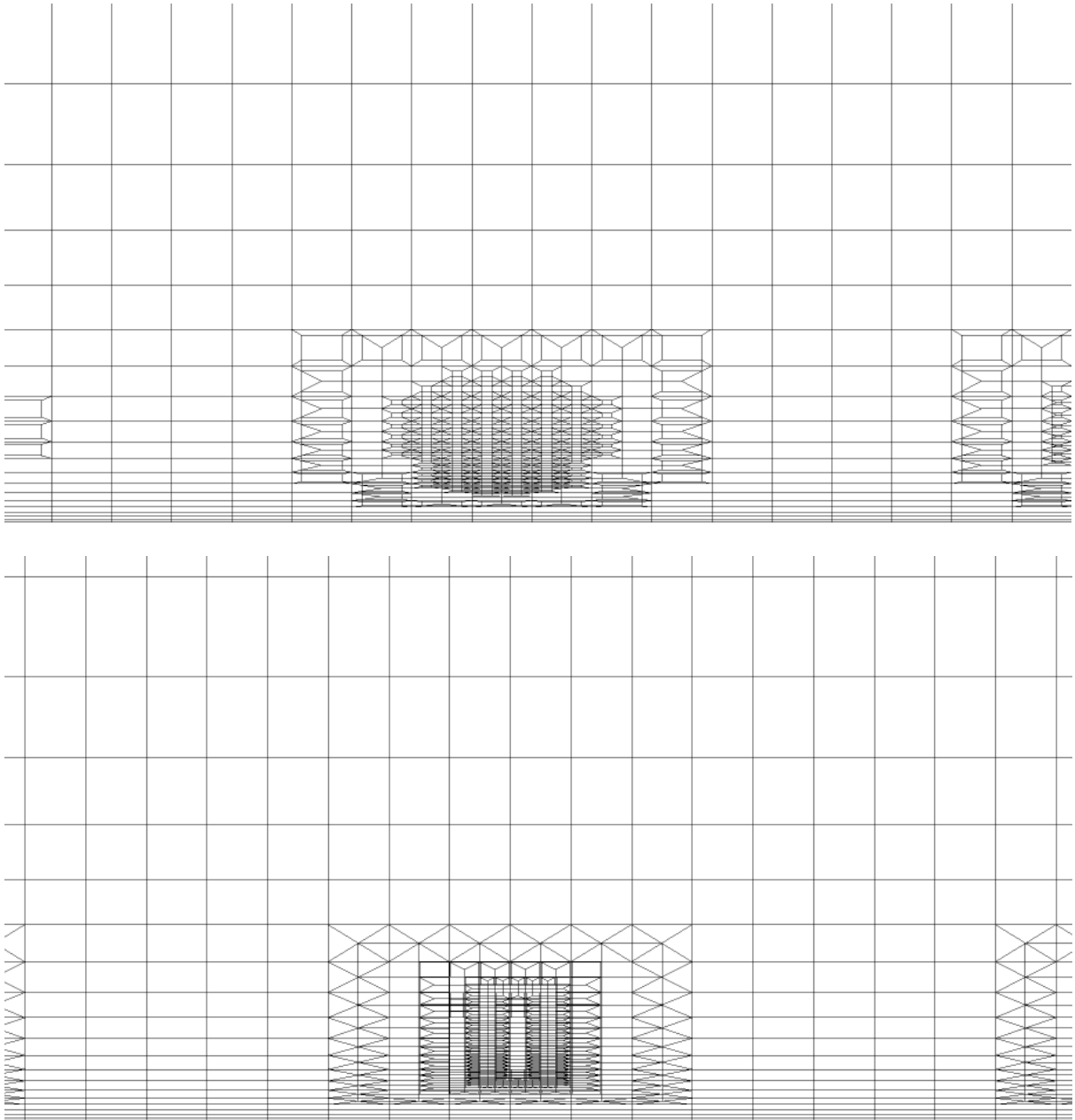


Figure B4 Vertical mesh structure around actuator disks from the front (top) and side (bottom). Note that the mesh refinement process does not always result in symmetrical mesh structures around each disk owing to flow direction and complexity. For reference, the largest cells are 50m wide and the height of the cells outside of the mesh-adaption regions increase with height from 2m at the domain surface.

Bibliography

- [1] “Directive 2009/28/EC of 23 April 2009 on the promotion of the use of energy from renewable sources and amending and subsequently repealing Directives 2001/77/EC and 2003/30/EC,” *Official Journal of the European Union*, vol. 140, pp. 16-62, 2009.
- [2] S. Hsu, “Models for Estimating Offshore Winds from Onshore Meteorological Measurements,” *Boundary-Layer Meteorology*, vol. 20, pp. 341-351, 1981.
- [3] S. C. Pryor and R. J. Barthelmie, “Comparison of Potential Power Production at On- and Offshore Sites,” *Wind Energy*, vol. 4, pp. 173-181, 2001.
- [4] K. Hansen and G. Larsen, “Characterising Turbulence Intensity for Fatigue Load Analysis of Wind Turbines,” *Wind Engineering*, vol. 29, no. 4, pp. 319-329, 2005.
- [5] A. Sathe and W. Bierbooms, “Influence of Different Wind Profiles due to Varying Atmospheric Stability on the Fatigue Life of Wind Turbines,” *Journal of Physics: Conference Series*, vol. 75, pp. 012056-012062, 2007.
- [6] J. Larsen, H. Soerensen, E. Christiansen, S. Naef and P. Vølund, “Experiences from Middelgrunden 40 MW Offshore Wind Farm,” in *Copenhagen Offshore Wind*, Copenhagen, 2005.
- [7] R. Barthelmie and J. Palutikof, “Coastal Wind Speed Modelling for Wind Energy Applications,” *Journal of Wind Engineering and Industrial Aerodynamics*, vol. 62, pp. 213-236, 1996.
- [8] D. McQueen and S. J. Watson, “Validation of Wind Speed Prediction Methods at Offshore Sites,” *Wind Energy*, vol. 9, pp. 75-85, 2006.
- [9] A. Sempreviva, R. Barthelmie and S. Pryor, “Review of Methodologies for Offshore Wind Resource Assessment in European Seas,” *Surveys in Geophysics*, vol. 29, no. 6, pp. 471-497, 2008.
- [10] “FINO1,2,3-Homepage,” [Online]. Available: <http://www.fino-offshore.de/en>.

[Accessed 1 May 2013].

- [11] U. Högström, A. Smedman and H. Bergström, "Calculation of Wind Speed Variation With Height Over the Sea," *Wind Engineering*, vol. 30, pp. 269-286, 2006.
- [12] M. Motta, R. J. Barthelmie and P. Vølund, "The Influence of Non-logarithmic Wind Speed Profiles on Potential Power Output at Danish Offshore Sites," *Wind Energy*, vol. 8, p. 219-236, 2005.
- [13] R. Stull, *An Introduction to Boundary Layer Meteorology*, Dordrecht: Kluwer Academic Publishers Group, 1988.
- [14] E. Batchvarova and S. Gryning, "Applied Model for the Growth of the Daytime Mixed Layer," *Boundary-Layer Meteorology*, vol. 56, pp. 261-274, 1990.
- [15] G. Csanady, "Equilibrium Theory of the Planetary Boundary Layer with an Inversion Lid," *Boundary-Layer Meteorology*, vol. 6, pp. 63-79, 1974.
- [16] P. Seibert, F. Beyrich, S. Gryning, S. Joffre, A. Rasmussen and P. Tercier, "Review and Intercomparison of Operational Methods for the Determination of the Mixing Height," *Atmospheric Environment*, vol. 34, no. 7, pp. 1001-1027, 2000.
- [17] B. Lange, S. Larsen, J. Højstrup and R. Barthelmie, "The Influence of Thermal Effects on the Wind Speed Profile of the Coastal Marine Boundary Layer," *Boundary-Layer Meteorology*, vol. 112, pp. 587-617, 2004.
- [18] J. Businger, J. Wyngaard, Y. Izumi and E. Bradley, "Flux-Profile Relationships in the Atmospheric Surface Layer," *Journal of Atmospheric Science*, vol. 28, pp. 181-189, 1971.
- [19] S.-E. Gryning, E. Batchvarova, B. Brümmner, H. Jørgensen and S. Larsen, "On the Extension of the Wind Profile Over Homogeneous Terrain Beyond the Surface Layer," *Boundary-Layer Meteorology*, vol. 124, pp. 251-268, 2007.
- [20] A. Peña, S. Gryning and C. Hasager, "Measurements and Modelling of the Wind Speed Profile in the Marine Atmospheric Boundary Layer," *Boundary-Layer Meteorology*, vol. 129, pp. 479-495, 2008.

- [21] J. Højstrup, R. Barthelmie, M. Courtney and P. Sanderhoff, "Wind and Turbulence in the Near-Coastal Offshore Environment," in *European Wind Energy Conference and Exhibition*, Thessaloniki, 1994.
- [22] H. Charnock, "Wind Stress on a Water Surface," *Quarterly Journal of the Royal Meteorological Society*, vol. 81, pp. 639-640, 1955.
- [23] J. Garratt, *The Atmospheric Boundary Layer*, Cambridge: Cambridge University Press, 1994.
- [24] J. Wu, "Wind-Stress Coefficients Over Sea Surface Near Neutral Conditions - A Revisit," *Journal of Physical Oceanography*, vol. 10, pp. 727-740, 1980.
- [25] J. Tambke, M. Lange, U. Focken, J. Wolff and J. Bye, "Forecasting Offshore Wind Speeds Above the North Sea," *Wind Energy*, vol. 8, no. 1, pp. 3-16, 2005.
- [26] P. Argyle and S. Watson, "Assessing the Atmospheric Stability's Dependence on Measurement Height in Offshore Locations," *Journal of Wind Engineering and Industrial Aerodynamics*, vol. 131, pp. 88-99, 2014.
- [27] H. Johnson, J. Højstrup, H. Vested and S. Larsen, "On the Dependence of Sea Surface Roughness on Wind Waves," *Journal of Physical Oceanography*, vol. 28, no. 9, pp. 1702-1716, 1998.
- [28] N. Mortensen, L. Landburg, I. Tron and E. Peterson, "Wind Analysis and Application Program (WAsP) - User's Guid," Report Risø-I-666(EN) (v.2), Risø National Laboratory, Roskilde, 1993.
- [29] B. Lange, J. Højstrup, S. Larsen and R. Barthelmie, "A Fetch Dependent Model of Sea Surface Roughness For Offshore Wind Power Utilisation," in *European Wind Energy Conference and Exhibition*, Copenhagen, 2001.
- [30] B. Lange, S. Larsen, J. Højstrup and R. Barthelmie, "Modelling the Vertical Wind Speed and Turbulence Intensity Profiles at Prospective Offshore Wind Farm Sites," in *Global Windpower Conference and Exhibition*, Paris, 2002.
- [31] H. Frank, S. Larsen and J. Højstrup, "Simulated Wind Power Offshore Using Different Parametrizations for the Sea Surface Roughness," *Wind Energy*, vol. 3, pp. 69-79, 2000.

- [32] R. Barthelmie, "Evaluating the Impact of Wind Induced Roughness Change and Tidal Range on Extrapolation of Offshore Vertical Wind Speed Profiles," *Wind Energy*, vol. 4, no. 3, pp. 99-105, 2001.
- [33] R. Barthelmie, S. Frandsen, N. Nielsen, S. Pryor, P. Rethore and H. Jørgensen, "Modelling and Measurements of Power Losses and Turbulence Intensity in Wind Turbine Wakes at Middelgrunden Offshore Wind Farm," *Wind Energy*, vol. 10, pp. 517-528, 2007.
- [34] R. Barthelmie, S. Frandsen, P. Rethore and L. Jensen, "Analysis of Atmospheric Impacts on the Development of Wind Turbine Wakes at the Nysted Wind Farm," in *European Offshore Wind Energy Conference and Exhibition*, Berlin, 2007.
- [35] A. Sathe, S. Gryning and A. Peña, "Comparison of the Atmospheric Stability and Wind Profiles at Two Wind Farm Sites over a Long Marine Fetch in the North Sea," *Wind Energy*, vol. 14, pp. 767-780, 2011.
- [36] R. Barthelmie, "The Effects of Atmospheric Stability on Coastal Wind Climates," *Meteorological Applications*, vol. 6, pp. 39-47, 1999.
- [37] D. Heard, K. Read, J. Methven, S. Al-Haider, W. Bloss, G. Johnson, M. Pilling, P. Seakins, S. Smith, R. Sommariva, J. Stanton, T. Still, T. Ingham, B. Brooks, G. De Leeuw, A. Jackson, J. McQuaid, R. Morgan, M. Smith, L. Carpenter, N. Carslaw, J. Hamilton, J. Hopkins, J. Lee, A. Lewis, R. Purvis, D. Wevill, N. Brough, T. Green, G. Mills, S. Penkett, J. Plane, A. Saiz-Lopez, D. Worton, P. Monks, Z. Fleming, A. Rickard, M. Alfarra, J. Allan, K. Bower, H. Coe, M. Cubison, M. Flynn, G. McFiggans, M. Gallagher, E. Norton, C. O'Dowd, J. Shillito, D. Topping, G. Vaughan, P. Williams, M. Bitter, S. Ball, R. Jones, I. Povey, S. O'Doherty, P. Simmonds, A. Allen, R. Kinnersley, D. Beddows, M. Dall'Osto, R. Harrison, R. Donovan, M. Heal, S. Jennings, C. Noone and G. Spain, "The North Atlantic Marine Boundary Layer Experiment(NAMBLEX). Overview of the campaign held at Mace Head, Ireland, in summer 2002," *Atmospheric Chemistry and Physics*, vol. 6, no. 8, pp. 2241-2272, 2006.
- [38] R. Barthelmie, J. Badger, S. Pryor, C. Hasager, M. Christiansen and B.

- Jørgensen, "Offshore Coastal Wind Speed Gradients: Issues for the Design and Development of Large Offshore Windfarms," *Wind Engineering*, vol. 31, no. 6, pp. 369-382, 2007.
- [39] S. Pryor and B. Barthelmie, "Analysis of the Effect of the Coastal Discontinuity on Near-surface Flow," *Annales Geophysicae*, vol. 16, pp. 882-888, 1998.
- [40] E. Hunter, R. Chant, L. Bowers, S. Glenn and J. Kohut, "Spatial and Temporal Variability of Diurnal Wind Forcing in the Coastal Ocean," *Geophysical Research Letters*, vol. 34, no. 3, p. L03607, 2007.
- [41] A. Smedman, H. Bergström and B. Grisogono, "Evolution of Stable Internal Boundary Layers over a Cold Sea," *Journal of Geophysical Research*, vol. 102, pp. 1091-1099, 1997.
- [42] M. Stunder and S. Sethuraman, "A Comparative Evaluation of the Coastal Internal Boundary-Layer Height Equations," *Boundary-Layer Meteorology*, vol. 32, pp. 177-204, 1985.
- [43] A. Van Wijk, A. Beljaars, A. Holtslag and W. Turkenburg, "Evaluation of Stability Corrections in Wind Speed Profiles Over the North Sea," *Journal of Wind Engineering and Industrial Aerodynamics*, vol. 33, pp. 551-566, 1990.
- [44] S. Hsu, "A Note on Estimating the Height of the Convective Internal Boundary Layer Near Shore," *Boundary-Layer Meteorology*, vol. 35, pp. 311-316, 1986.
- [45] A. Monin and A. Obukhov, "Osnovnye zakonomernosti turbulentnogo peremeshivaniya v prizemnom sloe atmosfery (Basic Laws of Turbulent Mixing in the Surface Layer of the Atmosphere)," *Trudy geofiz. inst. AN SSSR*, vol. 24, no. 151, pp. 163-187, 1954.
- [46] J. Edson and C. Fairall, "Similarity Relationships in the Marine Atmospheric Surface Layer for Terms in the TKE and Scalar Variance Budgets," *Journal of the Atmospheric Sciences*, vol. 55, pp. 2311-2328, 1998.
- [47] S. Wharton and J. Lundquist, "Assessing Atmospheric Stability and its Impacts on Rotor-disk Wind Characteristics at an Onshore Wind Farm," *Wind Energy*, vol. 15, pp. 525-546, 2012.
- [48] P. Argyle and S. Watson, "A Study of the Surface Layer Atmospheric Stability

- at Two UK Offshore Sites,” in *European Wind Energy Conference and Exhibition*, Copenhagen, 2012.
- [49] A. Peña and S. Gryning, “Charnock’s Roughness Length Model and Non-dimensional Wind Profiles Over the Sea,” *Boundary-Layer Meteorology*, vol. 128, pp. 191-203, 2008.
- [50] T. Foken, “50 Years of the Monin-Obukhov Similarity Theory,” *Boundary-Layer Meteorology*, vol. 119, no. 3, pp. 431-447, 2006.
- [51] P. Eecen, J. Wagenaar, N. Stefanatos, T. Pederson, R. Wagner and K. Hansen, “Final Report UpWind 1A2 Meteorology,” ECN-E--11-013, 2011.
- [52] P. Argyle and S. Watson, “The Influence of Measurement Height and Stability Calculation Methods for a Location in the Irish Sea,” in *European Offshore Wind Energy Conference and Exhibition*, Frankfurt, 2013.
- [53] D. Golder, “Relations Among Stability Parameters in the Surface Layer,” *Boundary-Layer Meteorology*, vol. 3, pp. 47-58, 1972.
- [54] J. Tambke, L. Claveri, J. Bye, C. Poppinga, B. Lange, L. Bremen, F. Durante and J. Wolff, “Offshore Meteorology for Multi-Mega-Watt Turbines,” in *European Wind Energy Conference and Exhibition*, Athens, 2006.
- [55] J. Coelingh, A. Van Wijk and A. Holtslag, “Analysis of Wind Speed Observations over the North Sea,” *Journal of Wind Engineering and Industrial Aerodynamics*, vol. 61, pp. 51-69, 1996.
- [56] B. Cañadillas, D. Muñoz-esparza and T. Neumann, “Fluxes Estimation and the Derivation of the Atmospheric Stability at the Offshore Mast FINO1,” in *European Wind Energy Offshore Conference and Exhibition*, Amsterdam, 2011.
- [57] A. Dyer and B. Hicks, “Flux-Gradient Relationships in the Constant Flux Layer,” *Quarterly Journal Royal Meteorological Society*, vol. 96, pp. 715-721, 1970.
- [58] T. H. Chen, A. Henderson-Sellers, P. C. D. Milly, A. J. Pitman, A. C. M. Beljaars, J. Polcher, F. Abramopoulos, A. Boone, S. Chang, F. Chen, Y. Dai, C. E. Desborough, R. E. Dickinson, L. Dümenil, M. Ek, J. R. Garratt, N. Gedney, Y. M. Gusev, J. Kim, R. Koster, E. A. Kowalczyk, K. Laval, J. Lean, D.

- Lettenmaier, X. Liang, J. -F. Mahfouf, H. -T. Mengelkamp, K. Mitchell, O. N. Nasonova, J. Noilhan, A. Robock, C. Rosenzweig, J. Schaake, C. A. Schlosser, J. -P. Schulz, Y. Shao, A. B. Shmakin, D. -L. Verseghy, P. Wetzel, E. F. Wood, Y. Xue, Z. -L. Yang and Q. Zeng, "Cabauw Experimental Results from the Project for Intercomparison of Land-Surface Parameterization Schemes," *Journal of Climate*, vol. 10, pp. 1194-1215, 1997.
- [59] S. Zilitinkevich, P. Johansson, D. Mironov and A. Baklanov, "A Similarity-theory Model for Wind Profile and Resistance Law in Stably Stratified Planetary Boundary Layers," *Journal of Wind Engineering and Industrial Aerodynamics*, Vols. 74-76, pp. 209-218, 1998.
- [60] A. Grachev and C. Fairall, "Dependence of the Monin–Obukhov Stability Parameter on the Bulk Richardson Number over the Ocean," *Journal of Applied Meteorology*, vol. 36, pp. 406-414, 1997.
- [61] C. Fairall, E. Bradley, J. Godfrey, G. Wick, J. Edson and G. Young, "Cool-Skin and Warm-Layer Effects on Sea Surface Temperature," *Journal of Geophysical Research*, vol. 101, pp. 1295-1308, 1996.
- [62] V. Canuto, "Critical Richardson Numbers and Gravity Waves," *Astronomy and Astrophysics*, vol. 384, pp. 1119-1123, 2002.
- [63] B. Galperin, S. Sukoriansky and P. Anderson, "On the Critical Richardson Number in Stably Stratified Turbulence," *Atmospheric Science Letters*, vol. 8, pp. 65-69, 2007.
- [64] G. Geernaert and S. Larsen, "On the Role of Humidity in Estimating Marine Surface Layer Stratification and Scatterometer Cross Section," *Journal of Geophysical Research*, vol. 98, pp. 927-932, 1993.
- [65] S. Frandsen and M. Thøgersen, "Integrated Fatigue Loading for Wind Turbines in Wind Farms by Combining Ambient Turbulence and Wakes," *Wind Engineering*, vol. 23, pp. 327-339, 1999.
- [66] K. Hansen, R. Barthelmie, L. Jensen and A. Sommer, "The Impact of Turbulence Intensity and Atmospheric Stability on Power Deficits due to Wind Turbine Wakes at Horns Rev Wind Farm," *Wind Energy*, vol. 15, pp. 183-196,

2012.

- [67] C. Alinot and C. Masson, "Aerodynamic Simulations of Wind Turbines Operating in Atmospheric Boundary Layer With Various Thermal Stratifications," *American Institute of Aeronautics and Astronautics*, vol. 42, pp. 206-215, 2002.
- [68] R. Barthelmie, K. Hansen, S. Frandsen, O. Rathmann, J. Schepers, W. Schlez, J. Phillips, K. Rados, A. Zervos, E. Politis and P. Chaviaropoulos, "Modelling and Measuring Flow and Wind Turbine Wakes in Large Wind Farms Offshore," *Wind Energy*, vol. 12, pp. 431-444, 2009.
- [69] R. Barthelmie, S. Pryor, S. Frandsen, K. Hansen, J. Schepers, K. Rados, W. Schlez, A. Neubert, L. Jensen and S. Neckelmann, "Quantifying the Impact of Wind Turbine Wakes on Power Output at Offshore Wind Farms," *Journal of Atmospheric and Oceanic Technology*, vol. 27, pp. 1302-1318, 2010.
- [70] D. Lenschow, X. Li, C. Zhu and B. Stankov, "The Stably Stratified Boundary Layer Over the Great Plains I: Mean and Turbulence Structure," *Boundary-Layer Meteorology*, vol. 42, pp. 95-121, 1988.
- [71] A. Holtslag, "Estimates of Diabatic Wind Speed Profiles from Near-Surface Weather Observations," *Boundary-Layer Meteorology*, vol. 29, pp. 225-250, 1984.
- [72] I. Antoniou, H. Jørgensen, T. Mikkelsen, S. Frandsen, R. Barthelmie, C. Perstrup and M. Hurtig, "Offshore Wind Profile Measurements from Remote Sensing Instruments," in *European Wind Energy Association Conference and Exhibition*, Athens, 2006.
- [73] R. Barthelmie, O. Hansen, K. Enevoldsen, J. Højstrup, S. Frandsen, S. Pryor, S. Larsen, M. Motta and P. Sanderhoff, "Ten Years of Meteorological Measurements for Offshore Wind Farms," *Journal of Solar Energy Engineering*, vol. 127, pp. 170-176, 2005.
- [74] R. Barthelmie, "Monitoring offshore wind and turbulence characteristics in Denmark," in *Proceedings of the 21st British Wind Energy Association Conference*, Cambridge, 1999.

- [75] E. Rareshide, A. Tindal, C. Johnson, A. Graves, E. Simpson, J. Bleeg, T. Harris and D. Schoborg, "Effects of Complex Wind Regimes on Turbine Performance," in *AWEA Windpower Conference*, Chicago, 2009.
- [76] S. Frandsen, H. Jørgensen, R. Barthelmie, O. Rathmann, J. Badger, K. Hansen, S. Ott, P. Rethore, S. Larsen and L. Jensen, "The Making of a Second-generation Wind Farm Efficiency Model Complex," *Wind Energy*, vol. 12, pp. 445-458, 2009.
- [77] R. Barthelmie, G. Larsen, S. Pryor, H. Jørgensen, H. Bergström, W. Schlez, K. Rados, B. Lange, P. Vølund, S. Neckelmann, S. Mogensen, G. Schepers, T. Hegberg, L. Folkerts and M. Magnusson, "ENDOW (Efficient Development of Offshore Wind Farms): Modelling Wake and Boundary Layer Interactions," *Wind Energy*, vol. 7, no. 3, pp. 225-245, 2004.
- [78] L. Landberg, L. Myllerup, O. Rathmann, E. Petersen, B. Jørgensen, J. Badger and N. Mortensen, "Wind Resource Estimation - An Overview," *Wind Energy*, vol. 6, no. 3, pp. 261-271, 2003.
- [79] S. Salcedo-Sanz, B. Saavedra-Moreno, A. Paniagua-Tineo, L. Prieto and A. Portilla-Figueras, "A Review of Recent Evolutionary Computation-Based Techniques in Wind Turbines Layout Optimization Problems," *Central European Journal of Computer Science*, vol. 1, pp. 101-107, 2011.
- [80] Y. Eroğlu and S. Seçkiner, "Design of Wind Farm Layout using Ant Colony Algorithm," *Renewable Energy*, vol. 44, pp. 53-62, 2012.
- [81] P. Jackson and J. Hunt, "Turbulent Wind Flow Over a Low Hill," *Quarterly Journal of the Royal Meteorological Society*, vol. 101, no. 430, pp. 929-955, 1975.
- [82] I. Troen and A. De Baas, "A Spectral Diagnostic Model for Wind Flow Simulation in Complex Terrain," in *European Wind Energy Conference and Exhibition*, Rome, 1986.
- [83] GL Garrad Hassan, "WindFarmer 4.2," May 2011. [Online]. Available: www.glgarradhassan.com.
- [84] I. Ammara, C. Leclerc and C. Masson, "A Viscous Three-Dimensional

- Differential/Actuator-Disk Method for the Aerodynamic Analysis of Wind Farms,” *Journal of Solar Energy Engineering*, vol. 124, no. 4, pp. 345-356, 2002.
- [85] A. Kasmi and C. Masson, “An Extended κ - ϵ Model for Turbulent Flow Through Horizontal-Axis Wind Turbines,” *Journal of Wind Engineering and Industrial Aerodynamics*, vol. 96, pp. 103-122, 2008.
- [86] G. Smith, A. Neubert and W. Schlez, “Impact of Large Neighbouring Wind Farms on Energy Yield of Offshore Wind Farms,” in *European Wind Energy Association Offshore Conference*, Amsterdam, 2011.
- [87] P. Lissaman and E. Bate, “Energy Effectiveness of Arrays of Wind Energy,” Aerovironment Inc. Report AV FR 7058, Pasadena, USA, 1977.
- [88] J. Ainslie, “Development of an Eddy Viscosity Model for Wind Turbine Wakes,” in *British Wind Energy Conference and Exhibition*, Oxford, 1985.
- [89] P. Vermeulen, “An Experimental Analysis of Wind Turbine Wakes,” in *Third International Symposium on Wind Energy Systems*, Lyngby, 1980.
- [90] I. Katić, J. Højstrup and N. Jensen, “A Simple Model for Cluster Efficiency,” in *European Wind Energy Conference and Exhibition*, Rome, 1986.
- [91] P. Lissaman, “Energy Effectiveness of Arbitrary Arrays of Wind Turbines,” *Journal of Energy*, vol. 3, no. 6, pp. 323-328, 1979.
- [92] S. Voutsinas, K. Rados and A. Zervos, “The Effect of the Non-Uniformity of the Wind Velocity Field in the Optimal Design of Wind Parks,” in *European Wind Energy Association Conference and Exhibition*, Madrid, 1990.
- [93] D. Smith and G. Taylor, “Further Analysis of Turbine Wake Development and Interaction Data,” in *BWEC Wind Energy Conversion*, Swansea, 1991.
- [94] P. Builtjes and P. Vermeulen, “Turbulence in Wind Clusters,” in *Proc. 4th Int. Symp. on Wind Energy Systems*, Stockholm, 1982.
- [95] M. Méchali, R. Bathelmie, S. Frandsen, L. Jensen and P. Réthoré, “Wake Effects at Horns Rev and their Influence on Energy Production,” in *European Wind Energy Assosiation Conference and Exhibition*, Athens, 2006.

- [96] R. Barthelmie and L. Jensen, "Evaluation of Wind Farm Efficiency and Wind Turbine Wakes at the Nysted Offshore Wind Farm," *Wind Energy*, vol. 13, pp. 573-586, 2010.
- [97] A. Crespo, J. Hernández and S. Frandsen, "Survey of Modelling Methods for Wind Turbine Wakes and Wind Farms," *Wind Energy*, vol. 2, pp. 1-24, 1999.
- [98] B. Newman, "The Spacing of Wind Turbines in Large Arrays," *Energy Conversion*, vol. 16, pp. 169-171, 1977.
- [99] S. Frandsen, "On the Wind Speed Reduction in the Center of Large Clusters of Wind Turbines," *Journal of Wind Engineering and Industrial Aerodynamics*, vol. 39, pp. 251-265, 1992.
- [100] A. Rados, G. Larsen, R. Barthelmie, W. Schlez, B. Lange, G. Schepers, T. Hegberg and M. Magnisson, "Comparison of Wake Models With Data for Offshore Windfarms," *Wind Engineering*, vol. 25, pp. 271-280, 2001.
- [101] S. Emeis and S. Frandsen, "Reduction of Horizontal Wind Speed in a Boundary Layer with Obstacles," *Boundary-Layer Meteorology*, vol. 64, pp. 297-305, 1993.
- [102] E. Bossanyi, C. Maclean, G. Whittle, P. Dunn, N. Lipman and P. Musgrove, "The Efficiency of Wind Turbine Clusters," in *Third International Symposium on Wind Energy Systems*, Lyngby, 1980.
- [103] D. Milborrow, "The Performance of Arrays of Wind Turbines," *Journal of Industrial Aerodynamics*, vol. 5, pp. 403-430, 1980.
- [104] K. Rados, J. Prospathopoulos, N. Stefanatos, E. Politis, P. Chaviaropoulos and A. Zervos, "CFD Modeling Issues of Wind Turbine Wakes Under Stable Atmospheric Conditions," in *European Wind Energy Association Conference and Exhibition*, Marseilles, 2009.
- [105] C. Wang and R. Prinn, "Potential Climatic Impacts and Reliability of Very Large-scale Wind Farms," *Atmospheric Chemistry and Physics*, vol. 10, no. 4, pp. 2053-2061, 2010.
- [106] W. Schlez, A. Umaña, R. Barthelmie, G. Larsen, K. Rados, B. Lange, G. Schepers and T. Hegberg, "ENDOW: Improvement of Wake Models Within

- Offshore Wind Farms,” *Wind Engineering*, vol. 25, pp. 281-287, 2001.
- [107] J. Ainslie, “Calculating the Flowfield in the Wake of Wind Turbines,” *Journal of Wind Engineering and Industrial Aerodynamics*, vol. 27, pp. 213-224, 1988.
- [108] A. Crespo, F. Manuel, D. Moreno, E. Fraga and J. Hernández, “Numerical Analysis of Wind Turbine Wakes,” in *Proceedings of the Delphi Workshop on Wind Energy-Applications*, Delphi, 1985.
- [109] B. Lange, H. Waldl, R. Barthelmie, A. Guerrero and D. Heinemann, “Modelling of Offshore Wind Turbine Wakes with the Wind Farm Program FLAP,” *Wind Energy*, vol. 6, no. 1, pp. 87-104, 2003.
- [110] A. Tindal, “Dynamic Loads in Wind Farms, Final Technical Report,” CEC Project JOUR-0084-C, 1993.
- [111] A. Crespo, J. Hernández, E. Fraga and C. Andreu, “Experimental Validation of the UPM Computer Code to Calculate Wind Turbine Wakes and Comparison with Other Models,” *Journal of Wind Engineering and Industrial Aerodynamics*, vol. 27, pp. 77-88, 1988.
- [112] A. Jiménez, A. Crespo, E. Migoya and J. Garcia, “Advances in Large-Eddy Simulation of a Wind Turbine Wake,” *Journal of Physics: Conference Series*, vol. 75, p. 012041, 2007.
- [113] G. Smith, W. Schlez, A. Liddell, A. Neubert and A. Peña, “Advanced Wake Model for Very Closely Spaced Turbines,” in *European Wind Energy Association Annual Conference and Exhibition*, Athens, 2006.
- [114] O. Coceal, T. Thomas and S. Belcher, “Spatially-Averaged Flow Statistics within a Canopy of Large Bluff Bodies: Results from Direct Numerical Simulations,” *Acta Geophysica*, vol. 56, no. 3, pp. 862-875, 2008.
- [115] F. Cadieux, J. Domaradzki, T. Sayadi, S. Bose and F. Duchaine, “DNS and LES of Separated Flows at Moderate Reynolds Numbers,” in *Center of Turbulence Research Proceedings of the Summer Program*, Stanford, 2012.
- [116] R. Stoll and F. Porté-Agel, “Dynamic Subgrid-scale Models for Momentum and Scalar Fluxes in Large-eddy Simulations of Neutrally Stratified Atmospheric Boundary Layers Over Heterogeneous Terrain,” *Water Resources Research*,

vol. 42, p. W01409, 2006.

- [117] F. Castellani and A. Vignaroli, "An Application of the Actuator Disc Model for Wind Turbine Wakes Calculations," *Applied Energy*, vol. 101, pp. 432-440, 2013.
- [118] F. Porté-Agel, Y. Wu, H. Lu and R. Conzemius, "Large-Eddy Simulation of Atmospheric Boundary Layer Flow Through Wind Turbines and Wind Farms," *Journal of Wind Engineering and Industrial Aerodynamics*, vol. 99, pp. 154-168, 2011.
- [119] A. Jiménez, A. Crespo, E. Migoya and J. Garcia, "Large-Eddy Simulation of Spectral Coherence in a Wind Turbine Wake," *Environmental Research Letters*, vol. 3, p. 015004, 2008.
- [120] Y. Wu and F. Porté-Agel, "Simulation of Turbulent Flow Inside and Above Wind Farms: Model Validation and Layout Effects," *Boundary-Layer Meteorology*, vol. 146, pp. 181-205, 2013.
- [121] Á. Jiménez, A. Crespo and E. Migoya, "Application of a LES Technique to Characterize the Wake Deflection of a Wind Turbine in Yaw," *Wind Energy*, vol. 13, pp. 559-572, 2010.
- [122] G. Corten and P. Schaak, "Heat and Flux, Increase of Wind Farm Production by Reduction of the Axial Induction," in *European Wind Energy Association Annual Conference*, Madrid, 2003.
- [123] M. Calaf, C. Meneveau and J. Mayers, "Large-Eddy Simulation Study of Fully Developed Wind-Turbine Array Boundary Layers," *Physics of Fluids*, vol. 22, p. 015110, 2010.
- [124] S. Aubrun, S. Loyer, P. Hancock and P. Hayden, "Wind Turbine Wake Properties: Comparison Between a Non-Rotating Simplified Wind Turbine Model and a Rotating Model," *Journal of Wind Engineering and Industrial Aerodynamics*, vol. 120, pp. 1-8, 2013.
- [125] P. Krogstad and P. Eriksen, "'Blind Test' Calculations of the Performance and Wake Development for a Model Wind Turbine," *Renewable Energy*, vol. 50, pp. 325-333, 2013.

- [126] J. Ainslie, "Wake Modelling and the Prediction of Turbulent Properties," in *British Wind Energy Conference and Exhibition*, Cambridge, 1986.
- [127] R. Barthelmie, L. Folkerts, G. Larsen, K. Rados, S. Pryor, S. Frandsen, B. Lange and G. Schepers, "Comparison of Wake Simulations with Offshore Wind Turbine Wake Profiles Measured by Sodar," *Journal of Atmospheric and Oceanic Technology*, vol. 23, pp. 888-901, 2006.
- [128] W. Schlez and A. Neubert, "New Developments in Large Wind Farm Modelling," in *European Wind Energy Association Conference and Exhibition*, Marseilles, 2009.
- [129] J. Cleve, M. Greiner, P. Enevoldsen, B. Birkemose and L. Jensen, "Model-based Analysis of Wake-flow Data in the Nysted Offshore Wind Farm," *Wind Energy*, vol. 12, pp. 125-135, 2009.
- [130] PHOENICS Reference Manual TR200, London: CHAM, 1991.
- [131] C. Montavon, I. Jones, C. Staples, C. Strachan and I. Gutierrez, "Practical Issues in the use of CFD for Modelling Wind Farms," in *European Wind Energy Association Conference and Exhibition*, Marseilles, 2009.
- [132] Y. Wu and F. Porté-Agel, "Large-Eddy Simulation of Wind-Turbine Wakes: Evaluation of Turbine Parametrisations," *Boundary-Layer Meteorology*, vol. 138, pp. 345-366, 2011.
- [133] P. Réthoré, N. Sørensen and F. Zahle, "Validation of an Actuator Disc Model," in *European Wind Energy Association Conference and Exhibition*, Warsaw, 2010.
- [134] B. Launder and D. Spalding, "The Numerical Computation of Turbulent Flows," *Computer Methods in Applied Mechanics and Engineering*, vol. 3, pp. 269-289, 1974.
- [135] D. Cabezón, J. Sans, I. Martí and A. Crespo, "CFD Modelling of the Interaction Between the Surface Boundary Layer and Rotor Wake Comparison of Results Obtained with Different Turbulence Models and Mesh Strategies," in *European Wind Energy Association Conference and Exhibition*, Marseilles, 2009.
- [136] P. Réthoré, N. Sørensen, A. Bechmann and F. Zahle, "Study of the

- Atmospheric Wake Turbulence of a CFD Actuator Disc Model,” in *European Wind Energy Association Conference and Exhibition*, Marseille, 2009.
- [137] J. Sørensen and W. Shen, “Numerical Modeling of Wind Turbine Wakes,” *Journal of Fluids Engineering*, vol. 124, pp. 393-399, 2002.
- [138] UpWind, “Design Limits and Solutions for Very Large Wind Turbines,” The European Wind Energy Association, Brussels, 2011.
- [139] N. Sørensen and J. Johansen, “UPWIND, Aerodynamics and Aero-Elasticity Rotor Aerodynamics in Atmospheric Shear Flow,” in *European Wind Energy Association Conference and Exhibition*, Milan, 2007.
- [140] F. Porté-Agel, M. Pahlow, C. Meneveau and M. Parlange, “Atmospheric Stability Effects on Subgrid-Scale Physics for Large-Eddy Simulation,” *Advances in Water Resources*, vol. 24, pp. 1085-1102, 2001.
- [141] L. Chamorro and F. Porté-Agel, “Effects of Thermal Stability and Incoming Boundary-Layer Flow Characteristics on Wind-Turbine Wakes: A Wind-Tunnel Study,” *Boundary-Layer Meteorology*, vol. 136, pp. 515-533, 2010.
- [142] H. Versteeg and W. Malalasekera, *An Introduction to Computational Fluid Dynamics: The Finite Volume Method (Second Edition)*, Harlow: Pearson Education Limited, 2007.
- [143] F. Menter, “Zonal Two Equation $k-\omega$ Turbulence Models for Aerodynamic Flows,” *AIAA*, p. 2906, 1993.
- [144] F. Menter, “Influence of Freestream Values on $k-\omega$ Turbulence Model Predictions,” *AIAA*, vol. 30, no. 6], 1992.
- [145] F. Menter, M. Kuntz and R. Langtry, “Ten Years of Industrial Experience with the SST Turbulence Model,” in *Proc of the 4 th International Symposium on Turbulence, Heat and Mass Transfer*, Antalya, 2003.
- [146] S. Wylie and S. Watson, “A Computational Fluid Dynamics (CFD) Study of Wind Flow Around a Model Forest: Comparison of Different Turbulent Closure Schemes and Varying Leaf Area Density (LAD),” in *European Wind Energy Association Conference and Exhibition*, Brussels, 2011.

- [147] C. Montavon, S. Hui, J. Graham, D. Malins, P. Housley, E. Dahl, P. de Villiers and B. Gribben, "Offshore Wind Accelerator: Wake Modelling Using CFD," in *European Wind Energy Association Conference and Exhibition*, Brussels, 2011.
- [148] C. Montavon and I. Jones, "Atmospheric Stability and Coriolis Effects in the Simulation of Large Array Losses," in *European Wind Energy Association Conference and Exhibition*, Vienna, 2013.
- [149] G. Carney, P. Housley, C. Montavon and I. Jones, "Practical Usage of CFD for Wake Effects Prediction Within Offshore Wind Farms," in *European Wind Energy Association Conference and Exhibition*, Copenhagen, 2012.
- [150] M. Brower, J. Vidal and P. Beaucage, "Evaluation of Four Numerical Wind Flow Models," in *EWEA Technology Workshop: Resource Assessment*, Dublin, 2013.
- [151] G. Crasto and F. Castellani, "Wakes Calculation in a Offshore Wind Farm," *Wind Engineering*, vol. 37, no. 3, pp. 269-280, 2013.
- [152] C. Montavon, *Simulation of Atmospheric Flows Over Complex Terrain for Wind Power Potential Assessment*, 1998.
- [153] S. Zilitinkevich and D. Mironov, "A Multi-Limit Formulation for the Equilibrium Depth of a Stably Stratified Boundary Layer," *Boundary-Layer Meteorology*, vol. 81, pp. 325-351, 1996.
- [154] S. Seshadhri, C. Montavon and I. Jones, "Coriolis Effects in the Simulation of Large Array Losses: Preliminary Results on 'Wall Effect' and Wake Asymmetry," in *Offshore '13*, Frankfurt, 2013.
- [155] V. Riedel and T. Neumann, "RANS-Modelling of Wind Flow through Large Offshore Wind Farms," in *European Wind Energy Association Annual Conference and Exhibition*, Milan, 2007.
- [156] A. Bechmann, N. Sorensen and N. Johansen, "Atmospheric Flow over Terrain using Hybrid RANS/LES," in *European Wind Energy Association Annual Conference and Exhibition*, Milan, 2007.
- [157] K. Hansen, P. Eecen, J. Wagenaar, N. Stefanatos, T. Pedersen and R.

- Wagner, "Classification of Atmospheric Stability for Offshore Wind Farms. In UPWIND 1A2 Meteorology, Final Report, Chapter 10, ECN-E--11-013," 2011.
- [158] A. Monin и A. Obukhov, «Basic Laws of Turbulent Mixing in the Surface Layer of the Atmosphere,» *Tr. Akad. Nauk SSSR Geophys. Inst.*, т. 24, № 151, pp. 163-187, 1954.
- [159] P. Argyle and S. Watson, "Application of CFD to Two Offshore Wind Turbine Wakes Incorporating Atmospheric Stability," in *European Wind Energy Association Conference and Exhibition*, Vienna, 2013.
- [160] F. Porté-Agel, Y. Wu, H. Lu and R. Conzemius, "Large-Eddy of Atmospheric Boundary Layer Flow Through Wind Turbines and Wind Farms," *Journal of Wind Engineering and Industrial Aerodynamics*, vol. 99, no. 4, pp. 154-168, 2011.
- [161] D. Muñoz-Esparza, B. Cañadillas, T. Neumann and J. van Beeck, "Turbulent Fluxes, Stability and Shear in the Offshore Environment: Mesoscale Modelling and Field Observations at FINO1," *Journal of Renewable and Sustainable Energy*, vol. 4, pp. 063136-063152, 2012.
- [162] O. Texier, C. Bezault, N. Girard, J.-C. Houbart and S. Pham, "Results of Integration of Atmospheric Stability in Wind Power Assessment Through CFD Modelling," in *European Wind Energy Association Annual Conference and Exhibition*, Copenhagen, 2012.
- [163] T. Neumann, K. Nolopp, V. Riedel, M. Strack, K. Herklotz and J. Stein, "Assessment of One Year Wind Measurements on the First Offshore Wind Research Platform in the German Bight - FINO1," in *DEWEK*, Wilhelmshaven, 2004.